Magnetic and magnetoelectric properties of lithium orthophosphates

Fogh, Ellen

Publication date:
2018

Document Version
Publisher's PDF, also known as Version of record

Magnetic and magnetoelectric properties of lithium orthophosphates

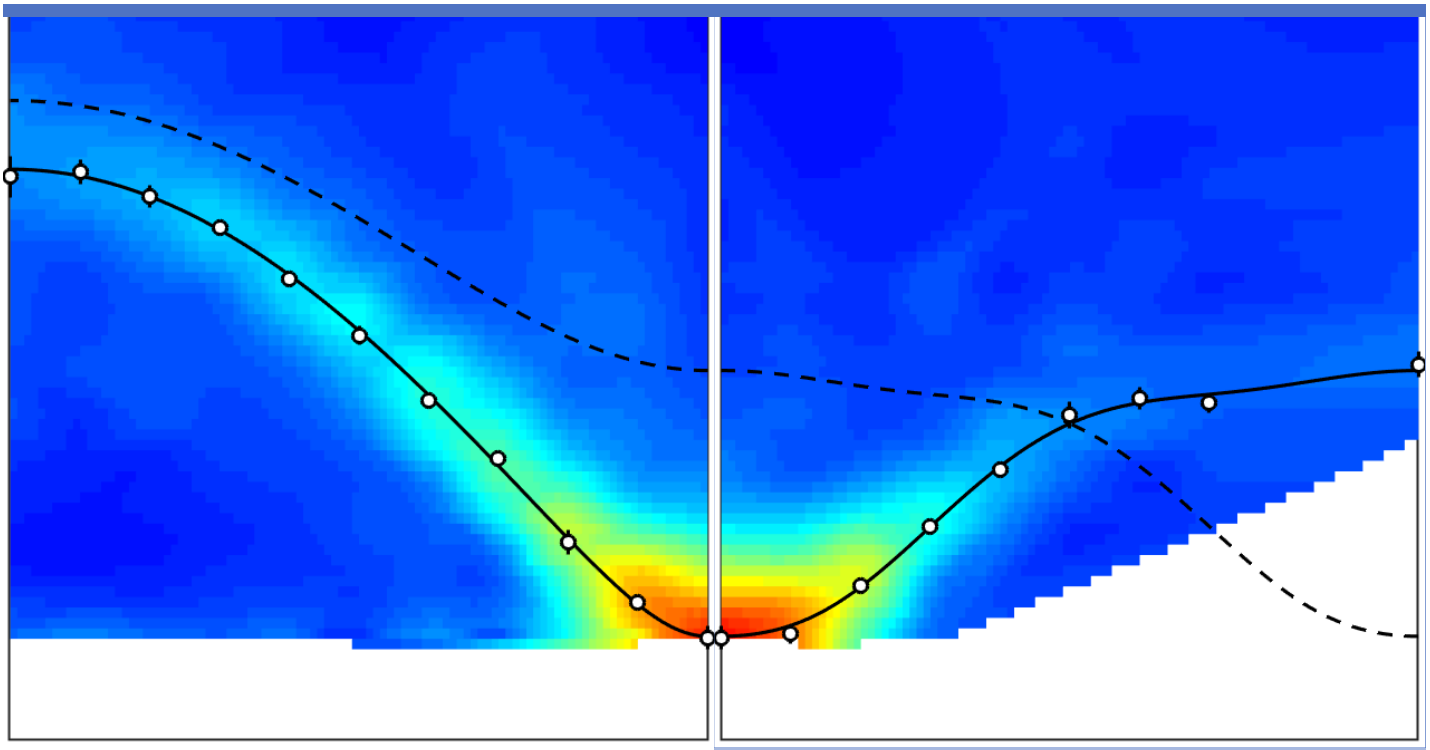

Ellen Fogh
November 2018

DTU Physics
Department of Physics

For mum, who shared my passion for patterns

Magnetic and magnetoelectric properties of lithium orthophosphates,

This thesis was prepared by
Ellen Fogh

Supervisors
Niels Bech Christensen, DTU Physics
Rasmus Toft-Petersen, DTU Physics

Due date: November 16th 2018
Comments: This thesis is part of the requirements to achieve the Doctorate of Philosophy (PhD) at the Technical University of Denmark. The studies were funded by Department of Physics and beam-time travels were covered by the Danish Agency for Science and Higher Education under DANSCATT.

Department of Physics
Technical University of Denmark

Fysikvej, Buildings 307-309-311-312
DK-2800 Kongens Lyngby
Denmark
Tel: (+45) 45 25 33 44
E-mail: info@fysik.dtu.dk
www.fysik.dtu.dk

Acknowledgements

Throughout this project a number of people have been of invaluable help to me – some work related, some for general well-being and some both. I would like to thank all of you. First of all, I would like to thank my supervisors Niels Bech Christensen and Rasmus Toft-Petersen for guiding me through four years of exciting research, for good company and for giving me a second chance.

A thousand thanks to all the instrument scientists who have assisted in setting up and running experiments as well as helping with data analysis and interpretation. I would especially like to thank Eric Ressouche for his enourmous help with solving the cycloid structure in $LiCoPO_4$, Maciej Bartkowiak for his patience teaching me Python/Mantid, Hiroyuki Nojiri for introducing us to his inpiring pulsed-field world and Oksana Zaharko for double checking my analysis regarding the zero-field structure in $LiCoPO_4$. Great thanks to Olav Syljuåsen who mentored me on the simulation side of the project. I am grateful to Jens Wenzel Andreasen for helping me out with the problems constantly showing up at the old Risø X-ray Laue camera. Thanks to Thomas T. Stibius Jensen, Mogens O. Stibius Jensen and Ole Trinhammer for getting the graps of group theory together with me. I would also like to thank all my colleagues at DTU Physics with whom I have shared many agreable lunch times and coffee breaks.

Thanks to friends – old and new – for being good company and equally happy to chat or party. Especially thanks to Henrik Jacobsen for all the nitty-gritty comments on the manuscript but mostly for being a great friend. Also thanks to Alex Gessner for making such effort to come see us all the time.

Thanks to my parents for always supporting my choices. I want to be like that for my children! Thanks to my brother for chats about everything from life to death and for good laughs. A special thanks to Ingerlise & Erik and Pia & Bjarne for providing a cozy base and lots of good food and wine in Copenhagen. Many thanks to everyone in the extended family who are always genuinely interested in how things are going and who are generally just good company. I am extremely grateful for having such a loving family.

Finally, I would like to thank Mark for always supporting me, for being such an amazing person and a great dad. Thanks to our little Ida for being such a bright ray of sunshine and for forcing me to slow down and enjoy the moment. I am so happy to have you both!

Abstract

Understanding the interplay between magnetic and electric properties in condensed matter is of importance in both fundamental science and in applications such as data storage. In this thesis, magnetic and magnetoelectric properties of the lithium orthophosphates were studied by means of magnetization, pyrocurrent and heat capacity measurements as well as neutron diffraction, inelastic neutron scattering and Monte Carlo simulations.

The magnetic phase diagram of $LiCoPO_4$ was established up to 25.9 T applied along the easy b-axis and several magnetic phases were characterized. For fields in the interval $11.9 - 20.5$ T, a magnetized elliptic cycloid structure was identified. In the hysteresis region just below 11.9 T, supplementing magnetic phases with longer periods coexist and a simple model was proposed in an endeavour to explain the observed behavior. For $20.5 - 21.0$ T, the periodicity of the magnetic structure stays the same as for the cycloid but a spin re-orientation takes place. For fields greater than 21.0 T, a commensurate magnetic structure which supports the magnetoelectric effect resides. Furthermore, for magnetic fields applied along a, the induced ferromagnetic moment couples via the Dzyaloshinskii-Moriya interaction to yield a field-induced spin canting. This canting is speculated to be linked to the magnetoelectric effect in the low-field commensurate phase of $LiCoPO_4$.

Using both DC and pulsed magnetic fields together with time-of-flight Laue neutron diffraction, magnetic structures of $LiNiPO_4$ were directly probed up to a staggering 42 T applied along the easy c-axis. For fields in the interval $20.9 - 37.6$ T, magnetic structure refinements indicate that a spiral is formed. Like for $LiCoPO_4$, there is then a short interval, $37.6 - 39.4$ T, where the period of the magnetic structure remains constant but the spins re-orient. Above 39.4 T, a commensurate phase which displays the magnetoelectric effect is established and the effect was encapsulated by a microscopic model. The discovery of yet another commensurate magnetoelectric phase in $LiNiPO_4$ thus consolidates the tie between commensurability and magnetoelectricity in the lithium orthophosphates in general.

Subtituting Fe on the magnetic site in $LiNiPO_4$ creates interesting new magnetic and magnetoelectric phases in the mixed compounds, $LiNi_{1-x}Fe_xPO_4$. At low Fe contents, the magnetic behavior of the parent compound, $LiNiPO_4$, is mostly preserved. However, the manner and number of discrepancies from the stoichiometric material only increase when the Fe content is raised. In case of $LiNi_{0.8}Fe_{0.2}PO_4$, the major spin component in the ground state is along a as opposed to along c for

$LiNiPO_4$ and along b for $LiFePO_4$. Moreover, for a temperature interval in between the ground state and paramagnetic state, another commensurate antiferromagnetic phase with spins along b exists. Upon applying a magnetic field along a at low temperatures, there is a broad phase transition at $\sim 8\,\mathrm{T}$ where the magnetic structure remains commensurate but the spin orientation changes. Abnormal behavior of the energy gap in the spin-wave dispersion was observed at this field-induced transition. All observed magnetic phases in $LiNi_{0.8}Fe_{0.2}PO_4$ are commensurate and as with the other lithium orthophosphates, they also support the magnetoelectric effect. The temperature and field dependencies of the magnetoelectric tensor elements prove extremely complex. Furthermore, more finite tensor elements were observed in $LiNi_{0.8}Fe_{0.2}PO_4$ than in the parent compounds, $LiNiPO_4$ and $LiFePO_4$.

Monte Carlo simulations were performed on the general $LiNi_{1-x}Fe_xPO_4$ system. The observed zero-field magnetic structures were reproduced, the understanding of the various phases extended and the importance of competing anisotropies in the system illuminated.

Competing exchange couplings and single-ion anisotropies lead to a plethora of magnetic phases in the lithium orthophosphates. Finding the optimal spin configuration is not trivial in such systems and introducing different ions on the magnetic site only intensifies the frustration. Although the relationship between magnetism and magnetoelectricity in the lithium orthophosphates is not yet completely clear-cut, one thing is clear: all commensurate phases are also magnetoelectric.

Resumé

Forståelsen af samspillet mellem magnetiske og elektriske egenskaber i faste stoffer er vigtig både for grundforskning og for anvendelser så som datalagring. I denne afhandling, blev de magnetiske og magnetoelektriske egenskaber af litiumortofosfaterne undersøgt ved hjælp af magnetiserings-, pyrostrøm- og varmefyldemålinger samt neutrondiffraktion, uelastisk neutronspredning og Monte Carlo-simuleringer.

Det magnetiske fasediagram for $LiCoPO_4$ blev etableret op til 25.9 T påført langs den nemme b-akse og flere magnetiske faser blev karakteriseret. For felter i intervallet $11.9 - 20.5$ T, blev en en magnetiseret elliptisk cykloidestruktur identificeret. I hystereseområdet lige under 11.9 T optræder supplerende magnetiske faser med længere perioder og en simpel model blev foreslået i en bestræbelse på at forklare den iagttagede opførsel. For $20.5 - 21.0$ T forbliver perioden af den magnetiske struktur den samme som for cykloiden men en nyorientering af momenterne finder sted. For felter større end 21.0 T eksisterer der en kommensurabel magnetisk struktur som understøtter den magnetoelektriske effekt. For magnetfelter påtrykt langs a kobler det inducerede ferromagnetiske moment desuden via Dzyaloshinskii-Moriya-vekselvirkningen og resulterer i en feltinduceret spinkantning. Der spekuleres om denne kantning er knyttet til den magnetoelektriske effekt i den kommensurable lavtemperaturfase i $LiCoPO_4$.

Ved at bruge både DC og pulsede magnetfelter sammen med time-of-flight Laue neutrondiffraktion blev de magnetiske strukturer i $LiNiPO_4$ probet direkte op til rekordhøje 42 T påtrykt langs den nemme c-akse. Magnetisk strukturraffinementer indikerer at en spiral dannes for felter i intervallet $20.9 - 37.6$ T. Ligesom for $LiCoPO_4$ er der et kort feltinterval, $37.6 - 39.4$ T, hvor perioden af den magnetiske struktur forbliver konstant og en spinnyorientering finder sted. En kommensurabel fase der udviser den magnetoelektriske effekt etableres for felter større end 39.4 T og effekten sammenfattedes i en mikroskopisk model. På den måde fastgør opdagelsen af endnu en kommensurabel magnetoelektrisk fase i $LiNiPO_4$ forbindelsen mellem kommensurabilitet og magnetoelektricitet i litiumortofosfaterne generelt.

Ved erstatning af Fe på den magnetiske ions plads i $LiNiPO_4$ skabes interessante nye magnetiske og magnetoelektriske faser i de blandede forbindelser, $LiNi_{1-x}Fe_xPO_4$. Den magnetiske opførsel af modersystemet, $LiNiPO_4$, er stort set intakt ved lavt indhold af Fe. Antal og karakter af afvigelserne fra det støkiometriske materiale øges imidlertid kun når indholdet af Fe stiger. I tilfælde af $LiNi_{0.8}Fe_{0.2}PO_4$ er hovedspinkomposanten langs a i grundtilstanden modsat langs c for $LiNiPO_4$ og langs b

for $LiFePO_4$. Derudover er der i et temperaturinterval ind imellem grundtilstanden og den paramagnetiske fase yderligere en kommensurabel antiferromagnetisk fase med spin langs b. En bred faseovergang ved $\sim 8\,\mathrm{T}$ induceres ved at påtrykke magnetfelt langs a. Over overgangen er strukturen fortsat kommensurabel men med en ny spinorientering. Anormal opførsel af energigabet i spinbølgedispersion observeredes ved denne feltinducerede faseovergang. Alle observerede magnetiske faser i $LiNi_{0.8}Fe_{0.2}PO_4$ er kommensurable og som med de andre litiumortofosfater understøtter de også den magnetoelektriske effekt. Temperatur- og feltafhængighederne af de magnetoelektriske tensorelementer er utroligt komplekse. Derudover blev der observeret flere endelige tensorelementer for $LiNi_{0.8}Fe_{0.2}PO_4$ end for modersystemerne, $LiNiPO_4$ og $LiFePO_4$.

Monte Carlo simulationer blev udført på det generelle $LiNi_{1-x}Fe_xPO_4$ system. De observerede magnetiske nulfeltsstrukturer blev reproduceret, forståelsen af de forskellige faser udvidet og betydningen af konkurrerende anisotropier i systemet belyst.

Konkurrencen mellem exchange-vekselvirkninger og enkelt ion anisotropier fører til en mangfoldighed af magnetiske faser i litiumortofosfaterne. Den optimale spinkonfiguration er ikke triviel at finde i et sådant system og introduktionen af forskellige magnetiske ioner forstærker kun frustationen. Selvom sammenhængen mellem magnetisme og magnetoelektricitet i litiumortofosfaterne endnu ikke er forstået fuldt ud så står én ting klart: Alle kommensurable faser er også magnetoelektriske.

Contents

Acknowledgements **i**

Abstract **iii**

Resumé **v**

Contents **vii**

List of Figures **xi**

List of Tables **xvii**

List of Publications **xix**

Introduction **1**

I Scientific background **3**

1 Magnetism and ferroelectricity **5**

1.1 Elements of magnetism 5

1.2 Ferroelectrics, multiferroics and magnetoelectrics 9

2 Neutron scattering: probing magnetic structures and dynamics **13**

2.1 Basic properties of the neutron 13

2.2 Neutron scattering cross sections 14

2.3 Interaction potentials 15

2.4 Scattering from ordered systems 16

2.5 Polarized neutrons 18

3 Material background **21**

3.1 The lithium orthophosphates 21

3.2 Mixed anisotropy magnets 27

4 Experimental Techniques **29**

4.1 Macroscopic material characterization methods 29

4.2 Neutron diffraction 33

4.3 Inelastic neutron scattering 35

4.4 Polarized neutrons 36

5 Monte Carlo simulations **39**

5.1 Model, assumptions and other considerations 39

5.2 Implementation 41

5.3 Code testing 44

II Results & discussion **49**

6 Magnetic order in $LiCoPO_4$ **51**

6.1 Magnetic phase diagram 51

6.2 Investigations at zero field 54

6.3 Magnetic structure at intermediate fields 60

6.4 Hysteresis, phase coexistence and stacking faults 63

6.5 Magnetic structures at high fields 69

6.6 The enigmatic phase 71

6.7 Field-induced spin canting and the Dzyaloshinskii-Moriya interaction 72

6.8 Summary 76

7 Magnetic structures in $LiNiPO_4$ at high fields **77**

7.1 Magnetic phase diagram 77

7.2 Magnetic structure in phase IV 83

7.3 Magnetic structures in phases V and VI 84

7.4 Magnetic structure and magnetoelectric effect in phase VII 86

7.5 Summary 87

8 Magnetism and magnetoelectricity in $LiNi_{1-x}Fe_xPO_4$ 89

8.1 $LiNi_{0.94}Fe_{0.06}PO_4$ 89

8.2 $LiNi_{0.8}Fe_{0.2}PO_4$ 97

8.3 Monte Carlo simulations 118

8.4 Summary and outlook 128

Conclusions 131

A Monte Carlo code testing and additional simulations 135

A.1 Comparison with analytical results 135

A.2 Symmetry checks 138

A.3 More Monte Carlo simulations 141

B Data analysis on the HFM/EXED and NOBORU experiments on $LiNiPO_4$ 145

B.1 Zero-field data and background subtraction on NOBORU 145

B.2 Integrated peak intensities on HFM/EXED 145

C Pyrocurrent background subtraction 151

D Details on the data analysis of the inelastic neutron scattering experiment on $LiNi_{0.8}Fe_{0.2}PO_4$ 155

Bibliography 161

Paper I 171

Paper II 181

Paper III 193

List of Figures

1.1 Spin states for magnetic ions as found by following Hund's rules . . 6

1.2 Transition metal ion in an octahedral environment 7

1.3 Energy level splitting due to an octahedral crystal field 7

1.4 Relationship between different magnetic and electric material categories 10

1.5 Magnetic moments of two transition metal ions interacting via indirect exchange through an oxygen ion 11

1.6 Sketch of a MERAM device 11

2.1 Fission and spallation for neutron production 14

2.2 Neutron scattering cross section and scattering triangle 15

2.3 Definition of coordinate system used for polarization analysis 19

3.1 Crystal and commensurate magnetic structure of LiMPO$_4$ 22

3.2 Magnetic susceptibility curves, magnetization measurements and magnetic phase diagrams for the lithium orthophosphates 23

3.3 Temperature dependencies of the magnetoelectric coefficients for LiMPO$_4$ 25

3.4 Temperature dependence of SHG tensor elements representing spin components along b and c in LiNi$_{0.8}$Fe$_{0.2}$PO$_4$ and proposed spin orientations for the two different magnetic phases 26

3.5 Magnetic phase diagrams of systems with competing order parameters. 28

4.1 VSM and AC susceptibility experimental setup 30

4.2 Magnet pulse shape and setup for magnetization measurements . . . 31

4.3 Heat capacity experimental setup 31

4.4 Insert and samples for pyrocurrent measurements 32

4.5 Two-axis diffractometer 33
4.6 Time-of-flight Laue diffractometer 34
4.7 Triple-axis spectrometer 36
4.8 Polarized neutron setup 37

5.1 Ion positions within unit cell as used in simulations 42
5.2 Sketch of simulation unit cell with only one nearest-neighbor exchange coupling 44
5.3 Energy vs. temperature for four simple cases 45
5.4 Energy as a function of MCS for runs with different levels of Fe . . . 46
5.5 Comparison of runs with different system sizes 47
5.6 Comparison of runs with different start configurations 48

6.1 Temperature scans of magnetization, heat capacity and integrated neutron intensity of the (3,0,1) Bragg peak at different fields 52
6.2 Field scans of the magnetization and neutron intensity of the (3,0,1) Bragg peak at different temperatures 53
6.3 Magnetic phase diagram of $LiCoPO_4$ for magnetic fields applied along b 53
6.4 Inverse susceptibility as a function of temperature for $LiCoPO_4$ . . . 54
6.5 Observed vs. calculated intensities as obtained by refining the atomic positions of $LiCoPO_4$ in FULLPROF 55
6.6 Refinement results for the zero-field magnetic structure of $LiCoPO_4$ 56
6.7 Neutron diffraction data from RITA-II and projections in the (b, c)-plane of the magnetic structures of $LiCoPO_4$ for zero field and for $\mathbf{H}||\mathbf{a}$ 58
6.8 Neutron scattering intensity as a function of $(3, K, 1)$ for selected fields at 2 K 61
6.9 Calculated vs. observed scattering intensities for the refined magnetic structure in the $\frac{1}{3}$ magnetization phase 61
6.10 Magnetic structure for $11.9 - 20.5$ T applied along b 62
6.11 Color plots of the intensity of $(3, K, 1)$ as a function of magnetic field applied along b 64
6.12 Stacking faults 66
6.13 Magnetic susceptibiliy and magnetization measurements of $LiCoPO_4$ as obtained with the pulsed-field technique 68
6.14 Neutron diffraction results from HFM/EXED 71

6.15 Spontaneous magnetization of $LiCoPO_4$ as a function of temperature 72

6.16 Magnetization, field-induced canting angle and integrated neutron intensity of $(0, 2, 1)$ for magnetic fields applied along a 73

7.1 Magnetic phase diagram of $LiNiPO_4$ up to 42 T applied along c . . . 78

7.2 Commensurate magnetic structures of $LiNiPO_4$ in phases I, IV and VII 78

7.3 Magnetization and electric polarization along a in $LiNiPO_4$ as measured at 4.2 K as a function of applied magnetic field along c 79

7.4 Temperature and field dependence of the $(0, K, 0)$ magnetic Bragg peaks as measured by neutron diffraction up to 23 T 80

7.5 Pulsed-field Laue neutron diffraction up to 42 T 82

7.6 TOF profiles of $(0, -1, 0)$, $(-1, -2, 0)$ and $(1, -1, 0)$ as measured at HFM/EXED 83

7.7 Cartoons illustrating structures refined in FULLPROF in phase V . . 85

7.8 Model of the magnetoelectric effect in $LiNiPO_4$ in phase VII 86

8.1 Magnetic phase diagrams of $LiNi_{0.94}Fe_{0.06}PO_4$ for magnetic fields applied along a and b 90

8.2 Magnetic phase diagram of $LiNi_{0.94}Fe_{0.06}PO_4$ for magnetic fields applied along c 90

8.3 Magnetic susceptibility measurements for $LiNi_{0.94}Fe_{0.06}PO_4$ at 0.5 T applied along the three principal crystal directions 91

8.4 Magnetization as a function of decreasing temperature and as a function of increasing magnetic field for $LiNi_{0.94}Fe_{0.06}PO_4$ 92

8.5 Neutron diffraction results on $LiNi_{0.94}Fe_{0.06}PO_4$ 93

8.6 Neutron counts as a function of energy transfer along $(H, 1, 0)$ and $(0, K, 0)$ in $LiNi_{0.94}Fe_{0.06}PO_4$ 95

8.7 Spin-wave dispersion along $(H, 1, 0)$ and $(0, K, 0)$ for $LiNi_{0.94}Fe_{0.06}PO_4$ 97

8.8 Magnetic phase diagram of $LiNi_{0.8}Fe_{0.2}PO_4$ for magnetic fields applied along a 98

8.9 Magnetic phase diagram of $LiNi_{0.8}Fe_{0.2}PO_4$ for magnetic fields applied along b 98

8.10 Magnetic phase diagram of $LiNi_{0.8}Fe_{0.2}PO_4$ for magnetic fields applied along c 98

8.11 Magnetic susceptibility measurements for $LiNi_{0.8}Fe_{0.2}PO_4$ at 0.5 T applied along the three principal crystal directions 99

8.12 Magnetization as a function of decreasing temperature and as a function of increasing magnetic field for $LiNi_{0.8}Fe_{0.2}PO_4$ 100

8.13 Comparison of magnetization and pyrocurrent data 101

8.14 Pyrocurrent as a function of temperature for selected field values . . 103

8.15 Electric polarization as a function of temperature for selected field values 103

8.16 Rocking curves of selected Bragg peaks as measured on $LiNi_{0.8}Fe_{0.2}PO_4$ at RITA-II 106

8.17 Neutron intensity of $(0, 0, \bar{1})$, $(0, 1, 0)$ and $(3, 0, \bar{1})$ as a function of increasing temperature as measured on $LiNi_{0.8}Fe_{0.2}PO_4$ at E5 107

8.18 Temperature scans of the peak intensity of $(0, 1, 0)$, $(0, 0, 1)$ and $(0, 1, 2)$ as measured on $LiNi_{0.8}Fe_{0.2}PO_4$ at 4F1 108

8.19 The angle, ϕ, as calculated from the polarized neutron intensities of $(0, 1, 2)$ and sketches of the zero-field magnetic structures in $LiNi_{0.8}Fe_{0.2}PO_4$ 111

8.20 Intensities of magnetic Bragg peaks $(0, 0, 1)$ and $(0, 1, 0)$ as well as nuclear Bragg peak $(0, 2, 0)$ as a function of magnetic field applied along a 113

8.21 Energy scans at constant $\mathbf{Q} = (0, 1, 0)$ at different field values 115

8.22 Color plot of the measured neutron intensities at $\mathbf{Q} = (0, 1, 0)$ as a function of field and energy transfer 115

8.23 Neutron counts as a function of energy transfer along $(0, K, 0)$ and $(0, 1, L)$ or $(0, 3, L)$ in $LiNi_{0.8}Fe_{0.2}PO_4$ 116

8.24 Spin-wave dispersion along $(0, K, 0)$ and $(0, 1, L)$ or $(0, 3, L)$ for $LiNi_{0.8}Fe_{0.2}PO_4$ 116

8.25 Sketch of the different ways to place N nearest Fe neighbors in the (b, c)-plane for a given magnetic ion, M 117

8.26 Single-ion anisotropy energies as a function of Fe concentration . . . 119

8.27 Color plots of the single-ion anisotropy energy landscape 120

8.28 Simulation of optimal spin direction as a function of Fe concentration 121

8.29 Temperature scans for simulations with $x = 0.0, 0.3$ and 1.0 122

8.30 Color plot of the heat capacity as a function of x and T 123

8.31 Color plots of the C type order parameter as a function of x and T . 123

8.32 Temperature scans with different Ni-Fe interaction strengths for $x = 0.3$ 124

8.33 Temperature scans of the C order parameter for the simplified model for $x = 0.3$ and with different values of J_b 125

8.34 Temperature scans for simulations with $x = 0.0, 0.3$ and 1.0 for the simple model 125

8.35 Color plot of the heat capacity as a function of x and T for the simple model . . . 126

8.36 Color plots of the C type order parameter as a function of x and T for the simple model . . . 126

8.37 Comparison of polarized neutron diffraction data from 4F1 and Monte Carlo simulations . . . 127

A.1 Coordinates of spins 1 and 2. . . . 136

A.2 Symmetry equivalent configurations . . . 140

A.3 Total energy as a function of MCS for 10 different runs . . . 140

A.4 Temperature scans for simulations with $x = 0.0, 0.3$ and 1.0 . . . 141

A.5 Color plot of the heat capacity as a function of x and T using a new set of parameters . . . 143

A.6 Color plots of the C type order parameter as a function of x and T using a new set of parameters . . . 143

B.1 Zero-field data from NOBORU . . . 146

B.2 Detector images from the HFM/EXED experiment on $LiNiPO_4$ . . . 147

B.3 Lineshape of $(1, -1, 0)$ as a function of TOF without and with background subtraction . . . 147

C.1 Temperature scans of the pyrocurrent at various magnetic field values for $\mathbf{H}||\mathbf{a}$ . . . 152

C.2 Temperature scans of the pyrocurrent at various magnetic field values for $\mathbf{H}||\mathbf{b}$ . . . 153

C.3 Temperature scans of the pyrocurrent at various magnetic field values for $\mathbf{H}||\mathbf{c}$ . . . 154

D.1 Scan through $\Delta E = 0$ at $(0, 1, 0)$ at 40 K, 0 T and with $k_f = 1.3\text{Å}^{-1}$ 156

D.2 Scans of $(0, 1, 0)$ through $\Delta E = 0$ at different field values . . . 156

D.3 Scans of incoherent scattering at $(0, 0.75, 0.5)$ through $\Delta E = 0$ at different field values . . . 157

D.4 Individual plots of neutron intensities as a function of energy transfer for measurements performed along $(0, K, 0)$ at 12 T, 1.7 K . . . 158

List of Tables

1.1 Electronic configurations and magnetic ground states following Hund's rules 6

2.1 Separation of spin components by polarization analysis 19

3.1 Crystallographic, magnetic and magnetoelectric properties of LiMPO$_4$. 24

4.1 List of instruments used for neutron diffraction in the presented work. 33

4.2 List of time-of-flight diffractometers used during the presented work. 34

4.3 List of three-axis spectrometers used during the presented work. . . 36

5.1 Ion numbers and positions as used in simulations 42

6.1 Atomic positions for LiCoPO$_4$ as obtained from refinement of TriCS data 55

6.2 Refinement results for the zero-field magnetic structure of LiCoPO$_4$ as obtained in FULLPROF 56

6.3 Magnetic basis vectors reflected by the key Bragg peaks used to establish the magnetic structure of LiCoPO$_4$ 57

6.4 Irreducible representations for *Pnma*. 59

6.5 Atomic positions for LiCoPO$_4$ obtained from FULLPROF refinement 61

7.1 Magnetic basis vectors reflected by the commensurate magnetic Bragg peaks observed in phases I, IV and V at the HFM/EXED experiment 84

7.2 Observed vs. calculated intensities for proposed structures in phase V 85

8.1 Parameters obtained by fitting the Curie-weiss law to the magnetic susceptibility curves of LiNi$_{1-x}$Fe$_x$PO$_4$ 91

8.2 Exchange and single-ion anisotropy parameters for LiNi$_{1-x}$Fe$_x$PO$_4$. 96

8.3 Magnetic basis vectors reflected by selected magnetic Bragg peaks observed in the RITA-II, EIGER, E5, E4 and 4F1 experiments . . . 106

8.4 Probed spin components for the different scattering vectors measured at 4F1 . . . 108

8.5 Magnetic point groups and linear magnetoelectric tensor forms for spin arrangements of symmetry (↑↑↓↓) . . . 109

8.6 Probability for having N nearest Fe neighbors . . . 117

8.7 Single-ion anisotropy constants . . . 119

8.8 Exchange parameters for Ni-Ni, Ni-Fe and Fe-Fe bonds as used in the Monte Carlo simulations . . . 122

8.9 Exchange parameters for all bonds as used in the simplified model . 124

8.10 Single-ion anisotropy constants for Ni and Fe as used in the simplified model . . . 124

A.1 Symmetry checks for all parameters set to zero except one . . . 139

A.2 Symmetry checks for all parameters set to 1 meV except one . . . 139

A.3 Symmetry checks for all parameters set to zero except one or two anisotropy constants . . . 139

A.4 Symmetry checks for all parameters set to 1 meV except one, with simulated annealing . . . 139

A.5 Exchange parameters for Ni-Ni, Ni-Fe and Fe-Fe bonds as used in the Monte Carlo simulations . . . 142

A.6 Single-ion anisotropy constants for Ni and Fe . . . 142

B.1 List of TOF intervals and detector indices for calculating integrated peak intensities . . . 148

B.2 Integrated intensities as found in Mantid for the HFM/EXED experiment on $LiNiPO_4$ . . . 149

List of Publications

Paper I
Field-induced reentrant magnetoelectric phase in $LiNiPO_4$
R. Toft-Petersen, E. Fogh, T. Kihara, J. Jensen, K. Fritsch, J. Lee, G. E. Granroth, M. B. Stone, D. Vaknin, H. Nojiri and N. B. Christensen
Physical Review B **95**, 064421 (2017)

Paper II
Magnetic order, hysteresis and phase coexistence in magnetoelectric $LiCoPO_4$
E. Fogh, R. Toft-Petersen, E. Ressouche, C. Niedermayer, S. L. Holm, M. Bartkowiak, O. Prokhnenko, S. Sloth, F. W. Isaksen, D. Vaknin and N. B. Christensen
Physical Review B **96**, 104420 (2017)

Paper III
Dzyaloshinskii-Moriya interaction in magnetoelectric $LiCoPO_4$
E. Fogh, O. Zaharko, J. Schefer, C. Niedermayer, S. Holm-Dahlin, M. K. Sørensen, A. B. Kristensen, N. H. Andersen, D. Vaknin, N. B. Christensen and R. Toft-Petersen
(To be submitted to Physical Review B)

Introduction

Magnetism was discovered in ancient times when people noticed that lodestone (magnetite) attracts iron and the phenomenon found its very first application in compasses for navigation[1]. Today, of course, technologies based on magnetic materials are encountered in numerous places: motors, burglar alarms, magnetic resonance imaging, loudspeakers, data storage etc. Especially data storage has been revolutionized by breakthroughs such as the giant magnetoresistance and the magnetic tunnel junction and digital memory technology research is ever striving towards higher information density, higher read/write speeds and lower energy consumption. In recent years, the so-called *solid-state drives (SSDs)* consisting of grids of transistors provide non-volatile memory with many advantages over traditional disk drives[2]. SSDs are based on semiconductor technology rather than magnetic media and without moving parts, SSD offers faster, quieter, lower power and more reliable data storage. However, a number of crucial disanvantages such as high cost and a finite number of write cycles means that more conventional disk drive technologies continue to attract attention in research and industry.

One promising class of materials for data storage applications is the magnetoelectrics. In these materials, an electric field induces a magnetization and thus information may be written by applying a voltage which would be much faster and less energy-consuming than today's magnetically manipulated storage devices. Moreover, solid-state memory cells may be created by combining magnetoelectric and ferromagnetic materials in the so-called cross-point architecture, where bits are addressed by two arrays of perpendicular conducting lines[3].

In any case, in order to push forward the techological progress and thereby contribute to advancements in society, culture and medicine, we much first understand the underlying nature of a given problem. Understanding atomic and magnetic interactions offers the possibility to engineer new materials with taylored properties, leaving fundamental material research as one of the most important building blocks in modern society. Consequently, material science has seen a formidable development in experimental techniques that enables observation of the world on

atomic level. Among these are electron microscopy, various scattering techniques as well as X-ray, ion and optical spectroscopy. Developments in instrumentation drives new discoveries that potentially lead to new applications.

Turning from the above somewhat lofty discussion of science and society, my work is focussed on the interplay between the magnetic structures and the magnetoelectric effect in the lithium orthophosphates. Some of these materials contain a single magnetic ion – like $LiCoPO_4$ and $LiNiPO_4$ – and some contain a mixture of two different magnetic ions – like $LiNi_{0.8}Fe_{0.2}PO_4$ and $LiCo_{0.7}Ni_{0.3}PO_4$. [Note that results on the latter compound are excluded due to incomplete analysis.] The magnetic phase diagrams of the stoichiometric compounds are already well-investigated. In this thesis, our knowledge of these materials is extended by studying phase transitions and magnetic structures for applied magnetic fields up to 42 T. The mixed compounds, on the other hand, are far less explored. Mixing magnetic ions with different single-ion anisotropies introduces elements of disorder and frustration and brings about interesting new behavior of both magnetic and magnetoelectic properties. The lithium orthophosphates provide a relatively simple system where the effects of competeting anisotropies may be explored.

Magnetoelectric properties of the materials were studied by means of electric polarization and pyrocurrent measurements while magnetic structures and dynamics were characterized using magnetization measurements and neutron scattering. The magnetic moment of the neutron enables direct probing of magnetic structures and is an invaluable tool in this study. Since the first implementation of neutron scattering in the first half of the last century, the technique has experienced a tremendous development branching out from core studies on magnetic and other strongly correlated electron systems to pharmaceuticals, re-newable energy, biology and life sciences. One of the many advantages of neutron scattering is the possibility for parametric studies, i.e. following material behavior as a function of e.g. applied pressure or magnetic field. In the present work, magnetic properties were studied as a function of temperature and applied magnetic field.

Monte Carlo simulations were performed in order to gain better insight as to the magnetic order of the mixed lithium orthophosphates. Based on random numbers, the Monte Carlo methods is ideal for describing disordered systems. Additionally, the simulations assist in the interpretation of neutron diffraction results.

This thesis consists of two parts: I Scientific background and II Results & discussion. The first part is made up of Chapters 1-5. Here, the basics of magnetism, magnetoelectricity, neutron scattering and the lithium orthophosphates are covered together with an overview of experimental techniques and Monte Carlo simulations. The second and longer part holds Chapters 6-8 where results regarding $LiCoPO_4$, $LiNiPO_4$ and the mixed compounds, $LiNi_{1-x}Fe_xPO_4$, are presented.

Part I

Scientific background

Chapter 1

Magnetism and ferroelectricity

This chapter is meant as a summary of the relevant concepts of magnetism and the magnetoelectric effect. More detailed descriptions are found in text books such as Refs. 4, 5 or review papers such as Refs. 6, 7.

1.1 Elements of magnetism

Magnetism is a phenomenon originating from electron interactions in crystalline materials. In classical electromagnetism, the magnetic moment of an electron orbiting a nucleus is associated with its angular momentum. In the quantum mechanics, the *orbital angular momentum* depends on the state of the electron, given by the usual quantum numbers, l and m_l. On top of that, the electron possesses an intrinsic *spin angular momentum* (or just *spin* for short), characterized by quantum numbers $s = \frac{1}{2}$ and $m_s = \pm\frac{1}{2}$. In general, both spin and orbital momenta may contribute to the electronic state.

The isolated atom. Atoms generally contain more than one electron and they will seek to mimize the overall energy described by the following Hamiltonian:

$$\hat{\mathcal{H}} = \sum_{i=1}^{Z} \left(\frac{p_i^2}{2m_e} + U_i \right) + \sum_{\langle i,j \rangle} V_{ij} + \sum_{i=1}^{Z} \xi_i \, \mathbf{l}_i \cdot \mathbf{s}_i,$$

where the first term describes the kinetic energy of the electrons with momentum, $\mathbf{p}_i$, mass, m_e, and the Coulomb interactions between electrons and nucleus with potential, U_i. The second term accounts for electron-electron interactions with potential, V_{ij}, and the third term includes a relativistic effect arising from the interaction between an electron's spin and its orbital motion – the so-called *spin-orbit coupling*. In the rest frame of the electron, the nucleus appears to orbit the electron and this creates a magnetic field at the electron position given in special relativity by $\mathbf{B}_i = \frac{\boldsymbol{\varepsilon}_i \times \mathbf{v}_i}{c^2}$. Here $\mathbf{v}_i$ is the velocity of the nucleus as seen by the electron, c the speed of light and $\boldsymbol{\varepsilon}_i = -\nabla V(r_i)$ the electric field at the electron position due to the nucleus with the corresponding potential energy, $V(r_i)$.

Table 1.1: *Electronic configurations and magnetic ground states for the 3d transition metal ions relevant to this thesis as found by following Hund's rules.*

Ion	Configuration	S	L	J
Mn^{2+}	[Ar]$3d^5$	5/2	0	5/2
Fe^{2+}	[Ar]$3d^6$	2	2	4
Co^{2+}	[Ar]$3d^7$	3/2	3	9/2
Ni^{2+}	[Ar]$3d^8$	1	3	4

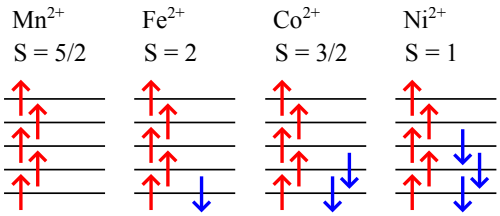

Figure 1.1: *Spin states for the magnetic ions relevant to this thesis as found following Hund's rules.*

The magnetic field interacts with the electron spin to yield the spin-orbit coupling term in the Hamiltonian: $\hat{\mathcal{H}}_{\mathrm{SO}} = \sum_{i=1}^{Z} \frac{eh^2}{2m_e c^2 r_i} \frac{dV(r_i)}{dr_i} \mathbf{l}_i \cdot \mathbf{s}_i$. The spin-orbit coupling parameter is then identified as $\xi_i = \frac{eh^2}{2m_e c^2 r_i} \frac{dV(r_i)}{dr_i}$.

The above many-body Hamiltonian is in general difficult to solve and various approaches using pertubation theory exist. Only unfilled shells contribute to the angular momenta and the electronic ground state configuration can be estimated by using *Hund's rules*: (1) Maximize the total spin, S. (2) Maximize the total orbital moment, L. (3) Choose the total angular momentum as $J = |L - S|$ for less than half full shells and $J = |L + S|$ for more than half full shells. The first rule arises from minimzing the Coulomb repulsion by placing electrons in different orbitals. In a classical cartoon picture, the second rule also minimizes the Coulomb repulsion by ensuring that as many electrons as possible travel around the nucleus in the same direction and are therefore less likely to meet. The third rule optimizes the energy arising from the spin-orbit coupling. The magnetic ground states found by applying Hund's rules for the 3d transition metal ions relevant for this thesis are listed in Table 1.1 and the spin configurations are illustrated in Fig. 1.1.

Applying a magnetic field to an isolated magnetic moment may yield a *diamagnetic* and/or *paramagnetic* response with a negative and positive magnetic susceptibility respectively. These effects are described in more detail elsewhere, see e.g. Ref. 4.

Crystal fields. So far the considered magnetic moments possessed spherical symmetry, i.e. they were free to point in any direction. However, in many crystals, electrons belonging to a given ion interact strongly with neighboring electrons – usually the ones belonging to non-magnetic ions such as oxygen, sulphur or phosphorous. The result is that orbital energy levels are shifted and the ground state may be different compared to that of the free atom. Moreover, the overall magnetic moment may be restricted to certain crystallographic directions or planes. The results is magnetic *single-ion anisotropy*.

The local electronic environment, or *crystal field*, is determined by the shape of surrounding occupied orbitals. This thesis exclusively concerns magnetic ions, M^{2+}, in LiMPO$_4$, belonging to the 3d transition metals and hence they serve as an example of crystal field effects here. The partly filled 3d orbitals have relatively large spacial extents and their shapes have pronounced angular dependencies. In LiMPO$_4$, each transition metal ion is surrounded by 6 oxygen ions in an octahedral arrangement as shown in Fig. 1.2(a). The neighboring oxygen ions have partially filled 2p orbitals and electrons occupy states such that the Coulomb energy is

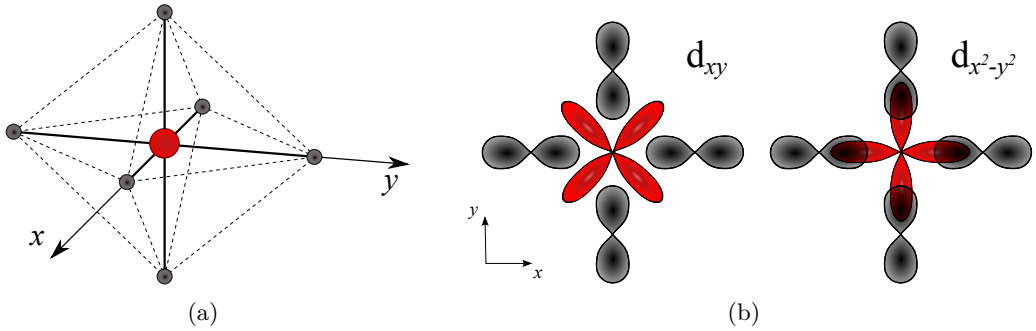

Figure 1.2: ***(a)*** *The transition metal ion (red) surrounded by oxygen (black) in an octahedral arrangement as realized to first order in $LiMPO_4$.* ***(b)*** *Octahedral environment projected to the (x, y)-plane and with the d orbital of the magnetic ion (red) and the p orbitals of the surrounding oxygen (black). The d_{xy} orbital has lower energy than the $d_{x^2-y^2}$ orbital due to less overlap.*

minimized by minimizing the orbital overlap as illustrated in Fig. 1.2(b). In this example, the d_{xy} orbital has lower energy than the $d_{x^2-y^2}$ orbital. In fact, the five 3d orbitals split into two groups in an octahedral environment: d_{xy}, d_{xz} and d_{yz} constitute the threefold degenerate t_{2g} levels whereas d_{z^2} and $d_{x^2-y^2}$ make up the twofold degenerate e_g levels. The diagrams in Fig. 1.3 show how the splitting may have consequences for the spin configuration and hence the ground state of the magnetic ion. The spin quantum number stays the same in the case of Ni^{2+} but the total spin may change in the case of Co^{2+}. If the energy gap, Δ, between the levels t_{2g} and e_g is sufficiently large, it becomes favorable for the spins to fill up the lower t_{2g} levels first instead of following Hund's rules. As a consequence, Co^{2+} may exist in a high spin state, $S = 3/2$, or a low spin state, $S = 1/2$. Even more dramatic is the difference for Fe^{2+} with high spin state, $S = 2$, versus low spin state, $S = 0$. It should be mentioned that the oxygen octahedron is merely the dominant part of the crystal field in the lithium orthophosphates. In reality the octahedra are destorted and the energy levels are all non-degenerate[8].

In summary, the large spacial extent of the 3d orbitals render the transition metals highly affected by the local electronic environment as compared to e.g. 4f ions with more localized orbitals. The result is that the crystal field may play a more important role than the spin-orbit interaction and hence Hund's third rule is not always obeyed. The 3d transition metals are therefore often said to display *orbital quenching* and $\langle L \rangle \approx 0$. The effects of the crystal field can be included in the spin

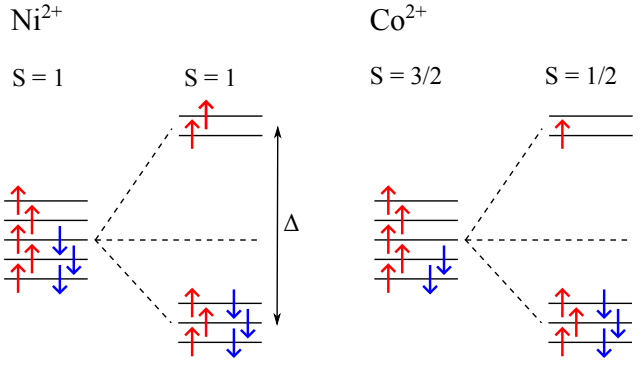

Figure 1.3: *Energy level splitting due to an octahedral crystal field illustrated for the Ni^{2+} and Co^{2+} ions. The size of the energy gap between the t_{2g} and e_g levels is denoted Δ. The total spin is the same with and without the crystal field for Ni^{2+} but the spin configuration changes for Co^{2+}.*

Hamiltonian with the following single-ion anisotropy term:

$$\hat{\mathcal{H}}_{\text{ani}} = \sum_i \sum_{\mu,\nu} \mathfrak{D}^{\mu\nu}\, S_i^\mu S_i^\nu,$$

where $\mathfrak{D}^{\mu\nu}$ are elements of the single-ion anisotropy tensor with $\mu, \nu = \{a, b, c\}$ the crystallographic directions. The lowest (highest) energy direction is named the *easy (hard) axis*. Often $\mathfrak{D}^{\mu\nu}$ is a diagonal tensor and we use the notation $\mathfrak{D}^{\mu\mu} = \mathfrak{D}^{\mu}$.

Inter-atomic interactions. Having discussed the interactions among the electrons of an isolated ion themselves as well as their interactions with the electrostatic environment, we now turn to the couplings between electrons located at different magnetic ions. These are essential for the formation of long range magnetic order and are the so-called *exchange interactions* described by the *Heisenberg model*:

$$\hat{\mathcal{H}}_{\text{ex}} = \sum_{\langle i,j \rangle} J_{ij}\, \mathbf{S}_i \cdot \mathbf{S}_j,$$

where the sum runs over all interacting spin pairs, $\langle i, j \rangle$. For *direct exchange*, the *exchange integrals*, J_{ij}, are defined by the overlap between wavefunctions describing the electronic states at ion site i and j. Since the distance between magnetic ions in an insulating crystal are generally relatively large compared to wavefunction extents, direct exchange is rarely an important mechanism. *Indirect exchange* or *superexchange*, on the other hand, plays a major role in many magnetically ordered materials. Here, the interaction is mediated through one or more non-magnetic ions – such as oxygen – where electrons are allowed to hop between ions. This electron de-localization lowers the energy through the Heisenberg uncertainty principle and the dominant term in the exchange integral is therefore kinetic energy driven rather than based on Coulomb repulsion as in the case of direct exchange.

Inter-atomic interactions may also occur via the spin-orbit couling where the ground state of the i'th ion is allowed to mix with exited states of the j'th ion. The effect is the so-called *anisotropic superexchange interaction* or *Dzyaloshinskii-Moriya (DM) interaction* after its formulators[9,10]. The resulting term in the spin Hamiltonian is:

$$\hat{\mathcal{H}}_{\text{DM}} = \sum_{<i,j>} \mathbf{D} \cdot (\mathbf{S}_i \times \mathbf{S}_j),$$

where the vector, $\mathbf{D}$, depends to first order on the spin-orbit coupling parameter. The DM interaction favors spins perpendicular to each other in the plane normal to $\mathbf{D}$. The result is often a rotation of the spins aways from a perfectly collinear alignment, i.e. a *spin canting*, and a small ferromagnetic moment perpendicular to the major spin axis may be introduced. The allowed non-zero elements of $\mathbf{D}$ are determined by the symmetry of the crystal and the DM interaction is generally prohibited in highly symmetric systems.

Superexchange constants, J_{ij}, may be either negative (ferromagnetic) or positive (antiferromagnetic) and couplings between different sites in a crystal may be of identical or opposite sign. This by itself or together with single-ion anisotropies, DM interactions and/or geometrical factors can result in competing interactions which gives rise to *frustration*. Frustrated spin systems experience lowered ordering temperatures compared to non-frustrated systems, exotic spin structures or no order at all. The extent of frustration is often quantified by the *frustration factor*, $f = \frac{\Theta_{\text{CW}}}{T_N}$[11], where Θ_{CW} is the Curie-Weiss temperature and T_N the ordering temperature or *Néel temperature*.

1.2 Ferroelectrics, multiferroics and magnetoelectrics

Apart from magnetic properties whose origins were described in the previous section, the compounds encountered in this thesis – the lithium-orthophosphates – all also possess *magnetoelectric (ME)* properties. It is therefore appropriate with a section outlining this phenomenon, including possible microscopic origins and applications. More rigorous descriptions may be found in review papers such as Refs. 12–14 or books such as Ref. 15.

Coupling of magnetic and electric properties. In analogy to a ferromagnetic material with a spontaneous net magnetization, a *ferroelectric* material spontaneously displays a non-zero electric polarization. This occurs at some critical temperature above which such materials behave like ordinary dielectrics. In the ferroelectric state the polarization can be reversed upon applying an electric field in the opposite direction, just like the magnetization of a ferromagnet may be reversed upon applying an opposing magnetic field. The electric polarization of a ferroelectric material is history dependent, i.e. it displays hysteresis.

On rare occations a material may spontaneously possess both ferroelectricity *and* ferromagnetism (or antiferromagnetism) and in this case the material is termed *multiferroic*. Depending on the mechanism(s) responsible for the two different properties, there may be no or only a weak coupling between the two or they may be closely linked. If the two properties have their origin in completely different mechanisms they typically have two very different ordering temperatures, most often with the material first becoming ferroelectric and then ferromagnetic upon cooling. However, if the two properties are caused by the same mechanism or somehow one is due to the other, the material will become ferroelectric and ferromagnetic at the same critical temperature.

In magnetoelectric materials, a magnetization is induced upon applying an electric field or similarly, an electric polarization is induced upon applying a magnetic field. Electric and magnetic order in these materials are not necessarily spontaneous but manipulating one property affects the other. Figure 1.4 offers an overview of the various material categories.

The magnetoelectric effect may be described using Landau theory where the free energy of the system, F, is written in terms of an applied magnetic field with components, H_i, and an applied electric field with components, E_i:

$$F = \frac{1}{2}\varepsilon_0\varepsilon_{ij}E_iE_j + \frac{1}{2}\mu_0\mu_{ij}H_iH_j + \alpha_{ij}E_iH_j + \frac{1}{2}\beta_{ijk}E_iH_jH_k + \frac{1}{2}\gamma_{ijk}H_iE_jE_k + ... \tag{1.1}$$

The two first terms on the right hand side describe the electric and magnetic responses to the electric and magnetic fields respectively. The vacuum permittivity and permeability are ε_0 and μ_0 and the relative permittivity and permeability are the second rank tensors ε_{ij} and μ_{ij} respectively. The third term describes the linear magnetoelectric effect with the coupling tensor of second rank, α_{ij}, or written out fully for later reference, $\boldsymbol{\alpha} = \begin{pmatrix} \alpha_{aa} & \alpha_{ab} & \alpha_{ac} \\ \alpha_{ba} & \alpha_{bb} & \alpha_{bc} \\ \alpha_{ca} & \alpha_{cb} & \alpha_{cc} \end{pmatrix}$. The tensors of third rank, β_{ijk} and γ_{ijk}, represent quadratic magnetoelectric effects.

The induced electric polarization, P_i, or magnetization, M_i, are then found from

the free energy by differentiating with respect to E_i or H_i, respectively, and then setting $E_i = 0$ or $H_i = 0$:

$$P_i = \alpha_{ij} H_j + \frac{1}{2}\beta_{ijk} H_j H_k + ...$$
$$M_i = \alpha_{ji} E_j + \frac{1}{2}\gamma_{ijk} E_j E_k + ...$$

Although the existence of the magnetoelectric effect was formulated already in 1894 by Curie[16], more than half a century elapsed before it was explicitely predicted in Cr_2O_3 by Dzyaloshinskii[17] and then experimentally confirmed by Astrov[18]. Since then a plethora of candidate materials to display the magnetoelectric effect have been identified. Among these are the litihium orthophosphates.

Time and space symmetry breaking. Since, upon space inversion, $\mathbf{r} \to -\mathbf{r}$, electric fields change sign, $E_i \to -E_i$ and likewise, upon time inversion, $t \to -t$, magnetic fields change sign, $H_i \to -H_i$, it is clear from Eq. (1.1) that the linear magnetoelectric tensor, α_{ij}, is both time- and space-antisymmetric. Therefore, the magnetoelectric effect is only allowed in systems where both time and space symmetry are violated or as Pierre Curie put it (1908): "C'est la dissymétrie qui crée le phénomène"[15]. Magnetically ordered systems generally break time reversal symmetry but not necessarily space inversion symmetry. Consequently only 58 out of 90 magnetic point groups allow for the magnetoelectric effect.[19]

Microscopic origin. The magnetoelectric effect is manifested by translating ions inside material upon applying a magnetic field such that a net electric polarization is created. Exactly how this comes about depends on the system in question and so far no all-embracing theory for the microscopic origin of the magnetoelectric effect exists.

In spiral magnets such as $TbMnO_3$, an electric polarization, $\mathbf{P}$, may be introduced via the so-called *inverse DM interaction* as $\mathbf{P} \propto \gamma\, \mathbf{e}_{ij} \times (\mathbf{S}_i \times \mathbf{S}_j)$ with γ proportional to the spin-orbit coupling constant and the superexchange interactions[6,20]. The propagation vector of the spiral is $\mathbf{e}_{ij}$.

Another similar mechanism is the *spin-lattice coupling*. Here, two indirectly coupled

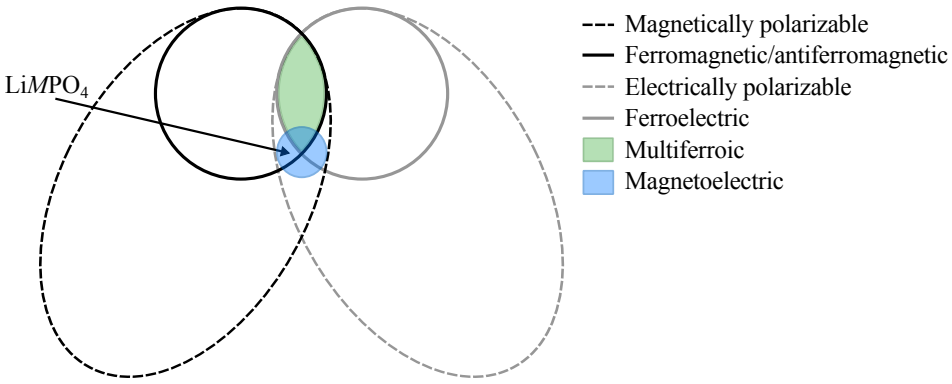

Figure 1.4: *Sketch after Ref. 13 showing how the different material categories are related. Ferromagnetic and (anti)ferromagnetic materials are represented by the solid circles with multiferroics constituting the green area. Magnetoelectric materials are represented by the blue area and the lithium orthophosphates belong to the category of materials that are both (anti)ferromagnetic and magnetoelectric but not ferroelectric.*

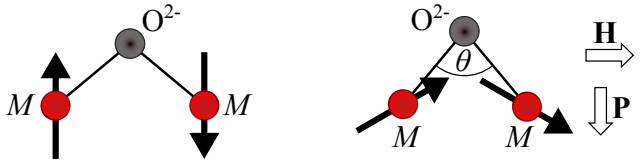

Figure 1.5: *The magnetic moments of two transition metal ions (red) interacting via indirect exchange through an oxygen ion (black). The zero-field configuration is shown on the left and on the right an applied magnetic field changes the orientation of the moments. As a consequence of the Anderson-Kanamori-Goodenough rules[21], the bond angle, θ, decreases and the oxygen ion is pushed away from the metalic ions and an electric polarization is induced. Figure after Ref. 20.*

magnetic moments may displace the oxygen jammed in between them as illustrated in Fig. 1.5. At zero field, the moments are anti-parallel but for an applied magnetic field, they change orientation with respect to each other. Following the Anderson–Kanamori–Goodenough rules[21], this change in moment orientations causes the bond angle, θ, to change and consequently, the oxygen ion is pushed away and an electric dipole moment created.

Other mechanisms may be based on toroidal moment, virtual electron transfer[20], single-ion anisotropy or changes in the g-tensor[22].

Applications. The coupling between magnetic and electric properties in magnetoelectric materials carries the prospect of new technological advances in sensors, memory devices, spintronics and magnonics. In practice, electric fields are much easier to manipulate than magnetic fields and magnetoelectric devices open up for the possibility of switching magnetic domains by application of a voltage. Moreover, the magnetoelectric effect is likely to offer new functionalities such as more than two logic states[23–25] and may potentially open up for a whole new range of applications.

One of the promising technologies is the electric-field controlled *magnetoelectric random access memory (MERAM)*. In heterostructured thin films, the magnetoelectric coupling is combined with interfacial exchange coupling and the magnetization of

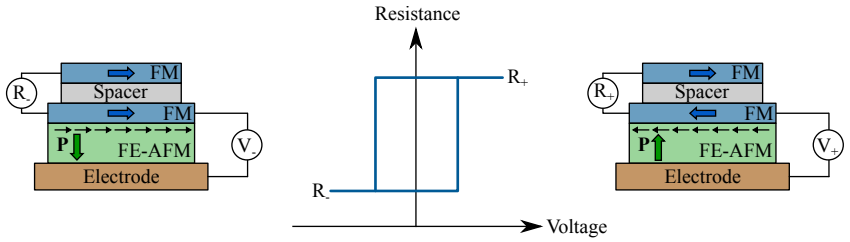

Figure 1.6: *Sketch of a MERAM device made of a sandwich of ferromagnetic (FM) layers, a non-magnetic spacer layer and a ferroelectric (FE) and antiferromagnetic (AFM) layer. Information is stored in the magnetization of the bottom FM layer which is read by the resistance of the magnetic trilayer, R_+ (R_-) for (anti)parallel magnetizations. The electric polarization in the multiferroic is controlled by applying a voltage. In turn, the polarization manipulates – via the magnetoelectric coupling – the spin orientation which then dictates the magnetization direction in the bottom FM layer. The response in resistance displays a hysteresis loop with respect to the applied voltage as shown. Figure adapted from Ref. 25.*

a ferromagnetic layer may be switched by application of a voltage to a magnetoelectric layer as illustrated in Fig. 1.6. This type of device has been demonstrated using multiferroic $BiFeO_3$[26,27] and $YMnO_3$[28] and provides a low-power alternative to the so-called *spin transfer* magnetic random access memory where a current is used for switching[25]. Other mechanisms for domain switching by applying a voltage include orbital reconstruction on a MnO/non-superconducting cuprate interface[29] and DM induced torque[30].

Despite the potentiel applications of magnetoelectric materials, a number of challenges impose themselves. First of all, $BiFeO_3$ is the only material known so far to be multiferroic and magnetoelectric at room temperature[25]. Secondly, all single-phase multiferroics have a dominant antiferromagnetic response and therefore no or only little magnetization, rendering control of the magnetization via an electric field impossible. In addition, the fundamental size of the linear magnetoelectric coupling tensor is limited by the vacuum permitivity and permeability, $\alpha_{ij}^2 \leq \varepsilon_0 \mu_0 \varepsilon_{ij} \mu_{ij}$[13,20].

Alternatively, tayloring of artificial multiferroics has been enabled by developments in nanofabrication processes. By combining materials with ferromagnetic, ferroelectric, magnetostrictive, electrostrictive and/or piezostrictive properties, stacks exhibiting magnetoelectric responses of 3-5 orders of magnitude larger than single-phase materials may be created[14]. This approach of structuring materials at the nanoscale can bring about new functionalities as was so outstandingly illustrated in the case of the giant magnetoresistance[3].

In order to further develop the field of magnetoelectric-based devices, we need to understand the underlying physics governing this profound effect. Our research contributes to this task by focusing on how the magnetic structures are connected to the magnetoelectric effect in the lithium orthophosphates. The basic properties of these materials are outlined in Chapter 3 but before that, we shall have a brief description of our main tool for directly probing magnetic structures and dynamics: neutron scattering.

Chapter 2

Neutron scattering: probing magnetic structures and dynamics

The basic properties of the neutron and how it may be used for probing magnetic structures and dynamics are outlined in this chapter. More rigorous theoretical descriptions and derivations are found in texts such as Squires[31], Lovesey[32] or Furrer[33]. Instrumental setups for various types of neutron scattering experiments are presented later in Sections 4.2-4.4.

2.1 Basic properties of the neutron

As its name suggests, the neutron is a neutral particle. Its mass, $m_N = 1.675 \times 10^{-27}$ kg, is close to that of the proton and it is a fermion with spin, $S = \frac{1}{2}$. The life time of the free neutron is ~ 15 min, decaying in the process $n^0 \rightarrow p^+ + e^- + \bar{v}_e$ and producing a proton, an electron and an electron antineutrino.

The neutron does not possess a charge so it interacts directly with the nuclei in condensed matter as opposed to other probes such as X-rays or electrons which mainly interact with the surrounding atomic electron cloud. The neutron interaction range is short and depends heavily on the atom or isotope in question and its spin state. Additionally, the neutron spin gives rise to a magnetic moment that allows it to interact with any magnetic fields created by atomic spin or orbital momenta. Since these find their origin in unfilled electronic shells, the magnetic interaction has a longer range than the nuclear interaction and the individual atom can no longer be approximated entirely by a point particle.

The wavelengths of cold and thermal neutrons correspond well to typical crystalline material lattice parameters. Furthermore, the kinetic energies of those same neutrons are similar to that of nuclear and magnetic excitations in condensed matter. Hence, neutrons constitute a fantastic probe for atomic and magnetic structures as well as lattice and spin excitations. In fact, the properties of the neutron are so well suited for condensed matter research that it prompted B. N. Brockhouse to exclaim[34]: "it might well be said that, if the neutron did not exist, it would need

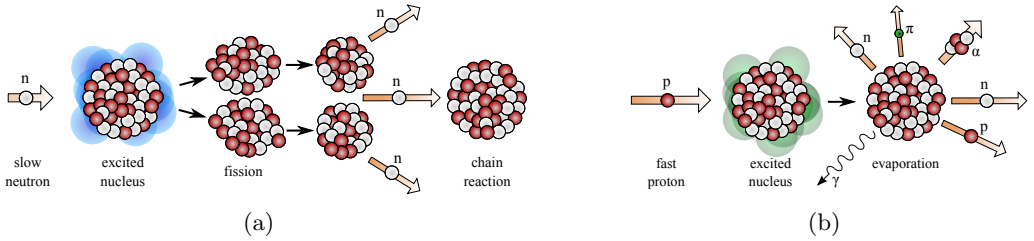

Figure 2.1: *Neutron production via (a) fission and (b) spallation.*

to be invented!" On the flip side, the interaction strength between neutrons and matter is relatively weak and the obtainable neutron flux at experimental facilities is limited.

Neutrons for scattering experiments are produced in either a research reactor or a spallation source. The processes are illustrated in Fig. 2.1. In a nuclear reactor, neutrons are produced by fission where a heavy and unstable nucleus (e.g. U^{235}) is excited by bombarding it with a slow neutron. The nucleus then splits into smaller parts and more neutrons are released. Some of these are used for maintaining a chain reaction whereas the surplus can be used for scattering experiments. The spallation process is somewhat different. Here, a target (e.g. Pb or liquid Hg) is hit by fast protons. The excited nucleus emits a shower of various particles in order to get rid of the excess energy. Some of these particles are neutrons which can then be used for scattering experiments. The fast protons seeding the process are accelerated in pulses and the resulting neutron beam is therefore also pulsed. The fission process, on the other hand, is continuous. In both cases, the neutrons need to be moderated to the desired energies and guided to the instruments.

2.2 Neutron scattering cross sections

When neutrons in a beam of a given flux, Φ, impinge upon a nucleus, some may be scattered. The *total scattering cross section*, σ, is essentially the probability of a scattering event taking place, i.e. the total number of scattered neutrons per unit time divided by Φ. σ has the unit of area and can therefore be pictured as the effective area of the nucleus as seen by the neutrons. These areas are tiny, in the order of $1\,\text{barn} = 1\,\text{b} = 10^{-24}\,\text{cm}^2$, reflecting the weak interaction of neutrons with matter. However, as always, numbers may seem large or small depending on one's perspective. In particle physics, neutron scattering cross sections appear rather large compared to e.g. a proton-proton event with a cross section in the mb range.

The total scattering cross section tells how likely it is for a neutron to scatter when hitting a given nucleus. However, it says nothing about whereto this neutron might scatter and valuable information is kept in this angular dependency. Suppose a number of neutrons with initial wavevector, $\mathbf{k}$, scatter into the solid angle $d\Omega$ and have final wavevector, $\mathbf{k}'$ [see Fig. 2.2]. The *scattering angle*, 2θ, is defined as the angle between $\mathbf{k}$ and $\mathbf{k}'$ and the momentum transfer or *scattering vector* is defined as $\mathbf{Q} = \mathbf{k} - \mathbf{k}'$. The *differential scattering cross section*, $\frac{d\sigma}{d\Omega}$, then equals the number of neutrons scattered into $d\Omega$ per unit time divided by Φ and $d\Omega$. In order to obtain

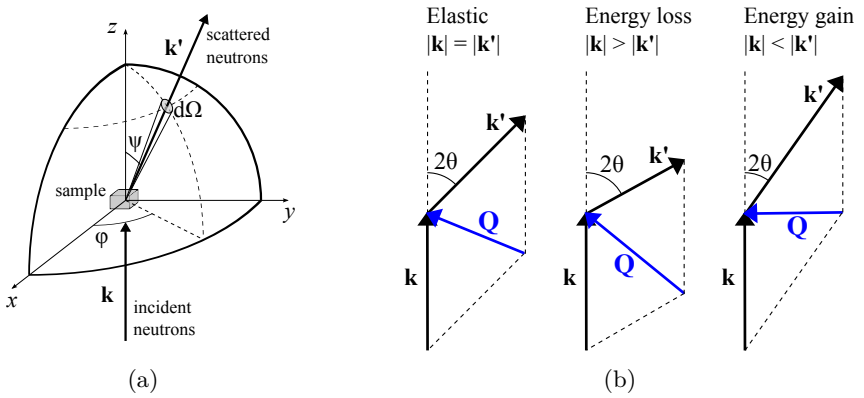

Figure 2.2: *(a) The geometry of a neutron scattering experiment, after Lovesey[32]. Neutrons are scattered into the solid angle, $d\Omega$, upon hitting the sample. (b) The scattering triangle is spanned by* $\mathbf{k}$ *and* $\mathbf{k}'$ *and defines the momentum transfer,* $\mathbf{Q}$*, and the scattering angle, 2θ. Neutrons may be scattered elastically or with either energy loss or gain.*

σ from $\frac{d\sigma}{d\Omega}$ one simply needs to integrate over all possible angles, $\sigma = \int d\Omega \, \frac{d\sigma}{d\Omega}$.

The differential cross section counts any neutron scattered in $d\Omega$ – regardless if it were scattered elastically or inelastically. The vast majority of neutrons are scattered elastically and when performing a diffraction experiment one measures $\frac{d\sigma}{d\Omega}$ assuming that all detected neutrons are indeed scattered just so. Nevertheless, a small fraction of neutrons do scatter inelastically and they carry information about the dynamics of the probed material. The energy difference is defined as $\hbar\omega = E - E'$, where E and E' are the initial and final energies of the scattered neutron respectively. The neutron either delivers ($\hbar\omega > 0$) energy to or gains ($\hbar\omega < 0$) energy from the sample. The *partial differential cross section*, $\frac{d^2\sigma}{d\Omega dE'}$, may then be defined as the number of neutrons per unit time scattered into $d\Omega$, with energies in the interval $[E', E' + dE']$ and divided by Φ, $d\Omega$ and dE'. Again, in order to obtain either $\frac{d\sigma}{d\Omega}$ or σ, one merely needs to integrate over all energies or, additionally, all angles, $\frac{d\sigma}{d\Omega} = \int dE' \, \frac{d^2\sigma}{d\Omega dE'}$ or $\sigma = \int dE' \, d\Omega \, \frac{d^2\sigma}{d\Omega dE'}$.

2.3 Interaction potentials

In the *Born approximation* the neutron is described by a plane wave and the interaction potential between the neutron and atom is sufficiently weak such that it may be considered as a perturbation to the Hamiltonian of a free neutron. The transition rate from neutrons in initial state, ψ, to neutrons in final state, ψ', is then given by *Fermi's Golden Rule*:

$$W = \frac{2\pi}{\hbar} \rho_{\mathbf{k}'}(E') \left| \left\langle \psi' | \hat{V} | \psi \right\rangle \right|^2,$$

where $\rho_{\mathbf{k}'}(E')$ is the density of final states and $\hat{V}$ is the interaction potential.

In case of neutrons scattering off a nucleus the potential finds its origin in the strong nuclear forces between the incident neutron and the core constituents. The

exact physical potential is essentially unknown and most likely rather complicated. However, it is effectively described by the *Fermi pseudo-potential*, $V(\mathbf{r}) \propto \delta(\mathbf{r})$, which yields the correct behavior in the limit far away from the nucleus.

In case of magnetic scattering the potential arises from the interaction between the neutron dipole moment, $\boldsymbol{\mu}_N$, and the ionic dipole moment. The interaction potential simply has the form $V = -\boldsymbol{\mu}_N \cdot \mathbf{B}$, where $\mathbf{B}$ is the ion dipole field originating from the spin and orbital momenta of partly filled electron shells.

2.4 Scattering from ordered systems

The above considerations only account for scattering from a single site but in a real experiment neutrons are scattered off a collection of sites (on the order of 10^{23} in fact). Furthermore, in this project, these are ordered in a single crystalline array where interference cause the neutrons to scatter in a pattern. Using Fermi's Golden Rule, the interaction potentials and the discreet translational symmetry of a crystal, the differential scattering cross section may be derived:

$$\frac{d\sigma}{d\Omega} = N\frac{(2\pi)^3}{V}e^{-2W}\,|F(\mathbf{Q})|^2 \sum_{\mathbf{G}} \delta(\mathbf{Q}-\mathbf{G}), \tag{2.1}$$

where N is the number of unit cells of volume, V. Note that this may refer to either the nuclear or magnetic unit cell. W is the Debye-Waller factor which takes into account thermal smearing of the atomic positions. The δ-function ensures that scattering only occurs whenever the scattering vector equals a reciprocal lattice vector, $\mathbf{G} = H\mathbf{a}^* + K\mathbf{b}^* + L\mathbf{c}^*$. Here H, K, L are the *Miller indices* and $\mathbf{a}^*, \mathbf{b}^*, \mathbf{c}^*$ are the reciprocal lattice vectors. The requirement $\mathbf{Q} - \mathbf{G} = 0 \Leftrightarrow \mathbf{k} - \mathbf{k}' = \mathbf{G}$ is also known as the *Laue condition* and may also be stated in the form of *Bragg's law*, $n\lambda = 2d\sin\theta$. Here n is a positive integer, $\lambda = \frac{2\pi}{k}$ the neutron wavelength and $d = \frac{2\pi}{Q}$ the lattice spacing. The term $F(\mathbf{Q})$ is the *structure factor* and it depends on the type of scattering encountered, i.e. either nuclear or magnetic scattering. For nuclear scattering it simply reads:

$$F_N(\mathbf{Q}) = \sum_j b_j\, e^{i\mathbf{Q}\cdot\mathbf{r}_j},$$

where b_j is the *scattering length* of the individual atoms and $\mathbf{r}_j$ are their positions. The sum runs over all atoms in a nuclear unit cell. Similarly, the structure factor for magnetic scattering is:

$$F_M(\mathbf{Q}) = (\gamma r_0)\left(\frac{g}{2}f(\mathbf{Q})\right)\sum_j \hat{\mathbf{Q}}\times(\mathbf{s}_j\times\hat{\mathbf{Q}})\, e^{i\mathbf{Q}\cdot\mathbf{r}_j}.$$

Here, $\gamma = -1.913$ is the neutron gyroscopic ratio, $r_0 = 2.818\,\text{fm}$ the classical electron radius and g the g-factor. The *magnetic form factor*, $f(\mathbf{Q})$, is the Fourier transform of the electron density around the nucleus and decreases monotonically with the length of the scattering vector, Q. The sum term in the magnetic structure factor is very similar to that of the nuclear structure factor with b_j being replaced by the spin component perpendicular to the scattering vector, $\hat{\mathbf{Q}}\times(\mathbf{s}_j\times\hat{\mathbf{Q}})$, along with the factor $(\gamma r_0)\left(\frac{g}{2}f(\mathbf{Q})\right)$. As a consequence of the quantity $\hat{\mathbf{Q}}\times(\mathbf{s}_j\times\hat{\mathbf{Q}})$ –

also known as the *Halpern-Johnson vector*[35] – the direction of the moment may be determined. Note also that the sum now runs over all sites in the magnetic unit cell, which may be equal to the nuclear unit cell or larger.

For inelastic scattering, we need to consider the partial differential cross section[36]:

$$\frac{d^2\sigma}{d\Omega dE'} = \frac{k'}{k}\underbrace{\left(\frac{m_N}{2\pi\hbar^2}\right)^2 \sum_{\lambda} p_\lambda \sum_{\lambda'} \left|\langle\varphi'\lambda'|V(\mathbf{Q})|\varphi\lambda\rangle\right|^2 \delta(E'-E-\hbar\omega)}_{S(\mathbf{Q},\omega)}, \tag{2.2}$$

where the δ-function expresses energy conservation and the matrix element $\langle\varphi'\lambda'|V(\mathbf{Q})|\varphi\lambda\rangle$ describes the process leading from inital state, φ, and neutron wavelength, λ, to final state, φ', and wavelength, λ'. The factor, p_λ, denotes the occupation probability of the initial state. Everything in Eq.(2.2) after $\frac{k'}{k}$ is also collectively named the *scattering function*, $S(\mathbf{Q},\omega)$, and contains all the information about a given system.

When considering lattice vibrations, the Fermi pseudo-potential is used and only one-phonon processes are taken into account, i.e. the creation/annihilation of a single phonon in the scattering event. The resulting scattering function is:

$$S_N(\mathbf{Q},\omega) \propto \sum_{\mathbf{G}} \frac{(\mathbf{Q}\cdot\mathbf{e_q})^2}{\omega_\mathbf{q}}\Big[(n_\mathbf{q}+1)\delta(\omega-\omega_\mathbf{q})\delta(\mathbf{Q}-\mathbf{G}-\mathbf{q}) + n_\mathbf{q}\delta(\omega+\omega_\mathbf{q})\delta(\mathbf{Q}-\mathbf{G}+\mathbf{q})\Big],$$

where $\mathbf{q}$ is the excitation wave vector, $\omega_\mathbf{q}$ the excitation frequency, $\mathbf{e_q}$ the directional unit vector of the vibration and $n_\mathbf{q} = \frac{1}{e^{\hbar\omega_\mathbf{q}/k_BT}-1}$ the Bose population factor. The term, $(\mathbf{Q}\cdot\mathbf{e_q})^2$, means that only atomic displacements parallel to the scattering vector may be detected. Moreover, signals are stronger for longer scattering vectors as, $S_N(\mathbf{Q},\omega) \propto Q^2$. At low temperatures it is easier to create a phonon compared to destroying one since, $n_\mathbf{q} \to 0$ for $T \to 0$, and hence neutron energy loss is usually measured only, i.e. $E' < E$. In general, phonons may be either longitudinal – $\mathbf{e_Q}||\mathbf{q}$ – or transverse – $\mathbf{e_Q} \perp \mathbf{q}$.

For magnetic excitations, the corresponding scattering function reads:

$$S_M(\mathbf{Q},\omega) \propto \sum_{\mathbf{G}} \frac{f^2(\mathbf{Q})}{\omega_\mathbf{Q}}\Big[(n_\mathbf{Q}+1)\delta(\omega-\omega_\mathbf{Q})\delta(\mathbf{Q}-\mathbf{G}-\mathbf{q}) + n_\mathbf{Q}\delta(\omega+\omega_\mathbf{Q})\delta(\mathbf{Q}-\mathbf{G}+\mathbf{q})\Big].$$

As in the case of diffraction, neutrons only scatter from spin deviations perpendicular to the scattering vector. The scattering function thus also contains a factor $\hat{\mathbf{Q}}\times(\delta\mathbf{s}_j\times\hat{\mathbf{Q}})$ in parallel with $\hat{\mathbf{Q}}\times(\mathbf{s}_j\times\hat{\mathbf{Q}})$ in the magnetic structure factor.

The experimental strategy to measure these vary since lattice vibrations are detected parallel to $\mathbf{Q}$ whereas spin excitations are only seen for deviations perpendicular to $\mathbf{Q}$. It is possible to distinguish between phonon and magnon signals by following either their temperature or Q dependency since $S_N(\mathbf{Q},\omega) \propto Q^2$ and $S_M(\mathbf{Q},\omega) \propto f(\mathbf{Q})^2$. Hence, magnetic excitations get weaker with longer Q because the magnetic form factor, $f(\mathbf{Q})$, decreases with Q and more importantly, they generally do not exist above the magnetic ordering temperature.

All the above cross sections only concern coherent scattering, i.e. Bragg scattering and scattering from lattice and magnetic excitations. However, neutrons may also be scattered incoherently or absorbed and multiple nuclear or magnetic excitations may be simultaneously excited.. These mechanisms are not discussed here although it is mentioned that incoherent scattering has two origins: variations in scattering lengths for a random distribution of different isotopes and nuclear spin states. Incoherent scattering is usually isotropic and is most often considered background in neutron scattering experiments.

2.5 Polarized neutrons

Using a spin polarized incident neutron beam and analyzing the final neutron spin state, one may obtain additional information about the scattering processes in a given system by measuring the intensities for non spin-flip (NSF) and spin-flip (SF) scattering. The experimental realization of this kind of measurement is described in Section 4.4 but the appropriate cross sections are stated and interpreted in this section.

A magnetic field at the sample position defines the polarization direction, $\mathbf{P}$, and we use the coordinate system described in Ref. 37 and illustrated in Fig. 2.3. Here, $\mathbf{x}||\mathbf{Q}$, $\mathbf{y} \perp \mathbf{Q}$ in the horizontal scattering plane and $\mathbf{z} \perp \mathbf{Q}$ is vertical. In general, the NSF channel is sensitive to spin components parallel to the neutron polarization, $\mathbf{S}||\mathbf{P}$, and the SF channel is sentitive to $\mathbf{S} \perp \mathbf{P}$ and as always only the components, $\mathbf{S} \perp \mathbf{Q}$, are probed. Combining these rules yields the results given in Table 2.1 (note that generally $\mathbf{x} \nparallel \mathbf{a}$, $\mathbf{y} \nparallel \mathbf{b}$, $\mathbf{z} \nparallel \mathbf{c}$. Instead x, y, z are defined by the scattering vector, $\mathbf{Q}$). Consequently, magnetic and nuclear scattering contributions may be separated and the direction of the magnetic moment may be determined . Furthermore, nuclear coherent and isotope incoherent scattering is entirely found in the NSF channel while spin incoherent scattering is distributed with $\frac{1}{3}$ in the NSF channel and $\frac{2}{3}$ in the SF channel. Polarization analysis therefore also allows for characterization and separation of the incoherent signals.

When performing an experiment, the beam polarization, $P = \frac{N_+ - N_-}{N_+ + N_-}$, is not perfect and the flipping ratio is defined as $F = \frac{N_+}{N_-}$, where N_+ (N_-) is the number of neutrons in the up (down) state. Typically, $F = 20 - 30$ and correspondingly $P = 90 - 95\%$. As a consequence of the imperfect polarization, the measured cross sections, $\left(\frac{d\sigma}{d\Omega}\right)_{\mathrm{NSF}}$ and $\left(\frac{d\sigma}{d\Omega}\right)_{\mathrm{SF}}$, need to be corrected as follows[38]:

$$\begin{aligned} \left(\frac{d\sigma}{d\Omega}\right)^{\mathrm{corr}}_{\mathrm{NSF}} &= \left(\frac{d\sigma}{d\Omega}\right)_{\mathrm{NSF}} + \frac{1}{F-1}\left[\left(\frac{d\sigma}{d\Omega}\right)_{\mathrm{NSF}} - \left(\frac{d\sigma}{d\Omega}\right)_{\mathrm{SF}}\right], \\ \left(\frac{d\sigma}{d\Omega}\right)^{\mathrm{corr}}_{\mathrm{SF}} &= \left(\frac{d\sigma}{d\Omega}\right)_{\mathrm{SF}} - \frac{1}{F-1}\left[\left(\frac{d\sigma}{d\Omega}\right)_{\mathrm{NSF}} - \left(\frac{d\sigma}{d\Omega}\right)_{\mathrm{SF}}\right]. \end{aligned} \tag{2.3}$$

where $\left(\frac{d\sigma}{d\Omega}\right)^{\mathrm{corr}}_{\mathrm{NSF}}$ and $\left(\frac{d\sigma}{d\Omega}\right)^{\mathrm{corr}}_{\mathrm{SF}}$ are the corrected cross sections.

In the above, a single quantization axis was chosen for both incoming and outgoing neutrons. However, it should be mentioned that one may define distinct initial and final polarization directions and hence obtain 9 different possible combinations. On top, there are of course still 2 NSF and 2 SF channels, yielding in total 36 cross

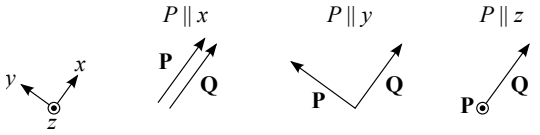

Figure 2.3: *Definition of coordinate system used for polarization analysis.*

Table 2.1: *Separation of spin components by polarization analysis.*

	P||x	**P||y**	**P||z**
NSF	–	S_y	S_z
SF	$S_y + S_z$	S_z	S_y

sections. Fortunately, it is rare that one need to measure them all! It is also pointed out that polarized neutron experiments only work for antiferromagnets, paramagnetic or disordered systems. The neutron beam is depolarized in the presence of a finite magnetization as in e.g. ferromagnets and also depolarized in superconductors where perfect diamagnetism causes $\mathbf{B} = 0$ inside the material.

Chapter 3

Material background

In this chapter the previously known material properties of the lithium orthophosphates are outlined, thus providing a background for studying these compounds. The lithium orthophosphates are not by any means new compounds in condensed matter research and basic properties such as crystal structure and zero-field magnetic behavior have been known since the 1960's[39–43]. Nevertheless, they still prove highly interesting and new exciting behaviors are repeatedly revealed as development in experimental techniques progresses and as our fundamental understanding of physics becomes increasingly sophisticated.

As this thesis involves both stoichiometric compounds and compounds containing a mixture of two different magnetic ions, a short section reviewing mixed anisotropy magnets is also included here. These are a highly interesting class of materials where properties may be taylored by substituting one element for another.

3.1 The lithium orthophosphates

The crystal structure of the lithium orthophosphates, LiMPO$_4$ (M = Co, Ni, Fe, Mn), is orthorhombic (space group no. 62, $Pnma$[41,44]). The ion positions in the crystallographic unit cell, the antiferromagnetic ground state spin structure and exchange interactions are shown in Figure 3.1. Lattice parameters, magnetic and magnetoelectric properties are summarized in Table 3.1. One unit cell contains four formula units and hence four magnetic ions which are located on the 4c Wyckoff positions in a nearly face-centered arrangement with coordinates $\mathbf{r}_1 = (1/4 + \varepsilon, 1/4, 1 - \delta)$, $\mathbf{r}_2 = (3/4 + \varepsilon, 1/4, 1/2 + \delta)$, $\mathbf{r}_3 = (3/4 - \varepsilon, 3/4, \delta)$ and $\mathbf{r}_4 = (1/4 - \varepsilon, 3/4, 1/2 - \delta)$. The displacements, ε and δ, are listed in Table 3.1.

With four magnetic ions in a unit cell there are four magnetic basis vectors. Two notations are used in this thesis depending on which is more convenient in each case. The notations are $\{A, G, C, F\} = \{(\uparrow\downarrow\downarrow\uparrow), (\uparrow\downarrow\uparrow\downarrow), (\uparrow\uparrow\downarrow\downarrow), (\uparrow\uparrow\uparrow\uparrow)\}$. Moreover, $x = a$, $y = b$, $z = c$ may be used interchangeably. For example, the basis vector $A = (\uparrow\downarrow\downarrow\uparrow)$ describes a spin structure where spins 1 and 4 are parallel to each other

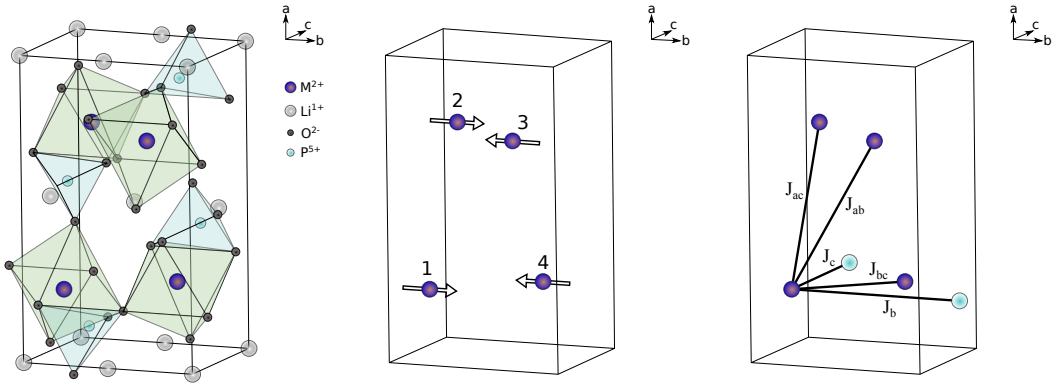

Figure 3.1: *Crystal and commensurate magnetic structure of $LiMPO_4$. One nuclear unit cell contains four formula units and hence four magnetic ions. The magnetic ions are surrounded by oxygen in an octahedral environment and they interact via super-exchange paths such as M-O-M and M-O-P-O-M. The middle panel shows the commensurate ($\uparrow\uparrow\downarrow\downarrow$) antiferromagnetic spin arrangement with major spin component along b as is the case for M = Co, Fe. The rightmost panel shows the exchange interactions. Note that the light blue atoms belong to neighboring cells.*

and antiparallel to spins 2 and 3. Added subscripts denote the spin orientation, e.g. A_x or $(\uparrow\downarrow\downarrow\uparrow)_a$.

Each magnetic ion is surrounded by oxygen in an octahedral environment which together with the magnetic ion in question dictates the single-ion anisotropy of the system as described in Section 1.1. Below the Néel temperature the magnetic ions order antiferromagnetically with symmetry ($\uparrow\uparrow\downarrow\downarrow$) [also denoted C] and with the major spin component along the easy axis. Néel temperatures, Curie-Weiss temperatures and easy axes for the different LiMPO$_4$ compounds are also listed in Table 3.1. Some minor spin canting and/or rotation away from the easy axis is typically reported as well[47,48,54].

Magnetic phase transitions are induced in LiMPO$_4$ upon applying a magnetic field along their easy directions . For M = Co, Ni, Mn the relevant magnetization curves and phase diagrams are shown in Fig. 3.2. For M = Fe no transitions were observed up to 16 T[56,57] but may exist for higher fields. Temperature dependencies of the magnetoelectric coefficients listed in Table 3.1 are shown in Fig. 3.3. In the following, features and properties of already known phases of the respective compounds are outlined.

LiCoPO$_4$. The phase diagram of LiCoPO$_4$ was studied by magnetization and magnetoelectricity measurements. This was done by Wiegelmann[59] using DC magnetic fields up to 20 T applied along b. Furthermore, Kharchenko et. al performed pulsed-field magnetization measurements up to 30 T and found the saturation field at 1.7 K to 28.3 T[58]. Two distinct phase transitions were observed at $\sim$ 12 T and $\sim$ 22 T. Both the magnetic susceptibility curve[58] and the phase diagram[59] are shown in Fig. 3.2(a). Below 12 T the magnetic structure is commensurate with spins primarily along b in an ($\uparrow\uparrow\downarrow\downarrow$) symmetry. In addition, a small spin component away from the easy axis[47], a weak ferromagnetic component[63] and a torroidal moment[20,64–66] have been reported. The commensurate phase is also magnetoelectric with non-zero tensor elements, α_{ab} and α_{ba}. LiCoPO$_4$ has the strongest magnetoelectric effect in

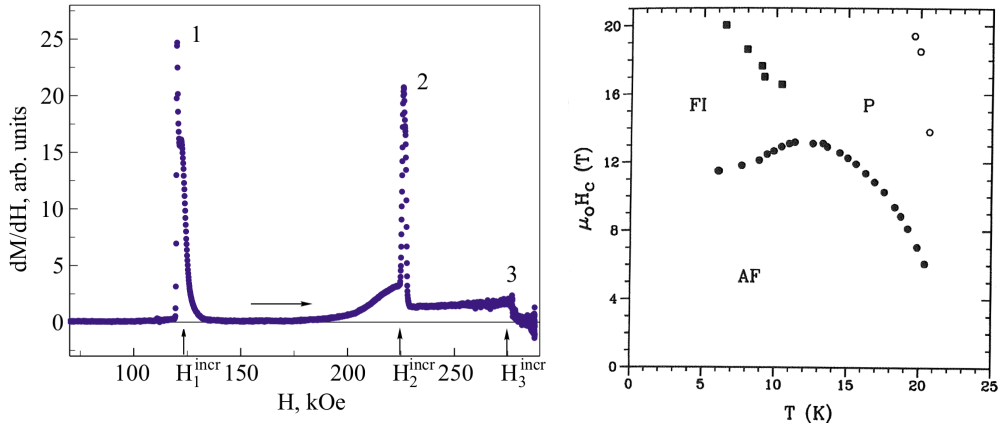

(a) Pulsed field magnetic susceptibility[58] at 4.2 K and phase diagram[59] up to 20 T along b for $LiCoPO_4$. The open symbols are for fields applied along a.

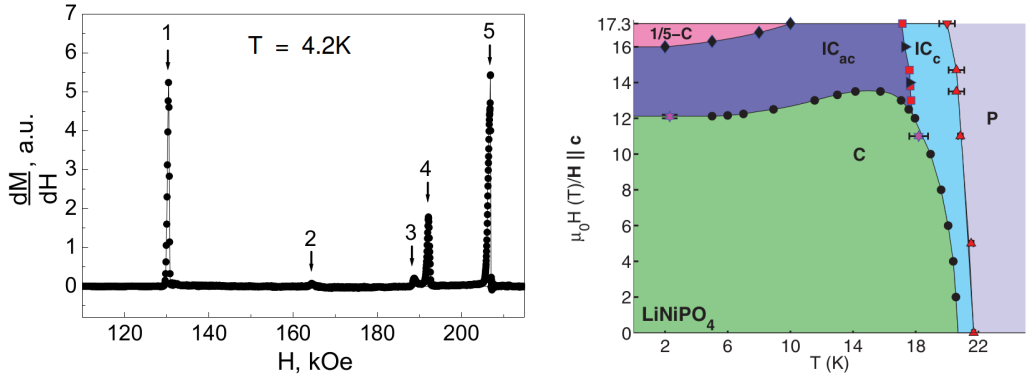

(b) Pulsed field magnetic susceptibility[60] at 4.2 K and phase diagram[61] up to 17.3 T along c for $LiNiPO_4$.

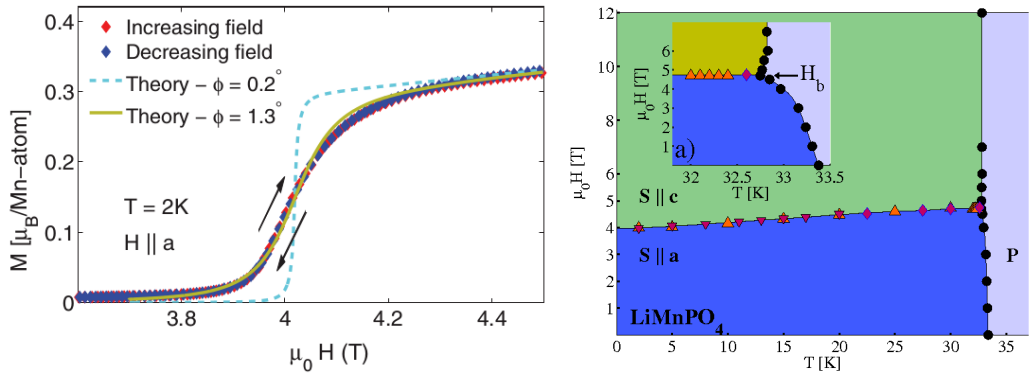

(c) Vibrating sample magnetization curve at 2 K and phase diagram up to 12 T along a for $LiMnPO_4$[62]. The insert shows details around the bicritical point.

Figure 3.2: *Magnetic susceptibility curves, magnetization measurements and magnetic phase diagrams for $LiMPO_4$ with (a)-(c) M = Co, Ni, Mn. Magnetic fields are applied along the respective easy directions, i.e. b, c and a. Figures are from Refs. 58-62.*

Table 3.1: *Crystallographic[42,43,45,46], magnetic[42,43,47–50] and magnetoelectric[39,49,51,52] properties of $LiMPO_4$. Lattice parameters are a, b and c. Ion displacements are δ and ϵ. Transition and Curie-Weiss temperatures are T_N and Θ_{CW} respectively. $\mu_0 H_S$ and M_S are the saturation field and moment respectively. For the magnetoelectric tensor, $\boldsymbol{\alpha}$, large dots denote non-zero elements and small dots denote zero elements. $|\alpha_{\max}|$ is the maximum magnitude element of the magnetoelectric tensor. Exchange (J's) and single-ion anisotropy ($\mathfrak{D}$'s) parameters[53–55] are defined in Eq.* (3.1).

M	Co	Ni	Fe	Mn
a [Å]	10.20	10.03	10.31	10.46
b [Å]	5.92	5.83	6.00	6.10
c [Å]	4.70	4.68	4.69	4.75
ε	0.0286	0.025	0.0320	0.028
δ	0.0207	0.0175	0.0252	0.028
T_N [K]	21.6	20.7	50.0	34.9
Θ_{CW} [K]	121	79	88	85
$\mu_0 H_S$ [T]	28.3	∼84	–	–
M_S [μ_B]	3.6	2.2	4.2	–
Elec. config.	$3d^7$	$3d^8$	$3d^6$	$3d^5$
S	3/2	1	2	5/2
Easy axis	**S**||**b**	**S**||**c**	**S**||**b**	**S**||**a**
ME tensor, $\boldsymbol{\alpha}$	$\begin{pmatrix} \cdot & \bullet & \cdot \\ \bullet & \cdot & \cdot \\ \cdot & \cdot & \cdot \end{pmatrix}$	$\begin{pmatrix} \cdot & \cdot & \bullet \\ \cdot & \cdot & \cdot \\ \bullet & \cdot & \cdot \end{pmatrix}$	$\begin{pmatrix} \cdot & \bullet & \cdot \\ \bullet & \cdot & \cdot \\ \cdot & \cdot & \cdot \end{pmatrix}$	$\begin{pmatrix} \bullet & \cdot & \cdot \\ \cdot & \bullet & \cdot \\ \cdot & \cdot & \bullet \end{pmatrix}$
$\lvert\alpha_{\max}\rvert$ [ps/m]	30	1.7	4.2	0.8
J_{bc} [meV]	–	1.04	0.77	0.48
J_b [meV]	–	0.670	0.30	0.200
J_c [meV]	–	-0.05	0.14	0.076
J_{ac} [meV]	–	-0.11	0.05	0.062
J_{ab} [meV]	–	0.30	0.14	0.036
$\mathfrak{D}^a$ [meV]	–	0.339	0.62	0
$\mathfrak{D}^b$ [meV]	–	1.82	0	0.0089
$\mathfrak{D}^c$ [meV]	–	0	1.56(3)	0.0069

the family, see Table 3.1. The phase in the interval $12 - 22\,\mathrm{T}$ has a magnetization of $\sim \frac{1}{3} M_S$ and the saturation magnetization is $M_S = 3.6\,\mu_B$[58]. No magnetoelectric effect was observed in this phase. However, above 22 T, α_{ab} and α_{ba} become non-zero again although with values ~ 5 times smaller than below 12 T[67,68]. The magnetic structures of the two phases above 12 T are as of yet still to be unambiguously determined although collinear spin arrangements with spins along b and ordering vectors along c have been suggested by Kharchenko et al.[58]. The current work includes detailed investigations of the zero-field structure [Section 6.2] and studies of the magnetic order in the field-induced phases [Sections 6.3-6.5].

$LiNiPO_4$. The magnetic structures[48,61] and spin dynamics[53,61] of $LiNiPO_4$ have been determined up to 17.3 T. The phase diagram shown in Fig. 3.2(b) is constructed from neutron diffraction and magnetization measurements[61]. At low temperatures, the magnetic structure is commensurate with the major spin component along c and with $(\uparrow\uparrow\downarrow\downarrow)$ symmetry[42]. The material is magnetoelectric in this phase with finite tensor elements α_{ac} and α_{ca}. An additional spin canting component of $\sim 8^\circ$ and symmetry $(\uparrow\downarrow\downarrow\uparrow)_z$ was reported at zero field[48]. This canting component is field dependent and faciliated by the DM interaction. In fact it turns out to provide the microscopic origin for the magnetoelectric effect in the low-field com-

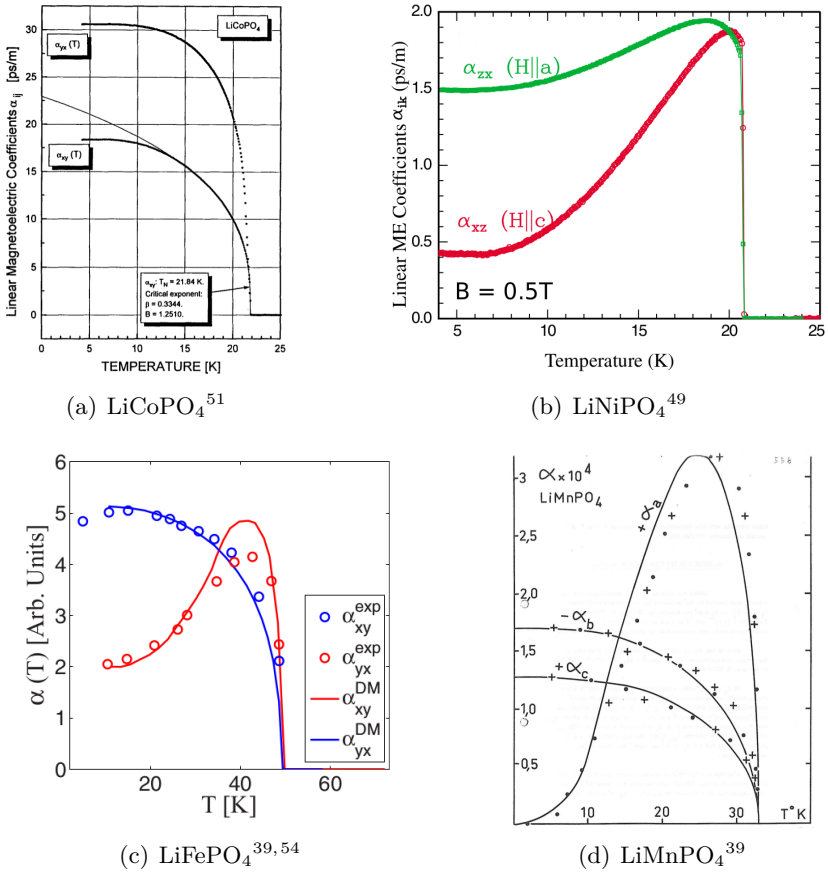

(a) $LiCoPO_4$[51] (b) $LiNiPO_4$[49]

(c) $LiFePO_4$[39,54] (d) $LiMnPO_4$[39]

Figure 3.3: *Temperature dependencies of the magnetoelectric coefficients for $LiMPO_4$ with (a)-(d) M = Co, Ni, Fe, Mn. From Refs. 39, 49, 51, 54.*

mensurate phase[48]. The microscopic model is based on a field-induced asymmetry in the spin canting angles and a minimization of elastic energy and energy associated with a change in the exchange constants. At zero field and just above the Néel temperature an incommensurate spin density wave resides for a narrow temperature interval (of width $\sim 1-2$K) for all fields up to 17.3 T. At low temperatures and above 12 T, an incommensurate spiral phase with spins in the (a,c)-plane exists, the period of which locks in to five times the crystallographic unit cell at 16 T. Further pulsed-field magnetization and neutron diffraction studies up to 30 T show more phase transitions at 19 and 21 T[60,69]. At 30 T the material is only $\sim \frac{1}{3}$ magnetized ($M_S = 2.2\mu_B$). With the saturation field estimated to ~ 90 T[70] the existence of even more phases at higher fields is expected. Interestingly, all incommensurate phases of $LiNiPO_4$ fail to support the magnetoelectric effect whereas the commensurate phases do support this effect[69].

$LiFePO_4$. This compound orders with the major spin component along the easy axis, b[43,71]. In addition to the major ($\uparrow\uparrow\downarrow\downarrow$) symmetry component there is a spin rotation towards a as well as a canting with symmetry ($\uparrow\downarrow\downarrow\uparrow$) along c with an overall deviation from the b-axis of 1.3°[54]. No phase transitions were observed upon applying a magnetic field along the easy axis up to 16 T[56,57] but transitions may occur for higher fields. Like the other members of the lithium orthophosphate

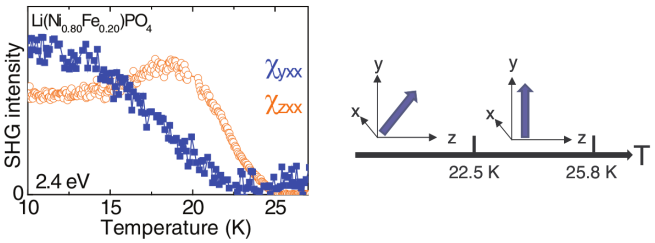

Figure 3.4: *Temperature dependence of SHG tensor elements representing spin components along b (orange) and c (blue) in $LiNi_{0.8}Fe_{0.2}PO_4$ and proposed spin orientations for the two different magnetic phases. Figures from Ref. 73.*

family, $LiFePO_4$ displays the magnetoelectric effect in the commensurate phase and the active tensor elements are α_{ab} and α_{ba}. A microscopic model successfully explains the temperature dependence of the magnetoelectric tensor elements in $LiFePO_4$. The model is similar to that suggested for $LiNiPO_4$, but based on changes in the DM interaction rather than changes in exchange interactions.

$LiMnPO_4$. Like the other compounds in the family, $LiMnPO_4$ orders in an antiferromagnetic structure of symmetry $\uparrow\uparrow\downarrow\downarrow$) – in this case with spins purely along a – and with non-zero diagonal terms in the magnetoelectric tensor[62]. A field-induced spin-flop transition is observed at 4.5 T applied along a where the spins re-orient along the c-direction. The corresponding magnetization curve and phase diagram is shown in Fig. 3.2(c). The low-field, spin-flop and paramagnetic phases meet in a bicritical point where the phase boundary is suppressed and the intensity of the critical scattering is increased.

$LiNi_{1-x}Fe_xPO_4$. Part of this thesis regards systems with, Ni and Fe, distributed on the magnetic site, M. These compounds are less well understood compared to the stoichiometric compounds, but some investigations have been conducted. Mössbauer spectroscopy experiments were performed on $LiNi_{0.99}Fe_{0.01}PO_4$[72] and optical second harmonic generation (SHG) spectra were recorded for $LiNi_{0.94}Fe_{0.06}PO_4$[73]. The magnetic ground states of these compounds with small x were – not too surprisingly – found to be very close to that of the parent compound, $LiNiPO_4$. As the Fe content is increased, the magnetic properties change. In $LiNi_{0.8}Fe_{0.2}PO_4$, the incommensurate phase just above the Néel temperature has disappeared[73,74] and the spins are suggested to be orientated in the (b,c)-plane below $T_{N2} = 22.5\,\mathrm{K}$. Furthermore, a second magnetic phase was discovered with transition temperature, $T_{N1} = 25\,\mathrm{K}$ [see Fig. 3.4]. The spins in the intermediate phase, $22.5 - 25\,\mathrm{K}$, are aligned along b[73]. The magnetoelectric effect has not – to our best knowledge – been characterized in any of the $LiNi_{1-x}Fe_xPO_4$ compounds.

Spin Hamiltonian. Exchange interactions and single-ion anisotropy constants of the lithium orthophosphates were determined using inelastic neutron measurements and the following spin Hamiltonian:

$$\hat{\mathcal{H}} = \sum_{\langle i,j \rangle} J_{ij}\, \mathbf{S}_i \cdot \mathbf{S}_j + \sum_{i,\alpha} \mathfrak{D}_i^{\alpha}\, (S_i^{\alpha})^2 + \sum_{\langle i,j \rangle} \mathbf{D}_{ij} \cdot (\mathbf{S}_i \times \mathbf{S}_j), \tag{3.1}$$

where J_{ij} are the exchange constants, $\mathfrak{D}_i^{\alpha}$ the single-ion anisotropy constants, $\mathbf{D}_{ij}$ the Dzyaloshinskii-Moriya interaction vectors – all parameters introduced in Section 1.1. The exchange paths are also shown in Fig. 3.1. Parameters were obtained for $LiNiPO_4$[53,61], $LiFePO_4$[8] and $LiMnPO_4$[55] but not for $LiCoPO_4$ and are listed in Table 3.1 for comparison. In general, $J_{bc}/J_b \approx 2$ for all compounds. Parameters

were also found for $LiNi_{0.8}Fe_{0.2}PO_4$[74] and these are discussed later in Chapter 8.

Battery materials. It is worth briefly mentioning that apart from being interesting for their magnetic and magnetoelectric properties, the lithium orthophosphates also serve as promising battery material candidates. Lithium-based batteries are omnipresent in our everyday lives as reliable, cheap, compact, rechargeable and relatively environmentally friendly power sources for electronic devices but also promise high-density storage for sustainable energy such as solar or wind power. Since at the moment – and most likely for many years to come – Li-based batteries are the first choice for portable energy storage, improving their cost and performance attracts lots of interest. The layered rocksalt systems, $LiMO_2$ (M =Co, Ni, Mn)[75–77], were the first to be discovered as potential battery cathodes and today $LiCoO_2$ is the most widely used commercial Li-battery material[78]. A range of other compounds are also used in the battery industry, including $LiFePO_4$. $LiFePO_4$ has the advantage of being based on the abundant and cheap transition metal ion, Fe, but battery researchers also investigate $LiMnPO_4$ and $LiCoPO_4$[78].

3.2 Mixed anisotropy magnets

Some of the materials investigated in this thesis contain a mixture of magnetic ions with different single-ion anisotropies. The simplest of such systems with non-trivial behavior has two constituents with orthogonal anisotropies and one may think of the system as having two competing order parameters. According to renormalization group theory, the phase diagrams of such systems either display a first-order *spin-flop* transition and a bicritical point or a *mixed* phase and a tetracritical point[79], see schematic in Fig. 3.5(a). Note that the variable, g, in Fig. 3.5(a) may denote different quantities such as applied magnetic field, stress or as in our case concentration of one magnetic ion. A well-studied example exhibiting competing order parameters is the uniaxial antiferromagnet in a longitudinal magnetic field where spins orient parallel to the field for low fields and transverse to the field above some critical value[80]. The uniaxial antiferromagnet thus displays a bicritical point. Systems with a random distribution of two magnetic components more often display a tetracritical point[79]. Realizations of such systems are found in mixed compounds such as $Mn_{1-x}Fe_xWO_4$[81], $K_2Mn_{1-x}Fe_xF_4$[82], $Fe_xCo_{1-x}Cl_2$[83,84] and $Fe_xNi_{1-x}F_2$[85]. In the following, we look a bit closer into the two latter examples.

The parent compounds of $Fe_{1-x}Co_xCl_2$, $FeCl_2$ and $CoCl_2$, both have rhombohedral crystal structures with similar lattice constants and they order in identical antiferromagnetic structures except for the spin orientation. The Fe spins order along the hexagonal c-axis and the Co spins order in the (a, b)-plane. The alloyed compound, $Fe_{1-x}Co_xCl_2$, therefore represents a mixture of 3D Ising system and a 3D XY antiferromagnet. Extensive studies of the magnetic (x, T) phase diagram were conducted in Refs. 83 and 86. The results are based on magnetic susceptibility and neutron diffraction experiments and lead to a phase diagram with a tetracritical point at $x = 0.307$ [see Fig. 3.5(b)]. Although the magnetic phase diagram of $Fe_{1-x}Co_xCl_2$ resembles the theoretical predictions [compare Fig. 3.5(a) and (b)] there are still some crucial differences. The lines describing the phase boundaries, A-M-C and B-M-D in Fig. 3.5(b), should be smooth but experience kinks at the

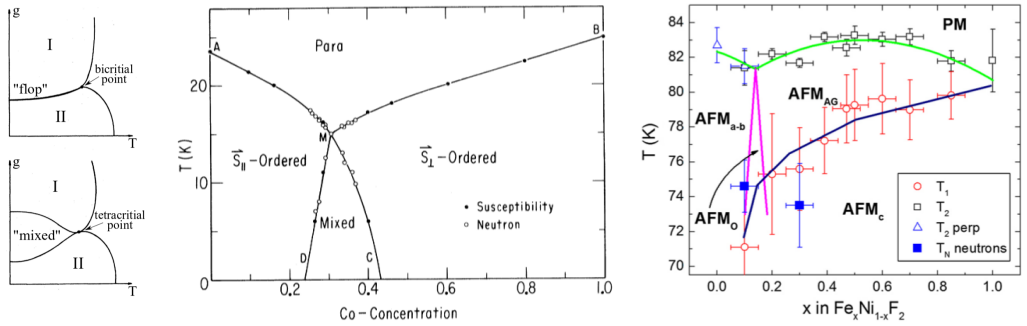

(a) (b) (c)

Figure 3.5: *Magnetic phase diagrams of systems with competing order parameters. (a) Theoretical schematics[79] with phases I and II corresponding to two separate order parameters as well as a mixed phase. Bi- and tetracritical points are indicated. (b) $Fe_{1-x}Co_xCl_2$[83] with phases $S_{||}$ [ordering along the hexagonal c-axis], $S_\perp$ [ordering in the (a,b)-plane] and a mixed phase. (c) $Fe_xNi_{1-x}F_2$[85] with phases AFM_{a-b} [ordering in the (a,b)-plane], AFM_c [ordering along c], AFM_{AG} [glass phase], AFM_O [oblique phase] and PM [paramagnetic phase]. The lines in (b) are a guide to the eye whereas in (c), the green and magenta curves are phase boundaries as calculated using mean-field theory and the dark blue curve is a guide to the eye.*

critical point, M. Furthermore, the nature of the mixed phase is not entirely clear, i.e. is it exhibiting phase separation or long-range order? In Ref. 83, it is discussed how the microscopic symmetry of the system is lower than the macroscopic symmetry. As a result, off-diagonal terms are allowed in the Hamiltonian as the random distribution of magnetic ions generates different environments at each magnetic site.

The magnetic phase diagram of $Fe_xNi_{1-x}F_2$ was determined using magnetization measurements, neutron diffraction and mean-field theory[85]. Again, the parent compounds, FeF_2 and NiF_2, both have tetragonal crystal structure with similar lattice parameters and they order identically – but for the spin orientation – in an antiferromagnetic ground state. The Fe spins order along the c-axis and the Ni spins order in the plane perpendicular to the c-axis. The phase diagram of $Fe_xNi_{1-x}F_2$ is shown in Fig. 3.5(c) and has some similarities with that of $Fe_{1-x}Co_xCl_2$ [compare with Fig. 3.5(b)]. Both materials have a mixed phase for an intermittent range of x and the mixed phase in $Fe_xNi_{1-x}F_2$ displays oblique ordering with finite spin components both along c and in the (a,b)-plane. Moreover, $Fe_xNi_{1-x}F_2$ hosts a glassy phase not seen in $Fe_{1-x}Co_xCl_2$ and so-called *Griffiths-like*[87] short range order exists in this region as a result of the random anisotropy.

The above examples are highlighted in order to show how random magnetic anisotropy may lead to interesting magnetic phase diagrams and also to provide some background for the investigations of the mixed compound, $LiNi_{1-x}Fe_xPO_4$, later on in Chapter 8.

Chapter 4

Experimental Techniques

A number of different experimental techniques were employed in the present work. These include both macroscopic material characterization methods such as magnetization, AC susceptibility, pyrocurrent and heat capacity measurement but also neutron scattering techniques including elastic, inelastic and polarized neutron experiments. These techniques probe various different material properties and are described in the following sections.

4.1 Macroscopic material characterization methods

Characterizing material properties such as heat capacity or magnetization is effective in order to obtain an overview of the phase diagram of a material. Phase transition can be traced in changes in the measured quantities as a function of externally applied quantities. In our case these variables are temperature and magnetic field but it might equally well be electric field, pressure, doping, solvant concentration etc. depending on the field of work. In this work, transition temperatures and fields are determined upon cooling or increasing field unless otherwise stated. Most often these kind of experiments can be done at one's home institution or a collaborator's laboratory. However, they only probe macroscopic properties and other methods are needed in order to determine microscopic properties such as crystal and magnetic structures. On the plus side, the macroscopic characterization methods are relatively straight forward, produce a lot of information in a short time (on the order of days) and are generally associated with low costs.

VSM and AC susceptibility measurements. Vibrating sample magnetization (VSM) and alternating current (AC) susceptibility measurements were carried out using a CRYOGENIC cryogen free measurement system (CFMS) at DTU Risø Campus and at the Quantum Design Physical Properties Measurement System (PPMS) at DTU Chemistry. The former is described here. The latter is of similar setup.

The magnetometer consists of a cryostat to control the sample temperature and

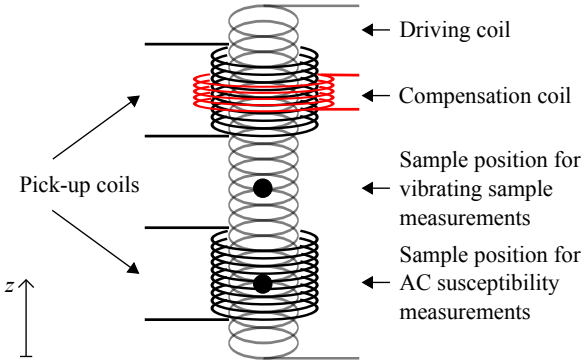

Figure 4.1: *VSM and AC susceptibility experimental setup. Note that the AC driving coil is actually positioned outside the pick up and compensation coils but is shown on the inside in order to maintain a clearer illustration.*

a DC magnetic field up to 16 T can be applied along the vertical direction. Two pick-up coils, a compensation coil and a driving coil are placed around the sample chamber as shown in Fig. 4.1. Since the pick-up coils are not perfectly identical a compensating coil is placed around the upper coil and is controlled by a lock-in amplifier. The driving coil is placed outside all the other coils and is used to generate an alternating magnetic field for the AC susceptibility measurements. For the VSM measurements the sample is moved quickly up and down, i.e. vibrated, inside the coils. In either case a magnetic sample induces a signal in the pick up coils. For both VSM and AC susceptibility measurements, a positioning scan is made prior to the actual measurement in order to optimize the signal.

Pulsed-field magnetization measurements. For non-destructive magnetization measurements at very high magnetic fields (approaching 100 T[88]), pulsed fields are needed. Here a capacitor is discharged into a copper coil. In our case this produce a maximum current of 30 kA resulting in a maximum field of 60 T with a rise time of 7 ms and a total pulse duration of 25 ms. The pulse shape is shown in Fig. 4.2(a). The magnetization is measured by a pick-up coil surrounding the sample [see Fig. 4.2(b)]. The setup is described in more detail in Ref. 89. The recorded values are actually $\frac{dH}{dt}$ and $\frac{dM}{dt}$, i.e. the time derivatives of the applied field and the magnetization respectively. Curves for $M(H)$ are then obtained by integration. Background measurements are performed with an empty cryostat. The absolute value of the magnetization is then calibrated to previous VSM measurements collected at lower fields. Measurements of this kind were performed on a $LiCoPO_4$ single crystal. Fields were applied along b up to 36 T which is larger than the saturation field of 28.3 T[58].

The pulsed-field magnetization measurements were performed at the Helmholtz-Zentrum Dresden-Rossendorf.

Similar measurements were performed on $LiNiPO_4$ at The Institute for Solid State Physics by Takumi Kihara from Tohoku Univerisity. Pulsed magnetic fields were applied along c up to 55 T. Takumi Kihara also carried out pulsed-field electric polarization measurements on $LiNiPO_4$. The technique is described elsewhere[90,91].

Heat capacity measurements. Heat capacity was measured using a Quantum Design PPMS. The sample is mounted on a platform as shown schematically in Fig. 4.3(a). Wires provide electrical connection to the platform where thermal contact is ensured with a thin layer of grease. A picture of the $LiCoPO_4$ crystal mounted on the platform is shown in Figure 4.3(b). The sample had a mass of 42.5 mg.

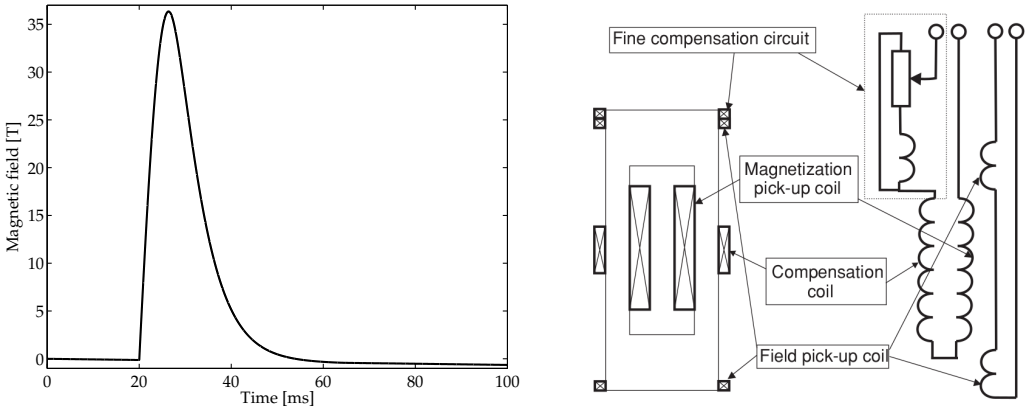

(a) (b)

Figure 4.2: *(a) Magnet pulse shape and (b) pulsed-field setup for magnetization measurements. From Ref. 89.*

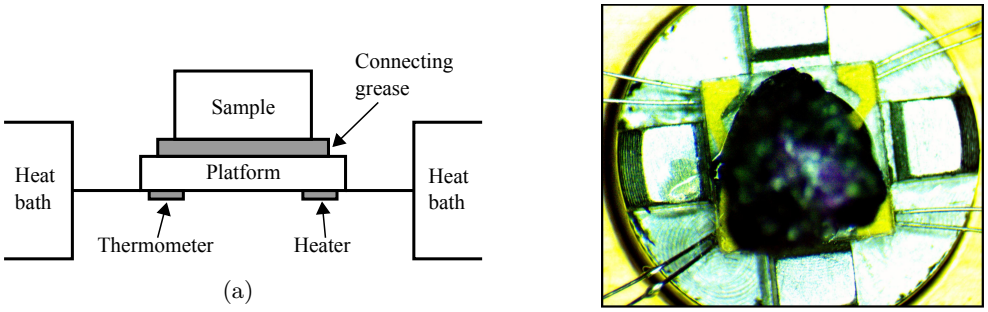

(a) (b)

Figure 4.3: *(a) Heat capacity experimental setup in the PPMS. After the PPMS user's manual[92]. (b) The $LiCoPO_4$ single crystal as mounted in the PPMS. The b axis is perpendicular to the plane of the picture.*

During a measurement, a known amount of heat is applied at constant power for a fixed time. The heating period is then followed by a cooling period of the same duration. From analyzing the temperature response the heat capacity of the sample can be determined. This way the specific heat is measured as function of temperature, which in this work was always carried out while heating. A magnetic field was applied along the *b*-axis of the crystal.

The heat capacity measurements were performed at Helmholtz-Zentrum Berlin (HZB).

Pyrocurrent measurements. Upon heating or cooling a *pyroelectric current* – or *pyrocurrent* for short – is generated in some materials. The electric polarization can be derived from this current and such experiment was carried out in order to investigate the magnetoelectric properties of the mixed compound, $LiNi_{0.8}Fe_{0.2}PO_4$. Measurements were performed using a PPMS with a special insert built by Sebastian Paeckel at the HZB and described in his bachelor's thesis[93], see also Fig. 4.4. The pyrocurrent was measured as a function of temperature and with applied magnetic fields up to 14 T using the quasi-stastic method with constant temperature

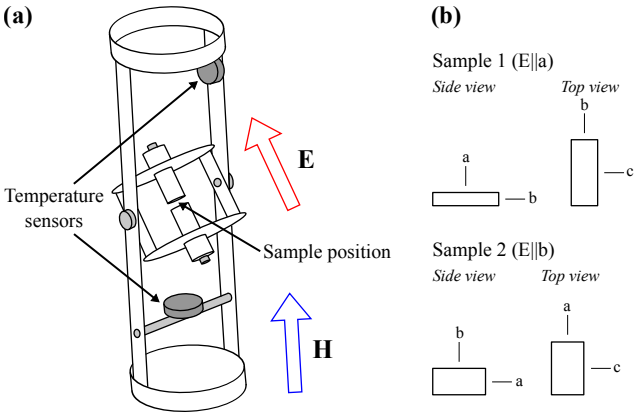

Figure 4.4: *(a) Insert for the pyrocurrent measurements. After Ref. 93. The sample temperature and magnetic field is controlled by the PPMS. The electric field is applied perpendicular to the axis of the rotatable sample stage. The capacitor plates clamping the sample have a diameter of 5 mm. (b) Sketches of the two samples used for the pyrocurrent measurements.*

ramp rate[94]. A voltage of 100 V was applied in the paramagnetic phase at 40 K to ensure formation of a single domain for the electric polarization and the sample was then field-cooled. After cooling the sample to base temperature, ~ 4 K, the voltage was switched off and data recorded while heating back up to 40 K with constant ramp rate, $\frac{dT}{dt}$. Different magnetoelectric tensor elements, α_{ij}, were probed by applying the electric and magnetic fields along the different principal directions of the crystal. The electric polarization may then be calculated from the measured pyrocurrent as follows:

$$I(t) = \frac{dQ}{dt} = A\frac{dP}{dt} \quad \Rightarrow \quad P(t_1) = \frac{1}{A}\int_{t_0}^{t_1} I(t)\, dt + P(t_0).$$

Changing variables from time to temperature yields:

$$P(T_1) = -\frac{1}{A}\int_{T_0}^{T_1} I(T)\, \frac{dt}{dT}\, dT + P(T_0), \tag{4.1}$$

where $\frac{dt}{dT}$ is the inverse of the temperature ramp rate and the negative sign is introduced since $\Delta P < 0$ for $\frac{dT}{dt} > 0$, i.e. when measuring while heating as in our case. The constant, $P(T_0)$, is chosen such that the polarization is zero in the paramagnetic phase. Note that it is very important to have a good description of the pyrocurrent background for subtraction prior to integration. This issue is explored in Appendix C.

Two plate-like samples were used in this experiment [see Fig. 4.4]. They were cut with faces perpendicular to a and b and with areas 2.7×1.1 and $2 \times 1\,\mathrm{mm}^2$ and thicknesses 0.5 and 0.9 mm respectively. The faces were polished and gold sputtered in order to obtain good contact with the sample holder electrodes. A droplet of ethanol was used in order to help placing the (very tiny and fiddly) samples in between the electrodes of the pyrocurrent insert. The rectangular sample shape enabled orientation by eye inside the insert in order to apply magnetic fields along different directions. Since such positioning is easier for the long axis of the samples, a larger misalignment is to be exptected for fields along c for both samples. However, the alignment is estimated to be within $\sim 2^\circ$ in all cases.

4.2 Neutron diffraction

Neutron diffraction serves as an excellent tool for crystal and magnetic structure determination. The microscopic structure – both nuclear and spin – is directly probed via the neutron's interactions with nuclei and electron spin as discussed in Chapter 2. Magnetic phase transitions can be tracked and characterized by following magnetic Bragg peaks as a function of temperature and applied magnetic field. However, neutron experiments are inherently time-consuming and therefore benefit massively from being supplemented by macroscopic measurements such as those described in the previous section. Nevertheless, some microscopic information is exclusively obtainable with neutron diffraction. The experimental setups of two different kinds of instruments for carrying out neutron diffractions are described in the following. The instrument details for each specific experiment are given in Chapters 6-8 together with the results.

Two-axis diffractometer. The basic principle of a two-axis diffractometer is shown in Fig. 4.5. The monochromator picks out a single wavelength, λ, from the polychromatic incoming neutron beam. The incoming beam can be either pulsed or continuous and usually each measurement is merely integrated over a certain amount of time and any time structure to the beam is neglected. The monochromator is a single crystal with a well-defined lattice constant such as PG(002) or Ge(311), and the wavelength is selected using Bragg's law. However, Bragg's law also picks out higher order neutrons – i.e. $\lambda/2$, $\lambda/3$ etc. Therefore, a filter may be placed after the monochromator, usually before the sample. In case of Ge(311), the second order neutrons are prohibited because of the diamond structure of Ge and in this case a filter is not necessary. A monitor is to be found after the monochromator and most often measurements are normalized with respect to its reading. Collimators and slits may be placed either before or after the sample – or in both locations. Especially the slits are helpful in order to lower the background signal

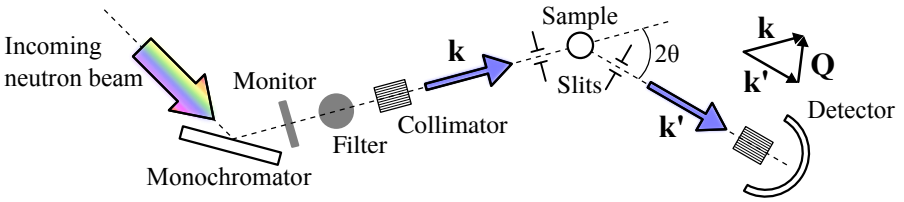

Figure 4.5: *Two-axis diffractometer with various components indicated. The scattering triangle is shown just above the detector.*

Table 4.1: *List of instruments used for neutron diffraction in the presented work. Triple-axis spectrometers operated in elastic mode are shown with brackets.*

Instrument	Institute	Source	Monochromator	Filter	Detector
E4	HZB	Reactor	PG(002) or Ge(311)	PG	2D (200x200 mm^2)
E5	HZB	Reactor	PG(002)	PG	2D (90x90 mm^2)
TriCS†	PSI	Spallation	PG(002) or Ge(311)	PG	2D (160x160 mm^2) or 1D
D23	ILL	Reactor	PG(002) or Cu(200)	PG	1D (lifting ±30°)
(RITA-II)	PSI	Spallation	PG(002)	Cooled Be	2D
(EIGER)	PSI	Spallation	PG(002)	PG	1D
(4F1)	LLB	Reactor	PG(002)	PG	1D

† Note that TriCS was upgraded in 2017. It is now called ZEBRA and offers energy discrimination.

from sample environment or other obstructions. Usually the detector is placed in the horizontal plane such that in order to reach a certain Bragg reflection one must rotate the sample appropriately. If no magnetic fields are needed this can be accomplished with a 4-circle stage where the crystal may be rotated nearly throughout all of 4π. Otherwise inside a standard vertical magnet, the accessible Bragg peaks are confined to whatever horizontal scattering plane the sample is oriented in. In the case of D23 at the ILL the detector is mounted on a lifting arm such that even with a magnet out-of-plane momentum transfers are possible.

When performing a diffraction experiment using a two-axis instrument one assumes that all neutrons are scattered elastically. This is not entirely true since some of them will lose or gain energy when scattered, i.e. they scatter inelastically. The detector does not distinguish between neutron scattered elastically or inelastically and this extra scattering therefore contributes to the background signal. If one wants to measure weak Bragg peaks, it can be beneficial to add an analyzer just before the detector. This ensures that only elastically scattered neutrons reach the detector but also complicates the Lorentz correction factor[95]. Most diffractometers do not offer this option and one must use a triple-axis spectrometer instead. Apart from the analyzer this setup works much the same way as the two-axis instrument.

Table 4.1 lists instruments used for neutron diffraction during this project.

Diffraction using time-of-flight. Another way of measuring a diffraction pattern is by exploiting the time structure of a pulsed neutron beam or, alternatively, chop a continuous beam into pulses and use the time-of-flight (TOF) method. The diagram in Fig. 4.6 shows the basic principle of a TOF diffractometer. The desired wavelength band is cut from the incoming neutron pulse. Several choppers may be involved in this process in order to cut away unwanted fast neutrons and to shape the pulse appropriately. The neutrons then travel the distance L_1 to the sample

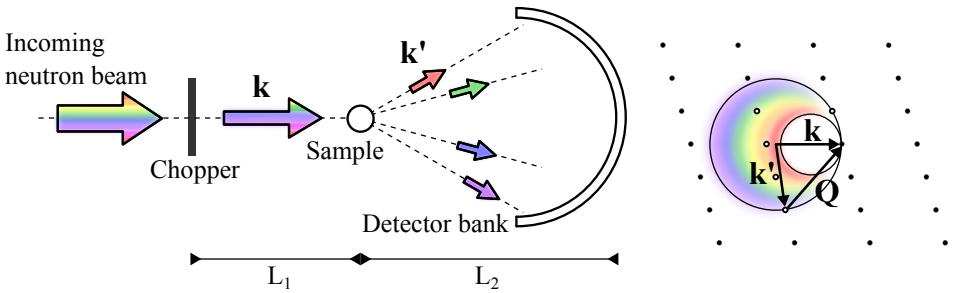

Figure 4.6: *TOF Laue diffractometer. The Ewald's sphere and scattering triangle is illustrated to the right. Reciprocal lattice points within the colored part of the sphere can be probed in the Laue experiment.*

Table 4.2: *List of TOF diffractometers used during the presented work. Instruments in brackets may also be operator in inelastic mode. Note that the SEQUOIA experiment was performed during my Master's project but part of the data analysis and subsequent paper writing was done during my PhD.*

Instrument	Institute	Source	Detectors
NOBORU	J-PARC	Spallation	Forward scattering, flat geometry
(EXED)	HZB	Reactor	Forward and backscattering, flat geometry
(SEQUOIA)	ORNL, SNS	Spallation	Forward scattering, cylindrical geometry

where they scatter and hit the detector placed a distance L_2 after the sample. The wavelength of a detected neutron is determined from the relationship:

$$t = \alpha(L_1 + L_2)\lambda, \tag{4.2}$$

where t is the measured neutron TOF from chopper to detector, $\alpha = 252.7\,\mu\text{s/m/Å}$ and the neutron is assumed to be traveling at non-relativistic speeds. TOF instruments most often have a detector bank covering a large area of reciprocal space. This way several Bragg peaks can be probed with the same sample orientation. The detector shown in Fig. 4.6 has cylindrical geometry such that L_2 is the same for all detector pixels at a certain height. However, some times the detector has flat geometry and L_2 varies depending on the pixel. In any case, the momentum transfer may be found from the pixel position, Eq. (4.2) and conservation of momentum, $\mathbf{Q} = \mathbf{k} - \mathbf{k}'$. The TOF Laue method is excellent for probing a large area of reciprocal space and to follow changes in Bragg peak positions and intensities as a function of external parameters such as temperature or magnetic field. However, one can obtain a much better $\mathbf{Q}$-resolution with a two-axis diffractometer. It should also be mentioned that TOF instruments with their large area detectors tend to generate immense amounts of data which may be difficult to handle.

Table 4.2 lists TOF instruments used for diffraction during this work.

4.3 Inelastic neutron scattering

Inelastic neutron scattering is used in order to probe material dynamics. This includes diffusion constants, molecular vibrational modes, phonons and spin-waves – the latter being of interest for the presented work. Spin-wave measurements allow for determination of sign and size of exchange interactions, Dzyaloshinskii-Moriya interactions and single-ion anisosotropy constants of a proposed spin Hamiltonian. In principle – given that the model is correct and sufficiently detailed – one then essentially knows everything there is to know about the magnetic interactions of a system. Spin-waves are measured with either a TOF spectrometer or a triple-axis spectrometer. Here, only the triple-axis spectrometer is described since all inelastic neutron scattering experiments in the present work were carried out using such instruments.

Triple-axis spectrometer. A sketch of a typical triple-axis spectrometer is shown in Fig. 4.7. The setup is very similar to the two-axis diffractometer described previously. A monochromatic neutron beam is incident on the sample where the neutrons scatter – both elastically and inelastically. The final energy is chosen by the analyzer after the sample such that the desired energy difference, $\hbar\omega = E - E'$, is probed along with the desired momentum transfer. Typically one performs energy scans at constant momentum transfer or scans of momentum transfer at constant energy in order to characterize the spin-wave dispersion. Due to the normalization factor in the partial differential cross section, $\frac{d^2\sigma}{d\Omega dE'} \propto \frac{k'}{k}$ [Eq. (2.2)], these scans are most conveniently carried out by keeping the final energy constant and changing the initial energy. This is because neutron counts are normalized with respect to monitor counts and the monitor sensitivity is proportional to $\frac{1}{\lambda}$ or k. With constant final energy the factor, $\frac{k'}{k}$, becomes constant, easing the data analysis.

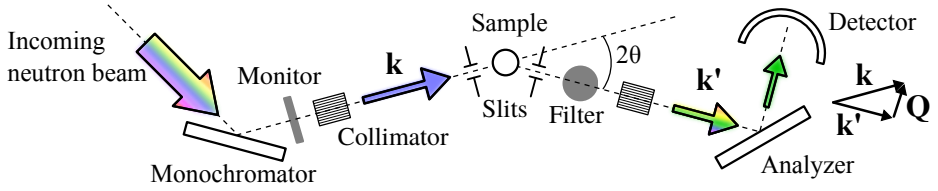

Figure 4.7: *Triple-axis spectrometer with various components indicated. The setup is very similar to that of the two-axis diffractometer except for the addition of an analyzer after the sample. In order to exclusively measure first order neutrons a filter is placed after the sample. Collimators may be placed both before and after the sample as well as after the analyzer (not shown). The scattering triangle is shown rightmost. Note that* $|\mathbf{k}| \neq |\mathbf{k}'|$.

Table 4.3: *List of three-axis spectrometers used during the presented work, some of which also have a polarized-neutron option.*

Instrument	Institute	Source	Monochromator	Analyzer	Pol.
FLEXX	HZB	Reactor	PG(002)	PG(002) or Heusler(111)	Yes
EIGER	PSI	Spallation	PG(002)	PG (002)	No
4F1	LLB	Reactor	PG (002)	PG (002) or Heusler(111)	Yes
ThALES	ILL	Reactor	PG(002), Si(111) or Heusler(111)	PG(002) or Heusler(111)	Yes

Most triple-axis spectrometers have a single analyzer and detector but some sport several analyzers with individual detectors [e.g. FlatCone at the Institute Laue-Langevin (ILL) or MultiFLEXX at the HZB] or combined with a 2D detector [e.g. RITA-II at the Paul Scherrer Institute (PSI)].

A list of triple-axis instruments used for measuring spin-waves during this work is presented in Table 4.3. Some of these offer the option of using polarized neutrons, the subject of the last section of this chapter.

4.4 Polarized neutrons

During this project a single diffraction experiment was conducted at the triple-axis spectrometer 4F1 at the LLB using polarized neutrons. The general setup is very similar to that of a conventional triple-axis spectrometer but for a couple of extra components [see Fig. 4.8]. A bending mirror is placed after the monochromator. In such mirror the refractive index of a neutron depends on its spin state resulting in one state being transmitted and the other reflected. In other words, the neutron beam is polarized. A spin flipper is added before the sample in case one wishes to flip the spin polarization of the incoming beam and Helmholtz coils control the direction of the polarization, $\mathbf{P}$, at the sample position. Various coordinate systems may be used to describe the setup but we adobt one like that used by Moon et al.[37] where $\mathbf{x}$ is along the scattering vector, $\mathbf{Q}$, $\mathbf{y}$ is perpendicular to $\mathbf{Q}$ but in the scattering plane and $\mathbf{z}$ is vertical [see Fig. 4.8 or Fig. 2.3]. Neutrons scattering at the sample position may do so without a change in spin direction or they may have their spins flipped. A Heusler analyzer serves both to pick out neutrons with the desired energy but it also only reflects spin up neutrons. This works because the interference of nuclear and magnetic Bragg scattering from the Heusler crystal is constructive for one spin state and desctructive for the opposite spin state. Adding a second flipper before the analyzer enables measurement of all four possible spin

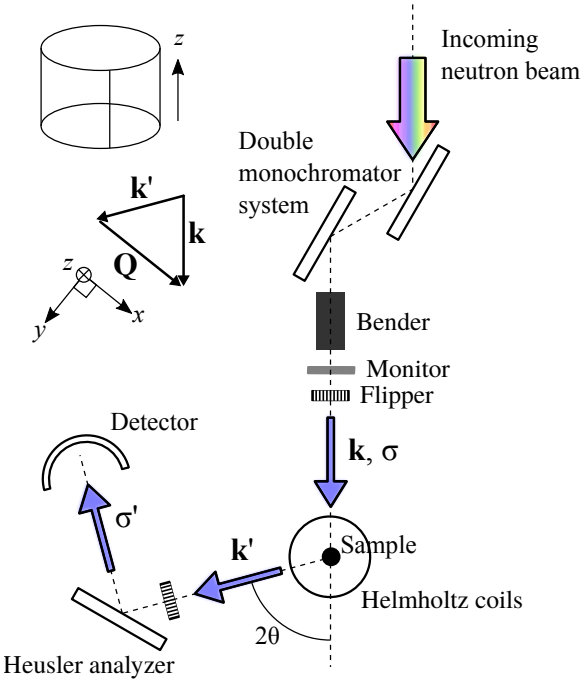

Figure 4.8: *Polarized neutron setup for diffraction at 4F1. The additional components compared to a regular triple-axis setup are the bender, flippers, Helmholtz coils and Heusler analyzer. Note that for clarity filter, collimators and slits are not shown. Furthermore, 4F1 employs a double monochromator system which ensures that the incoming beam always has the same direction and hence the instrument may be operated in a relatively compact space. The Helmholtz coils are illustrated in the upper left corner together with the scattering triangle and defined coordinate axes.*

flip configurations, i.e. (↑↑), (↑↓), (↓↑) and (↓↓). For most purposes, however, it is sufficient with just one non spin-flip and one spin-flip channel. The theory necessary for polarization analysis was outlined in Section 2.5 and the results from the 4F1 experiment are presented later in Section 8.2.

Chapter 5

Monte Carlo simulations

The Monte Carlo method is an extremely succesful tool in describing an exceedingly broad range of physical phenomena. The method was first formulated and applied by, among others, Fermi, Ulam, von Neumann and Metropolis. The idea is to use random sampling to solve a problem of such character that other methods prove difficult or even impossible. This could be problems involving many coupled degrees of freedom, competing interactions, disordered systems or biological structures. The Monte Carlo method is a particular good choice when considering disordered systems since the method is intrinsicly built on randomness. Furthermore, no assumptions on translational or other symmetries are needed.

Here, Monte Carlo simulations have been performed on mixed lithium orthophosphates, $\mathrm{Li}A_{1-x}B_x\mathrm{PO}_4$ with $A, B =$ Co, Ni, Fe, Mn. One of the many beauties of simulations is that they can play the role of either experiment or theory. In this work, they mainly play the role of theory while being compared to and assist in the interpretation of neutron diffraction data. Another advantage of simulations is that different mechanisms are easily switched on or off, allowing for isolation of their individual and collective effects. In an iterative process of comparing simulations with experimental results, the important physics of a system may be identified.

The basics of Monte Carlo simulations, implementation and some test results are found in the following sections. Simulation results on the actual physical systems are presented later in Chapter 8 along with experimental results.

5.1 Model, assumptions and other considerations

In this section, the adobted model is described and the very basics of Monte Carlo simulations are outlined.

Model. The minimum energy state for a proposed Hamiltonian is sought when performing Monte Carlo simulations on a spin system. Hence, in order to get anything useful out of a simulation, it is of utmost importance to have a solid

candidate for the Hamiltonian. In the case of $\mathrm{Li}A_{1-x}B_x\mathrm{PO}_4$ we have:

$$\hat{\mathcal{H}} = \sum_{\langle i,j \rangle} J_{ij}\, \mathbf{S}_i \cdot \mathbf{S}_j + \sum_{i,\alpha} \mathfrak{D}_i^{\alpha}\, (S_i^{\alpha})^2 + \sum_{\langle i,j \rangle} \mathbf{D}_{ij} \cdot (\mathbf{S}_i \times \mathbf{S}_j) + g\mu_B \sum_i \mathbf{H} \cdot \mathbf{S}_i, \quad (5.1)$$

restating the Hamiltonian from Eq. (3.1) where the extra term is the Zeeman energy with the externally applied magnetic field, $\mathbf{H}$, and g and μ_B are the gyroscopic ratio and Bohr magneton respectively. The sums in the first and third term run over all nearest neighbor spin pairs whereas the sums in the second and fourth term run over all individual spins in the system.

Experimentially determined values for parameters for the pure compounds are found in the literature: LiNiPO_4[53,61], LiFePO_4[8,54] and LiMnPO_4[55], but not for LiCoPO_4. Hence, magnetic exchange interactions between ions of the same type, A-A and B-B, are relatively well known, but interactions between different types, A-B, on the other hand, are not. This issue is postponed for now and explored later. The single-ion anisotropy constants arise from the crystal field at the magnetic site caused mostly by the surrounding cage of oxygen, phosphorous and lithium. Therefore, in our simulations, the crystal field is assumed independent on neighboring magnetic ions.

Algorithm, language and boundary conditions. Apart from being based on random numbers, a central concept for Monte Carlo simulations is the Markov chain[96]. This is a process where each state is independent of all preceding states except the one just before. Therefore, the Markov chain carries no memory of previous configurations more than one step back. In such process the principle of detailed balance holds:

$$P_n W_{n\to m} = P_m W_{m\to n},$$

where P_n is the probability the system being in state n and $W_{n\to m}$ the transition rate from state n to state m. The probability of the system being in state n is from classical statistical mechanics $P_n = \frac{e^{-E_n/k_BT}}{Z}$, where E_n is the energy, k_B the Boltzmann constant, T the temperature and Z the partition function which is often quite difficult to determine. This problem is avoided in the Markov chain where the relative probability is the ratio between individual probabilities, $\frac{P_m}{P_n}$, and hence the troublesome denominator cancels. Since the mth state is generated directly from the nth state, one only needs the energy difference, $\Delta E = E_n - E_m$. In the classical Metropolis method[97], the transition rate is:

$$\begin{aligned} W_{m\to n} &= \tau_0 e^{-\Delta E/k_BT} \quad \text{for} \quad \Delta E > 0 \\ &= \tau_0 \qquad\qquad\qquad\quad \text{for} \quad \Delta E < 0, \end{aligned}$$

where τ_0 is the time required to attempt a move and is most often set to unity. This scheme is employed in the present project and follows the steps below:

Metropolis importance sampling

(1) Choose an initial spin configuration.

(2) Choose a spin on site, i.

(3) Propose a new orientation for said spin.

(4) Calculate the energy change, ΔE.

(5) Generate a random number, r, such that $0 < r < 1$.

(6) Accept new spin orientation if $r < \exp(-\Delta E/k_B T)$.

(7) Go back to (2)

The algorithm is thus repeated an appropriate number of times. A natural measure of Monte Carlo simulation time is the Monte Carlo Step (MSC): the number of iterations corresponding to the total number of lattice sites, N. If the sites are chosen at random it is likely that within one MCS some sites are chosen twice or more and some not at all.

For this project, the choice of language for writing the Monte Carlo code is C. This is a versatile language which, as well as being relatively fast, may be compiled and run on any platform. It is also relatively easy to learn although as with any language (be it French or Fortran) it takes about a decade to fully master it. Therefore, my code is most likely optimizable to a great extent.

The regularity of a single crystal renders periodic boundaries the natural choice in this work. This way all spins have the same number of neighbors and any boundary effects are limited. Ideally the simulated system is sufficiently large such that the choice of boundary conditions is insignificant. However, the finite system size does impose a periodicity which one needs to have in mind when considering any incommensurate spin structures.

Once the model is implemented there are still a number of problems presenting themselves. The most important question is: how do we know when we have reached the "correct" solution, i.e. the lowest-energy configuration? We may not know the ground state or the relevant time scales for finding equilibrium or for domain switching. We wish to investigate mixed or disordered systems with competing interactions and the number of iterations necessary to reach the ground state is likely greater for such systems than for the stoichiometric compounds. Moreover, simulation volumes are always limited and we need to make sure that the system size does not influence the character of the ground state. These issues are addressed in the section after the next one but also later in Section 8.3 where simulation results on real systems are presented.

5.2 Implementation

Below, the implementation of the described model is outlined and more technical aspects are tackled.

Lattice and nearest neighbors. A three dimensional spin lattice is initialized according to the nearly face-centered arrangement of the magnetic ions in LiMPO$_4$. For the purpose of these simulations, the slight deviations from a perfect face-centered structure are neglected ($\epsilon, \delta \sim 0.02$ l.u., re-visit Section 3.1 or see Table

5.1). In principle, the exact ion positions are not needed in order to perform the simulation. Only the nearest neighbors, interaction parameters, single-ion anisotropy constants, magnetic field direction and strength as well as spin orientations and sizes are needed. The length of the simulation cube is denoted L.

A straightforward way of building up the lattice is by giving each spin indices along the three crystallographic axes, (i, j, k) where $i, j, k = \{0, L-1\}$. Only lattice sites fulfilling $i+j+k$ even are occupied and the total number of spins is then $N = \frac{L^3}{2}$. Nearest neighbors are found by adding or subtracting the indices by 2 combined. E.g. the nearest neighbors in the (b, c)-plane become $(i, j \pm 1, k \pm 1)$ and along the b-axis they become $(i, j \pm 2, k)$. When running out of sites in either end of the lattice, L is added or subtracted in order to bring the indices back into the simulation volume.

A somewhat less straightforward method is to label the spins $n = \{1, N\}$. Now each spin has just a single label instead of three. One way of doing this is by enumerating the four spins in a crystallographic unit cell as shown in Fig. 5.1. The cell is then stacked along b, then along c and at last along a to create a three dimensional grid. Each unit cell contains four ions and the total number of ions then becomes $N = 4L^3$. Identifying nearest neighbors is not trivial in this array.

Both of the above ways of creating a lattice were implemented. The second method resulted in ~ 5 times faster code and is therefore used henceforth.

In general the material is described in terms of ions of type A and B where the parameters for the two different magnetic ions are listed in an input file to the program. In case of $LiNi_{1-x}Fe_xPO_4$ the magnetic ions are $A = Ni^{2+}$ $(S = 1)$ and $B = Fe^{2+}$ $(S = 2)$ and with associated exchange and single-ion anisotropy parameters. The frequency of each ion is $(1-x)$ and x respectively and the flavor of each ion is assigned by use of a pseudo random number, s, generated between 0 and 1. If $s \leq x$ the site is assigned an ion of type B and otherwise type A.

The initial spin orientation at each site is similarly generated using pseudo random

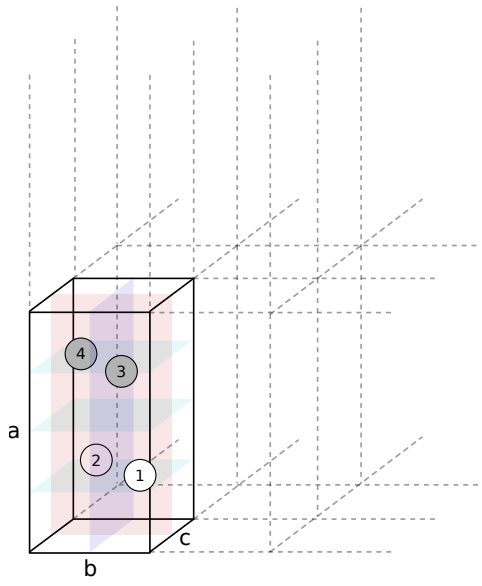

Figure 5.1: *Ion positions within unit cell. The cells are stacked first along c and then b to create a layer of ions in the (b, c)-plane. Thereafter, they are stacked along a to make a three dimensional lattice.*

Table 5.1: *Ion numbers and positions as used in simulations as well as how they are enumerated in Ref. 48.*

Ion number	Ref. 48	Position (l.u.)
1	4	$(\frac{1}{4}-\epsilon, \frac{3}{4}, \frac{1}{2}-\delta)$
2	1	$(\frac{1}{4}+\epsilon, \frac{1}{4}, -\delta)$
3	3	$(\frac{3}{4}-\epsilon, \frac{3}{4}, \delta)$
4	2	$(\frac{3}{4}+\epsilon, \frac{1}{4}, \frac{1}{2}+\delta)$

numbers. Two numbers, $r_1, r_2 \in [0,1]$, are picked and then $c_1 = 1-2r_1$, $c_2 = 1-2r_2$ and $c^2 = c_1^2 + c_2^2$ are calculated. If $c^2 < 1$ the spin coordinates are calculated as follows:

$$S_x = 2c_1\left(1-c^2\right)^{1/2}, \quad S_y = 2c_2\left(1-c^2\right)^{1/2}, \quad S_z = 1-2c^2.$$

If otherwise $c^2 \geq 1$ two new random numbers are picked and the procedure starts over. This method of picking random numbers on the surface of a sphere is described in Ref. 98.

Alternatively, an already existing spin configuration can be loaded in and used as a starting point for the simulation. This way a certain configuraton can be used for several simulations, e.g. in order to compare different codes. Special configurations including segregated or clustered configurations may also be tried out.

Once the spin lattice has been generated or loaded in, information such as ion flavors, spin coordinates nearest neighbors and exchange constants is stored in global look-up tables.

Calculating energies and performing a simulation. Five different neighbor interactions are taken into account in the simulation: J_{bc}, J_b, J_c, J_{ab} and J_{ac} [revisit Fig. 3.1]. Once the lattice is built and neighbors and interactions have been assigned, the total energy can be calculated. When looping over all N spins, each bond is counted twice and hence, the calculated exchange energy is divided by two in the end. The single-ion anisotropy energy is simply calculated by considering each individual ion with spin orientation and flavor. The total energy is stored as a global variable.

For each step in the simulation a random ion is chosen and a re-orientation to some new random coordinates is proposed. The energy change between the old and the new spin coordinates is calculated. The change in energy at each individual bond is taken into account and no factor one half appears in the exchange energy calculation. If the energy difference is negative the move is readily accepted, the spin is updated to its new orientation and the total energy is updated. If the energy difference is positive then the move is accepted if $r < e^{-\Delta E/k_bT}$ as described in the previous section. This process of moving spins is repeated until a suitable number of accepted moves is obtained. Exactly how many moves are needed depends on the system size, interaction parameters and anisotropy constants.

The total energy and measures for magnetic order of symmetry A, G, C and F are saved to a file as often as desired, e.g. every 100 MCS. The measures for magnetic order are calculated as a sum over all unit cells using the 4 basis vectors and 3 crystallographic directions. The measure for a C type magnetic structure is calculated as

$$C_\alpha = \frac{1}{N}\sum_{j=0}^{N/4-1}\left(S^\alpha_{4j+1} - S^\alpha_{4j+2} + S^\alpha_{4j+3} - S^\alpha_{4j+4}\right), \tag{5.2}$$

and with similarly expressions for the other three basis vectors. Note that the notation here differs from that in Ref. 48 [*cf.* Table 5.1].

The heat capacity is calculated from the total energy, $C = \frac{dE}{dT}$, and magnetic phase transitions are identified by peaks in the heat capacity as a function of temperature.

Temperature scans may be performed by *quenching* from a newly generated random initial spin configuration for each temperature step. This way a whole temperature range may be simulated in one go. Alternatively, for each successive temperature, the previous final configuration is used as a starting point. This is called *simulated annealing* and is not unlike a real experiment where the temperature is slowly decreased. For frustrated systems or other systems with many local minima in the energy landscape, it may be easier to reach the lowest energy state when employing simulated annealing rather than quenching. The issue is also briefly discussed in Appendix A.

5.3 Code testing

Before letting the Monte Carlo code loose on "real" systems, it is thoroughly tested. This is a very important (although not very exciting) part of writing code as it yields a way of validating results and finding errors.

Comparison with analytical results. The code is tested against a number of simple cases which are possible to evaluate analytically or numerically directly from statistical mechanics.

The first case is a single unit cell of Heisenberg spins with $J_{bc} = J = 1\,\text{meV}$ and all other interaction parameters set to zero [see Fig. 5.2(a)]. This system consists of two decoupled layers, each containing two interacting spins 1 and 2. In the absence of single-ion anisotropies, it is sufficient to look at the relative motion between the two spins since the energy only depends on their relative orientation. Assuming $S_1 = S_2 = 1$, the partition function can therefore we written as follows:

$$Z = 4\pi \int_0^{\pi} d\theta \, \sin\theta \int_0^{2\pi} d\varphi \, e^{-J\beta\cos\theta},$$

where $\beta = \frac{1}{k_B T}$ as usual, 4π is the integral of the motion of spin 1 and (θ, φ) are the angles giving the orientation of spin 2 with respect to spin 1 in a spherical coordinate system [see Fig. 5.2(b)]. The integral over φ readily gives another

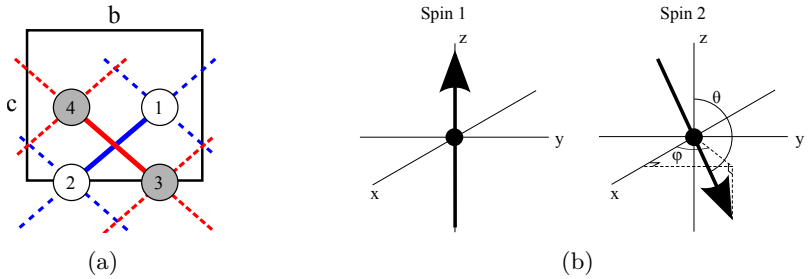

Figure 5.2: *(a) Sketch of simulation unit cell with only one nearest-neighbor exchange coupling. There are effectively two decoupled layers of interacting spins, 1-2 (blue line) and 3-4 (red line). The dashed lines illustrate how the periodic boundary conditions in effect render each interaction bond 4 times as strong. (b) Coordinates of spin 2 with respect to spin 1 used for calculating the energy of the simple Heisenberg system as described in the text.*

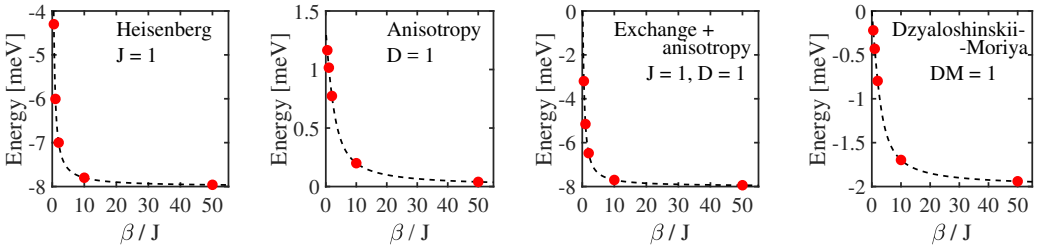

	Heisenberg		Anisotropy		Exchange + anisotropy		Dzyaloshinskii-Moriya	
β/J	E_{sim}	E_{exact}	E_{sim}	E_{exact}	E_{sim}	E_{num}	E_{sim}	E_{num}
1/2	-4.3011(38)	-4.2985	1.1646(9)	1.1645	-3.1951(43)	-3.1860	-0.2205(08)	-0.2205
1	-6.0039(30)	-6.0054	1.0157(9)	1.0148	-5.1523(44)	-5.1502	-0.4309(09)	-0.4312
2	-6.9988(22)	-7.0000	0.7737(8)	0.7737	-6.4778(38)	-6.4811	-0.7966(10)	-0.7955
10	-7.7992(10)	-7.8000	0.1996(3)	0.2000	-7.7004(18)	-7.6983	-1.6971(07)	-1.6972
50	-7.9601(04)	-7.9600	0.0398(1)	0.0400	-7.9395(07)	-7.9399	-1.9399(3)	-1.9399

Figure 5.3: *Energy vs. temperature for four simple cases. The dashed lines show the exact or numerical results whereas the red dots are simulation results for* $\beta/J = 1/2, 1, 2, 10, 50$. *A comparison of the simulation results with the exact or numerical results is shown in the table for these values of* β/J. *Non-zero parameters are stated on the plots and simulations were run for* 10^6 *MCS in all cases.*

factor 2π and the integral over θ can be simplified by changing variable: $x = \cos\theta$, $dx = -\sin\theta\, d\theta$ with the limits changing as $x(0) = 1$ and $x(\theta) = -1$. Thus:

$$Z = 8\pi^2 \int_{-1}^{1} dx\; e^{-J\beta x} = 8\pi^2 \left[\frac{1}{-J\beta} e^{-J\beta x}\right]_{-1}^{1} = \frac{8\pi^2}{J\beta}\left(e^{J\beta} - e^{-J\beta}\right).$$

Recognizing $\sinh(x) = \frac{1}{2}\left(e^x - e^{-x}\right)$ the partition function finally becomes:

$$Z = 16\pi^2\, \frac{\sinh(J\beta)}{J\beta}.$$

From this the energy can be found:

$$\begin{aligned} E &= -\frac{\partial}{\partial\beta} \ln Z = -\frac{1}{Z}\frac{\partial Z}{\partial\beta} = -\frac{J\beta}{\sinh(J\beta)}\left(-\frac{\sinh(J\beta)J}{(J\beta)^2} + \frac{\cosh(J\beta)J}{J\beta}\right) \\ &= J\left(\frac{1}{J\beta} - \coth(J\beta)\right). \end{aligned}$$

The exact energies can then be compared with simulated results. However, because of the periodic boundary conditions each coupling is in effect 4 times as strong and there are two layers in one unit cell. Therefore, the correct expression to compare simulated energies with is:

$$E = 2(4J)\left(\frac{1}{(4J)\beta} - \coth((4J)\beta)\right).$$

Analytical results for four such simple models were obtained. Calculations for the three other models are found in Appendix A. The models are as follows: one concerning single-ion anisotropy only, one with a single exchange interaction *and* single-ion anisotropy and one considering only the DM interaction. Simulations for different values of β/J for the four models yield the results shown in Fig. 5.3. It is clear that there is an excellent agreement between simulated and exact or numerical values.

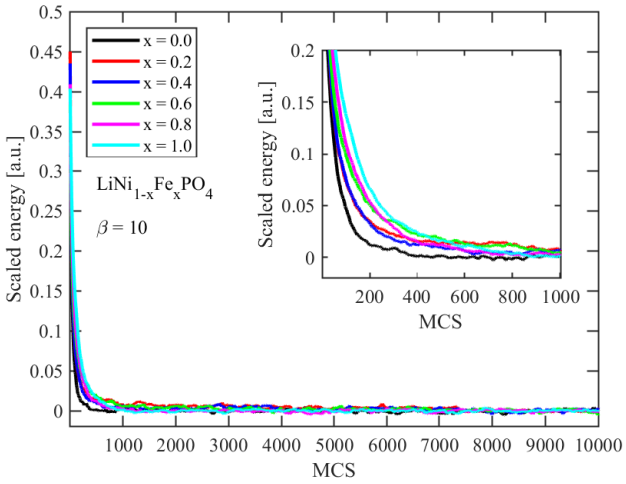

Figure 5.4: *Energy as a function of MCS for runs with $L = 10$, $\beta = 10$ (1.16 K) and different levels of Fe content, x. Simulated annealing was employed with relatively large steps $\beta = 0.5, 1, 2, 10$. The mean of the last 2000 MCSs is subtracted to scale each dataset for easy comparison of the relaxation times. The insert shows a zoom of the first 1000 MCS.*

Run time, system size and configuration effects. Before running a myriad of simulations, it is useful to explore the short-comings and limitations of the code. It assists in determining appropriate choices for lattice size, number of iterations etc. For this purpose experimentally determined exchange and single-ion anisotropy parameters are used for $LiNiPO_4$[53] and $LiFePO_4$[54] and it is assumed that exchange parameters for Ni-Fe bonds are an average of those for the known Ni-Ni and Fe-Fe bonds. Later on, in Section 8.3, this assumption is challenged and parameter space explored. Note also that the DM interaction is generally not taken into account in the spin-wave models providing the interaction parameters for the lithium orthophosphates. Therefore, it is disregarded in all simulations performed on $LiNi_{1-x}Fe_xPO_4$.

The necessary number of iterations are explored by simulating systems with $L = 10$ at $\beta = 10$ and for different Fe contents, x. Scaled energies as a function of MCS are plotted in Fig. 5.4. There is some variation in the convergence time but the energy has stabilized for all values of x around 1000 MCS. Therefore, as a precaution, all simulations are run for 10^4 MCS or longer.

Simulations with $x = 0$ and $x = 0.4$ were run with different system sizes ($L = 1, 2, 4, 10, 15, 20$). These were performed with 10^4 MCS, with simulated annealing for decreasing temperatures in the interval $T = 1 - 60$ K and 1 K step size. Energies and heat capacities as a function of temperature are compared in Fig. 5.5. For $x = 0$, the phase transition looks very similar for $L \geq 4$. For $x = 0.4$, the transition temperature appears to depend on the system size with a spread of ~ 3 K around 17 K. A second, less sharp transition is observed at lower temperatures. The cusp in the heat capacity at 17 K gets sharper for larger systems for both $x = 0$ and $x = 0.4$. Sharper transitions with larger systems is a well-known finite-size effect and if choosing too small systems one risks that any transitions are totally smeared out. Often one is interested in determining properties of a corresponding infinite system – such as critical exponents and temperatures – and then *finite scaling theory* must be employed[99–101]. This subject is not covered here.

The variation in transition temperature for $x = 0.4$ may not be due to the system size but rather slight variations in the exact distribution of Ni and Fe ions. To investigate this effect, 10 runs with $x = 0.4$, $L = 4$ and different start configations

were performed. They are compared in Fig. 5.6(a) and it is clear that there is a sizeable spread in the transition temperature. In Fig. 5.6(b), 10 similar runs but with the same start configuration are compared. There is almost no spread here. Finally, it is speculated that this effect is worse for smaller systems since here small variations in the ion distribution pose larger fractional changes. To test this, another 10 runs were performed with $x = 0.4$, $L = 10$ and different start configurations [see Fig. 5.6(c)]. Here the spread in transition temperatures is also rather small.

In summary, the different initial configurations introduce some variation in transition temperature for smaller systems. Therefore, when performing simulations on the mixed systems, one should do a number of runs with different start configurations and then average over them or one should run larger systems. Since, we do not know the "correct" result in advance it is most likely better to do both, i.e. run large systems several times.

It should be mentioned that the code was thoroughly tested with regards to symmetry equivalent configurations, i.e. various combinations of interaction parameters which should yield the same final energy. For instance, if all parameters are set to zero except J_{bc}, it is equivalent to having only J_{ab} or J_{ac} as the only active parameter. This provides a way to check if the neighbor-finding algorithms have been implemented correctly. The simulation results of such symmetry equivalent parameter combinations are presented in Appendix A. These tests were succesful but showed that simulations should always be run with simulated annealing.

Finally, results were also compared to runs performed using other independent codes written by bachelor student Rasmus Eilkær Hansen from Technical University of Denmark and Professor Olav Fredrik Syljuåsen from University of Olso. Indeed, the

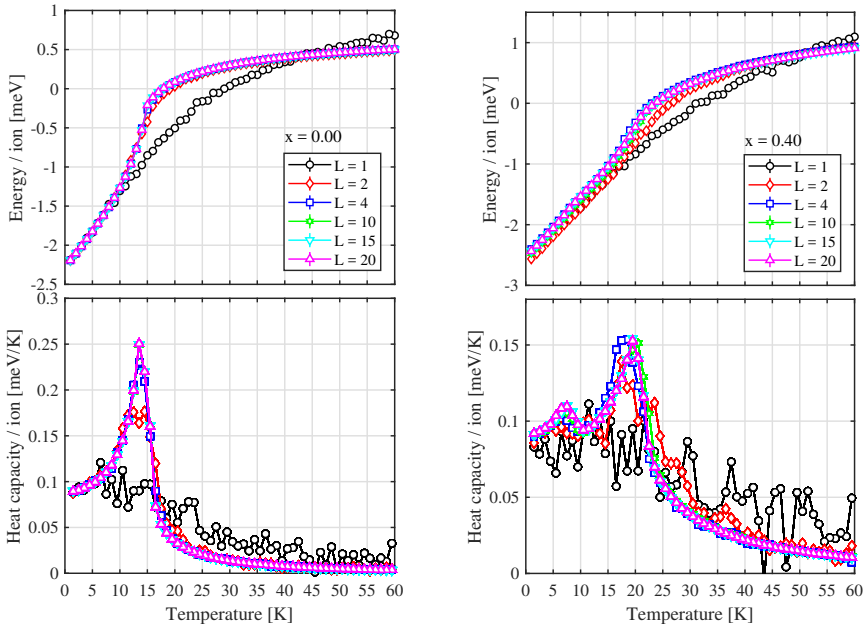

Figure 5.5: *Comparison of runs with different system sizes. The temperature range was T = 1-60 K with step size 1 K, decreasing temperature, simulated annealing and 10^4 MCS.*

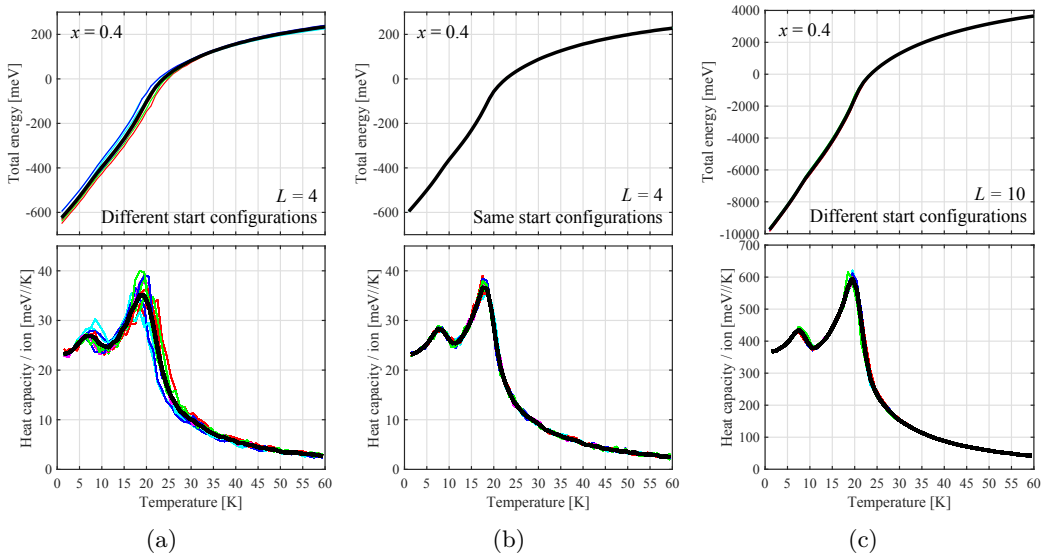

Figure 5.6: *Comparison of 10 runs for $x = 0.4$, with T = 1-60 K, step size 1 K, decreasing temperature, simulated annealing and 10^4 MCS. In (a) the runs all have different start configurations whereas in (b) they start off the same. The system size is $L = 4$ for both. The runs in (c) have $L = 10$ and start off with different configurations like in (a). The thick black curve shows the mean of the 10 curves and for (b) and (c) the energy curves are very close for all runs.*

three codes were written independently in order to be compare results. In general results agree well and a high degree of trust in our codes has been established. Monte Carlo simulations on the $LiNi_{1-x}Fe_xPO_4$ system are presented in Section 8.3. Typical runs were performed with $L = 10$, 10^5 MCS, temperature range $1 - 60$ K, temperature step 0.2 K, decreasing temperature and simulated annealing. A single such run would have a duration of ~ 20 h.

Part II

Results & discussion

Chapter 6

Magnetic order in $LiCoPO_4$

In this section results on $LiCoPO_4$ are laid out. The magnetic zero-field structure was previously determined[42,47] and several phase transitions were observed for magnetic fields applied along the easy b-axis[58]. In this thesis, the magnetic phase diagram is almost completed with magnetic structures and phase boundaries characterized up to 25.9 T. These results are published in Ref. 102 and are elaborated upon in Sections 6.1, 6.3-6.5. Details on the zero-field structure and consequences for the magnetic point group symmetry are presented in Section 6.2. Finally, results on an eluding phase only seen in the heat capacity are found in Section 6.6 and work with fields applied along a are presented in Section 6.7.

6.1 Magnetic phase diagram

The magnetic phase diagram of $LiCoPO_4$ for magnetic fields applied along the easy axis was previously determined up to 20 T using magnetometry and magnetoelectricity measurements (re-visit Fig. 3.2 and see Ref.59). Here, that work is extented and the phase diagram is nigh but completed. The phase boundaries have been outlined by magnetization and heat capacity measurements as well as by following selected magnetic Bragg peaks as a function of temperature and field. Examples of such measurements are shown in Figs. 6.1 and 6.2. The transition temperature at zero field is determined to 21.6(1) K in good agreement with literature.[42,47]

For all probed fields, a single transition is observed as a function of temperature in both the magnetization and neutron diffraction data. However, for fields above ~ 6 T, the heat capacity shows an additional transition situated at a temperature below the main paramagnetic-antiferromagnetic transition. Puzzlingly, evidence for a second transition was observed in neither the magnetization nor neutron diffraction data as illustrated in Fig. 6.1 showing datasets taken at low field and at 10 T. More is to be said about this enigmatic phase in Section 6.6.

At low temperatures, hysteresis is observed in the magnetization and neutron intensity of the $(3, 0, 1)$ Bragg peak, *cf.* Fig. 6.2. Furthermore, the shape of the

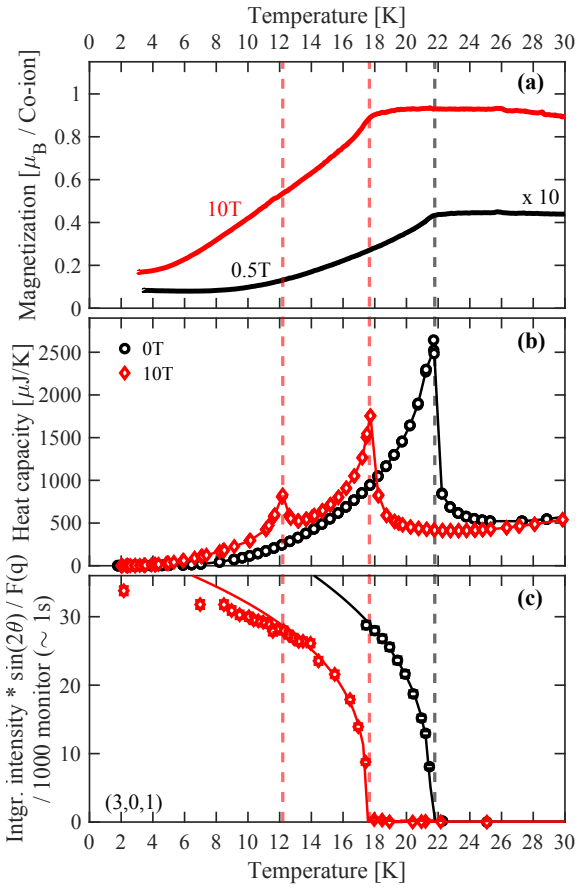

Figure 6.1: *Temperature scans at low field (black) and 10T (red) of (a) magnetization, (b) heat capacity and (c) integrated neutron intensity of the (3,0,1) magnetic Bragg peak with the nuclear background subtracted. The 0.5 T dataset in (a) has been multiplied by 10 in order to show the two datasets in the same plot. The lines in (b) are merely connecting datapoints in order to clarify trends whereas in (c) the lines are fits to a power law. Transitions are marked with vertical dashed lines. At low field, there is a single transition in all three measured quantities. At 10T, however, a second peak appears in the heat capacity which is neither present in the magnetization nor neutron intensity.*

curves for both measured quantities as a function of applied field depends on the field ramp direction. This behavior is further discussed in Section 6.4.

The resulting phase diagram is shown in Fig. 6.3. The phase boundary at 16 – 20 T is reproduced from Ref. 59 and fits well with our results. Field-induced phase transitions are observed at 11.9, 20.5 and 21.0 T at liquid He temperatures. Again, these correspond reasonably well with earlier findings based on pulsed-field magnetization measurements[58].

Magnetic susceptibilities. Curie-Weiss temperatures for both fields along a and b were determined by measuring the magnetic susceptibilities at 0.5 T and subsequentially fitting a Curie-Weiss law to the results:

$$\chi - \chi_0 = \frac{C}{T + \Theta_{\mathrm{CW}}}. \tag{6.1}$$

Here χ is the susceptibility, χ_0 a constant background, C the *Curie constant*, T the temperature and Θ_{CW} the Curie-Weiss temperature. The inverse susceptibilities and fits are shown in Fig. 6.4. The Curie-Weiss temperatures were found to 22(1) K and 121(1) K for the a and b direction respectively. This indicates that some degree of frustration is present for fields along b as the frustration parameter[11], $f = \frac{\Theta_{\mathrm{CW}}}{T_N} \approx 5$. On the other hand, for fields along a, $f \approx 1$; frustration is absent.

This short intermezzo about Curie-Weiss temperatures included data for both fields applied along a and b. We will re-visit any measurements performed with fields along a in the last section of this chapter (Section 6.7). However, the next five sec-

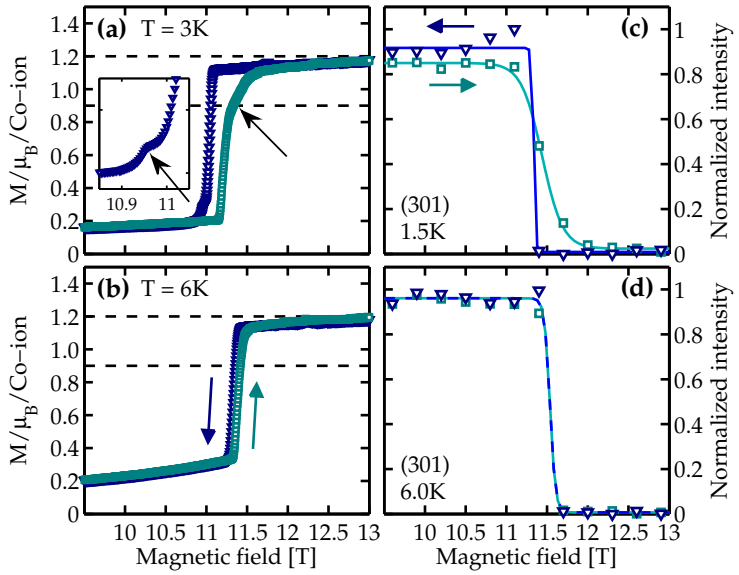

Figure 6.2: *Field scans of the magnetization and neutron intensity of the (3,0,1) Bragg peak at different temperatures. Data is shown for both increasing (green squares) and decreasing (blue triangles) field and with arrows emphasizing the ramp direction. (a) and (b) show the magnetization at 3 K and 6 K respectively. At 3 K, hysteresis is observed as well as pronounced differences in the curve shapes depending on field ramp direction. Special features are highlighted. At 6 K, these features are no longer present. The dashed lines indicate $\frac{1}{3}$ and $\frac{1}{4}$ of the saturation magnetization. (c) and (d) show the integrated neutron intensity of the (3,0,1) magnetic Bragg peak at 1.5 K and 6 K respectively. The lines are guides to the eye.*

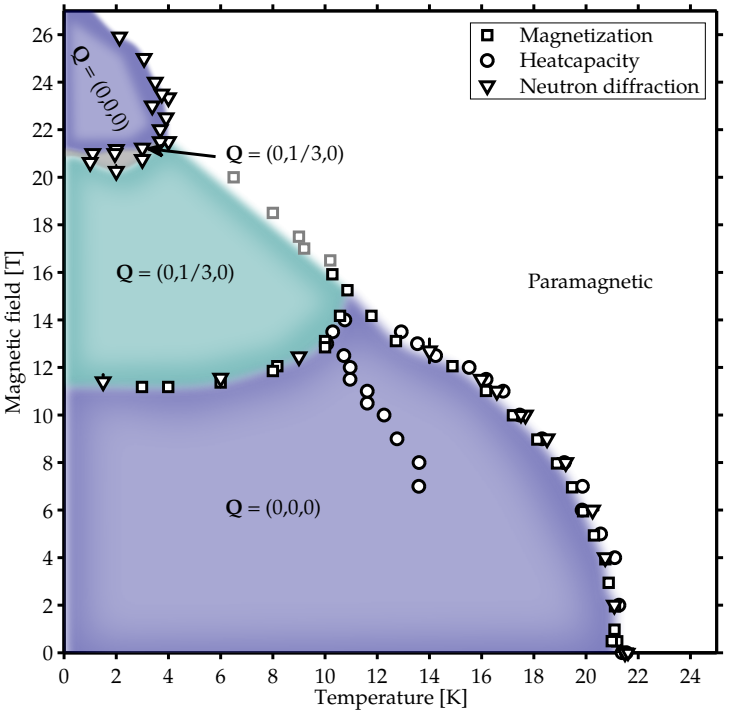

Figure 6.3: *Magnetic phase diagram of $LiCoPO_4$ for magnetic fields up to 25.9 T applied along b. The phase diagram is put together from magnetization (squares), heat capacity (circles) and neutron diffraction (triangles) measurements. The grey symbols are from Ref. 59. The transition fields and temperatures are determined for increasing fields and upon cooling below 16T and upon heating above. The propagation vectors identified from neutron diffraction are shown in the respective phases.*

tions are all about either zero-field measurements (Section 6.2) or results obtained with fields applied along the easy axis b (Sections 6.3-6.6).

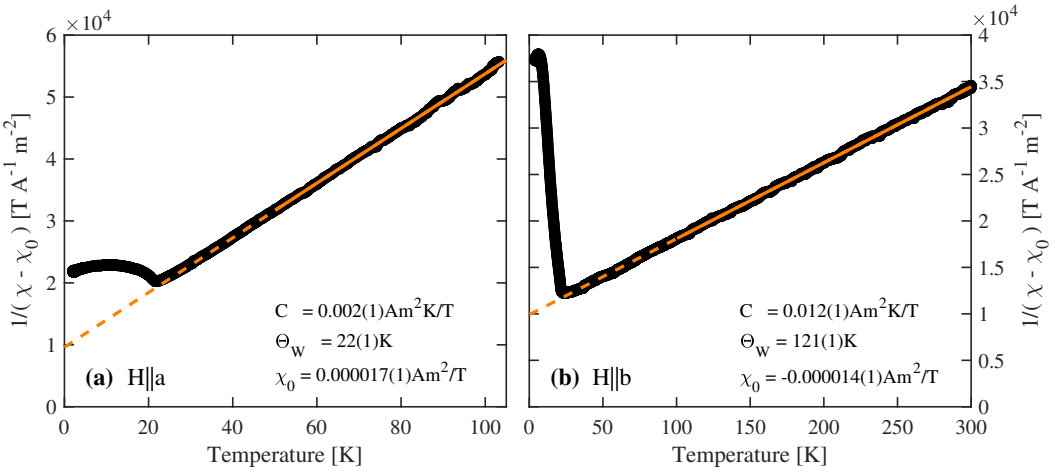

Figure 6.4: *Inverse susceptibility as a function of temperature for fields (0.5 T) applied along the (a) a-axis and (b) b-axis respectively. In both cases the lines show fits to the Curie-Weiss law as explained in the text. The solid part of a line shows the fitted interval and the dashed part is merely an extension of the fit.*

6.2 Investigations at zero field

Combining data from TriCS and RITA-II the zero-field magnetic structure of $LiCoPO_4$ was determined. The sample was – for both experiments – a 20 mg high quality $LiCoPO_4$ single crystal. The results largely correspond with literature, however, some exquisite details are revealed and later turn out to be important when viewed in relation to the Dzyaloshinskii-Moriya interaction, see Section 6.7.

An Eulerian cradle, a closed-cycle He refrigerator, open collimation, a Ge(311) monochromator delivering neutrons of wavelength $\lambda = 1.175$ Å and a 15 mm (50 mm) aperture before (after) the sample were employed for the TriCS experiment. Second order contamination was absent due to the diamond structure of Ge.

Minor spin components of the zero-field structure were investigated at the triple-axis spectrometer RITA-II. The instrument was operated with wavelength, $\lambda = 4.04$ Å, of both incoming and outgoing neutrons. A vertically focusing PG(002) monochromator, $80'$ collimation between monochromator and sample and a cooled Be filter before the analyzer were used. Energy discrimination ensured a very low background. Vertical magnetic fields up to 15 T were applied along b and momentum transfers were confined to the $(H, 0, L)$ plane.

Nuclear refinement. Atomic positions for $LiCoPO_4$ were refined in FullProf[103] based on the *Pnma* space group. This was done using commensurate peaks collected at $(0\,\mathrm{T}, 30\,\mathrm{K})$ at TriCS. The Co^{2+} ion experience relatively large absorption and extinction effects are present. Hence, strong Bragg peaks will appear weaker than expected. Consequently, some of the strongest peaks have been excluded in the following analysis and only 146 of 193 collected peaks were into account for refinement of atomic positions. Still, a single isotropic extinction parameter was refined. The results are shown in Table 6.1 and Fig. 6.5 and we find $\epsilon = 0.0279(4)$ and $\delta = 0.018(1)$ in fair agreement with literature[104].

Table 6.1: *Atomic positions for $LiCoPO_4$ as obtained from refinement in* FULLPROF *(R_F = 5.79 %) using 146 commensurate Bragg peaks collected at (0 T, 30 K) at TriCS and using the Pnma space group. A single isotropic extinction parameter was refined and the Debye-Waller factor was globally refined to $B_{\text{iso}} = 0.26(2)$.*

Atom	Site	x	y	z
Li	4*a*	0	0	0
Co	4*c*	0.2779(4)	0.25	-0.018(1)
P	4*c*	0.0939(2)	0.25	0.4174(5)
O1	4*c*	0.0969(2)	0.25	-0.2575(5)
O2	4*c*	0.4541(2)	0.25	0.2056(4)
O3	8*d*	0.1662(1)	0.0443(3)	0.2824(3)

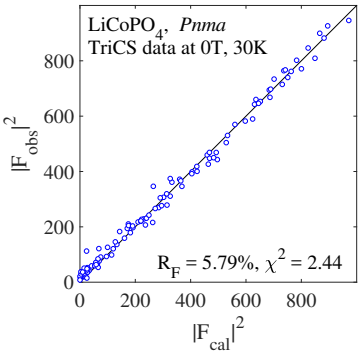

Figure 6.5: *Observed vs. calculated intensities as obtained by refining the atomic positions of $LiCoPO_4$ in* FULLPROF*, see also Table 6.1.*

Although the refinement is reasonably good, forbidden Bragg peaks such as $(1, 0, 0)$ are found to have a finite intensity at 30 K – despite the Ge monochromator prohibiting $\lambda/2$ contamination. This leads to the conclusion that $LiCoPO_4$ might in fact not belong to the *Pnma* or some local disorder is present. At the TriCS experiment we looked for the possibility of a monoclinic structure but the monoclinic angle was measured to 90° within the precision of the instrument. The issue was not further investigated.

Zero-field magnetic structure. The zero-field magnetic structure was refined from commensurate Bragg peaks collected at (0 T, 4.2 K) during the same experiment at TriCS. Again, very strong peaks are disregarded such that only 96 of 122 peaks are considered. We found that the main symmetry component is $(\uparrow\uparrow\downarrow\downarrow)$ with moments along b, a result consistent with earlier findings[42, 47]. As discussed in Section 3.1, a small spin component away from the easy axis[47] and a weak ferromagnetic moment[63] were previously reported. Therefore, additional refinements were performed including various spin cantings, rotations and a ferromagnetic moment. An overview of the results are given in Table 6.2 and the observed vs. calculated intensities for the pure $(\uparrow\uparrow\downarrow\downarrow)_y$ structure is shown in Fig. 6.6. None of the refinements stand out as being particularly brilliant and no clear conclusion as to the details of the zero-field structure can be drawn from the TriCS data. The magnetic moment for the pure $(\uparrow\uparrow\downarrow\downarrow)$ structure along b is refined to $3.36(2)\mu_B$/Co-ion. This is in relatively good agreement with previous pulsed-field magnetization measurements where the saturated moment was determined to $M_S = 3.6\mu_B$/Co-ion[58].

In order to assess how big a role the extinction factor plays, the entire analysis was repeated without this factor. The atomic positions stay the same within the uncertainties but the scaling factor changes slightly, leading to a marginally larger magnetic moment of $3.39(2)\mu_B$/Co-ion for the pure $(\uparrow\uparrow\downarrow\downarrow)_y$ structure. Generally, the refinements – both nuclear and magnetic – are not quite as good when taking out the extinction factor but the conclusions are consistent. For example, the nuclear refinement yields $\chi^2 = 4.47$, $R_F = 7.34\%$ without extinction as opposed to $\chi^2 = 2.44$, $R_F = 5.79\%$ with extinction but the results are robust and do not depend on whether extinction is considered. However, it appears that without an extinction factor, FULLPROF uses the Debye-Waller factor to try and obtain

Table 6.2: *Refinement results for the zero-field magnetic structure of $LiCoPO_4$ as obtained in* FULLPROF. *96 commensurate Bragg peaks collected at (0 T, 4.2 K) at TriCS were used and various different structures with the main component type ($\uparrow\uparrow\downarrow\downarrow$) along b were tried out. Atomic positions along with scaling and extinction factors were inherited from the nuclear refinement, see Table 6.1 and Fig. 6.5.*

Structure type		R_x	R_y	R_z	χ^2	R_F
$(\uparrow\uparrow\downarrow\downarrow)_y$		0	3.36(2)	0	2.553	23.8%
$(\uparrow\uparrow\downarrow\downarrow)_y + (\uparrow\downarrow\downarrow\uparrow)_x$	(canting)	0.9(1)	3.36(2)	0	2.412	20.9%
$(\uparrow\uparrow\downarrow\downarrow)_y + (\uparrow\uparrow\downarrow\downarrow)_x$	(rotation)	-0.1(1)	3.37(2)	0	2.679	23.6%
$(\uparrow\uparrow\downarrow\downarrow)_y + (\uparrow\downarrow\uparrow\downarrow)_x$	(canting)	0.23(6)	3.36(2)	0	2.510	23.0%
$(\uparrow\uparrow\downarrow\downarrow)_y + (\uparrow\uparrow\uparrow\uparrow)_x$	(ferromagnetic)	–	–	–	Fit not stable	
$(\uparrow\uparrow\downarrow\downarrow)_y + (\uparrow\downarrow\downarrow\uparrow)_z$	(canting)	0	3.36(2)	0.41(7)	2.457	22.4%
$(\uparrow\uparrow\downarrow\downarrow)_y + (\uparrow\uparrow\downarrow\downarrow)_z$	(rotation)	0	3.39(2)	0.15(7)	2.529	23.7%
$(\uparrow\uparrow\downarrow\downarrow)_y + (\uparrow\downarrow\uparrow\downarrow)_z$	(canting)	0	3.36(2)	0.28(4)	2.426	22.5%
$(\uparrow\uparrow\downarrow\downarrow)_y + (\uparrow\uparrow\uparrow\uparrow)_z$	(ferromagnetic)	–	–	–	Fit not stable	

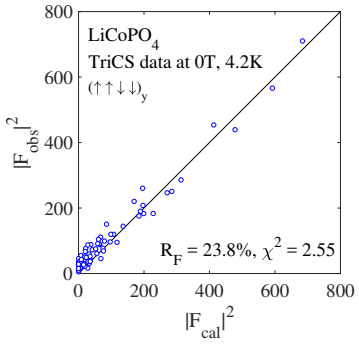

Figure 6.6: *Refinement results for the zero-field magnetic structure of $LiCoPO_4$. Observed vs. calculated intensities as obtained in* FULLPROF. *Here, only the results for the pure $(\uparrow\uparrow\downarrow\downarrow)_y$ component is shown. All other suggested structures from Table 6.2 yield similar plots.*

a better refinement. Without extinction, the Debye-Waller factor is refined to $B_{\text{iso}} = 0.060(72)$ – a result with an unreasonably large error bar and very different to the $B_{\text{iso}} = 0.26(2)$ as found with extinction. Even though at a glance the extinction factor is not needed, it is clear that FULLPROF does need some "fiddle" factor in order to get things right.

Spontaneous spin canting. Minor spin components in zero field and for magnetic fields applied along b and a were investigated at RITA-II by measuring a few key Bragg peaks: $(3,0,1)$, $(0,1,0)$, $(1,0,0)$, $(0,2,1)$, $(0,1,2)$ and $(0,0,1)$. Of these only $(0,1,0)$ has zero magnetic intensity. The calculated magnetic structure factors for the four basis vectors, $|S_R(\mathbf{Q})|^2$, $R = \{A, G, C, F\}$, and spin polarization factors, $|P_i(\mathbf{Q})|^2$, $i = \{x, y, z\}$, for these peaks are listed in Table 6.3. The magnetic neutron intensity may be expressed as:

$$I(\mathbf{Q}) \propto \langle S \rangle^2 f(\mathbf{Q})^2 \sum_R |S_R(\mathbf{Q})|^2 \sum_i |P_i(\mathbf{Q})|^2, \tag{6.2}$$

where $f(\mathbf{Q})$ is the magnetic form factor and $\langle S \rangle$ is the thermal average of the magnetic moment. The following analysis is based on a process of elimating possible structures.

In addition to the major C_y spin component, a smaller symmetry component was identified by observation of magnetic intensity at the $(1,0,0)$ position. This peak mainly represents magnetic structures of A symmetry with spins polarized along

Table 6.3: *Absolute squares of structure and polarization factors for the magnetic basis vectors reflected by the key Bragg peaks used to establish the magnetic structure of $LiCoPO_4$. The factors are normalized to unit spin lengths. Note that the crystallographic directions a, b and c may be used interchangeably with x, y and z.*

(H,K,L)	$\lvert S_R(\mathbf{Q})\rvert^2$				$\lvert P_i(\mathbf{Q})\rvert^2$		
	A	G	C	F	x	y	z
	$(\uparrow\downarrow\downarrow\uparrow)$	$(\uparrow\downarrow\uparrow\downarrow)$	$(\uparrow\uparrow\downarrow\downarrow)$	$(\uparrow\uparrow\uparrow\uparrow)$	a	b	c
$(3,0,1)$	0.07	0.22	11.73	3.98	0.34	1	0.66
$(0,1,0)$	0	0	16	0	1	0	1
$(1,0,0)$	15.51	0.49	0	0	0	1	1
$(0,2,1)$	0	15.71	0.29	0	1	0.28	0.72
$(0,1,2)$	0	1.14	14.86	0	1	0.86	0.14
$(0,0,1)$	0	15.71	0.29	0	1	1	0

either b or c. It is approximately one order of magnitude weaker than $(3,0,1)$ [compare Figs. 6.7(a) and 6.7(b)] which may be assumed to represent the major spin component when regarding the following argument: both $(3,0,1)$ and $(0,1,0)$ appear if a C component is present but the two peaks represent different spin directions. $(3,0,1)$ is present for any orientation whereas $(0,1,0)$ is only present for components along a or c. Since $(0,1,0)$ has no magnetic intensity [see Fig. 6.7(c)] we can exclude those two spin directions entirely. Hence, the $(3,0,1)$ magnetic Bragg peak may be assumed to solely represent a C_y spin arrangement.

The thermal average of the spin is most often maximized at low temperatures. Since an A type component with spins along b would produce spins of varying lengths, it is therefore reasonable to assume that the observed magnetic intensity at $(1,0,0)$ is instead due to a spin component along c. The result is a canting of the spins in the (b,c)-plane. The canting angle, φ, can be estimated by comparing the intensities of $(1,0,0)$ with that of $(3,0,1)$. Following the above arguments, it is assumed that $(3,0,1)$ represents only a C_y symmetry component and $(1,0,0)$ represents only an A_z component such that the measured intensities may be written as in Eq. (6.2)

$$I_{(1,0,0)} \propto \left|S_A^{(1,0,0)}\right|^2 \left|P_z^{(1,0,0)}\right|^2 f^2_{(1,0,0)},$$
$$I_{(3,0,1)} \propto \left|S_C^{(3,0,1)}\right|^2 \left|P_b^{(3,0,1)}\right|^2 f^2_{(3,0,1)}.$$

The spontaneous canting angle is then calculated from the corrected intensities, $I^{\text{corr}}_{(1,0,0)}$ and $I^{\text{corr}}_{(3,0,1)}$, as $\tan\varphi = \sqrt{I^{\text{corr}}_{(1,0,0)}/I^{\text{corr}}_{(3,0,1)}}$. The usual Lorentz factor for two-axis diffractometers, $\sin(2\theta)$, is also employed and although not entirely correct for the triple-axis setup[95], the correction is here estimated to introduce an error of maximum 10% for the two implicated Bragg peaks. The calculated angle is shown in Fig. 6.7(e) where both data at 0 T and 10 T along b are shown. The canting angle is temperature independent below the transition temperature and it is also independent of the applied magnetic field. The magnetic structure is thus locked in with a spontaneous canting angle of $\varphi = 7(1)^\circ$ as estimated from a weighed mean of all data points in Fig. 6.7(e). The resulting zero-field structure is illustrated in Fig. 6.7(f). Note that the $(3,0,1)$ Bragg peak is relatively strong compared to $(1,0,0)$ and is therefore, to a larger extent, subject to extinction and absorption effects. Consequently, the calculated angle may be overestimated.

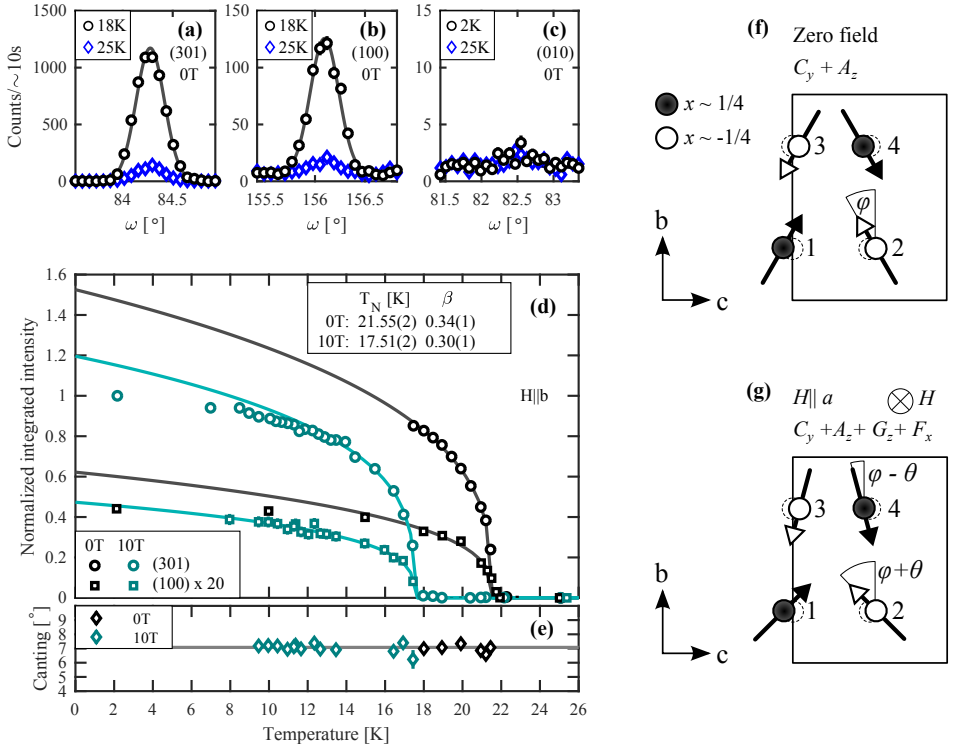

Figure 6.7: *Neutron diffraction data from RITA-II. (a)-(c) rocking curves of (3,0,1), (1,0,0) and (0,1,0) at 18 or 2 K (black circles) and 25 K (blue diamonds), all at 0 T. The solid lines are Gaussian fits from which the integrated intensities are calculated. The canting angle of the zero-field structure is estimated from the intensity ratio between the magnetic contributions of (3,0,1) and (1,0,0). (d) Integrated magnetic intensity of (3,0,1) (circles) and (1,0,0) (squares) as a function of temperature at 0 T (black symbols) and 10 T along b (green symbols). The intensities have been normalized to the value of (3,0,1) at the lowest temperature and the intensity of (1,0,0) has been multiplied by 20 for a better comparison of the temperature profiles. Backgrounds at 25 K have been subtracted. The solid lines show fits to a power law, $I \propto (T - T_N)^{\beta}$, for T>17 K at 0 T and T>13 K at 10 T. The transition temperature, T_N, and critical exponent, β, were fitted collectively for the two peaks. (e) Spontaneous canting angle calculated from the intensity ratio of (1,0,0) and (3,0,1) for measurements done at 0 T (black symbols) and 10 T (green symbols). The horizontal line shows the value of the weighed mean of all data points, φ =7(1)°. Projections in the (b, c)-plane of the magnetic structures of $LiCoPO_4$ for (f) zero field and for (g) $\mathbf{H}||\mathbf{a}$. For clarity, only the four magnetic ions of the unit cell are shown and all angles are largely exaggerated. The ion positions deviate slightly from the high-symmetry positions (dashed circles). The applied field results in asymmetric total canting angles.*

Both $(3, 0, 1)$ and $(1, 0, 0)$ appear at the same transition temperature [see Fig. 6.7(d)] and therefore reflect the same order parameter. Indeed, at zero field a power law with collectively fitted transition temperature, $T_N = 21.55(2)$ K, and critical exponent, $\beta = 0.34(1)$, describe the recorded data well. However, the C type structure polarized along b and the A type structure polarized along b or c are not contained within the same irreducible representation of the lithium orthophosphates, see Table 6.4.

The Bragg peaks $(0, 2, 1)$, $(0, 1, 2)$ and $(0, 0, 1)$ also have magnetic intensity at 0 T. These peaks are all present for a C_y structure but may also represent a G type

Table 6.4: *Irreducible representations for Pnma.*

Γ_1	Γ_2	Γ_3	Γ_4	Γ_5	Γ_6	Γ_7	Γ_8
	F_x		G_x	C_x		A_x	
G_y		F_y			A_y		C_y
	G_z		F_z	A_z		C_z	

component polarized along either a or b, see Table 6.3. A G_y component is unlikely due to maximized moments at low temperatures and is not compatible with the observed magnetoelectric effect, toroidal moment and weak ferromagnetism[19]. Furthermore, G_x is paired with F_z in the irreducible representations, see Table 6.4, and F_z is not present[63]. Therefore, the magnetic intensity at the $(0, 2, 1)$, $(0, 1, 2)$ and $(0, 0, 1)$ positions at 0 T may be ascribed to the major C_y spin component.

It is commented that the zero-field structure determined above does not fully agree with earlier findings. A C_z type rotation of the spins away from the b-axis was reported in Ref. 47 based on the observation of the $(0, 1, 0)$ magnetic peak. However, as seen in Fig. 6.7(c), we observe zero magnetic intensity at the $(0, 1, 0)$ position. A maximum of the rotation angle of $0.7(3)^\circ$ is estimated from the error on the measured zero intensity. This is contrasted by the 4.6° reported in Ref. 47. At present, we have no explanation for the discrepancy.

It has been repeatly suggested[47,105,106] that the zero-field structure of $LiCoPO_4$ has lower symmetry than the originally proposed magnetic point group mmm'[42], corresponding to only a C_y component. The observed 4.6° rotation of spins restricts symmetry to $2'_x/m_x$ which is further reduced to $2'_x$ when requiring a weak ferromagnetic component along b. Indeed, optical SHG measurements advocate that the point group symmetry is $2'_x$[106]. This point group allows for a toroidal moment[19] and the linear magnetoelectric effect with tensor elements $\alpha_{ab}, \alpha_{ba} \neq 0$[7], consistent with measurements[51]. In addition, $2'_x$ allows the tensor elements $\alpha_{ac}, \alpha_{ca} \neq 0$ which are not measurably different from zero[51] but the spin rotation angle introduces only a small deviation from mmm'. Furthermore, as the point group merely yields the *allowed* magnetoelectric tensor elements they are not *necessarily* finite.

Thus neutron diffraction[47], SQUID[107] and optical second harmonic generation measurements[65,66] all paint a picture of $LiCoPO_4$ having magnetic point group $2'_x$ in its zero-field state. In contrast, our observation of a spontaneous spin canting rather than a rotation leads to the magnetic point group $2_z/m'_z$. This point group also allows for a toroidal moment and the magnetoelectric tensor elements $\alpha_{aa}, \alpha_{ab}, \alpha_{ba}, \alpha_{bb}, \alpha_{cc} \neq 0$[19] where only the off-diagonal elements are measurably different from zero. Again, we note that the canting angle only presents a small deviation from mmm'. $2_z/m'_z$ does not support a ferromagnetic moment along b rendering it inconsistent with observations[63,108]. However, removing the twofold axis enables a ferromagnetic moment in the (a, b)-plane. Thus, the magnetic point group m'_z is consistent with our neutron diffraction data and a weak ferromagnetic moment along b.

Interestingly, m'_z is also in agreement with the previous neutron diffraction study[47] when using a different – but still correct – interpretation of the data therein. The rotation of the spins towards c was established based on observation of the $(0, 1, 0)$

magnetic Bragg peak. However, this rotation might equally well be towards a. Assuming such a rotation instead results in magnetic point group $2_z/m'_z$ which again needs relaxing to m'_z to allow for a ferromagnetic moment along b. In addition, the C_x component belongs to the same irreducible representation as the A_z component, see Table 6.4, and as is deducted later in Section 6.7, the two components combined yield a favorable energy term in the Hamiltonian via the Dzyaloshinskii-Moriya interaction. Therefore, our observations may in fact be consistent with the previous studies and the magnetic point group of the zero-field structure of $LiCoPO_4$ is m'_z. Note however, m'_z is not consistent with the observed optical SHG signal[105].

In conclusion the zero-field magnetic structure of $LiCoPO_4$ has major symmetry component ($\uparrow\uparrow\downarrow\downarrow$) with spins along b and minor component ($\uparrow\downarrow\downarrow\uparrow$) along c. This results in a spin canting of $\varphi = 7(1)^\circ$ and magnetic point group m'_z, consistent with a previous neutron study,[47] weak ferromagnetic moment[107] and observed magnetoelectric tensor elements[39,51]. Next up are phase transitions and magnetic structures for magnetic fields applied along b in Sections 6.3-6.5 before turning to results for magnetic fields applied along a in Section 6.7.

6.3 Magnetic structure at intermediate fields

In this section, we have a closer look at the phase in the field interval $11.9 - 20.5\,\mathrm{T}$, the magnetic structure of which was determined using neutron diffraction. The magnetization is $\frac{1}{3}\,M_S$ in this phase and the commensurate peaks characteristic of the low-field phase are absent as seen in Figs. 6.2(c) and (d). We searched extensively for incommensurate magnetic Bragg peaks in the $(H, 0, L)$ scattering plane – with no luck. The ordering vector is therefore neither along a nor c nor a number of plausible superpositions of the two. Furthermore, in the sister compound, $LiNiPO_4$, the ordering vector is along $(0, K, 0)$ with K attaining rational or irrational numbers depending on field and temperature[48,61]. It is therefore likely that the ordering vector of $LiCoPO_4$ in the phase at $11.9 - 20.5\,\mathrm{T}$ is also along this direction. However, with neutrons, one may only ever probe magnetic moments perpendicular to the scattering vector. Hence, with a magnetic moment along b and magnetic fields applied vertically along this direction too, probing an ordering vector along b poses a challenge at an ordinary neutron experiment setup.

Fortunately, D23 at the ILL is no ordinary instrument. Studies with magnetic fields up to 12 T along the b axis were performed utilizing neutrons of wavelength $\lambda = 1.279\,\text{Å}$ and with no collimation. A lifting detector and vertical field cryomagnet with large asymmetric opening angles, -3° to $+10^\circ$, allowed for measurements of momentum transfers with significant out-of-plane components. This proved pivotal for identifying the propagation vector in the $\frac{1}{3}$ magnetization phase. For crystal and magnetic structure determination, 86 commensurate peaks were collected at $(30\,\mathrm{K}, 0\,\mathrm{T})$, $(2\,\mathrm{K}, 0\,\mathrm{T})$, and $(2\,\mathrm{K}, 12\,\mathrm{T})$ and 91 incommensurate peaks were collected at $(2\,\mathrm{K}, 12\,\mathrm{T})$. Circular diaphragms of 15 and 6 mm were used for peak collection and for high-resolution scans along $(3, K, 1)$, respectively. Such scans were performed at various field strengths and for increasing and decreasing field.

Figure 6.8 shows intensity profiles as a function of K along the $(3, K, 1)$ direction at selected fields. The ordering vector was determined to $\mathbf{Q} = [0, 0.33(1), 0] \approx (0, \frac{1}{3}, 0)$

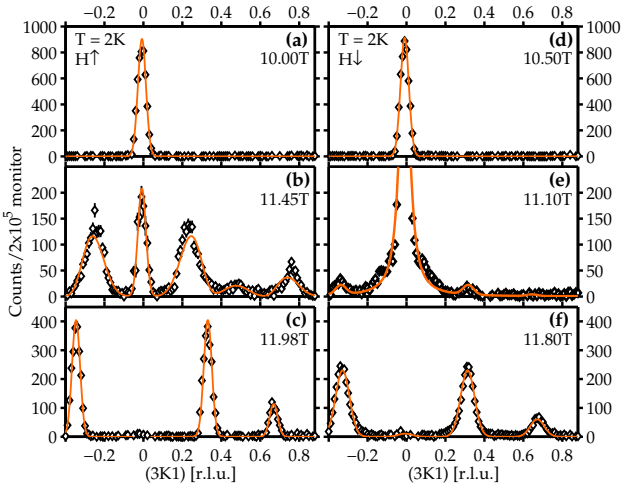

Figure 6.8: *Neutron scattering intensity as a function of (3,K,1) for selected fields at 2 K for (a)–(c) increasing and (d)–(f) decreasing field. The selected fields are in the low-field commensurate phase (top panels), in the transition region (middle panels), and in the* $\mathbf{Q} = (0, \frac{1}{3}, 0)$ *phase (bottom panels). The actual field values are given in the plots. The solid lines are fits to the respective datasets as described in the text.*

Table 6.5: *Atomic positions for* $LiCoPO_4$ *obtained from* FULLPROF *refinement* ($R_F = 5.23\%$) *of 86 commensurate peaks collected at D23 at (30 K, 0 T) and using the Pnma space group. The Debye-Waller factor was refined globally to* $B_{\rm iso} = 0.08(4)$ *and a Becker-Coppens type extinction correction has been applied. Fourier components for the cycloid formed by the magnetic* Co^{2+} *ions are given in the two rightmost columns. These were refined* ($R_F = 11.1\%$) *from 91 incommensurate peaks collected at (2 K,12 T).* R_m *and* I_m *denote the real and imaginary Fourier coefficient respectively. These correspond to the moment sizes in* μ_B *along the major and minor axes of the enveloping ellipsoid.*

Atom	Site	x	y	z	R_m	I_m
Li	4a	0	0	0	–	–
Co	4c	0.2771(9)	0.25	0.980(3)	4.13(5)	1.3(2)
P	4c	0.0951(6)	0.25	0.414(1)	–	–
O1	4c	0.0975(4)	0.25	0.744(1)	–	–
O2	4c	0.4542(4)	0.25	0.208(1)	–	–
O3	8d	0.1663(2)	–	0.2814(5)	–	–

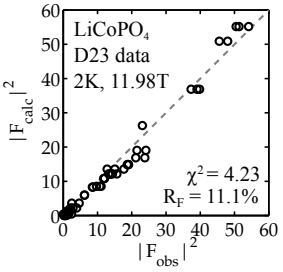

Figure 6.9: *Calculated vs. observed scattering intensities for the collected incommensurate peaks as obtained in* FULLPROF *for the refined magnetic structure in the* $\frac{1}{3}$ *magnetization phase. The dashed line shows* $|F_{\rm calc}|^2 = |F_{\rm obs}|^2$.

based on Gaussian fits to the observed resolution-limited incommensurate peaks at 2 K, 11.98 T [*cf.* Fig. 6.8(c)]. Consequently, the magnetic unit cell in the $\frac{1}{3}$ magnetization phase is tripled along the crystallographic b direction.

From the 91 incommensurate peaks collected at (2 K, 12 T), an elliptic cycloid structure was refined using FULLPROF[103]. All spins on Co sites having identical spatial coordinate y, along the b axis, are aligned and form a ferromagnetic layer in the (a, c) plane. Spins in subsequent layers rotate $\sim 120°$ in the (b, c) plane upon advancing along the b axis. The ratio between the major and minor axes of the enveloping ellipse is 3.2(5) with the major axis along b. Calculated versus observed intensities are shown in Fig. 6.9. Refinement results for the crystal structure and Fourier components of the magnetic structure are given in Table 6.5. Note that the atomic positions correspond well with those determined in the TriCS experiment [compare with Table 6.1].

The $\frac{1}{3}$ magnetization implies an additional ferromagnetic component to be com-

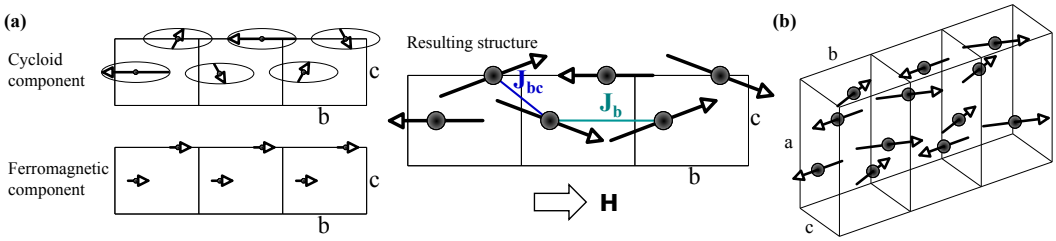

Figure 6.10: *Magnetic structure for 11.9-20.5 T applied along b shown in the (b, c) plane and in 3D for (a) and (b) respectively. The spins order in a superposition of an elliptic cycloid and a ferromagnetic component along b. This results in $\frac{2}{3}$ of the spins being almost parallel and $\frac{1}{3}$ being antiparallel to the field direction. In (a) the nearest- and next-nearest-neighbor interactions J_{bc} and J_b are shown.*

bined with the incommensurate structure. For the cycloid part of the structure there is as always an indeterminable phase shift which in this case has been set to $\frac{\pi}{3}$. This choice maximizes all spin lengths and allows $\frac{1}{3}$ of the spins to be along the easy b axis. The energy cost associated with the single-ion anisotropy is independent of the phase shift angle. Assuming $M_S = 3.6\,\mu_B$[58] and choosing the phase shift to $\frac{\pi}{3}$ the cycloid and ferromagnetic components result in the structure illustrated in Figs. 6.10. The moment lengths for this choice of phase shift are $3.45(7)\,\mu_B/2.94(6)\,\mu_B$ for moments parallel/antiparallel to the b direction. These values are consistent with a saturated moment of $3.36(2)\,\mu_B$ found at TriCS for the zero-field structure and the $3.6\,\mu_B$ determined from pulsed-field magnetization measurements as reported in Ref. 58.

At first glance, the cycloid structure in Figs. 6.10 seems counterintuitive when regarding the axial single-ion anisotropy and antiferromagnetic nearest-neighbor interactions since neither exchange nor the single-ion anistropy energies are minimized. However, the deviations of the moments from the b axis remain relatively small such that interacting spin pairs are either nearly antiparallel or parallel. It is also noteworthy that the spins are in the (b, c) plane as opposed to the (a, b) plane, signifying that the energy cost for spins along c is smaller than along a as expected from both susceptibility measurements[109] and density functional theory[110].

$LiCoPO_4$ has a strong magnetoelectric effect in the commensurate low-field phase[39]. Here, an electric polarization, P_a, is induced along a for magnetic fields applied along b and vice versa. The magnetoelectric properties of the phase with the $\frac{1}{3}$ magnetization plateau have also been studied with the conclusion that this phase does not display the same magnetoelectric effect[59,67]. However, from symmetry analysis the cycloid structure does actually support a magnetoelectric effect[6] but via a different mechanism: the inverse Dzyaloshinskii-Moriya effect for which the direction of the allowed electric polarization is along $\mathbf{Q} \times (\mathbf{S}_i \times \mathbf{S}_j)$. In the case of the cycloid structure observed in $LiCoPO_4$, $\mathbf{Q}||\mathbf{b}$ and $(\mathbf{S}_i \times \mathbf{S}_j)||\mathbf{a}$. Hence, the electric polarization would be along the c-axis for magnetic fields applied along b. To our best knowledge, only P_a was measured in the previous studies and the allowed component P_c has not yet been probed. Therefore, the possibility of a magnetoelectric effect in the $\mathbf{Q} = (0, \frac{1}{3}, 0)$ cycloid structure is not definitely rejected and should be further investigated.

6.4 Hysteresis, phase coexistence and stacking faults

Hysteresis is observed both in the magnetization measurements and in the neutron diffraction data at the transition from the low-field collinear phase to the magnetized cycloid phase. At a first order transition, one expects hysteresis to be present, but in the case of $LiCoPO_4$ the transition is accompanied by additional field ramp direction dependent characteristics. How this is manifested and possible explanations are described in the following paragraphs.

Hysteresis and phase coexistence. In the field scans of the magnetization shown in Fig. 6.2(a)-(b) hysteresis is present at 3 K but significantly reduced at 6 K. Furthermore, at 3 K the shape of the magnetization curve depends on the field ramp direction as follows: for increasing field the transition is first abrupt with the magnetization jumping to $\sim \frac{1}{4} M_S$. Hereafter it increases approximately linearly until the $\frac{1}{3}$ magnetization plateau is reached. Conversely, for decreasing field the transition is abrupt but the magnetization exhibits a minor bump before the system finally enters the low-field phase. At 6 K only minimal hysteresis is observed and the magnetization curves for increasing and decreasing field are similar to each other with just a single step from the low-field phase to $\frac{1}{3} M_S$.

Correspondingly, field scans of the strong $(3, 0, 1)$ magnetic peak measured by neutron diffraction are shown in Fig. 6.2(c)-(d). At 1.5 K a transition initiates at ~ 11.4 T as a function of increasing field strength, in good agreement with earlier findings[58]. For decreasing field, the transition appears at a somewhat lower field, ~ 11.3 T. Again the curve follows different trends depending on the field ramp direction: for increasing field the transition appears smooth whereas for decreasing field it is abrupt. At 6 K both hysteresis and any other ramp direction dependent behavior are absent. The slight differences in the observed transition fields when comparing neutron diffraction data and magnetization measurements may be explained by differences in temperature.

Likewise, a hysteretic region with a range of about 0.3 T is evident when comparing Fig. 6.11(a) and (b). For increasing field, the transition commences around 11.4 T where the intensity of the commensurate $(3, 0, 1)$ Bragg peak begins to decrease and new peaks show up at $\sim (3, \pm 0.2, 1)$. Upon further increasing the field they appear to move gradually to $(3, \pm 0.33, 1)$ where they lock in at ~ 11.9 T. In addition, a less intense peak is observed at $\sim (3, 0.5, 1)$ in the transition region, 11.4 T − 11.9 T, where some intensity is also still present at the commensurate position. In this region the incommensurate peaks are broadened and their shapes are asymmetric as can be seen by comparing Fig. 6.8(b) and (c). Above 11.9 T the peaks become resolution limited and symmetric. We therefore identify 11.9 T as the transition field for increasing fields.

One possible explanation for the above described behavior in the hysteresis region is incommensurate order with a field-dependent unit cell size. However, such long range order would result in resolution limited symmetric peaks and can therefore be ruled out. The peak broadening indicates finite domain sizes and the line shape asymmetry may find its origin in overlapping peaks, possibly signifying several structures with different propagation vectors. The seemingly changing peak positions seen in Fig. 6.11(a) may then be attributed to the change in volume ratio

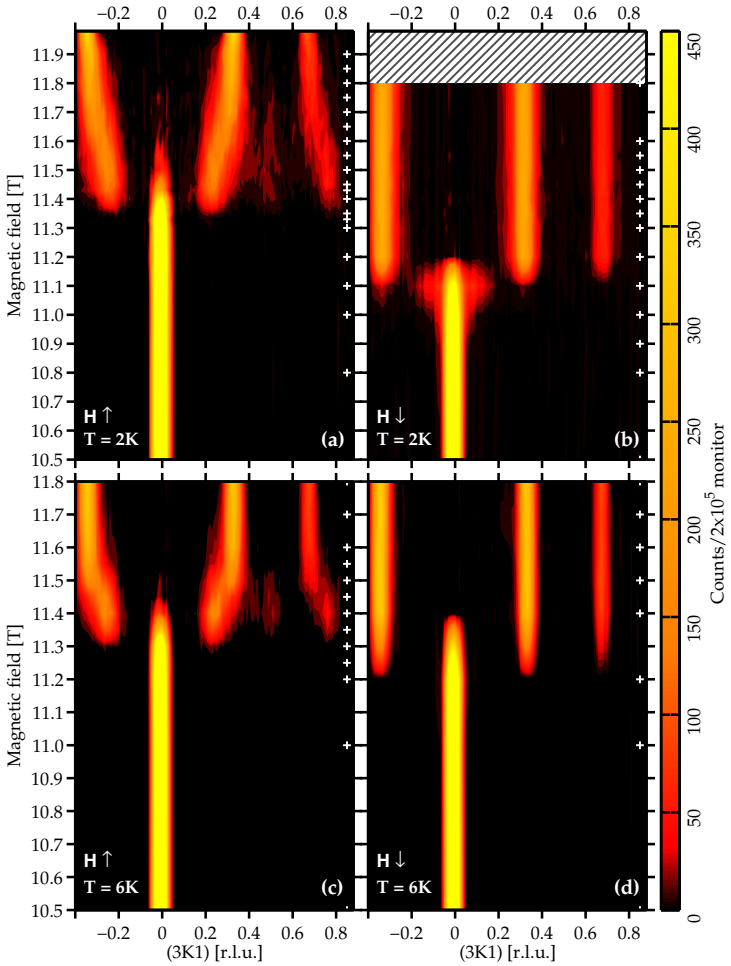

Figure 6.11: *Color plots of the intensity of (3,K,1) as a function of magnetic field applied along b at (a), (b) 2 K and (c), (d) 6 K for both increasing and decreasing field as measured at D23. The white crosses to the right in each plot denote the field values for which scans have been performed. Note the relatively few points in (d) and the difference in maximum field between the top and bottom panels. No data were collected in the hatched area.*

between the different structures involved.

The fit to the 11.45 T scan shown in Fig. 6.8(b) is based on a model with ordering vectors $\mathbf{Q} = (0, \frac{1}{3}, 0)$, $(0, \frac{1}{4}, 0)$ and $(0, \frac{1}{2}, 0)$. While the $(0, \frac{1}{3}, 0)$ propagation vector is kept fixed at the value found at 11.98 T, the other two are fitted globally to all datasets in the transition region. The peak intensities are allowed to vary between datasets but the intensities of the two peaks in a pair, $(3, \pm K, 1)$, are kept equal. The globally fitted propagation vectors are $(0, 0.26(1), 0) \approx (0, \frac{1}{4}, 0)$ and $(0, 0.48(3), 0) \approx (0, \frac{1}{2}, 0)$. Several other models were considered, including one involving an additional ordering vector $\mathbf{Q} = (0, \frac{1}{5}, 0)$ and another where the incommensurate peaks were fitted to a single but field-dependent position. Neither of these were successful.

The observation of several propagation vectors in the transition region suggests a substantial degree of frustration and the existence of a number of spin configura-

tions with only small energy differences. Steps in the magnetization accompanied by magnetic structures of rational periods, the so-called devil's staircase, are characteristica of the axial Ising antiferromagnet[111,112]. Even though $LiCoPO_4$ may not be an entirely adequate model material for an Ising system, its spin configurations still seem to occur with rational periods. Hence such behavior may not be limited to the strict Ising case.

Next, the behavior for decreasing field is examined. Here, the transition proceeds entirely differently with the incommensurate $(3, \frac{1}{3}, 1)$ peak abruptly giving way to the commensurate $(3, 0, 1)$ peak at 11.1 T, consistent with the RITA-II and magnetization data [compare Fig. 6.11(b) with Figs. 6.2(c) and (d)]. Note that the incommensurate peaks are wider for decreasing field than the resolution limited peak measured at 11.98 T for increasing field, compare Figs. 6.8(c) and 6.8(f). This is likely due to the fact that the field was only ramped to 11.8 T before starting the measurements that produced the data in Fig. 6.11(b). The peak widths at 11.8 T in Fig. 6.11(a) and (b) are equal within the errors of the fits. In the picture with separate domains with ordering vectors $\mathbf{Q} = (0, \frac{1}{3}, 0)$ and $(0, \frac{1}{4}, 0)$, the system is trapped in the 11.8 T state. This is below 11.9 T where the peaks become resolution limited and the structure is described purely by $\mathbf{Q} = (0, \frac{1}{3}, 0)$.

At 11.1 T [Fig. 6.8(e)], the commensurate $(3, 0, 1)$ peak is broadened and has a Lorentzian line shape, indicating disorder. Fitting a Lorentzian convoluted with a Gaussian describing the resolution, one can obtain the correlation length as $\xi = \frac{b}{2\pi\kappa}$, where b is the lattice parameter and κ is the Lorentzian width. The resolution is found by fitting the commensurate peak at 10.5 T (well below the transition) to a Gaussian [see Fig. 6.8(d)]. The correlation length is then found to be ~ 120 times smaller just at the transition (11.1 T) compared to below (10.5 T). Note that the observed peak broadening correlates with the bump seen in the magnetization [see Fig. 6.2(a)].

Stacking fault model. The features observed in the magnetization and the occurence of the $(3, \frac{1}{3}, 1)$, $(3, \frac{1}{4}, 1)$ and $(3, \frac{1}{2}, 1)$ incommensurate peaks in the interval $11.4 - 11.9$ T are consistent with the behavior of the $(3, 0, 1)$ intensity as a function of applied field seen in the RITA-II experiment. Likewise, field ramp direction dependent differences in the curve shapes of the electric polarization were presented in Ref.[67]. Hence, extra features in the transition regime are established in several measurable quantities. Upon increasing the temperature, the effects weaken: at $T \gtrsim 6$ K the difference in curve shape in the magnetization is absent and the transition regime with multiple ordering vectors is largely reduced for increasing field as well as the Lorentzian broadening for decreasing field [compare top and bottom panels in both Figs. 6.2 and 6.11]. In the following, a relatively simple model based on a mean-field approach is proposed in an attempt to understand these observations.

The magnetic structure above 11.9 T shown in Fig. 6.10 provides the starting point for our model. The period of this structure is $n = 3$ (i.e. the size of the magnetic unit cell triples) and spins with the same spatial y coordinate form a layer in the (a, c)-plane. The spins of each layer are then rotated with respect to those in the next layer upon advancing along b. In the present model, we crudely assume that all moments have maximum length, $M_S = 3.6\,\mu_B$, and that they are purely oriented along the easy axis. Hence the canting of $\sim 20^\circ$ away from the b-axis for 2/3 of

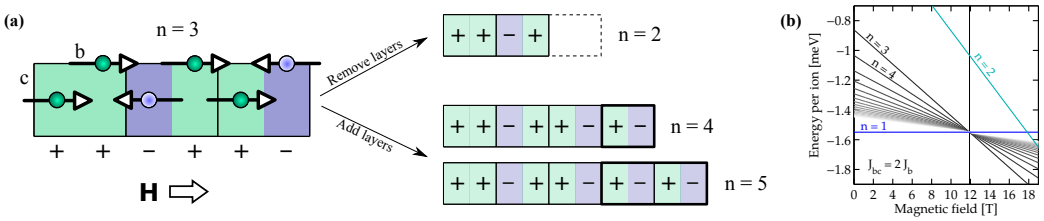

Figure 6.12: *Stacking faults. (a) Possible stacking fault structures with period $n \in \mathbb{N}$ for $n > 1$ and with magnetization $\frac{1}{n} M_S$. Spin direction is denoted by the ion color: green (along b) and blue (along $\bar{b}$). Only one layer of ions in the (b, c) plane is shown here. (b) Energy per magnetic ion as a function of applied field calculated from the stacking fault structures. $J_{bc} = 2J_b$ is assumed. The zero-field energy, E_1, is shown with the solid blue line and $E_n \to E_1$ for $n \to \infty$. The energies for $n > 2$ cross at this level exactly at the transition field H_C =11.9 T as shown with the vertical line.*

the spins is completely ignored here. The resulting structure consists of two kinds of layers or building blocks: (i) layers with spins parallel to b and (ii) layers with spins antiparallel to b. Each crystallographic unit cell consists of two such layers. These blocks are denoted "+" and "−" respectively and the $n = 3$ structure can then be described by the stacking sequence $[+ + - + +-]$.

Additional magnetic structures are now constructed from the same building blocks such that they have period $n \in \mathbb{N}$ for $n > 1$ and magnetization $\frac{1}{n} M_S$. This is done by adding or removing layers of "+" and "−" in pairs along b. Thus the $n = 4$ structure becomes $[+ + - + + - +-]$ – see Fig. 6.12(a). It can be described by introducing *stacking faults* to the $n = 3$ structure in analogy with atomic stacking faults in closed packed structures with layer stacking in e.g. either $ABABAB$ (hexagonal closed packed) or $ABCABC$ (face centered cubic) type sequences.

Note that the constructed structures are not associated with a single $(0, \frac{1}{n}, 0)$ ordering vector but require higher harmonics for a full description. However, the associated Bragg peaks are too weak to be detected in our experiment. Furthermore, sufficiently large domains of a structure of period n must exist in the sample in order to observe an $(0, \frac{1}{n}, 0)$ ordering vector. At this point it should also be emphasized that the proposed model is not the outcome of a full statistical treatment but rather the proposed stacking fault structures are deliberally chosen to be consistent with experimental observations. It is therefore fully possible that other choices of structures yield similar results. Nevertheless, as we shall see below, this rather crude model provides an explanation of the observed coexistence of several propagation vectors in the transition region.

To describe the energy of the system the following Hamiltonian is employed:

$$\mathcal{H} = -\sum_{i,j} J_{ij}\, \mathbf{S}_i \cdot \mathbf{S}_j - \mu H \sum_i S_i.$$

Here only J_{bc} and J_b are taken into account [see Fig. 6.10(a)] as the remaining exchange constants are generally small in the lithium orthophosphate family[53,54,113]. Since the easy axis is along b and the assumed spin structures have no components along a or c, no single-ion anisotropy terms are taken into account. H is the strength of the applied field along b and $\mu = g\mu_B S$ with the gyroscopic ratio $g \approx 2$, the Bohr magneton μ_B and $S = 3/2$. The energy per Co^{2+} ion of the assumed

stacking fault structures with period n is then:

$$E_n = \frac{1}{n}\Big(\left[2(n-2)J_{bc} + (4-n)J_b\right] S^2 - \mu H \Big), \qquad n > 2,\ n \in \mathbb{N}.$$

The zero-field structure, i.e. $n = 1$ [see Fig. 6.7(f)] has the energy per ion $E_1 = (2J_{bc} - J_b)S^2$. By solving $E_1 = E_n$ one can determine the transition field from the zero-field structure to any stacking fault structure accordingly:

$$H_C = \frac{4S^2}{\mu}\Big(- J_{bc} + J_b \Big), \qquad n > 2,\ n \in \mathbb{N}.$$

Peculiarly, the transition field is independent of the period n and hence all configurations of this particular kind are degenerate exactly at the phase transition. The energy difference between any two states m and n is readily calculated:

$$E_m - E_n = \left(\frac{m-n}{nm}\right) \mu\ (H - H_C), \qquad n, m > 2,\ n, m \in \mathbb{N}.$$

Hence, the energy difference does not depend directly on exchange interactions but merely on m and n as well as the field deviation from the transition value.

A short note on the $n = 2$ state is in place since the above calculations are only valid for $n > 2$. For $n = 2$ the stacking sequence results in a different expression for the energy, $E_2 = -\frac{1}{2}\mu H$, and a larger transition field follows. It is therefore unlikely that this structure is realized. Alternatively, the $n = 2$ Bragg peak seen in Fig. 6.11(a) could be due to nuclear distortion linked to the $n = 4$ magnetic structure or simply a completely different magnetic structure with period $n = 2$. An X-ray or polarized neutron experiment is needed in order to clarify this point.

Assuming $J_{bc} \approx 2J_b$ and using the measured transition field of 11.9 T the nearest neighbor coupling strength is estimated to $J_{bc} \approx -0.46$ meV. With this assumption, energies for different n configurations are shown as a function of applied field in Fig. 6.12(b). The estimate of the relative strengths of J_{bc} and J_b is based on the other members of the lithium orthophosphate family[8,53–55]. The resulting value of the nearest neighbor interaction is remarkably close to those found in $LiFePO_4$ ($J_{bc} = -0.46(2)$ meV[8]) and $LiMnPO_4$ ($J_{bc} = -0.48(5)$ meV[55]) and reasonably close to that measured for $LiCoPO_4$ ($J_{bc} = -0.7(2)$ meV[113†]. Note the large uncertainty). In Ref. 58 the nearest neighbor interaction of $LiCoPO_4$ was estimated to $J_{bc} = -0.23$ meV. However, this result is based on an incorrect magnetic propagation vector explaining the discrepancy from our result. It is worth emphasizing here that our result is obtained merely from a few simple but reasonable assumptions together with the measured transition field value.

It is clear from Fig. 6.12(b) that the energy difference between different m and n states is small close to the transition field. Hence, at low temperatures the thermal relaxation time may be sufficiently long such that regions of the sample are trapped in states with $n \neq 3$ in agreement with the observation of $n = 4$ order

[†]Rasmus Toft-Petersen have examined crystals from the same batch as that used in Ref. 113 and finds a significantly lower transition temperature, $T_N = 17.3(1)$ K. Furthermore, a Rietveld refinement of his neutron diffraction data yields satisfactory results exclusively when introducing Ni as well as Co on the magnetic site. Hence, the results suggest that the crystals may not be pure $LiCoPO_4$, but possibly Ni-doped from a crucible-growth.

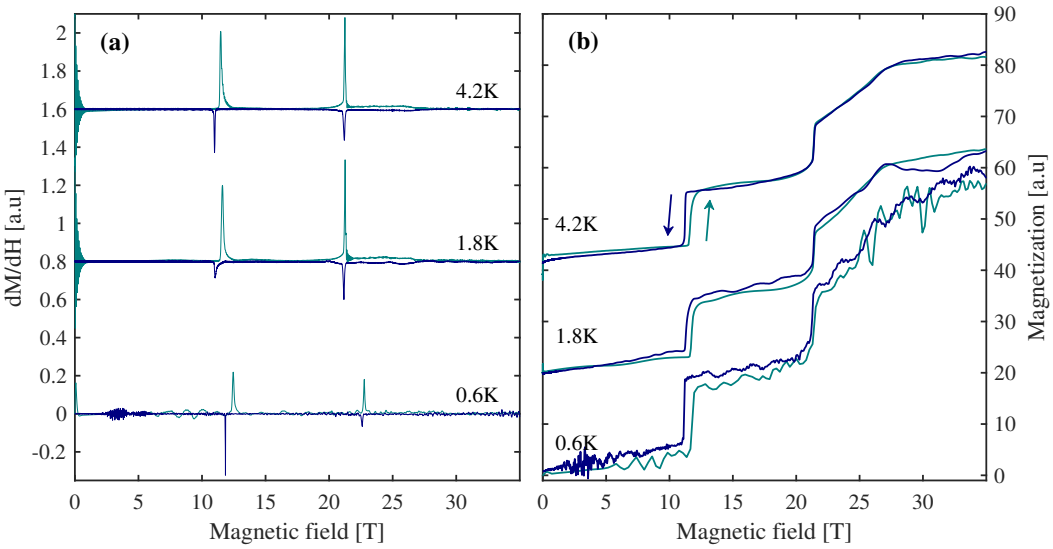

Figure 6.13: *Magnetic susceptibiliy, (a), and magnetization measurements, (b), of $LiCoPO_4$ as obtained with the pulsed-field technique. The measurements at different temperatures are shown with an offset of 0.8 a.u. and 20 a.u. for panels (a) and (b) respectively. Data for both increasing (green) and decreasing (blue) field is shown and the ramp direction is also shown with arrows in panel (b). The measurements at 0.6 K are done with a He-3 insert and the noise level is noticably different from the measurements at 1.8 and 4.2 K which are performed in a regular He-4 cryostat.*

in the transition interval, $11.4 - 11.9\,\mathrm{T}$. At $11.9\,\mathrm{T}$ the $n = 3$ structure stabilizes and the other structures withdraw. At higher temperatures the system is assisted by thermal fluctuations and rapidly finds its stable configuration. Thus, based on the disappearance of hysteresis at higher temperatures ($T \gtrsim 6\,\mathrm{K}$) it is suggested that more states, e.g. $n = 5, 6$, may be populated at very low temperatures (mK regime) and that the hysteresis region extends over a greater field range.

Further experiments were needed in order to falsify or substantiate this hypothesis. Hence, pulsed-field magnetization measurements at temperatures down to 600 mK were performed at the High Magnetic Field Laboratory at the Helmholtz-Zentrum Dresden Rossendorf. The pulsed-field technique is described in Section 4.1. To reach temperatures below $\sim 1.4\,\mathrm{K}$ a He-3 insert was employed but for all measurements above this temperature a regular He-4 cryostat was used. For each measurement the magnetic field, $H(t)$, and $\frac{dM}{dt}$ are recorded in order to obtain the susceptibility, $\frac{dM}{dH}$ or by integration the magnetization. Figure 6.13 shows results at three different temperatures. At 4.2 K, the difference in the curve shape of the magnetization at the transition at 12 T depending on field ramp direction is reproduced [compare Fig. 6.13(b) and Fig. 6.2(a)]. However, the knee feature clearly seen for increasing field in Fig. 6.2(a) is not as pronouced in the pulsed-field measurements. Furthermore, increasing noise levels at lower temperatures makes it impossible to tell whether there might be more features or steps as predicted by the stacking fault model discussed above. Unfortunately, the measurements performed with the He-3 insert are especially noisy. Hence, the hypothesis that more states such as $n = 5, 6$ are populated at lower temperatures still awaits a resolution. It may be necessary to perform magnetization measurements with DC fields or a neutron diffraction experiment at dilution temperatures in order to clarify the issue.

After this little pulsed-field magnetization intermezzo, the discussion regarding the stacking fault model is completed by considering the case of decreasing field. Here, the transition to the low-field antiferromagnetic ground state occurs abruptly even at low temperatures, see lefthand panels of Figs. 6.2 and 6.11. A broadening of the commensurate Bragg peak is observed in a short field interval at the transition around 11.1 T [see Fig. 6.8(e)]. Although very speculative, it may be suggested to originate from long wavelength stacking fault structures like those introduced above, i.e. for $n >> 1$. When a large number of $[+-]$ layer pairs are added the magnetization approaches zero and the structure resembles the zero-field structure.

The reason for the transition to occur more readily for decreasing field as compared to increasing field remains unexplained but an analogy may be found in the water solid-liquid transition. Upon heating water ice it slowly melts when the temperature is above 0°C. However, because of the need for nucleation sites, upon cooling, liquid water can reach temperatures below the freezing temperature (supercooling) before suddenly entering the ice phase. In this analogy heating corresponds to increasing field.

6.5 Magnetic structures at high fields

To access fields approaching the saturation field, $\mu_0 H_S = 28.3\,\mathrm{T}$[58], a neutron diffraction experiment was performed at the high field magnet facility at the HZB. The facility consists of the extreme environment diffractometer (EXED) and the high field magnet (HFM)[114–116]. The horizontal hybrid magnet provided DC magnetic fields up to 25.9 T. It has conical opening angles of 30° which together with the possibility of rotating the magnet with respect to the incoming beam and the TOF technique gives access to a considerable region of reciprocal space. This instrument thus enabled direct probing of the remaining magnetic phases at high fields indicated by the magnetization data of Ref. 58 [Fig. 3.2(a)] and our measurements [Fig. 6.13]. The sample was the 20 mg high-quality single crystal used at RITA-II and TriCS oriented with $(0,1,0)$ and $(1,0,1)$ in the horizontal plane and magnetic fields applied along b. The crystal orientation and the opening angle of the magnet limited the number of accessible Bragg peaks to $(\bar{3},0,\bar{1})$, $(\bar{2},0,\bar{1})$, $(\bar{1},0,\bar{1})$, $(1,0,\bar{1})$, $(\bar{1},0,0)$, $(0,0,\bar{1})$ and $(0,K,0)$ for $K \lesssim 10$. All peaks except $(0,K,0)$ were observed in the forward scattering detectors. Unfortunately, due to low flux at the required wavelengths, the neutron counting statistics of these peaks were only sufficient for alignment and confirmation of the zero-field structure. However, magnetic intensity above 20.5 T was observed in the backscattering detectors at the $(0,K,0)$ position. Intensity was found at $K = \frac{4}{3}$ for $20.5-21.0\,\mathrm{T}$ and at $K = 1$ above 21.0 T with the two peaks coexisting at 21.0 T. Neutron counts as a function of K along $(0,K,0)$ were obtained by integrating over a slice in reciprocal space of dimensions (given in r.l.u.) $\Delta H = 0.3$ and $\Delta L = 0.2$ and with bin sizes $\Delta K = 1 \times 10^{-3}$ and $\Delta K = 3 \times 10^{-3}$ for $K = 1$ and $K = \frac{4}{3}$ respectively. Background subtracted line profiles at selected field strengths are shown in Fig. 6.14(a) and integrated intensities of $(0,1,0)$ and $(0,\frac{4}{3},0)$ found from Gaussian fits are shown in Figs. 6.14(b) and (c), respectively.

The ordering vector in the interval $20.5-21.0\,\mathrm{T}$ is thus $\mathbf{Q} = (0,\frac{1}{3}0)$. This is the

same as for $11.9 - 20.5\,\mathrm{T}$ but the $(0, \frac{4}{3}, 0)$ Bragg peak was not observed at 12 T and 15 T, i.e. it is not present in the cycloid phase. Although the period of the magnetic structure stays the same, the spin orientation must then change around 20.5 T. In Fig. 6.14(c) the transition appears abrupt while it seems continuous in the magnetization data in Fig. 6.13(b). One possibility consistent with these observations is a gradual transition from the cycloid to a conical structure with the cone base perpendicular to the propagation vector. In such a structure the spins rotate in the (a, c)-plane and have a ferromagnetic component along the b-axis. However, since only a single magnetic Bragg peak was observed a rigorous structure determination was impossible.

Above 21.0 T the neutron intensity at $(0, \frac{4}{3}, 0)$ vanishes and a new peak appears at $(0, 1, 0)$. This peak reflects a commensurate spin structure with symmetry $(\uparrow\uparrow\downarrow\downarrow)$, the same as in the zero-field phase where the spins are predominantly along b. Since neutron scattering is only sensitive to spin components perpendicular to the scattering vector this Bragg is not observed in the zero-field phase. Conversely, the finite peak intensity above 21.0 T implies antiferromagnetic spin components in the (a, c)-plane instead of along b. Both susceptibility measurements and the magnetic structure refinement in the cycloid phase suggest that the c-axis is easier than a. Therefore, we infer that above 21.0 T the major antiferromagnetic spin component is along c. In addition, there is a ferromagnetic component with $\frac{2}{3}\,M_S$ at 21.0 T which increases approximately linearly until saturation is achieved at 28.3 T[58]. The magnetic structure above 21.0 T may therefore be described as a magnetized spin-flop structure. The spins rotate towards the b-axis with increasing field and the intensity of $(0, 1, 0)$ decreases with field accordingly. In fact, the field dependence of $(0, 1, 0)$ is consistent with its complete disappearance at saturation]see Fig. 6.14(b)].

The Bragg peaks at $(0, \frac{4}{3}, 0)$ and $(0, 1, 0)$ coexist in a short field interval [see Fig. 6.14(a)] suggesting that the phase transition from the $\mathbf{Q} = (0, \frac{1}{3}, 0)$ to the commensurate phase is of first order. This is also substantiated by hysteresis observed in previous pulsed-field magnetization measurements[58].

Although only a single magnetic peak was observed above 21.0 T it is possible to argue that the magnetic structure in this high-field phase is a commensurate, magnetized spin-flop structure with the same main antiferromagnetic symmetry component, $(\uparrow\uparrow\downarrow\downarrow)$, as the zero-field structure. Remarkably, this phase is magnetoelectric as was recently reported by Kharchenko et al.[67,68]. They found that an electric polarization, P_a, is induced along the a-axis for a magnetic field applied along b. The active magnetoelectric tensor element, α_{ab}, is the same as in the low-field phase but ~ 5 times weaker. Such reentrant magnetoelectric behavior has previously been observed by us in the sister compound $LiNiPO_4$[69,117]. In Ref. 69, it was shown that an extension of the microscopic model explaining the low-field magnetoelectric effect succeeds in accounting for the effect at higher fields too. In $LiCoPO_4$ there is of yet no such microscopic model but the two compounds have one characteristic in common: the magnetoelectric effect is linked to commensurate magnetic structures. This is interesting since other materials such as Cr_2BeO_4[118] and RMn_2O_5[119] (R = rare earth) generally display incommensurate magnetic structures in their magnetoelectric phases[6]. When recalling the above discussion on the possibility of a magnetoelectric effect in the cycloid structure, it

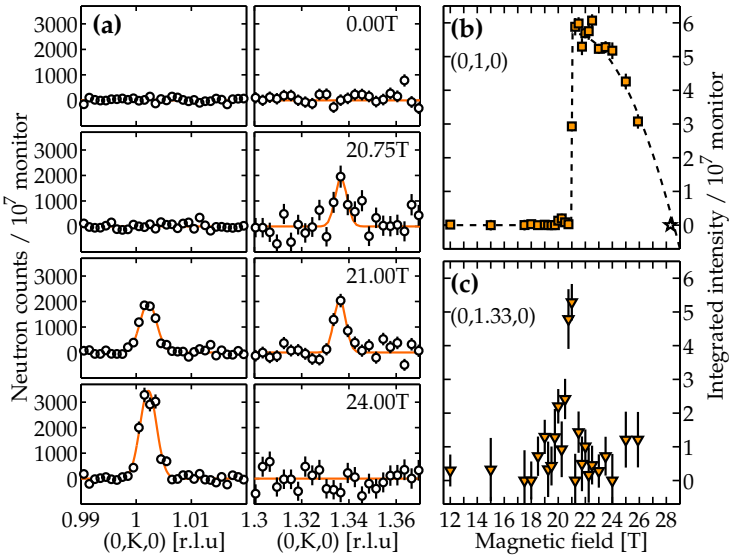

Figure 6.14: *Neutron diffraction results from HFM/EXED. (a) neutron counts as a function of (0,K,0) around $K = 1$ (left panels) and $K = \frac{4}{3}$ (right panels) at selected field values. Linear backgrounds have been fitted and subtracted for each dataset. Orange lines are subsequential Gaussian fits. (b) and (c) integrated intensity as a function of magnetic field up to 25.9 T of (0,1,0) and $(0,\frac{4}{3},0)$ respectively. The star symbol in (b) shows the expected zero intensity of (0,1,0) at saturation[58]. The dashed line is a guide to the eye.*

appears that $LiCoPO_4$ may support a magnetoelectric effect for both commensurate and incommensurate structures. If this is the case, the effects are most likely caused by two different mechanisms.

6.6 The enigmatic phase

This section concerns an elusive phase only observed in the heat capacity and with phase phase boundary shown in the phase diagram in Fig. 6.3. Apart from the peak in the heat capacity [Fig. 6.1(b)] marking the paramagnetic-antiferromagnetic transition, a second peak appears for fields above $\sim 6\,\mathrm{T}$ and temperatures in the range $10 - 15\,\mathrm{K}$. This peak is ~ 2 times smaller than the main peak but still very clear. Apart from magnetization measurements, we have performed thorough investigations by tracking numerous magnetic Bragg peaks in the $(H, 0, L)$-plane at both RITA-II and D23. None of the experiments showed any change in the temperature and field region in question. It is therefore unlikely that it is a magnetic phase transition. The heat capacity, however, merely shows if there is a change in entropy. Any other transition, such as crystal symmetry changes, electronic or orbital order would thus be picked up in the heat capacity. Although possible, it is difficult to imagine how one of these phase transition would not have consequences for the magnetic structure and hence have a signature in a related quantity. It is worth pointing that the second peak in the heat capacity was reprodoced using two different crystals.

Previously, a similar anomaly in the heat capacity was observed by Szewczyk et

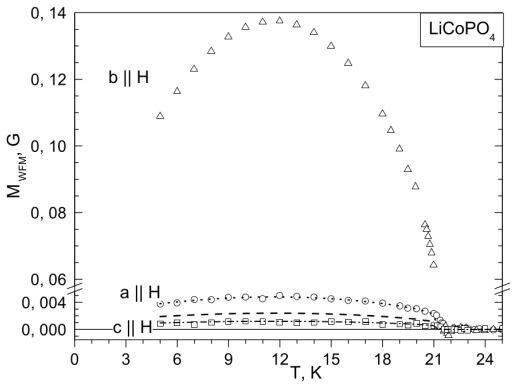

Figure 6.15: *Spontaneous magnetization of $LiCoPO_4$ as a function of temperature. For* $\mathbf{H}||\mathbf{b}$*, the magnetization increases at T_N and then has a maximum around 12 K. Dotted, dashed and dashed-dotted lines show the calculated values of the magnetization along a- or c-axis for deviations of the weak ferromagnetic moment from the b-axis of 2°, 1°, and 0.5° respectively. Figure from Ref. 63.*

al.[120]. The authors proposed that the anomaly is caused by a change in the stiffness of the magnons, i.e. a change in the exchange interactions or single-ion anisotropy constants. Magnetic torque showed that the transition may indeed be due to a change in magnetic anisotropy. The torque measurements were modelled using a spin structure with a modulated component perpendicular to the easy b-axis. However, we did not observe such modulation in our neutron diffraction measurements. The anomaly seen in the heat capacity in Ref. 120 has a different behavior of the phase boundary as a function of applied field compared to what we see.

Although, as of yet, there does not exist a satisfactory explanation to this second transition in $LiCoPO_4$, there may be a correlation to the observed weak ferromagnetic moment. The temperature dependency of the weak ferromagnetic moment was measured by Kharchenko et al.[63] [see Fig. 6.15]. After the initial onset at T_N, the moment displays a maximum around 12 K upon cooling, corresponding well with the second transition seen in the heat capacity at 10 T in Fig. 6.1(b). Therefore, it is proposed that the second transition observed in the heat capacity may be caused by the decrease in weak ferromagnetic moment. However, the heat capacity data suggests a sharp transition and the one observed in Ref. 63 is less so.

6.7 Field-induced spin canting and the Dzyaloshinskii-Moriya interaction

So far, the zero-field structure and various phases for magnetic fields along b were characterized. Now, we turn to investigations for magnetic fields applied along a, i.e. tranverse to the easy axis. For this field direction, the magnetization of $LiCoPO_4$ increases linearly with field as seen in Fig. 6.16(a). A ferromagnetic contribution to the zero-field spin structure is therefore induced with $S^a = \alpha H$ and the fitted slope $\alpha = 0.0395(1)\,\mu_B/\mathrm{T}$. Furthermore, yet another antiferromagnetic component exists in addition to the main structure of C_y symmetry and the minor A_z component established in Section 6.2. This extra component is manifested by an increase in the intensity of the $(0, 2, 1)$ magnetic Bragg peak as a function of applied field [see Fig. 6.16(b)]. The magnetic origin of the $(0, 2, 1)$ intensity is confirmed by its temperature dependence which follows a Curie-Weiss law squared [see Fig. 6.16(c)].

The $(0, 2, 1)$ peak represents mainly spin arrangements of symmetry G and to a smaller extent structures of symmetry C. All spin orientations are possible, *cf.* Table 6.3. More information is therefore needed in order to pin down which magnetic structure the additional intensity of $(0, 2, 1)$ signifies. The argument follows a process of elimination using two other magnetic Bragg peaks: $(0, 1, 2)$ and $(0, 0, 1)$.

The $(0, 1, 2)$ peak is present for any C spin structures. This peak has no additional field-induced intensity [see Fig. 6.16(b)] and consequently any additional C elements are ruled out. Similarly, $(0, 0, 1)$ represents G symmetry with spins polarized along a or b. Again, this peak shows no change upon applying a magnetic field along a [see Fig. 6.16(b)] and these magnetic structure types may be rejected too. The only remaining possible magnetic structure as a contributor to the $(0, 2, 1)$ field-induced intensity is then G_z. This component comes as an addition to the already established major C_y component and the smaller A_z component. Consequently, an asymmetry is introduced in the canting angles such that spins $(1, 2)$ and $(3, 4)$ form pairs with total canting angles $\varphi + \theta$ and $\varphi - \theta$ respectively. Here $\theta \equiv \theta(H)$ is the field-induced canting angle. The resulting magnetic structure for magnetic fields applied along a is shown in Fig. 6.7(g).

The size of θ is now estimated. As argued in Section 6.2, it may be assumed that at 0 T, $(0, 2, 1)$ only reflects the C_y structure. Any additional intensity upon applying a field then originates from the G_z component:

$$I_{(0,2,1)}(H) - I_{(0,2,1)}(0\,\mathrm{T}) \propto \left|S_G^{(0,2,1)}\right|^2 \left|P_z^{(0,2,1)}\right|^2,$$

where the structure and polarization factors, $S_R(\mathbf{Q})$ and $P_i(\mathbf{Q})$, were found in Table 6.3. This is to be compared to the intensity of $(0, 2, 1)$ at 0 T:

$$I_{(0,2,1)}(0\,\mathrm{T}) \propto \left|S_C^{(0,2,1)}\right|^2 \left|P_y^{(0,2,1)}\right|^2.$$

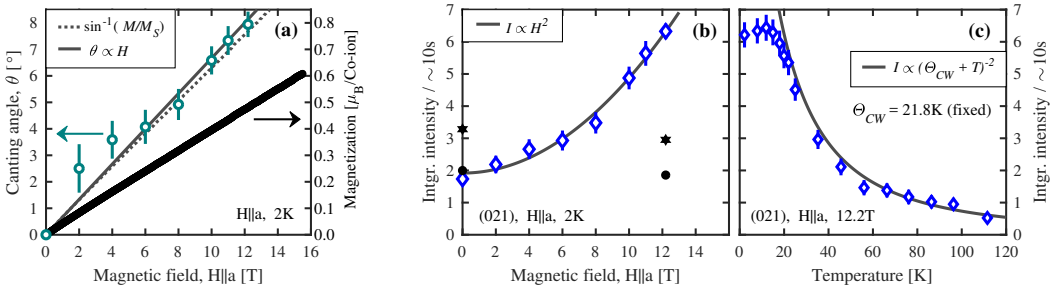

Figure 6.16: *Magnetization, field-induced canting angle and integrated neutron intensity of (0,2,1) for magnetic fields applied along a. (a) magnetization (thick black line) and field-induced canting angle (green circles) calculated from the neutron intensity of (0,2,1) as a function of applied field. Both are to a good approximation linearly proportional to the field strength. The solid line shows a linear fit to the canting angle whereas the dashed line shows the angle as calculated from the magnetization with $M_s = 3.6\,\mu_B$/ion. (b) and (c) integrated intensity (blue diamonds) of (0,2,1) as a function of applied field at 2 K and as a function of temperature at 12.2 T respectively. The field dependence in (b) and the temperature dependence in (c) have been fitted to a quadratic and a Curie-Weiss law squared respectively (solid lines). The black symbols in (b) show intensities for (0,1,2) [circles] and (0,0,1) [stars] at 0 T and 12.2 T. Note that the intensities for these peaks are scaled to appear together with the intensity of (0,1,2) in order to demonstrate that they show no or only little field dependency.*

Since only one peak is involved in the determination of the field-induced canting angle there is no need to correct for the magnetic form factor or Lorentz factor and any extinction or absorption effects may be neglected. The field-induced canting angle is then calculated from the corrected intensities, $I^{\rm corr}_{(0,2,1)}(H)$ and $I^{\rm corr}_{(0,2,1)}(0\,{\rm T})$, as $\tan\theta = \sqrt{\frac{I^{\rm corr}_{(0,2,1)}(H) - I^{\rm corr}_{(0,2,1)}(0\,{\rm T})}{I^{\rm corr}_{(0,2,1)}(0\,{\rm T})}}$ and is to a good approximation linear as a function of applied field along a: $\theta = \beta H$ with fitted slope $\beta = 0.012(1)\,{\rm rad/T}$ [see Fig. 6.16(a)]. The field-induced canting angle as deduced from the magnetization, $\sin\theta = M/M_S$, is also shown in Fig. 6.16(a) and substantiates the link between F_x and G_z. Furthermore, since the neutron intensity is proportional to the square of the ordered magnetic moment, a linear coupling between the ferromagnetic moment and canted moment would result in a quadratic increase in the neutron intensity of $(0,2,1)$ as a function of applied field. This is indeed the case as shown in Fig. 6.16(b). Here the solid line is a fit to a quadratic dependence, $I \propto H^2$. The measured intensity is clearly well described by the fit. Additionally, the symmetry elements G_z and F_x belong to the same irreducible representation, see Table 6.4.

An estimate of the size of the DM interaction in $LiCoPO_4$ may be obtained from the field-induced spin canting. A similar calculation was performed for the sister compound $LiNiPO_4$ and the analysis in Ref. 48 is directly applicable here. Symmetry arguments lead to the only allowed DM coefficients $\mathbf{D}_{14} = (0, D^b_{14}, 0) = -\mathbf{D}_{23}$ and $\mathbf{D}_{12} = (0, D^b_{12}, 0) = \mathbf{D}_{34}$. These yield terms in the Hamiltonian of the form:

$$\begin{aligned}
\mathcal{H}^1_{\rm DM} &= \mathbf{D}_{14}\cdot(\mathbf{S}_1\times\mathbf{S}_4) - \mathbf{D}_{14}\cdot(\mathbf{S}_2\times\mathbf{S}_3)\\
&= D^b_{14}\,(S^c_1S^a_4 - S^a_1S^c_4 - S^c_2S^a_3 + S^a_2S^c_3) \quad \text{and}\\
\mathcal{H}^2_{\rm DM} &= \mathbf{D}_{12}\cdot(\mathbf{S}_1\times\mathbf{S}_2) + \mathbf{D}_{12}\cdot(\mathbf{S}_3\times\mathbf{S}_4)\\
&= D^b_{12}\,(S^c_1S^a_2 - S^a_1S^c_2 + S^c_3S^a_4 - S^a_3S^c_4)\,.
\end{aligned}$$

The spin component along a is finite for $\mathbf{H}||\mathbf{a}$ and assumed equal at all sites, i.e. $S^a_1 = S^a_2 = S^a_3 = S^a_4 = S^a > 0$. In this case, both terms favor a G_z type order and this is exactly what we observe. The ferromagnetic moment along a therefore induces – via the DM interaction – an antiferromagnetic spin component of symmetry G_z.

Note that the field-induced G_z component leaves the nearest neighbor spin pairs $(1,4)$ and $(2,3)$ antiparallel and hence no energy change is to be expected from the term $\mathcal{H}^1_{\rm DM}$ or from the nearest neighbor exchange term. On the other hand, the term $\mathcal{H}^2_{\rm DM}$ does yield a finite energy contribution for a G_z component. The strength of the DM interaction may be estimated by balancing the different energy contributions for spins deviating from the easy axis, b:

$$\left.\begin{aligned}\mathcal{H}_{\rm DM} &= 4D^b_{12}S^aS\sin\theta\\ \mathcal{H}_{\rm ani} &= 4\mathfrak{D}^cS^2\sin^2\theta\end{aligned}\right\} \Rightarrow \frac{D^b_{12}}{\mathfrak{D}^c} = \frac{-S\sin\theta}{S^a} \approx -S\frac{\theta}{S^a},$$

where $\mathfrak{D}^c$ is the single-ion anisotropy constant for spin components along c, $S = 3.6\,\mu_{\rm B}$ the saturated moment, $\sin\theta \approx \theta$ holds for small canting angles, $\theta = \beta H$ and $S^a = \alpha H$. With the fitted coefficients $\beta = 0.012(1)\,{\rm rad/T}$ and $\alpha = 0.0395(1)\,\mu_{\rm B}/{\rm T}$ the ratio becomes $D^b_{12}/\mathfrak{D}^c \approx -1.1$. Note that this is an upper bound for the size of the DM interaction as the above simple calculation neglects any competing exchange interactions which may also influence the spin canting.

Thus, the DM interaction in $LiCoPO_4$ may be as large as the single-ion anisotropy along c. The full spin Hamiltonian of $LiCoPO_4$ has not been determined as of yet, but limited inelastic neutron scattering data shows an almost dispersionless spin excitation along the $(0, K, 0)$ direction and a single-ion anisotropy constant of $\mathfrak{D}^c \approx 2.5\,\mathrm{meV}$ is suggested[47].

The DM interaction is related to the spin-orbit coupling and as mentioned in the introduction, the spin-orbit coupling is believed to play a role in explaining the large low-temperature magnetoelectric tensor coefficients in $LiCoPO_4$. Previously, microscopic models based on the DM and exchange interactions were employed to explain the magnetoelectric effects in $LiFePO_4$[69] and $LiNiPO_4$[48,69] respectively. In fact, there are many similarities between $LiFePO_4$ and $LiCoPO_4$: both have a zero-field magnetic structure with major spin component C_y and smaller component A_z. They both have finite magnetoelectric tensor elements $\alpha_{ab}, \alpha_{ba} \neq 0$ and it appears that the DM interaction is at the core of explaining the magnetoelectric effect in both cases[48]. However, the temperature dependence of the magnetoelectric coefficient, α_{ab}, in $LiCoPO_4$ is very different from that of $LiFePO_4$. This emphasizes the need for more theoretical work and improved *ab initio* calculations in order to elucidate the missing mechanism(s) controlling the linear magnetoelectric effect in $LiCoPO_4$.

6.8 Summary

The magnetic phase diagram of $LiCoPO_4$ was established by combining magnetometry, heat capacity and neutron diffraction measurements for magnetic fields up to 25.9 T applied along b and up to 16 T along a. Based on neutron diffraction measurements, the zero-field magnetic structure was refined to a $(\uparrow\uparrow\downarrow\downarrow)$ arrangement with spins along the easy b-axis, corresponding with literature[42,47]. However, based on the observation of the $(1,0,0)$ magnetic Bragg peak, a spontaneous spin canting of $\varphi = 7(1)^\circ$ along c was found. As a consequence, the magnetic point group is reduced from mmm' as originally proposed[42] to m'_z. This point group is consistent with the observed active magnetoelectric tensor elements and weak ferromagnetic moment.

For magnetic fields applied along b, a series of transitions is observed in pulsed-field magnetization[58] and neutron diffraction at 11.9, 20.5 and 21.0 T. Scans along $(3,K,1)$ show that for fields greater than 11.9 T, the magnetic unit cell triples in size with propagation vector $\mathbf{Q} = (0,\frac{1}{3},0)$. A magnetized elliptic cycloid is formed with spins in the (b,c) plane and the major axis oriented along b. Such a structure allows for the magnetoelectric effect with an electric polarization along c induced by magnetic fields applied along b.

Intriguingly, additional ordering vectors $\mathbf{Q} \approx (0,\frac{1}{4},0)$ and $\mathbf{Q} \approx (0,\frac{1}{2},0)$ appear for increasing fields in the hysteresis region below the transition field. Traces of this behavior are also observed in the magnetization. A simple model based on a mean-field approach is proposed to explain these additional ordering vectors. The model suggests the existence of more ordering vectors of the type $\mathbf{Q} = (0,\frac{1}{n},0)$ at lower temperatures. However, this was not evident in pulsed-field magnetization measurements performed at 0.6 K

For the magnetic phases at very high magnetic fields, only a single magnetic Bragg peak was observed due to experimental restrictions. Hence, no rigorous structure refinement can be performed but the periodicity of the magnetic structure may be determined. In the field interval $20.5 - 21.0$ T, the propagation vector $\mathbf{Q} = (0,\frac{1}{3},0)$ remains but the spins orient differently compared to the cycloid phase. Above 21.0 T and up until saturation, a commensurate magnetic structure exists with a ferromagnetic component along b and an antiferromagnetic component along c.

For magnetic fields applied along a, the induced ferromagnetic moment couples via the DM interaction to yield an additional, field-induced spin canting. An upper limit to the size of the interaction is estimated to $|D^b_{12}| \approx |\mathfrak{D}^c|$ from the induced canting angle. In other words, the DM interaction, D^b_{12}, may be as large as the single-ion anisotropy constant along c, $\mathfrak{D}^c$.

A good description of the spin Hamitonian of $LiCoPO_4$ is still to be obtained – something that we are currently working on. Spin-waves should be measured in order to do so. Still, it is clear from our investigations so far that the magnetic anisotropy confines spins to the (b,c)-plane. Furthermore, the DM interaction may play an important role – both in understanding the magnetic structures but also in explaining the magnetoelectric effect.

Chapter 7

Magnetic structures in $LiNiPO_4$ at high fields

$LiNiPO_4$ is probably the most well-understood compounds in the lithium orthophosphate family. It possesses a multitude of different magnetic phases – some commensurate and some incommensurate – as a function of temperature and applied magnetic field along the easy axis, c. Previously, the magnetic phases and spin Hamiltonian of $LiNiPO_4$ were studied using neutron scattering in zero field[42,48,53] and with DC fields up to 17.3 T[48,61]. Additional neutron diffraction studies with pulsed magnetic fields up to 30 T revealed more magnetic phases, one of which displays a re-entrant magnetoelectric effect[69]. Part of the work published in Ref. 69 was carried out during the present project. A microscopic model was developed in Ref. 48 to explain the magnetoelectric effect in the low-field commensurate phase. With a few adaptations this model succesfully accounted for the effect in the high-field magnetoelectric phase too.

With a saturation field estimated to $\sim$ 90 T[70] there is most likely plenty more to discover in $LiNiPO_4$ and in this thesis the work is extended up to 42 T using neutron diffraction and a combination of DC and pulsed magnetic fields. Not only is 42 T astonishingly high but also, the phase transition at 39.4 T from phase VI to phase VII may be the highest ever to be probed with neutrons. The results are presented below starting with the magnetic phase diagram in Section 7.1 and magnetic structure determinations in Sections 7.2-7.4.

7.1 Magnetic phase diagram

The magnetic phase diagram of $LiNiPO_4$ [see Fig. 7.1] was characterized by magnetization measurements and by tracing the position of the scattering vector, $\mathbf{Q} = (0, K, 0)$, as a function of temperature and magnetic field applied along c. Phases are enumerated I-VII for increasing field. The commensurate structures in phases I, IV and VII as deduced from combining all measurements are sketched in Fig. 7.2 (more about these later).

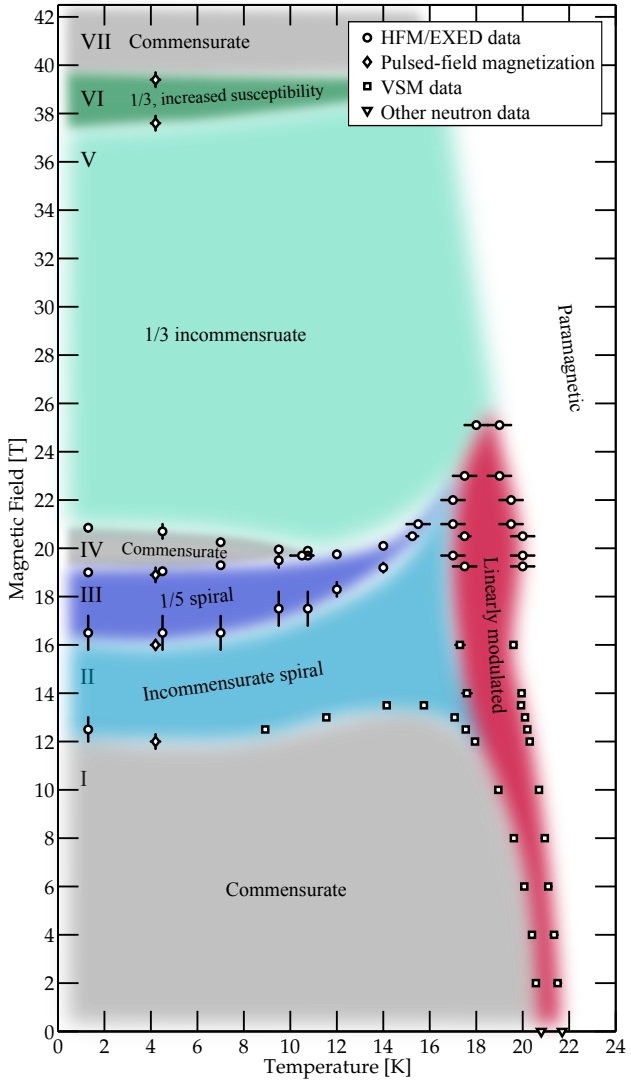

Figure 7.1: *Magnetic phase diagram of $LiNiPO_4$ up to 42 T applied along c as determined by magnetization measurements (diamonds and squares) and neutron diffraction (circles and triangles). Phases are colored as follows: commensurate/magnetoelectric (grey), linearly modulated (red), spirals (blue) and $\frac{1}{3}$ incommensurate (green). Phase boundaries at high fields are conjectured.*

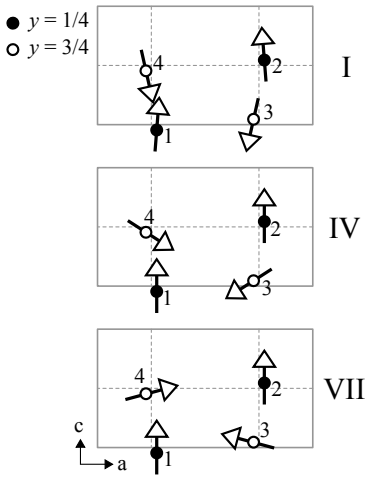

Figure 7.2: *Commensurate magnetic structures of $LiNiPO_4$ in phases I, IV and VII projected to the (a,c)-plane.*

Magnetization and electric polarization along a as a function of applied field was measured using the pulsed-field technique with fields up to 55 T along c [see Fig. 7.3]. These measurements were kindly performed by Takumi Kihara from Tohoku University, Japan. Magnetic phase transitions are observed at 12.0, 16.0, 19.1, 20.9, 37.6 and 39.4 T and phases I, IV and VII display the magnetoelectric effect.

Phase boundaries up to 25.1 T. Neutron diffraction measurements with magnetic fields up to 25.1 T were performed at the HFM/EXED instrument at the HZB [see also setup description in Section 6.5]. The sample was a 330 mg single crystal oriented with $(0, K, L)$ in the horizontal scattering plane, the magnetic field applied along c and $(H, 0, 0)$ vertical. The temperature was in the range $1.3 - 30$ K. The magnet rotation was $-6°$ with respect to the incoming beam with wavelength band $0.7 - 6.9$ Å. A number of Bragg peaks were observed on the forward and backscattering area detectors: $(\pm 1, K, 0)$, $(-2, -2, 0)$, $(0, K, 0)$, $(2, -1.33, 0)$, $(1, -0.67, 0)$, $(-2, -0.33, 0)$, $(0, 0, 4)$ and $(0, 0, 2)$ with $K \in [-2, 0]$.

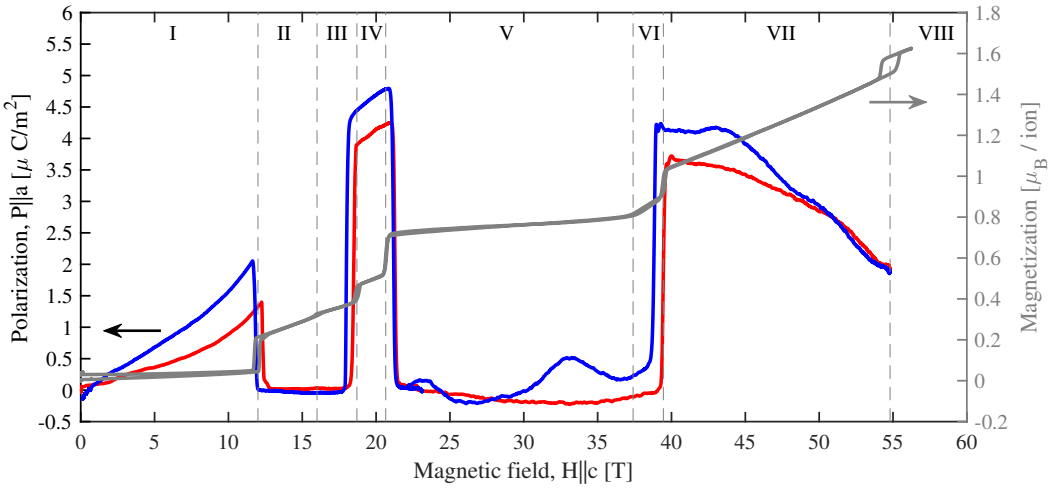

Figure 7.3: *Magnetization (right axis) and electric polarization (left axis) along a in $LiNiPO_4$ as measured at 4.2 K as a function of applied magnetic field along c. Phases I-VIII are indicated. Phases I, IV and VII display the magnetoelectric effect. These measurements were performed by Takumi Kihara from Tohoku University.*

Following the $(0, K, 0)$ magnetic Bragg peak as a function of temperature and magnetic field enabled the determination phase boundaries in $LiNiPO_4$. In order to obtain the intensity at a certain $(0, K, 0)$ position, data was summed in slices of thickness $H \in [-0.1, 0.1]$ and $L \in [-0.05, 0.05]$ – both in r.l.u. Subsequently, Gaussian profiles were fitted to the $(0, K, 0)$ lineshapes and the integrated intensity calculated. Note that no Vanadium or Lorentz correction were applied here since only phase transition were of interest and not absolute intensities.

The lefthand panels of Fig. 7.4 present the results from a field scan performed at 1.3 K. Intensity appears at positions: $(0, -1, 0)$, $(0, -1 \pm k, 0)$, $(0, -2k, 0)$ with the value of k depending on the phase. The $(0, -1, 0)$ reflection is present at $0-12.5(5)$ T as well as $19.0(1) - 20.9(2)$ T. The incommensurate peaks with $k \approx 0.2$ reflecting the spiral structure[48,61] appear in the interval $12.5(5)-19.0(1)$ T with the 5 unit cell period lock-in at ~ 16 T. Above 20.9(2) T, the scattering vectors change position to $k = \frac{1}{3}$. These observations are in excellent agreement with previous results[48,61,69]. No hysteresis was observed at the transitions 19.0(1) and 20.9(2) T.

Earlier neutron diffraction measurements above 17.3 T were performed using pulsed magnetic fields[69]. For this type of experiment, temperature control is challenging and hence the measurements were only performed at 4.2 K. On the contrary, the HFM/EXED setup is excellent for parametric studies, resulting in the much higher degree of details in the magnetic phase diagram of Fig. 7.1 below 25.1 T. Moreover, because of the time dependence of the magnetic field pulse and the limited frequency with which the pulses can be produced (one every $\sim 5-10$ min), it proves impractical to probe more than just a handful of selected snapshots of $(\mu_0 H, K)$ space using the pulsed-field technique. The obtained counting statistics are therefore compromised and the determined peak positions carry a relatively large uncertainty. The HFM/EXED instrument allows for improved position determination yielding $[0, -1.009(1), 0]$ for phase IV and $[0, -1.331(9), 0]$, and $[0, -0.68(1), 0]$ for phase V respectively as opposed to $[0, 0.99(1), 0]$ and $[0, 1.33(1), 0]$ as previously

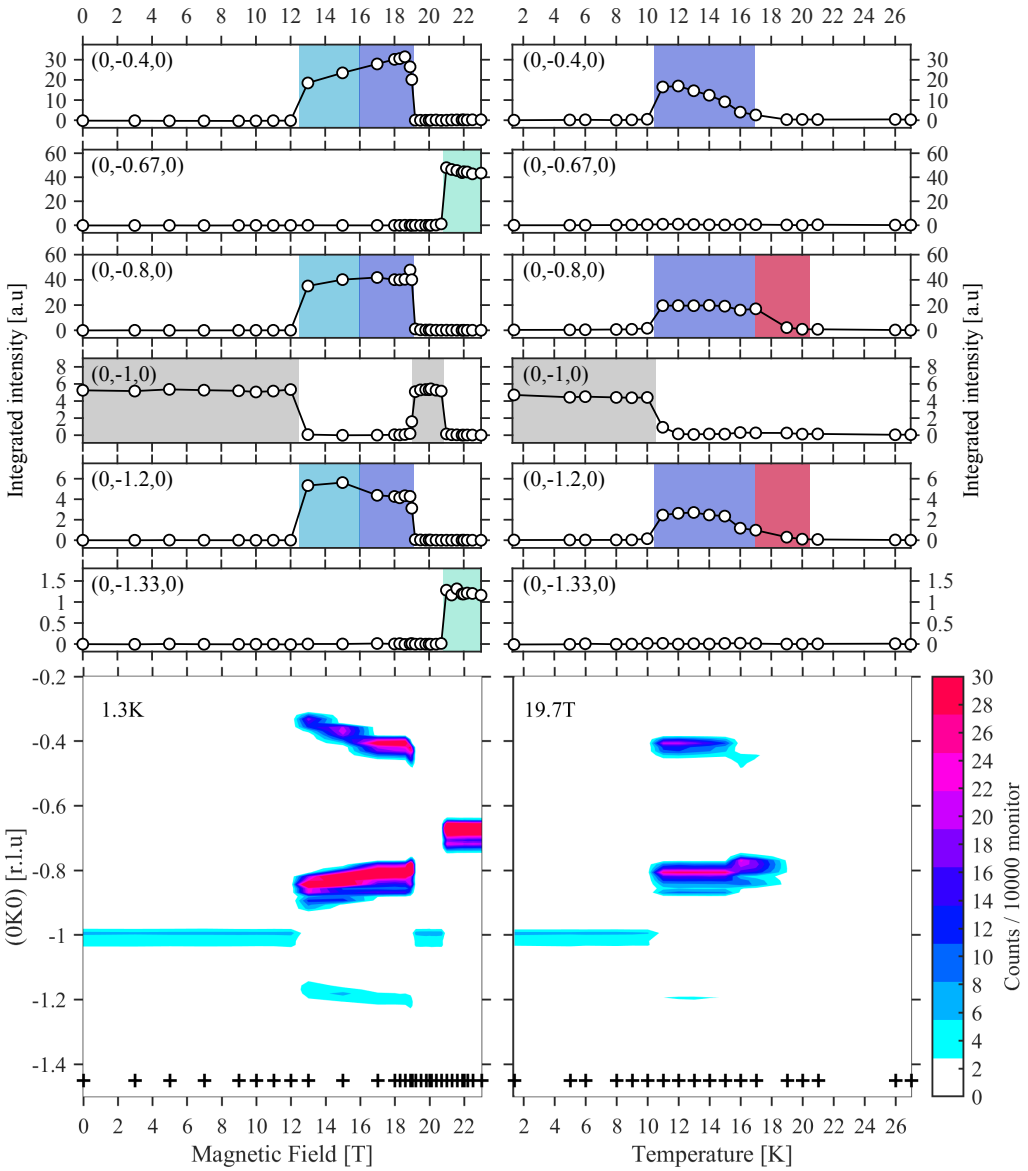

Figure 7.4: *Temperature and field dependence of the (0,K,0) magnetic Bragg peaks as measured by neutron diffraction up to 23 T. Lefthand panels show the behavior of the scattering vector as a function of applied magnetic field (increasing) at 1.3 K. Righthand panels show the same thing but as a function of temperature (cooling) at 19.7 T. Top six panels show integrated intensities for identified scattering vectors. Colored backgrounds indicate intervals with active scattering vectors corresponding to Fig. 7.1. The large bottom panels show color plots of the neutron intensities with scattering vector position – (0,K,0) – and varied quantity – field or temperature – on the axes. The black crosses at the bottom of each color plot indicate where datasets were taken. Background at 0 T, 43 K was subtracted for all datasets.*

determined[69]. These positions correspond to ordering vectors $\mathbf{Q}_{IV} = (0, 0, 0)$ and $\mathbf{Q}_V = (0, \frac{1}{3}, 0)$ as also previously proposed[69]. It is pointed out that the exact values $k = 1$ and $k = \frac{1}{3}$ are conjectured within our experimental resolution. It is possible that phase IV is ever so slightly incommensurate as well as the period of phase V is slightly smaller or larger than 3 crystallographic unit cells. On the other hand, the scattering vector in phase I – which is known to be commensurate – is determined

to $\mathbf{Q}_I = [0, -1.009(1), 0]$, thus within the errors precisely the same as in phase IV. We therefore believe that phase IV is truly commensurate.

The results of a temperature scan at 19.7 T are shown in the righthand panels of Fig. 7.4. Upon cooling the linearly modulated phase, spiral phases and the commensurate phase IV are encountered in succession, *cf.* phase diagram in Fig. 7.1. Intensity is observed at $(0, -1 \pm 0.2, 0)$ in the linearly modulated phase starting around $20 - 21$ K. At 16 K, the position of the vector changes slighly towards longer magnetic unit cell periods and an additional peak appears at $(0, -2k, 0)$, characterizing the spiral phases[61]. The incommensurate peaks give way to $(0, -1, 0)$ at 10 K upon entering phase IV.

Neutron diffraction and pulsed magnetic fields. The HFM/EXED instrument allowed for investigating the phase diagram of $LiNiPO_4$ up to 25.1 T but in order to probe magnetic structures at even higher fields, one must turn to pulsed fields. Hence, a second experiment was performed at the NeutrOn Beamline for Observation & Research Use (NOBORU) situated at the spallation source at the Japan Proton Accelerator Research Complex. NOBORU is a TOF diffractometer with wavelengths $\lambda < 10.5$ Å. Professor Hiroyuki Nojiri and co-workers from Tohoku University brought their own detectors (2 x 16 vertical PSDs with 128 pixels each and 10 μs time bins) which were placed in forward scattering positions 1.61 m from the sample. The pulsed magnetic field was generated by a copper coil mounted in an insert for a standard ^{4}He cryostat. The coil was immersed in liqiud nitrogen and connected to a capacitor bank delivering 10 ms pulses with maximum field up to 42 T. A time delay, Δt, between neutron pulse and magnet pulse and the maximum field, $\mu_0 H_{\max}$, were adjusted such that intensity at certain $(0, K, 0)$ positions was monitored. With each $(\Delta t, \mu_0 H_{\max})$ setting curves in field strength along c, $\mu_0 H_c$, and K (or TOF) were probed. The sample temperature was controlled by the cryostat. The sample was the same 330 mg single crystal used in the HFM/EXED experiment. It was oriented with the a-axis vertical and the c-axis in the scattering plane rotated 6° away from the field direction in order to reach momentum transfers along $(0, K, 0)$. Shutters ensured data collection only with the magnetic field on. The experimental technique is also described in Refs. 69 and 121.

An example of the raw data is shown in Fig. 7.5(a). Four distinguished peaks at 2.5, 3.7, 5 and 7.5 ms are seen, corresponding to momentum transfers $(0, 2, 0)$, $(0, \frac{4}{3}, 0)$, $(0, 1, 0)$ and $(0, \frac{2}{3}, 0)$ respectively. The conversion from the measured TOF, t, to $(0, K, 0)$ goes as $K = \frac{2\alpha L b \sin(\theta)}{t}$ where $\alpha = 252.7\,\mu$s/m/Å as in Eq. (4.2) and L is the total length of the neutron flight path. The nuclear peak, $(0, 2, 0)$, is present at all fields whereas the remaining peaks are magnetic and only appear in their respective phases. The colors in Fig. 7.5(a) represent the different phases and show that $(0, 1, 0)$ is present in magnetoelectric phase VII whereas $(0, \frac{4}{3}, 0)$ and $(0, \frac{2}{3}, 0)$ are present in phase V. Below 2 ms (not shown) the spectrum is dominated by background counts originating from high-energy particles but at higher TOFs the background is extremely low: 0-1 counts per 100 pulses.

Figures 7.5(b)-(d) show the integrated intensities for the field intervals $21 - 37$ T (phase V), $38 - 39$ T (phase VI) and $40 - 42$ T (phase VII), respectively. The field intervals were chosen with approximately ± 0.5 T distance to the phase boundaries as obtained from the magnetization measurements in Fig. 7.3. Due to the rapidly

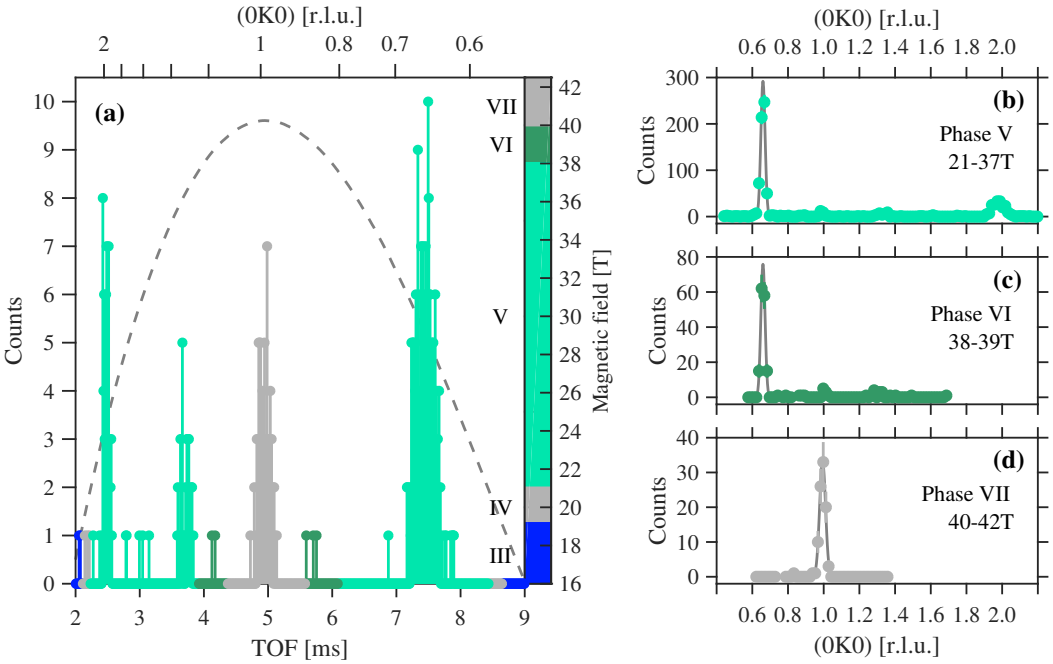

Figure 7.5: *Pulsed-field Laue neutron diffraction up to 42 T. (a) Example of accumulated raw data for 99 pulses for one magnet setting: maximum field 40.5 T, pulse delay 1000 µs. Neutron counts are shown as a function of TOF (bottom axis) as well as corresponding (0,K,0) [top axis]. The colors represent the field intervals at which each neutron has been detected – see colorbar on the right. Note that the scale starts at 16 T. The Roman numbers to the left of the colorbar identify the phases corresponding to the phase diagram in Fig. 7.1. The magnetic field pulse is shown with the grey dashed line in the background with field values read to the right of the colorbar. For clarity, errors of the neutron data are not shown but are simply $\sqrt{N}$ Poisson counting errors. Panels (b)-(d) show integrated neutron counts for each of the phases V, VI and VII as a function of (0,K,0) for all collected data. The errorbars show the propagated error and the bin size is $\Delta K = 0.015$ r.l.u. Solid lines show Gaussian fits to the observed peaks. Note that data is only shown for probed values of K, e.g. (0,2,0) was not probed at fields above 37 T.*

varying field this was judged necessary in order to exclusively sum up neutrons belonging to the individual phases. In phase V, a strong peak is observed at $(0, \frac{2}{3}, 0)$ as well as weaker ones at $(0, 1, 0)$, $(0, \frac{4}{3}, 0)$ and $(0, 2, 0)$. The situation is similar in phase VI with a strong peak at $(0, \frac{2}{3}, 0)$ and weaker ones at $(0, 1, 0)$ and $(0, \frac{4}{3}, 0)$. Finally in phase VII, the peaks at $(0, \frac{2}{3}, 0)$ and $(0, \frac{4}{3}, 0)$ give way to a sole peak at $(0, 1, 0)$. Note that $(0, 2, 0)$ was not probed in phases VI and VII.

Peak positions were obtained from fits to Gaussians profiles where the peak widths were fixed based on fitted values from the zero-field data. This was done in order to minimize the number of fitting parameters to achieve a stable fit from data with compromising statistics. The zero-field data has much superior statistics and clear peaks at $(0, K, 0)$, for $K = 1, 2, 3, 4, 6, 8, 10$ where K odd are magnetic peaks and K even are nuclear peaks. In principle, there should also be peaks for $K = 5, 7, 9$, but being magnetic their intensities are extinguished by the magnetic form factor. For $K < 6$ the peak widths approximately follow a linear trend: $\sigma(K) = \alpha K + \beta$, where $\alpha = 0.0143(1)$ and $\beta = 0.0022(7)$ r.l.u. were fitted. This relation is

used for fixing the peak widths in the field-on data. Details on the approach are found in Appendix B. The fitted peak positions in phase V are $(0, 0.6598(6), 0)$, $(0, 0.993(4), 0)$, $(0, 1.334(7), 0)$ and $(0, 1.980(3), 0)$, in phase VI they are similarly $(0, 0.660(1), 0)$, $(0, 1.00(1), 0)$ and $(0, 1.301(8), 0)$ and in phase VII a single peak is observed at $(0, 0.994(2), 0)$. It is assumed that the positions are independent on the field within the individual phases. This is valid in phase V up to 23 T [see lefthand color plot in Fig. 7.4] however, not necessarily so above 23 T in phases VI and VII.

The magnetic phase diagram of $LiNiPO_4$ was thus characterized up to 42 T by combining magnetization, electric polarization and neutron diffraction experiments using both DC and pulsed magnetic fields. The next couple of sections then regard magnetic structure determination for phases IV-VII and modelling of the magnetoelectric effect in phase VII.

7.2 Magnetic structure in phase IV

A magnetic structure in phase IV was proposed in Ref. 69 based on the observation of a single magnetic Bragg peak – $(0, 1, 0)$ – together with magnetization and electric polarization data. A model for the magnetoelectric effect further substantiated the proposed commensurate structure consisting of a $(\uparrow\uparrow\downarrow\downarrow)$ symmetry component along c as well as two equally large components of symmetries $(\uparrow\downarrow\downarrow\uparrow)$ and $(\uparrow\downarrow\uparrow\downarrow)$, both with spins polarized along a [see Fig. 7.2].

Apart from being excellent for parametric studies, the HFM/EXED experiment also allowed for the observation of a few more magnetic Bragg peaks in phase IV. These are listed in Table 7.1 together with the magnetic structure and spin polarization factors and Fig. 7.6 shows TOF profiles for selected peaks. Apart from $(0, -1, 0)$, the peaks $(\pm1, -2, 0)$ and $(\pm1, -1, 0)$ are also present in phase IV, representing structure components $(\uparrow\downarrow\downarrow\uparrow)$ and $(\uparrow\downarrow\uparrow\downarrow)$, respectively, and with spin polarization mostly along a. Hence, the observed magnetic peaks are consistent with the structure postulated in Ref. 69 although the supporting data in Fig. 7.6 is not very convincing.

The intensities are obtained in Mantid[122] as follows: (1) rectangular masks are created for each indidual peak on the detector, (2) a second order polynomial is

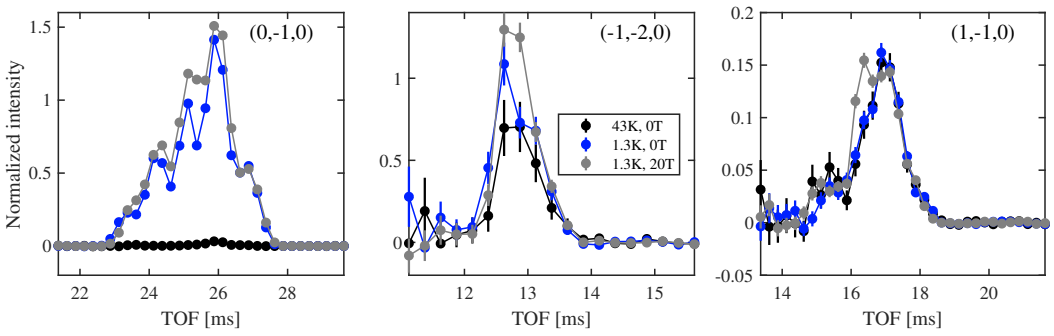

Figure 7.6: *TOF profiles of (0,-1,0), (-1,-2,0) and (1,-1,0) as measured at HFM/EXED. Intensities have been normalized to detector efficiency and the Lorentz factor. A fitted background was subtracted as described in the text.*

Table 7.1: *Absolute squares of structure and spin polarization factors for the magnetic basis vectors reflected by the commensurate magnetic Bragg peaks observed in phases I and IV at the HFM/EXED experiment. Factors are normalized to unit spin lengths.*

(H,K,L)	$\lvert S(\mathbf{Q})\rvert^2$				$\lvert P_i(\mathbf{Q})\rvert^2$		
	A	G	C	F	x	y	z
	$(\uparrow\downarrow\downarrow\uparrow)$	$(\uparrow\downarrow\uparrow\downarrow)$	$(\uparrow\uparrow\downarrow\downarrow)$	$(\uparrow\uparrow\uparrow\uparrow)$	a	b	c
$(\pm1,-2,0)$	15.37	0.63	0	0	0.92	0.08	1
$(\pm1,-1,0)$	0.63	15.37	0	0	0.75	0.25	1
$(0,-1,0)$	0	0	16	0	1	0	1

fitted to describe the background of the TOF spectrum and (3) the background is subtracted and Vanadium and Lorentz corrections applied. The procedure is explained in more detail in Appendix B where all obtained intensities are also listed.

The integrated intensities of the equivalent pairs $(-1,-2,0)$ / $(1,-2,0)$, and $(-1,-1,0)$ / $(1,-1,0)$ do not match up. In fact, they differ by a factor of ~ 4 and ~ 2 in the two cases. A number of reasons may account for the discrepancies: $(-1,-1,0)$ appears on the edge of the detector and some intensity is likely lost. Moreover, the detector is constructed of arrays of detector tubes with gaps in between. This means that some neutrons are not detected, but escape in between the tubes. This would affect peaks spanning a small detector area more than peaks spanning a larger area. In this respect, it is noted that $(1,-2,0)$ only spans 2 detector tubes whereas $(-1,-2,0)$ spans 3. However, of the two peaks in this pair, the latter has lower integrated intensity so the above argument does not hold. Alternatively, there may be something in the neutron beam – apart from the sample – shadowing parts of the detector. Unfortunately, in any case, the observed magnetic peaks can only be used as binary information, i.e. whether a peak is there or not.

In conclusion, the observed magnetic Bragg peaks in phase VI are consistent with the commensurate magnetic structure proposed in Ref. 69 and shown in Fig. 7.2. However, integrated intensities for equivalent peaks are not consistent and hence any quantitative analysis proved impossible.

7.3 Magnetic structures in phases V and VI

The magnetic structure in phase V was previously conjectured using neutron diffraction, magnetization measurements and mean-field theory[69]. It has propagation vector $\mathbf{Q} = (0, \frac{1}{3}, 0)$, i.e. a period of 3 crystallographic unit cells propagating along b, and the spin structure consists of a ferromagnetic component along c and a main symmetry component $(+ + -\beta - \beta)$ describing the incommensurate part of the structure. Here the notation is slightly altered such that $+$ $(-)$ denotes spin $\uparrow$ $(\downarrow)$ and $\beta e^{-i\pi/3}$ is a phase factor in accordance with Ref. 48.

The structure proposed in Ref. 69 was based on the observation of the $(0, \frac{4}{3}, 0)$ magnetic Bragg peak and the $\frac{1}{3}$ magnetization. A number of additional magnetic Bragg peaks were observed in the HFM/EXED experiment and a somewhat sounder structure determination is in principle possible. However, as pointed out in the

Table 7.2: *Observed vs. calculated intensities for proposed structures in phase V. The linearly modulated structure has spins polarized along c. The spiral and cycloid have spins in the (a,c)-plane with c the major axis for the cycloid structure.*

(H, K, L)	Obs. int.	Linear	Spiral	Cycloid
$(0, -\frac{2}{3}, 0)$	11.218(6)	11.38	11.36	18.38
$(1, -\frac{2}{3}, 0)$	0.526(9)	0	0.66	0.99
$(-2, -\frac{1}{3}, 0)$	3.76(33)	0.96	1.94	3.10
$(0, -\frac{4}{3}, 0)$	13.26(4)	5.44	5.43	8.78
$(-1, -\frac{4}{3}, 0)$	0.155(7)	0	0.39	0.59
$(1, -\frac{4}{3}, 0)$	0.112(16)	0	0.39	0.59
$(2, -\frac{4}{3}, 0)$	24.5(3.1)	4.28	4.50	7.29

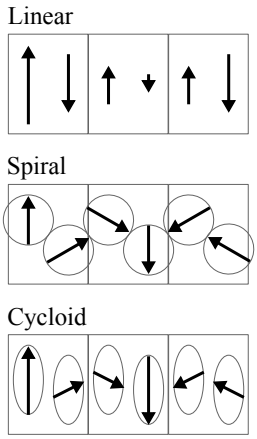

Figure 7.7: *Cartoons illustrating structures refined in* FULLPROF *in phase V.*

previous section, the integrated intensities are dubious. In this regards, it should be mentioned that $(-2, -\frac{1}{3}, 0)$ is situated near the edge of the detector. Still, the additional peaks may at least be used as binary information. In an attempt to determine the magnetic structure in phase V intensities for a number of model structures are refined using FULLPROF and compared with the observed intensities, see Table 7.2 and Fig. 7.7. The linearly modulated spin-density wave with spins polarized along c forbids neutron intensity for $(1, -\frac{2}{3}, 0)$ and $(\pm 1, -\frac{4}{3}, 0)$. Since these peaks are present in phase V, this model can readily be discarded. The spiral and cycloid structure both allow all observed Bragg peaks but the spiral yields a better χ^2 [7.52×10^3 vs. 1.14×10^6 (!)].

Comparing Figs. 7.5(b) and 7.5(c), phase VI looks very similar to phase V. Yet, the magnetic susceptibility is considerably larger in phase VI than in phase V, see magnetization curve in Fig. 7.3. Furthermore, the period of the structure is possibly longer with a peak observed at $(0, 1.301(8), 0)$ in phase VI as compared to at $(0, 1.334(7), 0)$ in phase V. This change in position may not be real if the systematic uncertainties are larger than estimated but it may be that the peak has indeed moved. When determining the peak position it was assumed field-independent but as also previously pointed out, this might not be the case. If K decreases with field from $K = 1.33$ to $K = 1.27$ within the field interval, the fitted position – given that the neutron intensity stays constant – would indeed be $K = 1.30$. In such case, the period of the magnetic structure would no longer be locked in to the crystal structure. However, if the peak is indeed moving with field, a peak broadening is expected when integrating over the field. This does not appear to be the case when inspecting Fig. 7.5(c).

The magnetic structure in phase V is thus most likely a spiral with spin components in the (a, c)-plane and magnetized along c. The spiral propagates along b with a period of 3 crystallographic unit cells. In phase VI, the period stays constant or possibly changes slightly towards longer periods. The magnetic susceptibility is larger in phase VI than in phase V.

7.4 Magnetic structure and magnetoelectric effect in phase VII

In this section, the magnetic structure and the magnetoelectric effect in phase VII are tackled. In many ways, phase VII looks similar to phase IV: the magnetization is linear as a function of applied field [Fig. 7.3] and a single magnetic Bragg peak – $(0, 1, 0)$ – was observed in the pulsed-field Laue neutron diffraction experiment. The magnetization is $\sim 1.1\,\mu_B = \frac{1}{2}M_S$ ($M_S = 2.2\,\mu_B$ for $LiNiPO_4$[48]) upon entering the phase at 39.4 T. This may be obtained by a further magnetized version of the structure in phase IV as shown in Fig. 7.2. In the proposed structure, spins 1 and 2 are aligned with the applied magnetic field and spins 3 and 4 are approximately antiparallel to each other as well as perpendicular to the field direction. The angle between spins 3 and 4 is $\varphi_0 = \pi$ upon entering phase VII and increases, $\varphi_0 + \Delta\varphi$, as the field is increased as also illustrated in the inset in Fig. 7.8.

The phase diagram of $LiNiPO_4$ consists of a series of alternating commensurate and incommensurate phases. Interestingly, only the commensurate structures support the magnetoelectric effect as observed in the electric polarization, see Fig. 7.3 where the measured electric polarization along a, P_a , is plotted as a funtion of magnetic field applied along c, H_c. A finite polarization is observed in phases I, IV and VII and for all three phases the non-zero tensor elements in $P_i = \alpha_{ij}H_j$ are α_{ac} and α_{ca} . From symmetry considerations it may be argued that these elements are activated by spins along c in a $(\uparrow\uparrow\downarrow\downarrow)$ configuration[19,39]. The electric polarization in phase VII decreases with field as opposed to the increasing polarizations in phases I and IV. Consequently, the magnetoelectric tensor component is negative in phase VII. Moreover, the polarization curve is non-linear.

Previously, a microscopic model succesfully described the magnetoelectric effect in both phases I and IV[48,69]. Using that same model as a starting point we attemp to describe the effect in phase VII. Extending the argument of Jensen et al.[48], the exchange energy for the two spin pairs is $E_0 = J_{12}S^2 + J_{34}S^2\cos(\varphi_0 + \Delta\varphi) \approx J_{12}S^2 + J_{34}S^2\left(-1 + \frac{1}{2}(\Delta\varphi)^2\right)$ when expanding the cosine around $\varphi_0 = \pi$. It is now assumed that any further spin rotation, $\Delta\varphi > 0$, introduces an asymmetric change

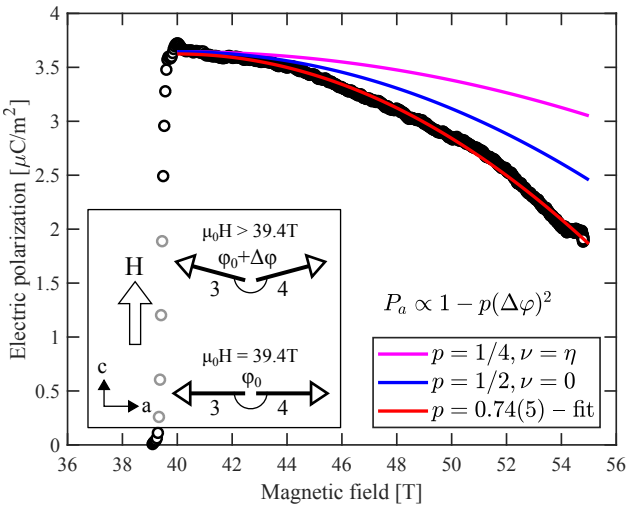

Figure 7.8: *Model of the magnetoelectric effect in $LiNiPO_4$ in phase VII. Electric polarization as a function of field in phase VII (circles) as measured by Takumi Kihara from Tohoku University. The solid lines show the polarization as a function of field as calculated using the model described in the text with different values of $p = \frac{\eta}{2(\nu+\eta)}$. The inset shows the mutual orientation of spin pair (3,4) as phase VII is entered ($\varphi_0 = \pi$) and as the field is increased ($\varphi_0 + \Delta\varphi > \pi$).*

in the exchange interactions such that $J_{12} \to J_{12} - \nu x$ and $J_{34} \to J_{34} + \eta x$, where ν and η are proportionality constants and x is the displacement of the PO_4 tetrahedra. This leads to a change in exchange energy of $\Delta E = xS^2\left(-\nu - \eta + \frac{\eta}{2}(\Delta\varphi)^2\right)$. Moving the PO_4 tetrahedra also introduces an elastic energy, $\epsilon_x x^2$. The equilibrium is found by minimizing the sum of the changes in the exchange and elastic energies yielding an expression for the electric polarization, $P = Kx$, as follows:

$$P_a = \frac{K(\nu+\eta)}{2\epsilon_x}\left(1 - \frac{\eta}{2(\nu+\eta)}(\Delta\varphi)^2\right),$$

where K is a constant. Hence, the polarization decreases with $(\Delta\phi)^2$ and fitting the above expression to the data for fields above 40 T yields $p = \frac{\eta}{2(\nu+\eta)} = 0.74(5)$ [see Fig. 7.8]. Note that in this case, $p > \frac{1}{2}$, and ν and η have opposite signs and hence both J_{12} and J_{34} increase (or decrease) in size with the magnetic field but J_{34} is doing so 5 times faster than J_{12}. Other cases are also shown in Fig. 7.8. For $p = \frac{1}{4}$, $\nu = \eta$ and the model collapses to the one demonstrated in Ref. 48 for phase I and in Ref. 69 for phase IV. For $p = \frac{1}{2}$, $\nu = 0$ and only J_{34} changes upon moving the PO_4 tetrahedra.

7.5 Summary

The magnetic phase diagram of $LiNiPO_4$ was characterized by magnetization, electric polarization and neutron diffraction to an impressive 42 T applied along the easy axis c. Phase transitions were observed at 12.0, 16.0, 19.1, 20.9, 37.6 and 39.4 T with the phases enumerated I-VII for increasing field.

Previously, a commensurate magnetic structure in phase IV (19.1 − 20.9 T) was proposed based on pulsed-field magnetization and neutron diffraction measurements[69]. Additionally, a microscopic model taking the proposed structure as a starting point succesfully explained the field-dependence of the magnetoelectric coefficient, α_{ab}, in this phase. In the present work, the proposed spin structure was consolidated by observation of additional magnetic Bragg peaks at HFM/EXED. Unfortunately, due to large variations in the intensity of symmetry equivalent peaks, observations could only be used qualitatively.

Integrated neutron intensities of Bragg peaks observed in phase V (20.9 − 37.6 T) are dubious too. Nonetheless, FULLPROF refinements indicate that the magnetic structure in this phase is a spiral with spins in the (a, c)-plane. The spiral is propagating along b and has a period of 3 crystallographic unit cells. Phase VI (37.6 − 39.4 T) is very similar to phase V but for an increased magnetic susceptibility and possibly a slightly longer period of the magnetic structure.

In phase VII (> 39.4 T), yet another commensurate magnetic structure is established based on pulsed-field neutron diffraction, magnetization and electric polarization measurements. This phase displays the magnetoelectric effect and the proposed spin structure is similar to the structures found in the other magnetoelectric phases I and IV. Moreover, an extended version of the microscopic model explaining the magnetoelectric effect in phases I and IV succeeds in describing the effect in phase VII too. Thus the model accomplishes to span all observed magnetoelectric phases in $LiNiPO_4$ and shows that they are connected in their origin.

Chapter 8

Magnetism and magnetoelectricity in $LiNi_{1-x}Fe_xPO_4$

All the results presented so far regarded the stoichiometric compounds, $LiCoPO_4$ and $LiNiPO_4$. Now we turn to investigations of the mixed compounds, $LiNi_{1-x}Fe_xPO_4$. We have crystals with 6% and 20% Fe available and results of various measurements on these two compounds as well as simulations on the general system, $x \in [0, 1]$, are presented below. Results on $LiNi_{0.94}Fe_{0.06}PO_4$ are considered in Section 8.1 and not too surprisingly, this compound is very similar to $LiNiPO_4$. This was also previously shown in SHG measurements[73]. Results on $LiNi_{0.8}Fe_{0.2}PO_4$ are presented in Section 8.2 and this compound displays numerous interesting effects due to the competition between the Ni^{2+} and Fe^{2+} single-ion anisotropies [see discussion in Section 3.2]. Previously, $LiNi_{0.8}Fe_{0.2}PO_4$ was investigated using SHG[73] and neutron scattering[74] and our results complement and extend earlier findings but also cover entirely new ground. Finally, Monte Carlo simulations on the general system, $LiNi_{1-x}Fe_xPO_4$, assist in the interpretation of the experimental results in Section 8.3.

8.1 $LiNi_{0.94}Fe_{0.06}PO_4$

A number of experiments were performed on samples with 6% Fe, including magnetization, neutron diffraction and inelastic neutron scattering measurements. The results are laid out in this section.

Magnetic phase diagrams. Magnetic phase boundaries of $LiNi_{0.94}Fe_{0.06}PO_4$ were determined by tracking the magnetization and selected magnetic Bragg peaks as a function of temperature and magnetic field employing procedures similar to those used for $LiCoPO_4$ and $LiNiPO_4$ in Chapters 6-7. The resulting magnetic phase diagrams for fields applied along the three principal crystallographic directions are shown in Fig. 8.1 and 8.2. For fields applied along a and b there is a single transition as a function of temperature at $\sim 20\,\mathrm{K}$ for all measured field values. At zero field and for fields along c there is, in addition, a transition at $\sim 21\,\mathrm{K}$.

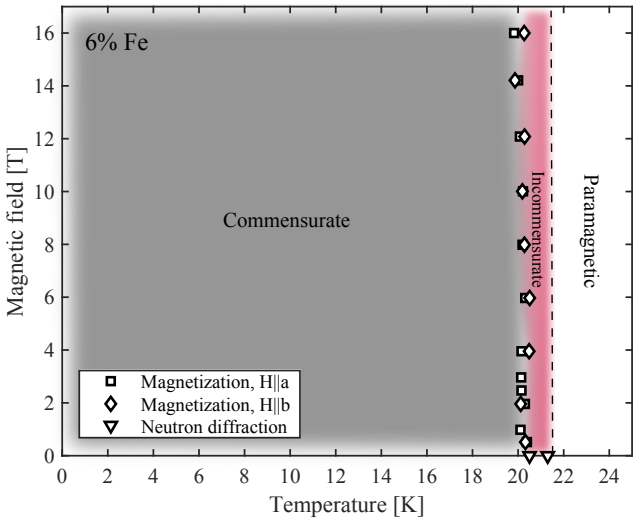

Figure 8.1: *Magnetic phase diagrams of $LiNi_{0.94}Fe_{0.06}PO_4$ for magnetic fields applied along a (squares) and b (diamonds) as determined by magnetization measurements. Neutron data at zero field is also shown (triangles). The paramagnetic-incommensurate phase boundary could not be experimentally verified for these field directions but the conjectured boundary is shown with the dashed line.*

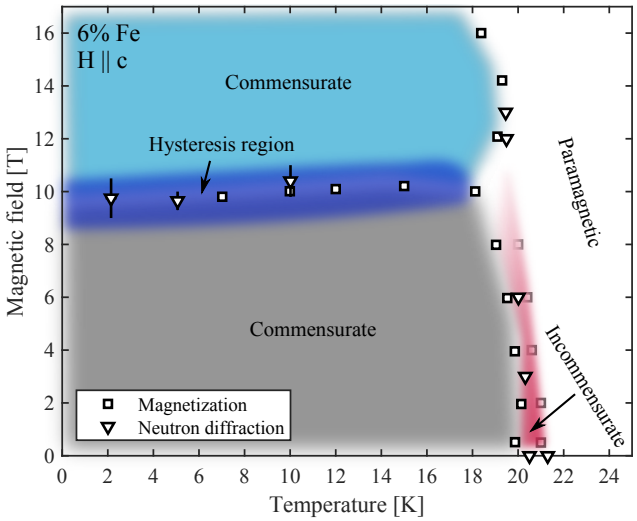

Figure 8.2: *Magnetic phase diagram of $LiNi_{0.94}Fe_{0.06}PO_4$ for magnetic fields applied along c as determined by magnetization measurements (squares) and neutron diffraction (triangles). An incommensurate magnetic phase exists in a ∼1K thick slice above the low-temperature and low-field commensurate phase. The paramagnetic-incommensurate phase boundary was detected in the magnetization up to 8 T. The corresponding feature is relatively small and data points are indicated with faded symbols to illustrate their uncertainty.*

Furthermore, for fields applied along c there is a field-induced phase transition at $\sim 10\,\mathrm{T}$. Details of the various measurements are described below.

For VSM measurements with magnetic fields applied along a, b and c, three single crystals of $LiNi_{0.94}Fe_{0.06}PO_4$ of mass 50.7, 20.7 and 38.6 mg were used respectively. The crystals were aligned prior to the measurements using X-ray Laue and the measurements were performed at the CFMS located at DTU Risø Campus. The magnetic susceptibility and its inverse as a function of temperature at 0.5 T are shown in Fig. 8.3. Transitions are observed for all three field directions and c is clearly the easy axis with a sudden drop in the susceptibility at the transition. The colored lines show fits to the Curie-Weiss law as stated in Eq.(6.1). The resulting fitting parameters and transition temperatures as determined from the susceptibility data are given in Table 8.1.

The magnetization as a function of temperature and applied magnetic field is shown in Fig. 8.4. For fields applied along c there is a sharp decrease in the magnetization upon cooling, indicating that c is the easy axis like in the parent compound,

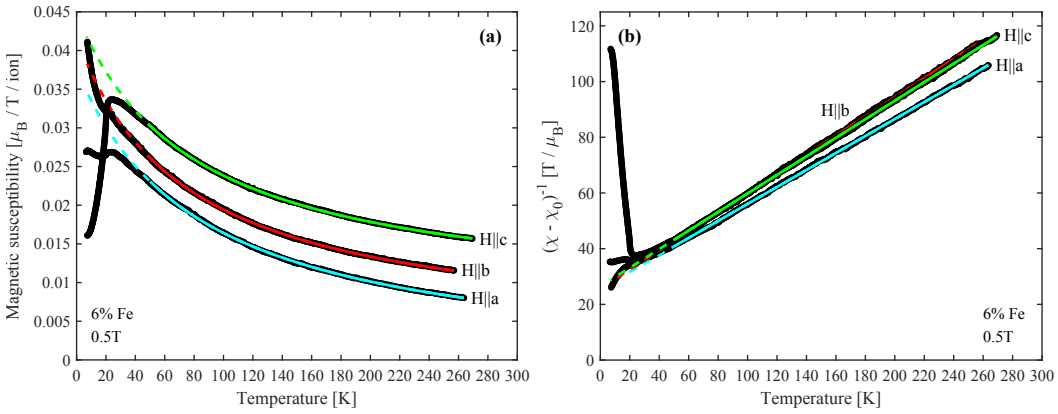

Figure 8.3: *(a) Magnetic susceptibility and (b) inverse susceptibility for $LiNi_{0.94}Fe_{0.06}PO_4$ at 0.5T applied along the three principal crystal directions. For clarity, the curves in (a) are displaced $+4\times10^{-3}\,\mu_B/T$ and $+8\times10^{-3}\,\mu_B/T$ vertically for fields along b and c respectively. Transitions are observed for all three field directions and c is clearly the easy axis. The colored lines show fits to the Curie-Weiss. The solid parts of the lines show the fitted interval and the dashed parts are extrapolations.*

Table 8.1: *Parameters obtained by fitting the Curie-weiss law, $\chi - \chi_0 = \frac{C}{T+\Theta_{CW}}$, to the magnetic susceptibility curves of $LiNi_{1-x}Fe_xPO_4$ measured at 0.5 T and shown in Fig. 8.3 for $x = 0.06$ and Fig. 8.11 for $x = 0.20$. All fits are performed for $T > 50\,K$. The effective moment is calculated from the fitted Curie constant, C, as $\mu_{\text{eff}} = \sqrt{\frac{3k_BC}{N_m\mu_B}}$, where $N_m = 1$ is the number of magnetic ions per formula unit, μ_B is the Bohr magneton and k_B the Boltzmann constant. Finally, the transition temperatures are listed as well as the frustration parameter, $f = \frac{\Theta_{CW}}{T_N}$ [11].*

x	**H**||	Θ_{CW} [K]	C [μ_BK/T]	χ_0 [$10^{-3}\mu_B$/T]	μ_{eff} [μ_B]	T_N [K]	f
0.06	**a**	84(5)	3.28	-1.42	3.83	20.4(1)	4.1(2)
	b	75(5)	2.91	-1.23	3.60	20.3(1)	3.7(2)
	c	80(5)	3.00	-0.89	3.66	19.9(1)	4.0(3)
0.20	**a**	91(2)	4.14	-1.52	4.30	19.7(1)	4.6(1)
	b	64(5)	3.72	0.05	4.08	25.2(1)	2.5(2)
	c	89(5)	3.55	-0.48	3.98	24.5(5)	3.7(2)

$LiNiPO_4$. For fields along a, the magnetization of $LiNi_{0.94}Fe_{0.06}PO_4$ behaves like expected for fields transverse to the easy axis[4], i.e. upon cooling a small feature is observed at T_N whereafter the it levels out. However, for fields applied along b the behavior of the magnetization is somewhat unexpected. Upon cooling, the magnetization continues to rise beyond T_N like in the paramagnetic state, but with a short plateau of $\sim 1\,K$ at T_N. This feature at low temperatures resembles a so-called *Curie tail* which usually orinates from free magnetic ions. The easy axis for $LiFePO_4$ is b and locally this must also hold for the individual Fe^{2+} ions in $LiNi_{0.94}Fe_{0.06}PO_4$. One may therefore perhaps think of the 6% Fe as magnetic impurities that are decoupled from the ordered Ni^{2+} ions and act as free magnetic ions upon applying a magnetic field along b.

A neutron diffraction experiment was performed at RITA-II at the PSI, Switzerland, in order to investigate magnetic structures in $LiNi_{0.94}Fe_{0.06}PO_4$. For all measurements 80' collimation was used before the sample and incoming and outgoing

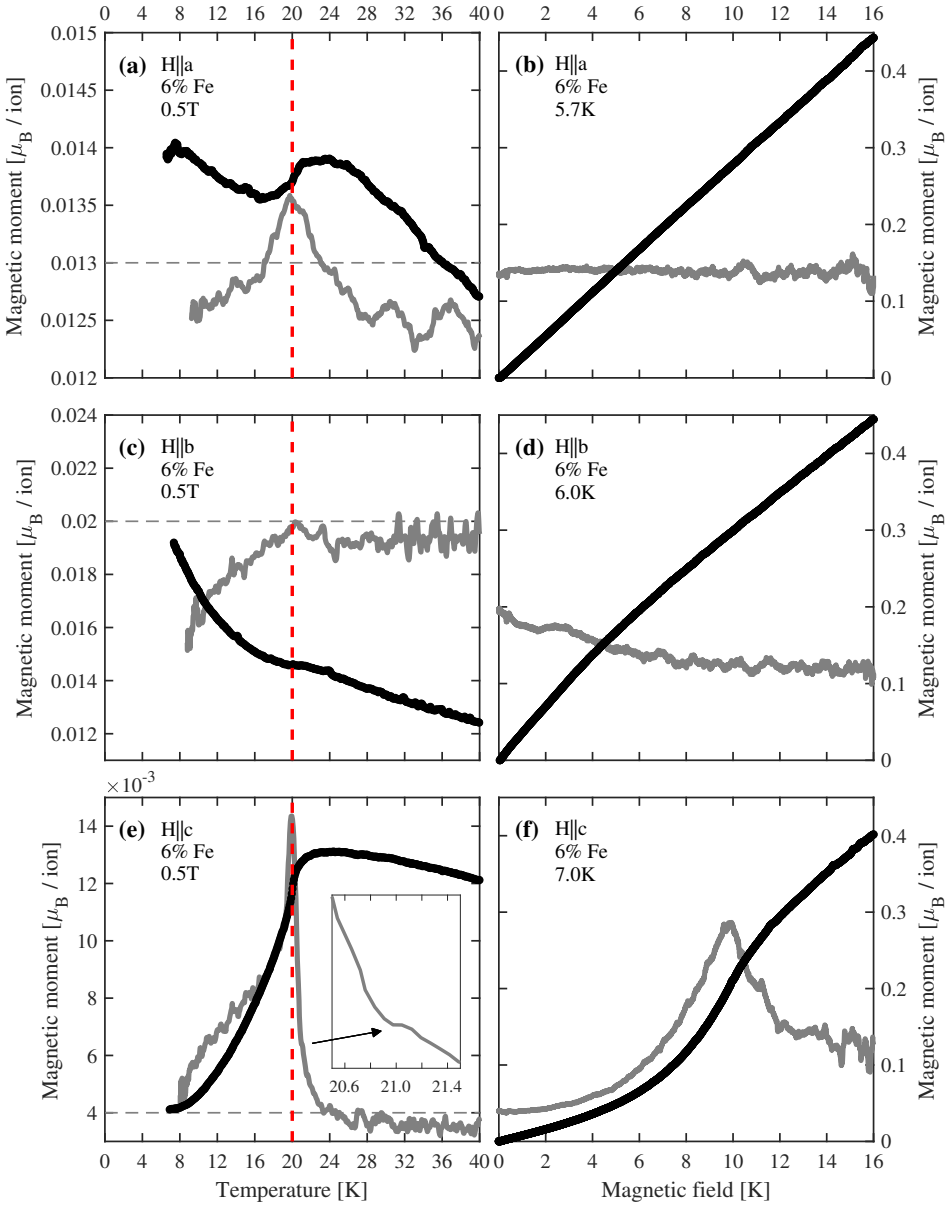

Figure 8.4: *Magnetization as a function of decreasing temperature (left panels) and as a function of increasing magnetic field (right panels) for $LiNi_{0.94}Fe_{0.06}PO_4$. Derivatives, $\frac{dM}{dT}$ and $\frac{dM}{dH}$, are shown with the grey curves in the background (a.u.). Zero slope is marked with grey horizontal dashed lines in the lefthand panels and coincides with zero magnetization in the righthand panels. $T_N = 20\,K$ is indicated with the red vertical dashed lines. The inset in (e) shows the feature correlating with the paramagnetic-incommensurate phase transition.*

neutrons had energy 5 meV. A cooled Be filter after the sample ensured suppression of higher order neutrons and a vertical-field cryomagnet was used to obtain temperatures and fields in the ranges $2-300\,\mathrm{K}$ and $0-13\,\mathrm{T}$ respectively. The sample was a high quality single crystal with mass 50.7 mg which was aligned with $(H, K, 0)$ in the scattering plane and hence magnetic fields applied along the crystallographic c-axis.

The commensurate $(0, 1, 0)$ magnetic Bragg peak was followed as a function of

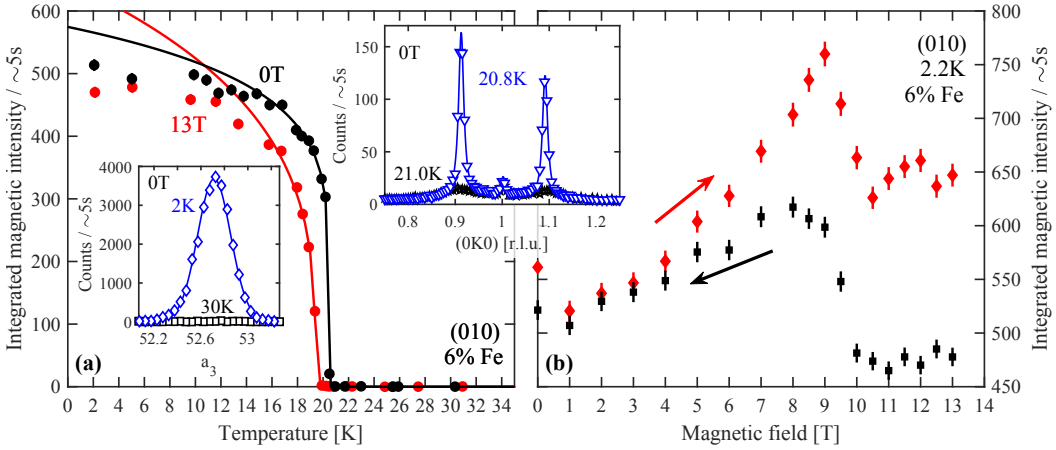

Figure 8.5: *Magnetic intensity of the (0,1,0) Bragg peak (a) as a function of temperature at 0 T (black symbols) and at 13 T (red symbols) and (b) as a function of magnetic field along c at 2.2 K. Power laws have been fitted to the temperature dependencies (solid lines) with T_N = 20.5(2) K at 0 T. A field-induced transition is observed at 8-10 T and the field dependence of (0,1,0) shows different behavior for increasing (red symbols) and decreasing (black symbols) field. The inset in (a) shows the rocking curve of (0,1,0) at 30 K and 2 K at 0 T with the solid line showing a Gaussian fit. The top middle inset shows neutron counts as a function of (0,K,0) at 20.8 K (blue symbols) and 21.0 K (black symbols), both at 0 T. The solid line is a fit to three Voigt functions with center positions (0,1-k,0), (0,1,0) and (0,1+k,0).*

temperature at various fixed magnetic field strengths and as a function of applied field for selected temperatures. Examples of such scans are shown in Fig. 8.5. The temperature dependence of $(0, 1, 0)$ shows a sharp transition at 20.5(2) K in zero field. Furthermore, intensity was observed at incommensurate positions along $(0, K, 0)$ for temperatures just above the transition to the commensurate phase [see middle inset in Fig. 8.5]. Evidence of an intermediate incommensurate phase in $LiNi_{0.94}Fe_{0.06}PO_4$ was also observed in optical SHG[73]. A Voigt function was fitted to the observed incommensurate peaks. The Voigt is a convolution of a Gaussian and a Lorentzian where the respective linewidths describe the instrumental resolution and the correlation length of the magnetic order. The fitted peak positions yield the propagation vector, $\mathbf{Q} = [0, 0.089(1), 0]$, signifying an elongation of the magnetic unit cell along b of approximately 11 times the commensurate unit cell. Moreover, it is likely that the propagation vector – and thereby the magnetic unit cell size – is temperature and/or field-dependent but scans of $(0, K, 0)$ were only recorded in zero field at 21.0 K and 20.8 K. An incommensurate phase just above the transition to commensurate antiferromagnetic order also exists in the parent compound, $LiNiPO_4$, and here the propagation vector is indeed temperature- and field-dependent. Moreover, in $LiNiPO_4$ the incommensurate phase persists upon applying a magnetic field along the easy axis up to the highest probed field of 17.3 T[61]. Therefore, it is believed that the incommensurate phase in $LiNi_{0.94}Fe_{0.06}PO_4$, too, may persist upon applying a magnetic field along c. An indication of whether this holds is found in the way the $(0, 1, 0)$ Bragg peak behaves as a function of temperature at different field values. At 0, 3 and 6 T, the transition is abrupt and indeed pointing towards an incommensurate-commensurate phase transition of first order like in $LiNiPO_4$[48]. At the highest probed fields, 12 and 13 T, the

transition is more gradual, compare 0 and 13 T data in Fig. 8.5(a). The gradual increase in the $(0, 1, 0)$ intensity points towards a continuous transition from the paramagnetic state to the commensurate state, i.e. the incommensurate state does not exist at high fields but may persist at least up to 6 T along c. Upon closer inspection of the temperature derivative of the magnetization, a shoulder is also observed corresponding to the paramagnetic-incommensurate phase transition, see inset in Fig. 8.4(e). The feature is so small that it was first overlooked but it is possible to detect for fields up to 8 T along c. In the phase diagram in Fig. 8.2, the corresponding data points are indicated with faded symbols to illustrate their uncertainty. The paramagnetic-incommensurate phase boundary could not be experimentally verified for fields along a and b but the conjectured boundary is shown in Fig. 8.1.

The field dependence of $(0, 1, 0)$ was recorded both as a function of increasing and decreasing magnetic field. It should be mentioned that these scans were performed disjointed in the experiment. The procedure commenced at 30 K and 0 T (13 T), then the sample was cooled to 2.2 K and rocking curves were collected at each set field value when ramping the field up (down). A broad field-induced phase transition was observed at $\sim 8 - 10$ T. For increasing field, the $(0, 1, 0)$ intensity goes up until 9 T. Hereafter, the intensity drops and levels out around 10.5 T. For decreasing field, the intensity is level down to 10 T where it increases until around 8 T. From here, the intensity continuously decreases with the field. The intensity for both ramp directions is expected to coincide once a phase has been established. In this case, however, the intensities at 13 T differ by ∼30%. It is possible that a stable state has not yet been reached at this field value and the system is still inside some hysteresis region. Alternatively, the system just needs time to drift into its equilibrium. The peak intensity of $(0, 1, 0)$ was measured at 10 K and 12 T for 2.5 h in order to test this hypothesis. The intensity did indeed decrease over time, but only by ∼6% and the measurement was performed at 10 K where the system is expected to equilibrize faster than at 2.2 K. More studies are needed to clarify spin relaxation dynamics and hysteresis in $LiNi_{0.94}Fe_{0.06}PO_4$.

Magnetic structures at zero and high field. The observed magnetic Bragg peak, $(0, 1, 0)$, represents $(\uparrow\uparrow\downarrow\downarrow)$ symmetry components with spins along a or c. The present neutron diffraction experiment together with the magnetization measurements and previous optical SHG measurements[73] indicate that the zero-field magnetic structure of $LiNi_{0.94}Fe_{0.06}PO_4$ is mainly an $(\uparrow\uparrow\downarrow\downarrow)$ spin arrangement with spins polarized along c, i.e. like the parent compound, $LiNiPO_4$[48,61]. Spin components along a could not be observed in the SHG experiment. Hence, a spin component along a cannot be ruled out. Furthermore, since any spin components along b are invisible for $(0, 1, 0)$, such components can neither be rejected.

Very little can be said about the magnetic structure above the transition at $\sim 8 - 10$ T. However, it is similar to the zero-field structure since the Bragg peak $(0, 1, 0)$ still has magnetic intensity in this phase. One possibility is a change in the spin component along b. Given that the zero-field structure has major spin component along c but a minor one along b, the peculiar behavior of the intensity of the $(0, 1, 0)$ may be explained as follows: upon increasing the field the spins turn more towards c. At the transition a re-orientation takes place such that the spin component along b suddenly increases. As evident in both neutron diffraction

and magnetization measurements, the transition is gradual and not sharp like a traditional spin-flop transition. The higher magnetic susceptibility above the transition compared to below [*cf.* Fig. 8.4(f)] also points towards a spin re-orientation since moments perpendicular to the applied field are more readily magnetized than moments parallel to the field.

Spin excitations. The spin-wave dispersion for $LiNi_{0.94}Fe_{0.06}PO_4$ was measured using inelastic neutron scattering. The experiment was performed at the triple-axis spectrometer, EIGER, at the PSI, Switzerland, using fixed $k_f = 2.66\,\text{Å}^{-1}$ ($E_f = 14.7\,\text{meV}$). The instrument employs a double-focusing PG monochromator, a PG filter after the sample and a horizontally focusing PG analyzer. The sample was the same 50.7 mg single crystal oriented with $(H, K, 0)$ in the scattering plane as used for the RITA-II experiment. The EIGER experiment was kindly carried out by Jonas Okkels Birk.

Neutron counts as a function of energy transfer was measured at different positions in reciprocal space along $(H, 1, 0)$ and $(0, K, 0)$. A selection of the measured spectra are found in Fig. 8.6. Mode positions are determined by fitting a Gaussian to each curve.

The following Hamiltonian results in a model dispersion to be fitted to the data:

$$\hat{\mathcal{H}} = \sum_{\langle i,j \rangle} J_{i,j} \mathbf{S}_i \cdot \mathbf{S}_j + \sum_{i,\alpha} \mathfrak{D}^\alpha (S_i^\alpha)^2, \tag{8.1}$$

with i denoting a sum over all magnetic ions, $\langle i, j \rangle$ a sum over nearest neighbor pairs and $\alpha = \{a, b, c\}$. Assuming spins entirely along c and $\mathfrak{D}^c = 0$, linear spin-wave theory yields the eigenvalues:

$$\hbar\omega = \sqrt{A^2 - (B \pm C)^2}, \tag{8.2}$$

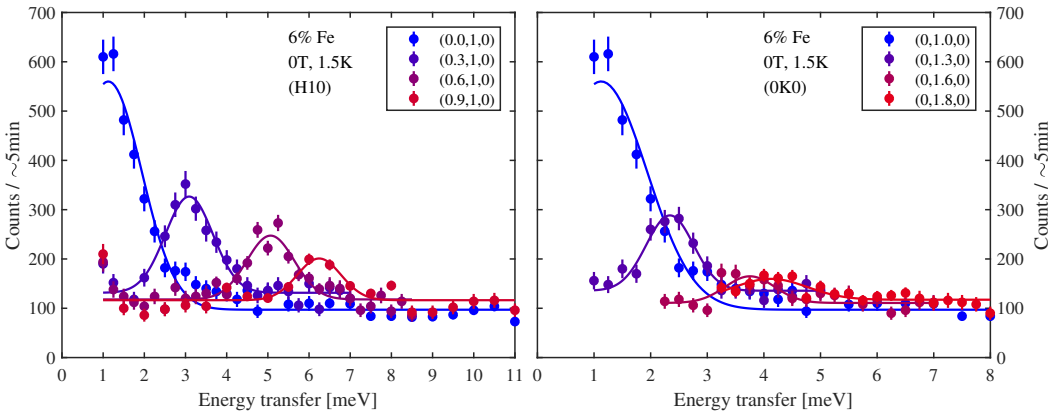

Figure 8.6: *Neutron counts as a function of energy transfer along (H,1,0) and (0,K,0) in $LiNi_{0.94}Fe_{0.06}PO_4$ for selected values of H and K. Peak positions are determined by Gaussian fits.*

Table 8.2: *Exchange and single-ion anisotropy parameters for $LiNi_{1-x}Fe_xPO_4$ as determined by fitting spin-waves to the dispersion in Eq. (8.2). The parameters for the pure compounds, $LiNiPO_4$ and $LiFePO_4$, are from Ref. 53 and 54 respectively. The parameters for $LiNi_{0.8}Fe_{0.2}PO_4$ are from Ref. 74. All values are given in meV.*

	$LiNiPO_4$	$LiNi_{0.94}Fe_{0.06}PO_4$	$LiNi_{0.8}Fe_{0.2}PO_4$	$LiFePO_4$
J_{bc}	1.04(6)	0.94(9)	0.88(15)	0.77(7)
J_b	0.670(9)	0.50(5)	0.44(4)	0.30(6)
J_c	-0.05(6)	0 (fixed)	0.087(20)	0.14(4)
J_{ab}	0.30(6)	0.19(4)	0.038(4)	0.14(2)
J_{ac}	-0.11(3)	-0.20(3)	-0.22(4)	0.05(2)
$\mathfrak{D}^a$	$0.708(2)^\dagger$	0.103(7)	0^*	0.62(12)
$\mathfrak{D}^b$	$1.45(3)^\dagger$	1.52(12)	$0.150(6)^{\dagger,*}$	0
$\mathfrak{D}^c$	0	0	$1.17(1)^{\dagger,*}$	1.56(3)

† These values have been scaled with respect to those originally given in Refs. 53 and 74 where $B = (S-1/2)\left(\mathfrak{D}^a - \mathfrak{D}^b\right)$ is defined in Eq. (8.2). This ensures that all parameters are comparable.

∗ The single-ion anisotropy constants for $LiNi_{0.8}Fe_{0.2}PO_4$ have been shuffled compared to Ref. 74 such that they reflect the observed preferred spin direction, a.

with

$$
\begin{aligned}
A &= 4S\left(J_{bc}+J_{ab}\right) - 2S\Big(J_b\left[1-\cos\left(\mathbf{Q}\cdot\mathbf{r}_5\right)\right] + J_c\left[1-\cos\left(\mathbf{Q}\cdot\mathbf{r}_6\right)\right] \\
&\quad + J_{ac}\left[2-\cos\left(\mathbf{Q}\cdot\mathbf{r}_7\right)-\cos\left(\mathbf{Q}\cdot\mathbf{r}_8\right)\right]\Big) + (S-1/2)\left(\mathfrak{D}^a+\mathfrak{D}^b\right), \\
B &= (S-1/2)\left(\mathfrak{D}^a-\mathfrak{D}^b\right)/2, \\
C &= 2S\Big(J_{bc}\left[\cos\left(\mathbf{Q}\cdot\mathbf{r}_1\right)+\cos\left(\mathbf{Q}\cdot\mathbf{r}_2\right)\right] + J_{ab}\left[\cos\left(\mathbf{Q}\cdot\mathbf{r}_3\right)+\cos\left(\mathbf{Q}\cdot\mathbf{r}_4\right)\right]\Big),
\end{aligned}
$$

and

$$
\begin{gathered}
\mathbf{r}_{1,2} = (0, b/2, \pm c/2), \quad \mathbf{r}_{3,4} = (a/2, \pm b/2, 0), \quad \mathbf{r}_5 = (0, b, 0), \\
\mathbf{r}_6 = (0, 0, c), \quad \mathbf{r}_{7,8} = (a/2, 0, \pm c/2).
\end{gathered}
$$

This result was derived in Ref. 123. Fitting the $(H, 1, 0)$ and $(0, K, 0)$ branches simultaneously leads to the exchange and single-ion anisotropy parameters listed in Table 8.2. The model describes the measured dispersion well as seen in Fig. 8.7 where color plots of the measured spin excitations are shown together with fitted mode positions and dispersion. A second low-intensity mode predicted by Eq. (8.1) is also indicated on the plot but could not be observed in our experiment. Note that since the dispersion has not been measured along c, it is impossible to fit J_c. As this coupling is expected to be relatively weak from comparison with the other lithium orthophosphates[53–55] it is here fixed to $J_c = 0$. The parameters obtained for $LiNi_{0.94}Fe_{0.06}PO_4$ to describe the dispersion are as expected: somewhere in between the parent compound, $LiNiPO_4$, and the mixed system, $LiNi_{0.8}Fe_{0.2}PO_4$ (see the upcoming Section 8.2). The ratio between the competing nearest and next-nearest neighbor interactions, J_{bc} and J_b, is $\sim 1/2$ in all cases [see Table 8.2]. The single-ion anisotropy parameter, $\mathfrak{D}^a$, is, however, notably smaller in $LiNi_{0.94}Fe_{0.06}PO_4$ compared to $LiNiPO_4$. The relatively small energy cost for spin components along

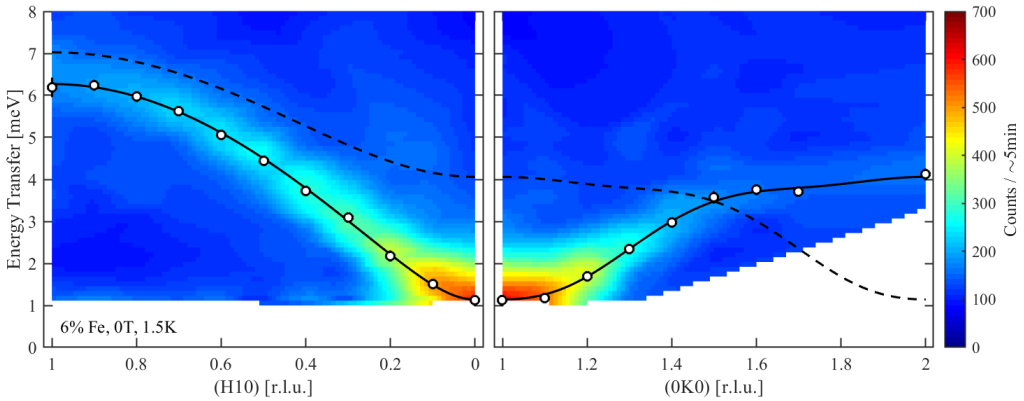

Figure 8.7: *Spin-wave dispersion along (H,1,0) and (0,K,0) for $LiNi_{0.94}Fe_{0.06}PO_4$. The color scale shows neutron counts and the circles mark fitted mode positions. The solid line shows the fitted dispersion as described in the text and with parameters given in Table 8.2. The dashed line shows a low-intensity mode which could not be detected in our experiment.*

a advocates a spin re-orientation along this direction rather than along b in the high-field phase.

To sum up, magnetization and neutron scattering experiments were performed on $LiNi_{0.94}Fe_{0.06}PO_4$ and magnetic phase diagrams as well as magnetic structures were investigated. Introducing 6% Fe on the magnetic site in $LiNiPO_4$ does not issue a massive change in the overall magnetic behavior. Thus, the easy axis is still c and the zero-field magnetic structure is of symmetry ($\uparrow\uparrow\downarrow\downarrow$). Furthermore, like in $LiNiPO_4$[48,61] an incommensurate phase exists just above the antiferromagnetic phase in a $\sim 1\,\mathrm{K}$ interval. However, where $LiNiPO_4$ displays an abrupt phase transition at 12 T along c from the commensurate low-field phase to a incommensurate spiral phase[48,61], $LiNi_{0.94}Fe_{0.06}PO_4$ has a gradual transition around $\sim 10\,\mathrm{T}$ where the commensurate unit cell persists but a spin re-orientation takes place. Spin wave measurements showed that the spin Hamiltonian of $LiNi_{0.94}Fe_{0.06}PO_4$ is very similar to that of $LiNiPO_4$ but for a lower single-ion anisotropy constant along a.

Having thus seen how 6% Fe brings only slight changes to the parent compound, $LiNiPO_4$, we now turn our attention to the system containing 20% Fe.

8.2 $LiNi_{0.8}Fe_{0.2}PO_4$

Numerous experiments were performed on samples with 20% Fe in order to understand the magnetic and magnetoelectric properties of this compound. Among the experiments are magnetization measurents, pyrocurrent measurements, diffraction with and without polarized neutrons and inelastic neutron scattering. All the results are presented in this section, and together they form a coherent picture of the magnetic structure and dynamics in $LiNi_{0.8}Fe_{0.2}PO_4$, although they also expose a number of open questions.

Magnetic phase diagrams. Magnetic phase diagrams of $LiNi_{0.8}Fe_{0.2}PO_4$ for magnetic fields applied along the three principal crystallographic directions were

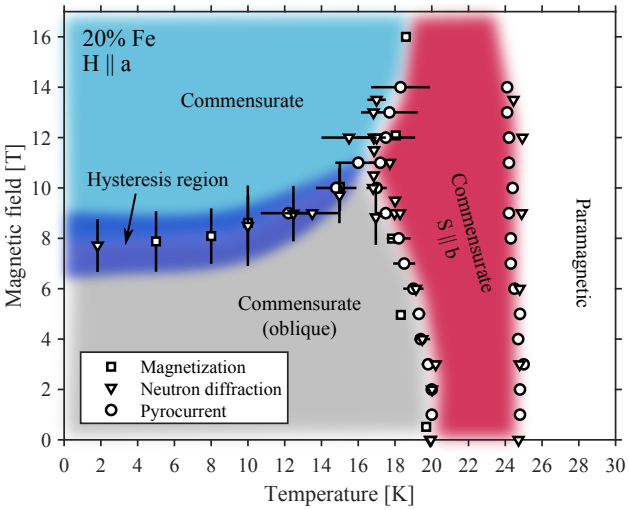

Figure 8.8: *Magnetic phase diagram of $LiNi_{0.8}Fe_{0.2}PO_4$ for magnetic fields applied along a as determined by magnetization measurements (squares), pyrocurrent measurements (circles) and neutron diffraction (triangles). The field-induced phase transition at ∼8T is broad as indicated by the dark blue region. The observed magnetic phases are all commensurate. Note the similarity to the phase diagram of $LiNi_{0.94}Fe_{0.06}PO_4$ for fields along c [Fig. 8.2].*

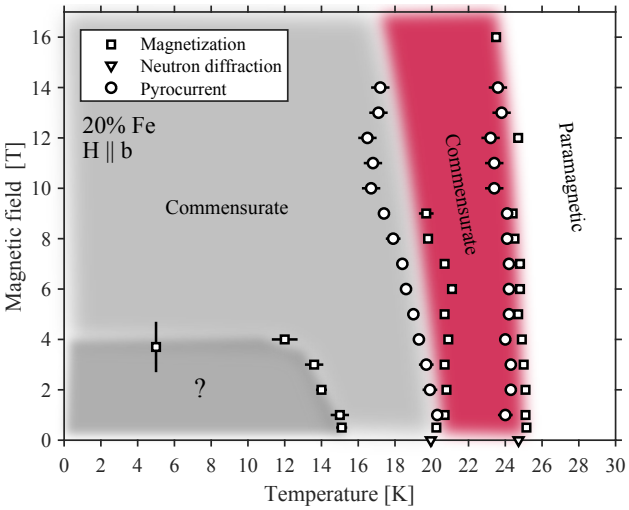

Figure 8.9: *Magnetic phase diagram of $LiNi_{0.8}Fe_{0.2}PO_4$ for magnetic fields applied along b as determined by magnetization measurements (squares) and pyrocurrent measurements (circles). Neutron data at zero field is also shown (triangles). Magnetization and pyrocurrent measurements yield slightly different transitions temperatures for the transition at ∼20K. However, it is believed to be a single transition. At low temperature and low fields, a small pocket of a phase is observed in the magnetization.*

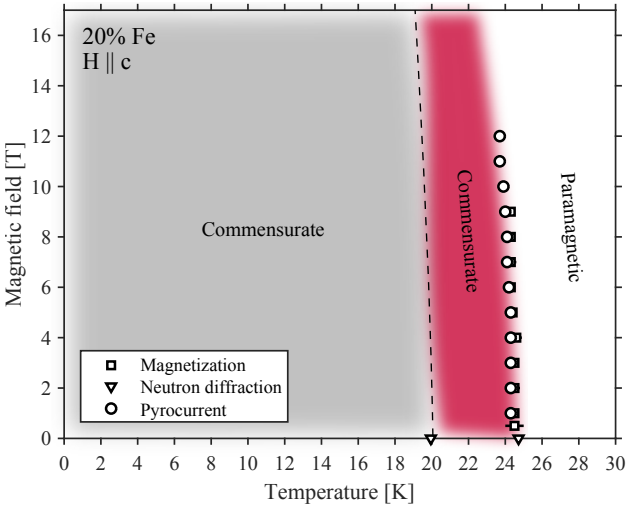

Figure 8.10: *Magnetic phase diagram of $LiNi_{0.8}Fe_{0.2}PO_4$ for magnetic fields applied along c as determined by magnetization measurements (squares) and pyrocurrent measurements (circles). Neutron data at zero field is also shown (triangles). A single phase transition as a function of temperature is observed at all probed field strengths. The conjectured second phase boundary at ∼20 K is indicated with the dashed line.*

determined – just like for the 6% Fe compound – by using magnetization measurements and neutron diffraction. In addition, pyrocurrent measurements were performed in order to investigate the magnetoelectric properties of $LiNi_{0.8}Fe_{0.2}PO_4$

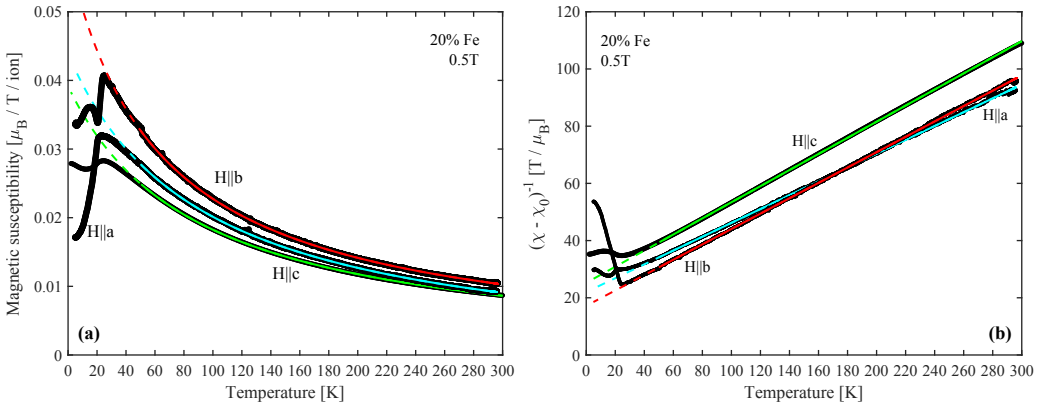

Figure 8.11: *(a) Magnetic susceptibility and (b) inverse susceptibility for $LiNi_{0.8}Fe_{0.2}PO_4$ at 0.5 T applied along the three principal crystal directions. The colored lines show fits to the Curie-Weiss law. The solid parts of the lines show the fitted interval and the dashed parts are extrapolations.*

and to see how they correlate with the various magnetic phases. Two phase transitions were observed as a function temperature at $\sim 20\,\mathrm{K}$ and $\sim 25\,\mathrm{K}$ in zero field and a broad field-induced transition was found at $\sim 8\,\mathrm{T}$ for fields applied along a [see Fig. 8.8]. For fields along b [see Fig. 8.9] the two temperature-driven transitions at ~ 20 and $\sim 25\,\mathrm{K}$ persist and a third phase is observed for $T \lesssim 15\,\mathrm{K}$ and $\mu_0 H \lesssim 4\,\mathrm{T}$. In contrast, a single phase transition as a function of temperature is found for fields applied along c [see Fig. 8.10].

VSM measurements were performed at the CFMS at DTU Risø Campus for magnetic fields up to 16 T applied along a and b and in the temperature range $5-300\,\mathrm{K}$. A Quantum Design PPMS at DTU Chemistry with a maximum field strength of 9 T and temperature range $2-300\,\mathrm{K}$ was used for measurements with fields applied along c. A box-shaped $LiNi_{0.8}Fe_{0.2}PO_4$ single crystal of 20.4 mg with facets cut perpendicular to the principal directions was aligned by eye in both setups. Facet directions were determined using X-ray Laue prior to the experiments. The temperature dependencies of the magnetic susceptibilities at 0.5 T are shown in Fig. 8.11. Fitting the curves to the Curie-Weiss law [Eq. (6.1)] yields parameters for Θ_{CW} and μ_{eff} as listed in Table 8.1.

A more detailed overview of the behavior of the magnetization as a function of temperature and field is given in Fig. 8.12. It is clear that the easy direction is along a since here the magnetization drops below the transition temperature [see Fig. 8.12(a)]. At a first glance, this is somewhat surprising since earlier investigatings based on optical SHG[73] pointed towards ordering of spins in the (b, c)-plane. Naïvely, such ordering is expected[79] since the easy directions for the parent compounds, $LiNiPO_4$ and $LiFePO_4$, are c and b respectively[42,43]. However, our data indicates that the system actually settles on a different option: the a-direction. Allowing for a moment of reverie, this choice is not too surprising since $LiNiPO_4$ and $LiFePO_4$ have hard axes b and c respectively – i.e. the parent compounds have opposite easy and hard axes. Therefore, the a-axis is a sound compromise. Finally, a broad field-induced phase transition is observed at around $\sim 8\,\mathrm{T}$, stretching over $\sim 2\,\mathrm{T}$ [see Fig. 8.12(b)]. More will be said about this transition later.

The temperature dependence of the magnetization for fields along b displays two

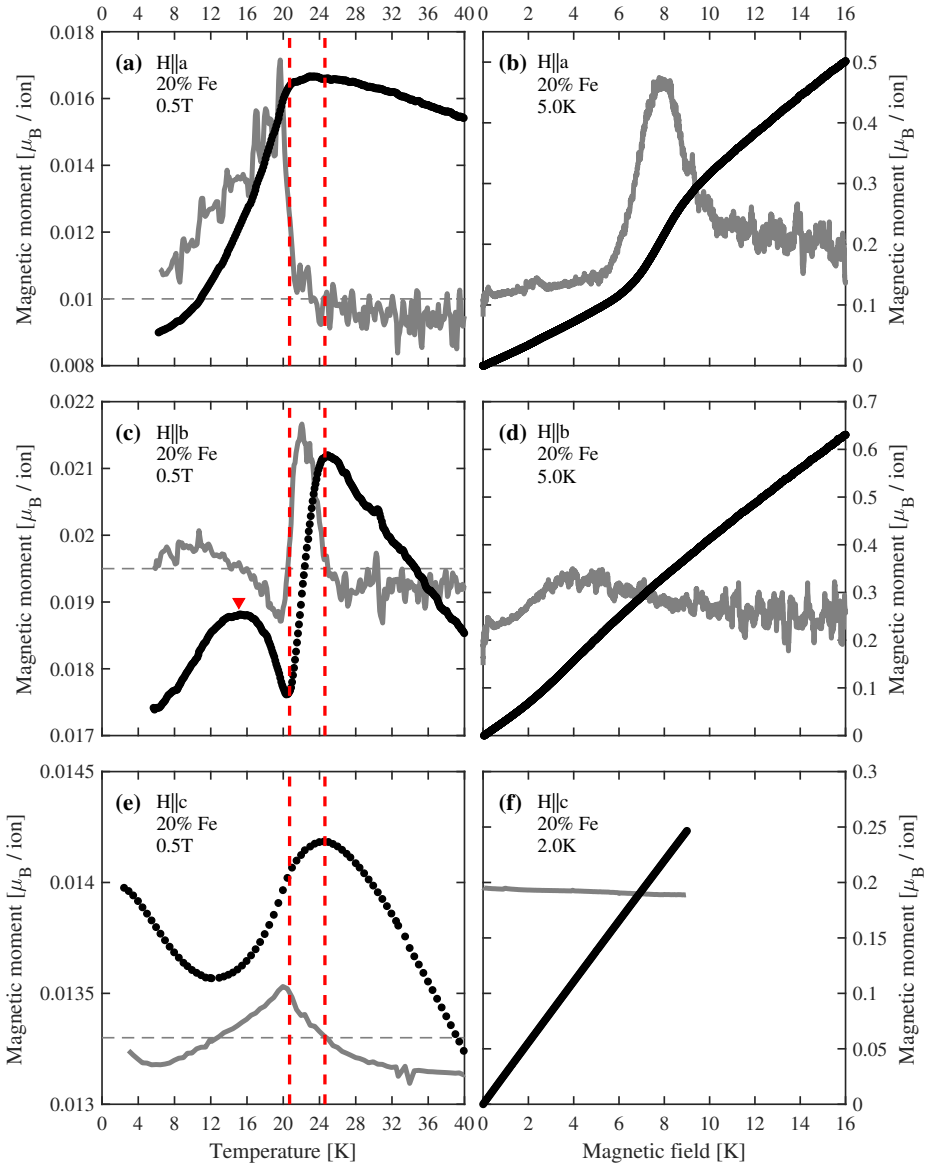

Figure 8.12: *Magnetization as a function of decreasing temperature (left panels) and as a function of increasing magnetic field (right panels) for $LiNi_{0.8}Fe_{0.2}PO_4$. Derivatives, $\frac{dM}{dT}$ and $\frac{dM}{dH}$, are shown with the grey curves in the background (a.u.). Zero slope is marked with grey horizontal dashed lines in the lefthand panels and coincides with zero magnetization in the righthand panels. $T_{N1} = 24.6\,K$ and $T_{N2} = 20.7\,K$ are indicated with the red vertical dashed lines. The additional transition at 15.1 K in (c) is indicated with the red triangle. Note that the CFMS measurements (a)-(d) are noisier than the PPMS measurements (e)-(f).*

transitions at ~ 25 and $\sim 20\,\mathrm{K}$ and possibly a third one at $\sim 15\,\mathrm{K}$ for low fields [see Fig. 8.12(c)]. The transition around 20 K corresponds well with the transition for fields along a. The magnetization as a function of magnetic field displays an almost linear behavior, however, around 4 T there is a slight increase in the slope indicating a very subtle field-induced phase transition [see Fig. 8.12(d)].

For fields along c [Figs. 8.12(e) and (f)] a single transition is observed around 25 K, corresponding to the first transition seen for fields along b. The field dependency

of the magnetization up to 9 T is linear and displays no transitions.

Magnetoelectric effect. The magnetoelectric properties of $LiNi_{0.8}Fe_{0.2}PO_4$ were characterized by pyrocurrent measurements. Technical details of the setup were described in Section 4.1 but a few key points are repeated here. A special-built insert enabled application of an electric field and measurement of a current across the sample. Plate-like samples were cut with faces perpendicular to a and b and with areas 2.7×1.1 and $2 \times 1\,mm^2$ and thicknesses 0.5 and 0.9 mm respectively. The faces were polished and gold sputtered in order to obtain good contact with the electrodes. The samples were field-cooled at the desired magnetic field strength and with 100 V applied to ensure formation of a single domain for the electric polarization. After cooling the sample to base temperature, the voltage was switched off. The pyrocurrent was then recorded in the range $4 - 40$ K while heating with constant temperature ramp rate and a fixed magnetic field of up to 14 T. The electric polarization is proportional the accummulated current [see Eq. (4.1)].

Six different magnetoelectric tensor elements, α_{ij}, were probed by applying magnetic fields along the different principal crystal directions of the two samples with **E**||**a** and **E**||**b** respectively. The probed elements are α_{aa}, α_{ab}, α_{ac}, α_{ba}, α_{bb} and α_{bc} [see Section 1.2], and their behavior as a function of temperature and field exhibits an enormous complexity. In order to gain an overview, examples of background subtracted pyrocurrent and calculated electric polarization as a function of temperature at 2 T are shown together with magnetization data in Fig. 8.13 (for details about background subtraction, see Appendix C). Data at 2 T was chosen because here the pyrocurrent signal is relatively strong compared to at lower field

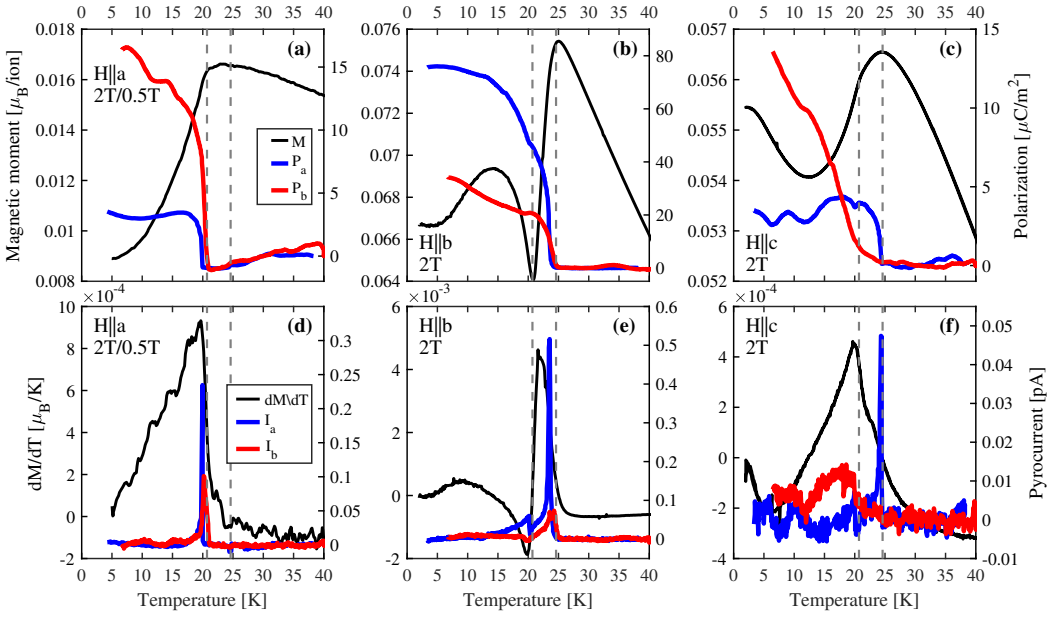

Figure 8.13: *The magnetization plotted together with the electric polarization (a)-(c) and the temperature-derivative of the magnetization plotted together with the pyrocurrent (d)-(f) as a function of temperature at 2 T. Curves for electric fields applied both along a (blue) and along b (red) are shown. Vertical dashed lines mark the transitions at ∼20 and ∼25 K. Note that the magnetization for* **H**||**a** *was not recorded at 2 T so here the dataset for 0.5 T is shown. Note also the different scales on the vertical axes.*

strengths. The pyrocurrent displays sharp peaks at $\sim 20\,\mathrm{K}$ and/or $\sim 25\,\mathrm{K}$ for all probed magnetic and electric field directions. Since the electric polarization is obtained by integrating the pyrocurrent [Eq. (4.1)], the polarization becomes non-zero at $\sim 20\,\mathrm{K}$ and/or $\sim 25\,\mathrm{K}$ correspondingly. In general, the pyrocurrent signal for $\mathbf{H}||\mathbf{c}$ is weak compared to that for $\mathbf{H}||\mathbf{a}$ and $\mathbf{H}||\mathbf{b}$. It should also be mentioned that there is no signal for any of the probed tensor elements at zero field and hence $LiNi_{0.8}Fe_{0.2}PO_4$ should indeed be termed *magnetoelectric* rather than *ferroelectric*. The elements α_{ab}, α_{bb} and α_{ac} have an onset at $\sim 25\,\mathrm{K}$ whereas the elements α_{aa} and α_{ba} have an onset at $\sim 20\,\mathrm{K}$. These temperatures correspond well with the transitions observed in the magnetization. The last element, α_{bc}, too has an onset at $\sim 20\,\mathrm{K}$ but the corresponding pyrocurrent signal displays no sharp peak at the transition.

Figures 8.14 and 8.15 show the pyrocurrent and electric polarization, respectively, for selected field values. The relative magnitudes of the probed magnetoelectric tensor elements vary with e.g. $P_a \approx 75\,\mu\mathrm{C/m^2}$ for $\mathbf{H}||\mathbf{b}$ at $2\,\mathrm{T}$ or $P_b \approx 220\,\mu\mathrm{C/m^2}$ for $\mathbf{H}||\mathbf{b}$ at $9\,\mathrm{T}$. In both cases, the this is remarkably large compared to the parent compounds, $LiNiPO_4$ and $LiFePO_4$ with maximum polarizations $P_{\max} \approx 3\,\mu\mathrm{C/m^2}$ [49] and $P_{\max} \approx 8\,\mu\mathrm{C/m^2}$ [39] at $2\,\mathrm{T}$ respectively. Even $LiCoPO_4$ with the largest magnetoelectric response in the lithium orthophosphate family only musters $P_{\max} \approx 60\,\mu\mathrm{C/m^2}$ [51] at $2\,\mathrm{T}$. The magnetoelectric effect in $LiNi_{0.8}Fe_{0.2}PO_4$ thus appears stronger than in the stoichiometric compounds. Admitttedly, the explanation might be found in an error in the conversion from pyrocurrent to electric polarization (to be double checked imminently). Similar measurement should be performed on e.g. $LiNiPO_4$ for direct comparison before too much excitement is stirred. Regardless of the absolute magnitude of the polarization more detailed descriptions of the observed pyrocurrent curves follow below.

$\mathbf{E}||\mathbf{a}$, $\mathbf{H}||\mathbf{a}$: for fields below $8\,\mathrm{T}$ there is a peak in the pyrocurrent at $\sim 20\,\mathrm{K}$. A smaller peak is seen at $\sim 25\,\mathrm{K}$ from around $4\,\mathrm{T}$ and up. As the field is increased a second less intense and broader peak develops at lower temperatures. The intensities of the sharp peak at $\sim 20\,\mathrm{K}$ as well the broader peak at lower temperatures decrease as the magnetic field increases. The opposite is true for the smaller peak at $\sim 25\,\mathrm{K}$. The magnitude of the polarization has a maximum around $9\,\mathrm{T}$, corresponding to field-induced transition seen in the magnetization [Fig. 8.12(b)]. Interestingly, the magnetoelectric effect is present in both phases and is strongest at the transition.

$\mathbf{E}||\mathbf{a}$, $\mathbf{H}||\mathbf{b}$: for $1-5\,\mathrm{T}$ there are two peaks in the pyrocurrent: a sharp, intense one at $\sim 25\,\mathrm{K}$ and a broad, weaker one at $\sim 20\,\mathrm{K}$. The sharp peak moves towards lower temperatures as the field increases and at $6-8\,\mathrm{T}$ there is only a single sharp peak at $21\,\mathrm{K}$. At $9-11\,\mathrm{T}$, there are again two peaks but now they are very close to each other, i.e. about $0.1\,\mathrm{K}$ apart, and the one at higher temperature is negative. The negative peak is 5-7 times more intense than the positive peak. Only the positive peak remains for fields larger than $11\,\mathrm{T}$. The polarization is at a maximum around $4\,\mathrm{T}$, possibly corresponding to the very subtle field-induced transition observed in the magnetization [*cf.* Fig. 8.12(d)]. The behavior of the pyrocurrent for this electric and magnetic field orientation is the most complicated of the measured orientations.

$\mathbf{E}||\mathbf{a}$, $\mathbf{H}||\mathbf{c}$: for all fields above $1\,\mathrm{T}$ two peaks at $\sim 20\,\mathrm{K}$ and $\sim 25\,\mathrm{K}$ are observed in

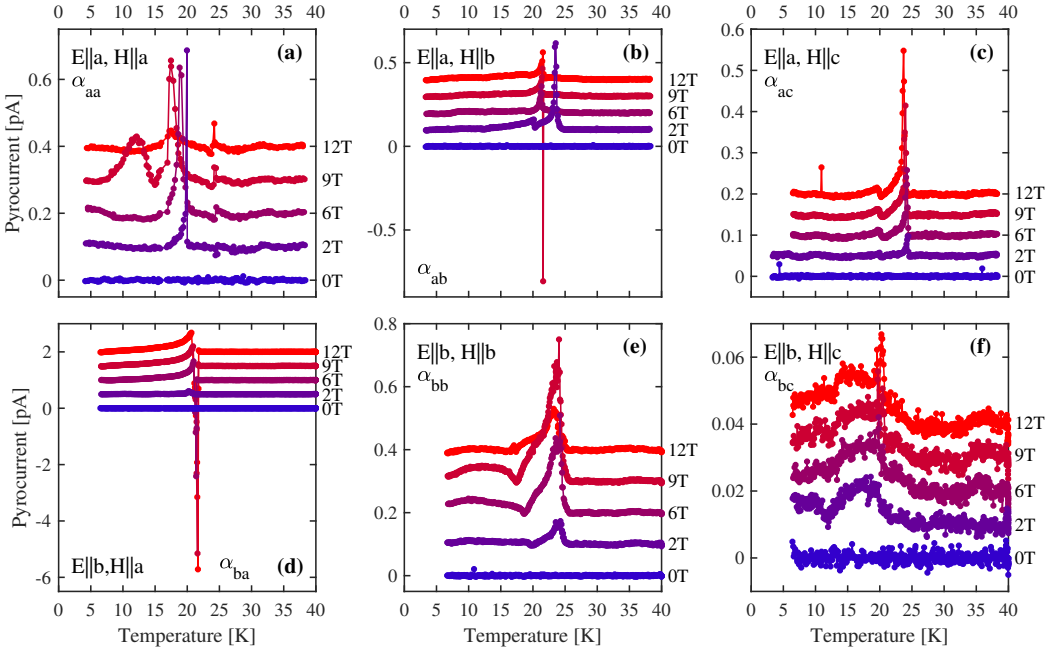

Figure 8.14: *Pyrocurrent as a function of temperature for selected field values. The curves are offset with 0.1,0.1,0.05,0.5,0.1,0.01 pA starting from top left to bottom right. Background has been subtracted as described in Appendix C. The probed magnetoelectric tensor element is given in each plot.*

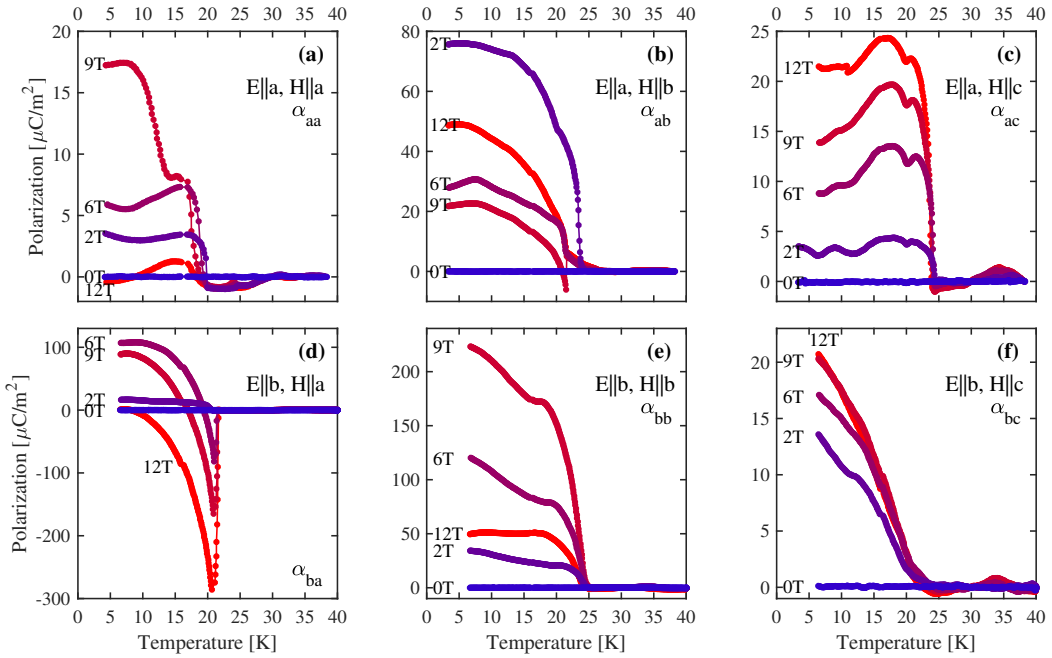

Figure 8.15: *Electric polarization as a function of temperature for selected field values corresponding to Fig. 8.14.*

the pyrocurrent. Their positions are field-independent.

E||b, H||a: for fields below and at 4 T there is a sharp peak in the pyrocurrent at $\sim$ 20 K. It moves slightly towards higher temperatures and gets more intense

as the magnetic field is increased. For fields above 4 T, a second, negative peak appears towards higher temperatures compared to the first peak. The magnitude of the negative peak is up to 10 times larger than the positive peak.

E||**b**, **H**||**b**: a broad peak with a shoulder on the low-temperature side is observed in the pyrocurrent around ~ 25 K for all fields. A second, very broad bump exists at lower temperatures.

E||**b**, **H**||**c**: the pyrocurrent signal for this configuration is very weak – 1-2 orders of magnitude weaker compared to all other orientations. Nevertheless, some broad feature is observed around ~ 20 K.

As already mentioned, the magnitude of the pyrocurrent for magnetic fields applied along c is noticeably smaller than for the other field directions. This is most likely due to leak signals from having small magnetic field components along b and a for the **E**||**a** and **E**||**b** measurements respectively. It was previously pointed out in Sestion 4.1 that such field misalignment would be more likely for fields along c due to the shape of the samples used for the measurement. Indeed, the observed weak signal for **E**||**a**, **H**||**c** has a similar temperature dependence as the low-field signal for **E**||**a**, **H**||**b** [compare curves in Fig. 8.14(c) with the 2 T data in Fig. 8.14(b)]. A similar argument can be made for the weak signal for **E**||**b**, **H**||**c** [compare curves in Fig. 8.14(f) with the 2 T data in Fig. 8.14(d)]. Hence, it is postulated that the magnetoelectric tensor elements, α_{ac} and α_{bc}, are in fact zero.

Evidently, the behavior of the magnetoelectric effect in $LiNi_{0.8}Fe_{0.2}PO_4$ as a function of magnetic field and temperature is extremely complex. Interestingly, the system still displays the effect and has more active magnetoelectric tensor elements than the parent compounds, $LiNiPO_4$ ($\alpha_{ac}, \alpha_{ca} \neq 0$) and $LiFePO_4$ ($\alpha_{ab}, \alpha_{ba} \neq 0$). The magnetoelectric tensors for the two zero-field phases in $LiNi_{0.8}Fe_{0.2}PO_4$ look as follows:

$$\alpha = \begin{pmatrix} \cdot & \bullet & \cdot \\ \cdot & \bullet & \cdot \end{pmatrix} \text{ for } T_{N2} < T < T_{N1} \qquad \text{and} \qquad \alpha = \begin{pmatrix} \bullet & \bullet & \cdot \\ \bullet & \bullet & \cdot \end{pmatrix} \text{ for } T < T_{N2}. \tag{8.3}$$

Large dots denote non-zero elements and small dots denote vanishing elements. The bottom row of the matrix was not probed and is shown empty. The magnetoelectric effect in $LiNi_{0.8}Fe_{0.2}PO_4$ is left here for now. However, the magnetoelectric tensor forms prove an important ingredient in the following where the zero-field magnetic structures are determined.

Zero-field magnetic structures. Magnetic structures of $LiNi_{0.8}Fe_{0.2}PO_4$ at zero field and for magnetic fields applied along a were investigated using neutron diffraction. The somewhat surprising and complex structures lead to several experiments using the following instruments: RITA-II and EIGER at the PSI, E5 and E4 at the HZB and 4F1 at the Laboratoire Léon Brillouin. Brief descriptions of each experiment follow below. Temperature and field dependencies of selected magnetic Bragg peaks yield the phase boundaries in Fig. 8.8. Results from individual experiments are presented here and then related to the magnetization and pyrocurrent data.

Neutrons with energies 5 and 13.7 meV (wavelengths 4.04 and 2.44 Å, respectively) were used at the triple-axis spectrometer RITA-II which was run in elastic mode. A nitrogen cooled Be filter placed after the sample and a PG filter placed before the sample, respectively, were used for the two different neutron energies to ensure no second order contamination of the beam. Collimation of 80' was employed between

monochromator and sample. The sample was a $LiNi_{0.8}Fe_{0.2}PO_4$ single crystal of mass 250.8 mg. It was oriented with $(0, K, L)$ in the scattering plane and vertical magnetic fields up to 12 T were applied along the a-axis. A series of magnetic Bragg peaks were collected at (35 K, 0 T), (1.6 K, 0 T) and (1.6 K, 12 T) as well as temperature and field-dependencies of selected Bragg peaks.

The zero-field magnetic structure was not entirely clear after having performed the experiment at RITA-II so another one was carried out at the triple-axis spectrometer EIGER – also in elastic mode. Neutrons with energy 14.7 meV (wavelength 2.36 Å) were used together with a collimation of 20' on the incoming beam and 40' on the outgoing beam, a PG filter before the sample and 2 cm horizontal slits before and after the sample. The same sample as used in the RITA-II experiment was used here too, but now oriented with $(H, K, 0)$ in the scattering plane. A number of magnetic Bragg peaks were collected at (35 K, 0 T) and (1.6 K, 0 T).

Temperature dependencies at zero field of a number of magnetic Bragg peaks were measured at the two-axis diffractometer E5. The neutron wavelength was 2.38 Å, second-order neutrons were suppressed using a PG filter and a 2D detector recorded scattered neutrons. An Euler cradle gave access to a large fraction of reciprocal space. The sample was the same high-quality single crystal used at RITA-II and EIGER.

Yet another neutron diffraction experiment was performed at the two-axis diffractometer E4. Here a number of key Bragg peaks were followed as a function of temperature like at E5 – except in this experiment a vertical cryo-magnet delivered magnetic fields up to 13.5 T along a. The phase boundaries at ~ 20 K and ~ 25 K were tracked as a function of applied magnetic field. The 250.8 mg sample was oriented with $(0, K, L)$ in the horizontal scattering plane. The instrument setup was similar to that at E4 with wavelength 2.406 Å, PG filter and a 2D detector.

The efforts at RITA-II and EIGER proved inadequate for an unambigious determination of the zero-field structures in $LiNi_{0.8}Fe_{0.2}PO_4$. Therefore, a polarized neutron diffraction experiment was performed in order to decompose spin components in the temperature interval $\sim 20 - 25$ K as well as below ~ 20 K. The experiment was carried out at the triple-axis spectrometer 4F1 with the 250.8 mg single crystal oriented in the $(0, K, L)$ scattering plane and incoming and outgoing energy 13.7 meV (wavelength 2.44 Å). Open collimation was employed and a bending mirror ensured polarization of the neutron beam before the sample. Flippers were placed before and after the sample and a Heusler analyzer allowed for distinguishing between "up" or "down" polarized neutrons. A Helmholtz coil at the sample position delivered magnetic fields (~ 10 G) sufficient to polarize the neutron beam along x, y or z [instrument coordinates following Moon et al.[37]]. A PG filter was placed after the bender and before the sample.

Rocking curves of a selection of Bragg peaks collected at (35 K, 0 T) and (1.6 K, 0 T) at RITA-II are shown in Fig. 8.16. Table 8.3 lists magnetic structure factors for the relevant peaks. The strong magnetic peaks $(0, 1, 0)$ and $(0, 1, 2)$ show that an $(\uparrow\uparrow\downarrow\downarrow)$ symmetry component is present. The peaks $(0, 0, 1)$ and $(0, 2, 1)$ are much weaker and it is possible that they, too, signify the $(\uparrow\uparrow\downarrow\downarrow)$ spin component. Alternatively, they might originate in an $(\uparrow\downarrow\uparrow\downarrow)$ component. The peak $(0, 1, 1)$ does not display magnetic intensity and hence any spin components of symmetry $(\uparrow\downarrow\downarrow\uparrow)$

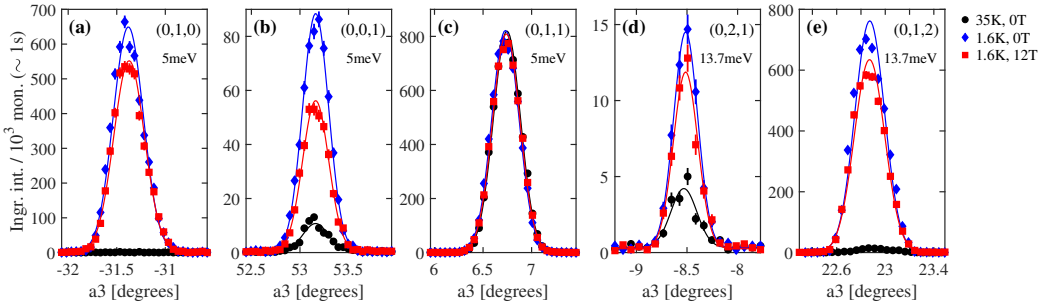

Figure 8.16: *Rocking curves of selected Bragg peaks as measured on $LiNi_{0.8}Fe_{0.2}PO_4$ at RITA-II. Data is recorded at (35 K, 0 T) [black circles], (1.6 K, 0 T) [blue diamonds] and (1.6 K, 12 T) [red squares]. Note that measurements performed with both 5 meV and 13.7 meV neutrons are shown. The data measured with 13.7 meV neutrons is multiplied by 3.2, a scaling factor extracted from 5 peaks measured at both energies.*

Table 8.3: *Absolute squares of structure and spin polarization factors for the magnetic basis vectors reflected by selected magnetic Bragg peaks observed in the RITA-II, EIGER, E5, E4 and 4F1 experiments. Factors are normalized to unit spin lengths.*

	$\lvert S(\mathbf{Q})\rvert^2$				$\lvert P_i(\mathbf{Q})\rvert^2$		
(H,K,L)	A	G	C	F	x	y	z
	$(\uparrow\downarrow\downarrow\uparrow)$	$(\uparrow\downarrow\uparrow\downarrow)$	$(\uparrow\uparrow\downarrow\downarrow)$	$(\uparrow\uparrow\uparrow\uparrow)$	a	b	c
$(0,1,0)$	0	0	16	0	1	0	1
$(0,0,1)$	0	15.78	0.22		1	1	0
$(0,1,1)$	15.78	0	0	0.22	1	0.61	0.39
$(0,2,1)$	0	15.78	0.22	0	1	0.28	0.72
$(0,1,2)$	0	0.88	15.12	0	1	0.86	0.14
$(6,0,0)$	0	0	10.17	5.83	0	1	1
$(3,0,1)$	0.04	0.18	12.65	3.13	0.34	1	0.66
$(0,2,0)$	0	0	0	16	1	0	1

can be ruled out.

The main symmetry component is then $(\uparrow\uparrow\downarrow\downarrow)$ but data from the RITA-II experiment did not allow for an unambigious determination of the spin direction. Therefore, an experiment was performed on EIGER with the $LiNi_{0.8}Fe_{0.2}PO_4$ sample oriented in a different scattering plane such that the $(6,0,0)$ Bragg peak could be reached. However, since this peak also has nuclear intensity it proved difficult to determine whether it had any additional magnetic intensity at (1.6 K, 0 T). Hence, the spin direction in the low-temperature zero-field phase could not be determined by unpolarized neutron diffraction alone. After having a look at results from the E5 and E4 experiments we shall return to this issue.

The magnetic phase existing between 20 and 25 K was observed in both the magnetization and pyrocurrent data as well as at neutron diffraction experiments at E5 and E4. Temperature scans of three different magnetic Bragg peaks representing different spin symmetries are plotted in Fig. 8.17. The peak $(0,1,0)$ follows a regular power law whereas $(0,0,\bar{1})$ displays linear behavior and $(3,0,\bar{1})$ appears to exhibit two phase transitions. All measured peaks (8 in total) were fitted to the

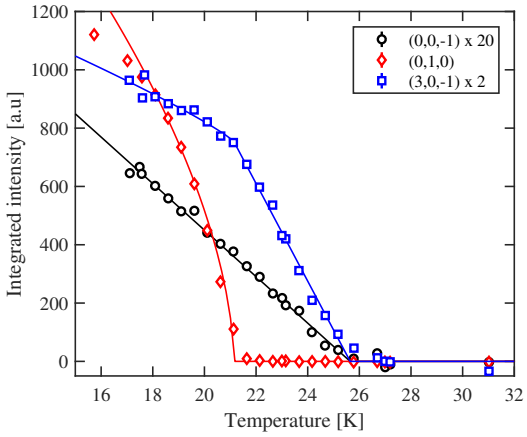

Figure 8.17: *Neutron intensity of (0,0,$\bar{1}$), (0,1,0) and (3,0,$\bar{1}$) as a function of increasing temperature as measured on $LiNi_{0.8}Fe_{0.2}PO_4$ at E5. The intensities are corrected for the Lorentz factor and the solid lines show fits as discussed in the text.*

following function consisting of a linear and a power law function:

$$I = \begin{cases} 0 & \text{for} \quad T > T_{N1} \\ A\ (T - T_{N1}) + C & \text{for} \quad T_{N2} < T \leq T_{N1} \\ B\ (T - T_{N2})^{\beta} + A\ (T_{N2} - T_{N1}) + C & \text{for} \quad T \leq T_{N2} \end{cases}$$

Here, A and B are scaling constants, β the power exponenta and C the background level. T_{N1} and T_{N2} are the transition temperatures with $T_{N2} \leq T_{N1}$. For each dataset, the parameters A, B, β and C are allowed to vary independently whereas T_{N1} and T_{N2} are fitted simulateneously across all dataset. The resulting fits are shown in Fig. 8.17 and describe the data well. Transition temperatures of $T_{N1} = 25.6(2)\,\mathrm{K}$ and $T_{N2} = 20.8(1)\,\mathrm{K}$ were obtained.

Based on the observed magnetic Bragg peaks, the main magnetic structure component in the temperature interval $T_{N1} < T < T_{N2}$ is most likely of ($\uparrow\uparrow\downarrow\downarrow$) symmetry with spins polarized along b. However, like for the the low-temperature zero-field phase discussed above, the spin direction could not be unambigiously determined. Therefore, a polarized neutron diffraction experiment was performed at 4F1. Here, individual spin components may be separately probed and finally, it was possible to determine the spin orientation in the two zero-field phases of $LiNi_{0.8}Fe_{0.2}PO_4$.

The basics for analyzing a polarized neutron experiment were outlined in Section 2.5 but a few key points are repeated here. The coordinate system is defined such that $\mathbf{x}||\mathbf{Q}$ and $\mathbf{y} \perp \mathbf{Q}$ are in the scattering plane and $\mathbf{z} \perp \mathbf{Q}$ is vertical. Generally, only spin components perpendicular to $\mathbf{Q}$ are visible and polarizing the incoming beam as well as probing the spin-polarization of the outgoing beam yields additional information. The non-spin-flip (NSF) channel is sensitive to $\mathbf{S} \perp \mathbf{P}$ and the spin-flip (SF) channel is sensitive to $\mathbf{S}||\mathbf{P}$, where $\mathbf{P}$ is the polarization direction along x, y or z. Note this is not necessarily along a crystallographic direction, i.e. in general $\mathbf{x} \nparallel \mathbf{a}$, $\mathbf{y} \nparallel \mathbf{b}$ and $\mathbf{z} \nparallel \mathbf{c}$, but depend on the chosen scattering vector, $\mathbf{Q}$.

Once positioned on a certain Bragg peak, 6 cross sections ($\mathbf{P}||\mathbf{x}, \mathbf{y}, \mathbf{z}$ and NSF as well as SF) were measured as a function of temperature in one go. All scans were performed upon cooling, i.e. $40 \rightarrow 4\,\mathrm{K}$, and the intensities of three key peaks – $(0, 1, 0)$, $(0, 0, 1)$ and $(0, 1, 2)$ – were collected. All three peaks represent an ($\uparrow\uparrow\downarrow\downarrow$) spin arrangement [Table 8.3] and the polarized neutrons then merely pinpoint the spin orientation. The probed spin components are listed in Table 8.4 and the temperature dependencies of the neutron intensities of said three peaks are shown

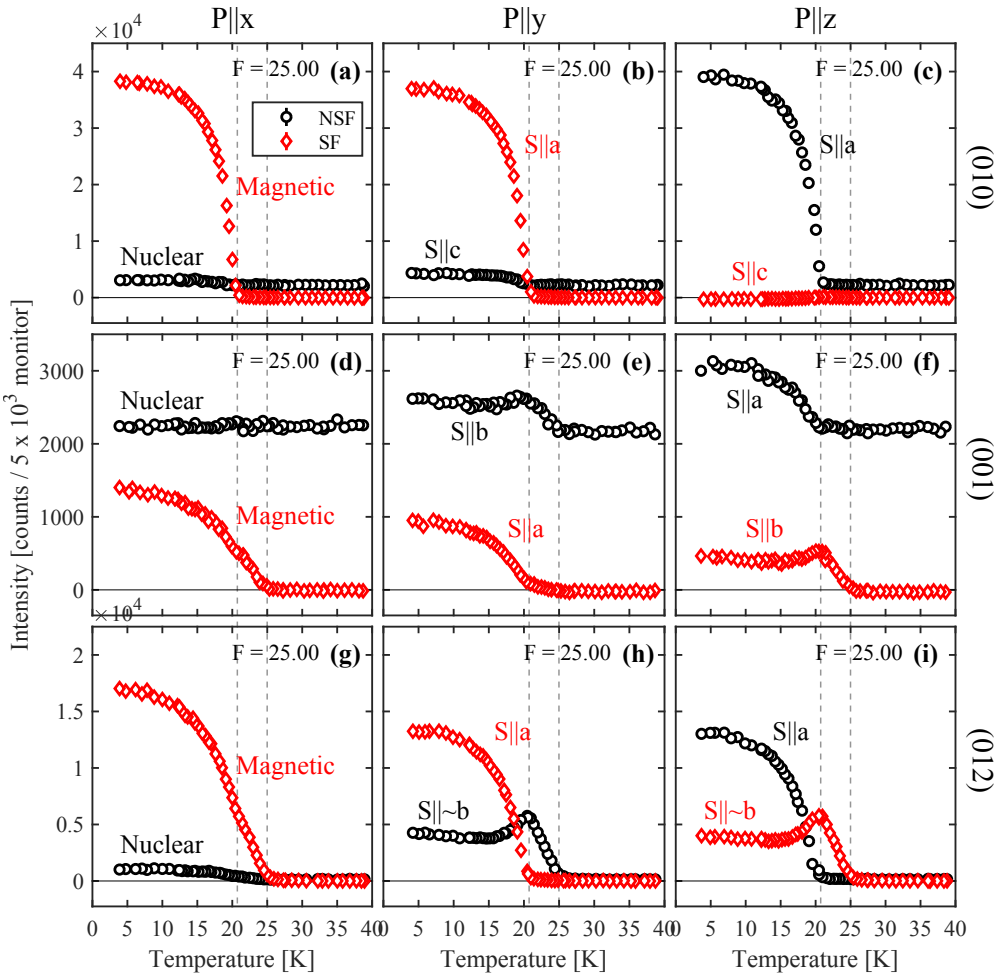

Figure 8.18: *Temperature scans of the peak intensity of (a)-(c) (0,1,0), (d)-(f) (0,0,1) and (g)-(i) (0,1,2) as measured on $LiNi_{0.8}Fe_{0.2}PO_4$ at 4F1. Bragg peaks are also listed to the right of each row. Three spin polarizations were recorded:* $\mathbf{P}||\mathbf{x}$, $\mathbf{P}||\mathbf{y}$ *and* $\mathbf{P}||\mathbf{z}$ *shown in the top of the plots. Both the NSF channel (black circles) and SF channel (red diamonds) are shown. Corrections for a flipping ratio of $F = 25$ were applied according to Eqs. (2.3). Vertical dashed lines indicate the transitions at $T_{N1} \approx 25\,K$ and $T_{N2} \approx 20\,K$.*

in Fig. 8.18. Data was corrected for a flipping ratio of $F = 25$ using Eqs. (2.3).

Data in the top row of Fig. 8.18 shows the results for $(0, 1, 0)$. For $\mathbf{P}||\mathbf{x}$ there is a large signal in the SF channel with onset at $\sim 20\,\mathrm{K}$, i.e. at T_{N2}. The weak temperature-dependent signal in the NSF channel is most likely due to an insufficient flipping ratio correction. Alternatively, a small change in the lattice parameter, b, may accompany the magnetic phase transition at T_{N2}. The signals for $\mathbf{P}||\mathbf{y}$ SF and $\mathbf{P}||\mathbf{z}$ NSF signify a spin component along $\hat{\mathbf{S}}_z = \hat{\mathbf{a}}$.

$\mathbf{Q}$	$\hat{\mathbf{S}}_z$	$\hat{\mathbf{S}}_y$
$(0, 1, 0)$	$\hat{\mathbf{a}}$	$\hat{\mathbf{c}}$
$(0, 0, 1)$	$\hat{\mathbf{a}}$	$\hat{\mathbf{b}}$
$(0, 1, 2)$	$\hat{\mathbf{a}}$	$0.93\,\hat{\mathbf{b}} + 0.37\,\hat{\mathbf{c}}$

Table 8.4: *Probed spin components for the different scattering vectors, $\mathbf{Q}$, measured at 4F1.*

The middle panels of Fig. 8.18 show the intensities collected as a function of temperature for $(0, 0, 1)$. Here, as expected, there is no temperature dependence for the nuclear signal for $\mathbf{P}||\mathbf{x}$ NSF. The recorded intensities for $\mathbf{P}||\mathbf{y}$ NSF and $\mathbf{P}||\mathbf{z}$ SF essentially show the same thing: an onset of magnetic order along $\hat{\mathbf{S}}_y = \hat{\mathbf{b}}$ at T_{N1} and then a dip in the order parameter at T_{N2}. Note that the intensity does not go to zero and hence this component still exists below T_{N2}. Likewise, $\mathbf{P}||\mathbf{y}$ SF and $\mathbf{P}||\mathbf{z}$ NSF reflect the spin component along $\hat{\mathbf{S}}_z = \hat{\mathbf{a}}$ and show an onset at T_{N2} only. Thus, in the interval $T_{N2} - T_{N1}$ the spins align along b and below T_{N2} they align in the (a, b)-plane.

The results of the measurements of the last peak, $(0, 1, 2)$, are shown in the bottom row of Fig. 8.18. These results are slightly more tricky to interpret since now the $\hat{\mathbf{S}}_y$ component is no longer along a single crystallographic axis [*cf.* Table 8.4]. However, the trends are very much like those for $(0, 0, 1)$: the $\hat{\mathbf{S}}_y$ component increases below T_{N1} and then has a dip at T_{N2} but does not go to zero. The $\hat{\mathbf{S}}_z$ component has a single onset at T_{N2} and this component is about 2.5-3 times stronger than $\hat{\mathbf{S}}_y$ at the lowest probed temperature. From Table 8.4 it is seen that $\hat{\mathbf{S}}_y = 0.93\,\hat{\mathbf{b}} + 0.37\,\hat{\mathbf{c}}$, i.e. $\hat{\mathbf{S}}_y$ represents spin components mostly along b, but also c. Hence, it is possible that for $T_{N2} - T_{N1}$ the spins are oriented in the (b, c)-plane and below T_{N2} the spins have components along all three crystallographic directions. Note that again it is believed that the temperature dependence of the $\mathbf{P}||\mathbf{x}$ NSF intensity is due to an insufficient flipping ratio correction rather than a structural phase transition.

The above results for the magnetic structures in the low-temperature and intermediate-temperature phases are consistent with all our previous neutron diffraction and magnetization measurements. Moreover, the measured magnetoelectric tensors hold important clues about the magnetic symmetry which may be related to the 4F1 results. The magnetoelectric tensors obtained for the two zero-field phases have the forms shown in Eq. (8.3) and are repeated here:

$$\alpha = \begin{pmatrix} \cdot & \bullet & \cdot \\ \cdot & \bullet & \cdot \end{pmatrix} \text{ for } T_{N2} < T < T_{N1} \qquad \text{and} \qquad \alpha = \begin{pmatrix} \bullet & \bullet & \cdot \\ \bullet & \bullet & \cdot \end{pmatrix} \text{ for } T < T_{N2}.$$

Comparing these tensors with those listed in Table 8.5 allows for determination of

Table 8.5: *Magnetic point groups and linear magnetoelectric tensor forms for spin arrangements of symmetry (↑↑↓↓). Large dots denote finite tensor elements whereas small dots denote prohibited elements. Tensor forms are found in e.g. Ref. 7 or 124.*

Spin orientation	Magnetic point group	Magnetoelectric tensor
a	$m'm'm'$	$\begin{pmatrix} \bullet & \cdot & \cdot \\ \cdot & \bullet & \cdot \\ \cdot & \cdot & \bullet \end{pmatrix}$
b	mmm'	$\begin{pmatrix} \cdot & \bullet & \cdot \\ \bullet & \cdot & \cdot \\ \cdot & \cdot & \cdot \end{pmatrix}$
c	$mm'm$	$\begin{pmatrix} \cdot & \cdot & \bullet \\ \cdot & \cdot & \cdot \\ \bullet & \cdot & \cdot \end{pmatrix}$
(a, b)-plane	$2_z/m'_z$	$\begin{pmatrix} \bullet & \bullet & \cdot \\ \bullet & \bullet & \cdot \\ \cdot & \cdot & \bullet \end{pmatrix}$
(b, c)-plane	$2'_x/m_x$	$\begin{pmatrix} \cdot & \bullet & \bullet \\ \bullet & \cdot & \cdot \\ \bullet & \cdot & \cdot \end{pmatrix}$
(a, c)-plane	$2_y/m'_y$	$\begin{pmatrix} \bullet & \cdot & \bullet \\ \cdot & \bullet & \cdot \\ \bullet & \cdot & \bullet \end{pmatrix}$
(a, b, c)	$1'$	$\begin{pmatrix} \bullet & \bullet & \bullet \\ \bullet & \bullet & \bullet \\ \bullet & \bullet & \bullet \end{pmatrix}$

the magnetic point group and spin orientation for the two respective phases. In the low-temperature phase, the finite elements correspond to the magnetic point group $2_z/m'_z$ with allowed spin components in the (a, b)-plane. This agrees outstandingly well with the results of the 4F1 experiment and rejects any $(\uparrow\uparrow\downarrow\downarrow)$ components along c.

The results are less clear for the intermediate-temperature phase since here the magnetoelectric tensor follows none of the possible forms listed in Table 8.5. If the spins are entirely along b as suggested by the 4F1 experiment, then $\alpha_{bb} = 0$ in contrast to observation. Only magnetic structures with symmetry $(\uparrow\uparrow\downarrow\downarrow)$ are considered in Table 8.5 and introducing other symmetry components may result in other point groups with accompanying magnetoelectric tensor forms. For instance, adding a $(\uparrow\downarrow\downarrow\uparrow)$ component along c to the main $(\uparrow\uparrow\downarrow\downarrow)$ component along b also yields magnetic point group $2_z/m'_z$ where $\alpha_{bb} \neq 0$ is allowed. Such additional canting component would most likely result in small diagonal tensor elements as the deviation from the collinear structure is minor. On the contrary, the corresponding observed electric polarization for $\mathbf{E}||\mathbf{b}$, $\mathbf{H}||\mathbf{b}$ is comparable in magnitude or even larger than the polarization for $\mathbf{E}||\mathbf{a}$, $\mathbf{H}||\mathbf{b}$ [*cf.* Fig. 8.15(b) and (e)]. The pyrocurrent and neutron results therefore appear to be conflicting for the intermediate-temperature phase. More investigations are needed to clarify this issue.

In summary, the main symmetry component in the low-temperature zero-field phase is $(\uparrow\uparrow\downarrow\downarrow)$ with the major spin component along a, followed by b. The orientation of the spins in the (a, b)-plane may be estimated from the neutron intensities of either $(0, 0, 1)$ or $(0, 1, 2)$. Here, $(0, 1, 2)$ is chosen because of its stronger signal and following the above dicussion it may be assumed that this peak only reflects spin components along b. The angle, ϕ, measured from the b-axis towards the a-axis [see sketch in Fig. 8.19(a)] is found from the following relation:

$$\tan\phi = \sqrt{\frac{I_a}{I_b}},$$

where the intensities $I_a = I_y^{\mathrm{NSF}} - I_x^{\mathrm{NSF}}$ or $I_a = I_x^{\mathrm{SF}} - I_y^{\mathrm{SF}}$ and $I_b = I_z^{\mathrm{NSF}} - I_x^{\mathrm{NSF}}$ or $I_b = I_x^{\mathrm{SF}} - I_z^{\mathrm{SF}}$. Here I_x^{NSF} denotes the neutron intensity in the NSF channel for $\mathbf{P}||\mathbf{x}$ etc. Furthermore, I_b is weighted with respect to the factor 0.93 as given in Table 8.4. Form factor and Lorentz corrections may be neglected when regarding a single Bragg peak. The temperature dependence of the calculated angle is shown in Fig. 8.19(a) and $\phi = 60.9(5)^\circ$ at the plateau below 10 K. [Note that using $(0, 0, 1)$ for the calculation yields a similar angle of $\phi = 56.1(9)^\circ$.]

In the intermediate phase, the spins also order in an $(\uparrow\uparrow\downarrow\downarrow)$ arrangement but with spins aligned along b. Both zero-field structures are sketched in Fig. 8.19(b).

Having determined the most likely zero-field structures of $LiNi_{0.8}Fe_{0.2}PO_4$ it is appropriate to compare our findings with previous results obtained by other groups as well as compare with other mixed anisotropy magnets mentioned in Section 3.2.

Neutron diffraction and magnetic susceptibility measurements were previously performed on $LiNi_{0.8}Fe_{0.2}PO_4$ by Li et al.[74]. Based on the observation of the $(0, 1, 0)$ magnetic Bragg peak, they concluded that the ground state is similar to that of $LiNiPO_4$, i.e. mainly a spin arrangement of symmetry $(\uparrow\uparrow\downarrow\downarrow)$ and with spins along c. The transition at $T_{N1} = 25.6(2)$ K was not observed in Ref. 74.

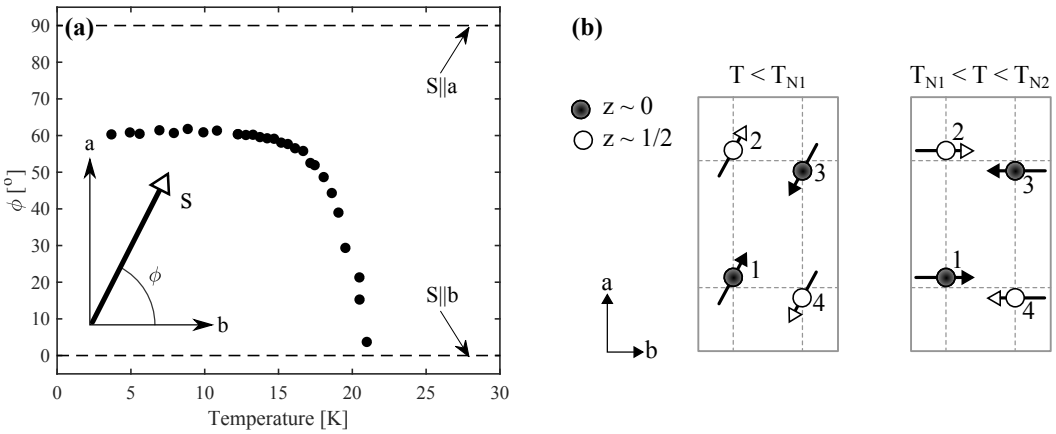

Figure 8.19: *(a) The angle, ϕ, as calculated from the polarized neutron intensities of (0,1,2). Above T_{N2} the angle is zero, i.e. the spins are entirely along b. At T_{N2}, the spins start rotating towards the a-axis and the angle reaches a plateau of $\phi = 60.9(5)°$ below 10 K. The inserted sketch shows the spin orientation on the plateau. (b) Sketches of the zero-field magnetic structures in $LiNi_{0.8}Fe_{0.2}PO_4$ projected onto the (a, b)-plane.*

In a different study performed by Zimmermann et al.[73], SHG spectra were recorded in order to determine the magnetic symmetry of $LiNi_{0.8}Fe_{0.2}PO_4$ at zero field. Observations of the SHG tensor elements χ_{yxx} and χ_{zxx} lead to the point group m_x with spins in the (b, c)-plane [tensor forms for the polar time-asymmetric SHG tensor of rank 3 may be looked up in books such as Ref. 15]. However, our polarized neutron data together with the electric polarization measurements unambigiously place the spins in the (a, b)-plane with point group $2_z/m'_z$. Still, the SHG spectra may be consistent with our conclusion as spin components along a were not observable in the experimental setup in Ref. 73. In Ref. 73, the spin orientation is described by the angle, $\varphi_{\text{spin}} = 40(3)°$, from the b-axis towards the c-axis. The angle is determined from the temperature dependence of χ_{zxx} as well as a low-temperature extrapolation of a power law fitted close to the transition temperature. If instead b and c are swapped for a and b respectively, the result is relatively close to our angle, $90° - \phi = 29.1°$, as determined using polarized neutron data. The intermediate-temperature phase was also observed in Ref. 73 where the tensor element χ_{zxx} is active but χ_{yxx} is not [re-visit Fig. 3.4]. The authors concluded – like us – that the spins are oriented along b in this phase.

In the end, our results are consistent with the observations in both Refs. 74 and 73. However, the additional information provided by neutron polarization analysis as well as electric polarization measurements, yield a different conclusion as to the ground state magnetic structure. Recalling the theoretical predictions [Section 3.2] on systems with competing anisotropies[79], $LiNi_{1-x}Fe_xPO_4$ does not exhibit a simple mixed phase or a spin-flop transition for intermediate values of x. Nor does it display a glassy phase like $Fe_xNi_{1-x}F_2$[85]. Fishman et al.[79] regarded systems with competing anisotropies in the form of a mixture of a 3D Ising system and a 3D XY antiferromagnet. However, such description is not entirely suitably for our system, $LiNi_{1-x}Fe_xPO_4$, and it is therefore not surprising that the theoretical predictions are not obeyed. Our system is better characterized by a mixture of two systems with opposite hard and easy axes. $LiNiPO_4$ has easy axis c and hard axis b whereas for $LiFePO_4$ it is exactly opposite with easy axis b and hard axis c. Moreover, both

parent compounds have a relatively soft a-axis which explains why the main spin component is along this direction for $LiNi_{0.8}Fe_{0.2}PO_4$. To our best knowledge, a theoretical treatment of such system is still to be carried out.

Field-induced phase transition and structure for fields along a. Having determined the zero-field magnetic structures in $LiNi_{0.8}Fe_{0.2}PO_4$ we now turn to the behavior of the system as a function of magnetic fields applied along the easy axis, a. A magnetic phase transition was observed at $\sim 8\,\mathrm{T}$ where an increase in the magnetic susceptibility is observed [see Fig. 8.12(b)]. The transition stretches over $\sim 2\,\mathrm{T}$ and is therefore rather broad. This is similar to the field-induced transition observed in $LiNi_{0.94}Fe_{0.06}PO_4$ for fields along c [Figs. 8.4(f) and 8.5(b)]. Furthermore, the response in the electric polarization measured for $\mathbf{E}||\mathbf{a}$, $\mathbf{H}||\mathbf{a}$ is at its maximum at this transition [see Fig. 8.15(a)]. The phase transition was also evident in our neutron diffraction measurements. The intensities of the magnetic Bragg peaks $(0,0,1)$ and $(0,1,0)$ as well as the nuclear Bragg peak $(0,2,0)$ are plotted as a function of applied field in Fig. 8.20.

The $(0,0,1)$ peak shows a gradual transition with an intensity decrease in the interval $\sim 6.5-9\,\mathrm{T}$. At higher fields, the intensity reaches a plateau and does not go to zero. Therefore, the high-field magnetic structure is commensurate unlike in the parent compound, $LiNiPO_4$, where an incommensurate spin spiral appears above 12 T. The field-induced phase transition in the magnetic phase diagram of $LiNi_{0.8}Fe_{0.2}PO_4$ [Fig. 8.8] was followed by field-dependencies of $(0,0,1)$ at different temperatures such as the curve at 1.8 K shown in Fig. 8.20(a).

The $(0,0,1)$ peak was only followed for increasing field. The $(0,1,0)$ peak, on the other hand, was measured both for increasing and decreasing field and a peculiar behavior was discovered. Upon decreasing the field from 11 T at 1.6 K, the intensity increases from $\sim 9\,\mathrm{T}$ until $\sim 6\,\mathrm{T}$ whereafter it decreases monotonically down to 0 T. When ramping back up, the intensity stays constant at the zero-field level until around 7 T where there is a slight increase before dropping to a plateau after the transition. The intensity at said plateau is *not the same* as the starting intensity at 11 T. The data shown in Fig. 8.20(b) was collected while continuously ramping the field and collecting the intensity at the $(0,1,0)$ peak position. However, the curve shape for increasing field was reproduced in a different measurement where the intensity of $(0,1,0)$ as a function of field was found by integrating full rocking curves at various field values [compare red diamonds and blue circles in Fig. 8.20(b)]. Hence, the remarkable field-dependent behavior of the $(0,1,0)$ neutron intensity appears reproducible – at least for increasing fields. Similar peculiar field-dependent behavior of the $(0,1,0)$ magnetic peak was seen for $LiNi_{0.94}Fe_{0.06}PO_4$ [Fig. 8.5(b)].

It should also be mentioned that the peak intensity of $(0,1,0)$ was measured as a function of time for the duration of 1 h at 6 T (decreasing field). No significant change in the intensity was observed. Hence, if the peculiar field-dependent behavior of the $(0,1,0)$ peak is a result of a non-equilibrium system, the dynamics are clearly on a longer time scale than 1 h.

The intensity of the nuclear Bragg peak $(0,2,0)$ was, too, measured for decreasing and increasing field in order to investigate whether a structural change occurs at the transition [see Fig. 8.20(c)]. Indeed, upon decreasing the field from 11 T at 1.6 K, a pronouced dip in the intensity of $(0,2,0)$ takes place at the transition.

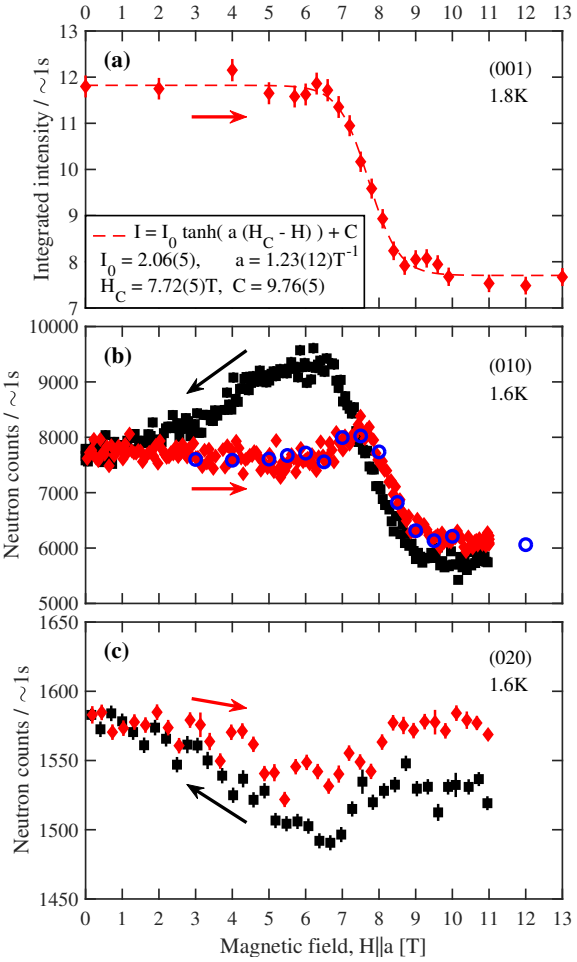

Figure 8.20: *Intensities of magnetic Bragg peaks (0,0,1) and (0,1,0) as well as nuclear Bragg peak (0,2,0) as a function of magnetic field applied along a for increasing field (red diamonds) and decreasing field (black squares) as measured at RITA-II. Integrated intensities were obtained from rocking curves at each field value in (a) whereas in (b) and (c) peak neutron counts were collected while continuously ramping the field. Arrows indicate the field ramp direction in each plot. The dashed line in (a) shows a fit to a hyperbolic tangent function with fitting parameters listed in the box. The blue circles in (b) mark scaled integrated intensities from a different field scan. Data points in (c) have been rebinned into bins of* $\Delta(\mu_0 H) = 0.25\,\mathrm{T}$ *for clarity.*

Hereafter, the intensity recovers and arrives at a higher level at 0 T compared to the starting point at 11 T. When increasing the field again, the intensity describes the same curve – although with a shallower dip. Like for the $(0, 1, 0)$ magnetic peak, the intensity of $(0, 2, 0)$ reaches a different level above the transition after ramping back up. Note that the intensity was measured at the $(0, 2, 0)$ peak position while ramping the field continuously. Therefore, it is unclear whether the change in intensity originates in a structural change, a change in the ferromagnetic moment or whether the crystal simply moves as a consequence of the applied magnetic field.

It is clear that more investigations are needed to be able to say exactly what happens during the phase transition at $\sim 8\,\mathrm{T}$. Although it is not entirely certain how the system transforms from one phase to another, it may be easier to determine the magnetic structures at the end points. The zero-field magnetic structure was determined in the previous section, and in addition, intensities of a number of magnetic Bragg peaks were collected at $(1.6\,\mathrm{K}, 12\,\mathrm{T})$ in order to determine the magnetic structure in the high-field phase. A selection of the corresponding rocking curves are found in Fig. 8.16 and all peaks display a decrease in the magnetic intensity at 12 T compared to 0 T. Such decrease of $(0, 1, 0)$ and $(0, 2, 1)$ may originate in spins re-orienting such that they obtain a larger component along b [*cf.* structure and polarization factors in Table 8.3]. Likewise, the intensity decrease of $(0, 0, 1)$ and $(0, 1, 2)$ may be the result of the spins gaining a component along c.

Such spin-flop-like structure would be easier to magnetize and hence have a larger magnetic susceptibility as was indeed observed [see Fig. 8.12(b)]. This kind of spin-reorientation was also proposed for the high-field phase in $LiNi_{0.94}Fe_{0.06}PO_4$ in Section 8.1.

Having thus treated the magnetic structures in $LiNi_{0.8}Fe_{0.2}PO_4$ – both with and without applied magnetic fields – we now turn to study the spin dynamics.

Spin excitations for magnetic fields applied along a. Previously, the spin-wave dispersion of $LiNi_{0.8}Fe_{0.2}PO_4$ was measured in zero field by Li et al.[74]. They showed that the dispersion is extremely similar to that of the parent compound, $LiNiPO_4$, and they determined the corresponding exchange interactions and single-ion anisotropy constants [see Table 8.2].

In the present study we extend the work of Li et al. by investigating spin-wave spectra as a function of applied field along a. To do so, inelastic neutron scattering measurements were performed at the triple-axis spectrometer FLEXX at the HZB. Vertical slits of 3.0 and 3.5 cm were placed before and after the sample respectively. Horizontal slits were 2.5 cm on both sides and the collimation configuration was open-open-open-open. Fixed final energies of $k_f = 1.2, 1.3, 1.55$ and $1.7\,\text{Å}^{-1}$ were used depending on the desired resolution. The 250.8 mg $LiNi_{0.8}Fe_{0.2}PO_4$ single crystal was oriented with $(0, K, L)$ in the scattering plane. Magnetic fields along a up to 14.8 T were provided by a vertical cryomagnet.

Energy scans at $(0, 1, 0)$ with $k_f = 1.3\,\text{Å}^{-1}$ and different field values are shown in Fig. 8.21. Mode positions are found by subtracting the incoherent signal as measured at $(0, 0.75, 0.25)$ and fitting the elastic as well as the inelastic signals to Gaussian line shapes. The details of this procedure are described in Appendix D. The energy width of the incoherent signal, 0.138(7) meV, also offers an estimate of the energy resolution. It is clear from Fig. 8.21 that below the field-induced transition the fits are good. In the interval $6-8.5$ T, the peak position and intensity are slightly undershot. At 9 T, the fit fails completely and above 9 T, the peak position is slightly overshot but the intensity is well described.

At zero field, a peak is observed around 1 meV and moves towards lower energy transfers with increasing field. Supplementing inelastic scattering measurements at zero field using polarized neutrons at 4F1 (not shown) demonstrated that the excitation is a conventional precession of the moments. In the region $6 - 9$ T the peak hovers around $0.3 - 0.4$ meV and it becomes sharper and more intense with maximum intensity around $8 - 9$ T. Upon further increasing the field, the peak moves back towards higher energy transfers. The behavior is summarized in the color plot in Fig. 8.22. It becomes clear that the mode position describes a "W" shape in the transition region, i.e. there are two minima in energy at 6 T and 8.5 T, corresponding well with the transition region observed in the magnetization [Fig. 8.12(b)] and with neutron diffraction [Fig. 8.20]. This behavior is most peculiar and points towards two transitions as opposed to the single transition observed in the magnetization, pyrocurrent and neutron diffraction measurements. However, the transition is broad in those measurements and could possibly "hide" several transitions. As mentioned earlier, the maximum in peak intensity coincides with the maximum in the electric polarization for $\mathbf{E}||\mathbf{a}$, $\mathbf{H}||\mathbf{a}$ [see Fig. 8.15(a)]. Moreover, the peak shapes in Fig. 8.21 are asymmetric with tails towards higher

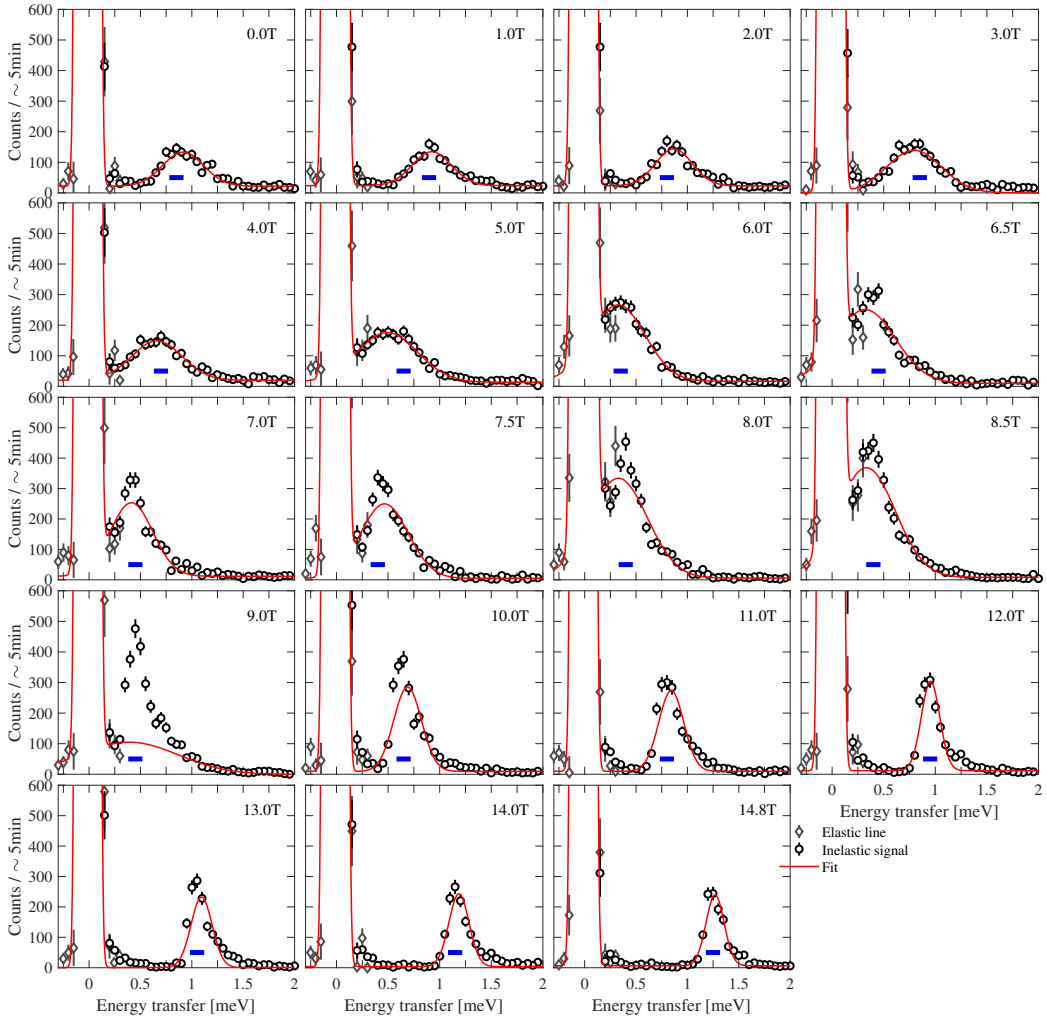

Figure 8.21: *Energy scans at constant* $\mathbf{Q}$ *=(0, 1, 0) at different field values (increasing field) measured with* $k_f = 1.3\,\text{Å}^{-1}$*. The peak is broader below the transition and becomes sharper above the transition. The peak intensity is at a maximum around 8-9 T. These curves are put together from two dataset: elastic line (grey diamonds) and inelastic signal (black circles). The fits (red line) are described in Appendix D. Note that the fit at 9 T is particularly bad. The blue bars illustrate the energy resolution as obtained by Gaussian fits to the incoherent signal at (0,0.75,0.25).*

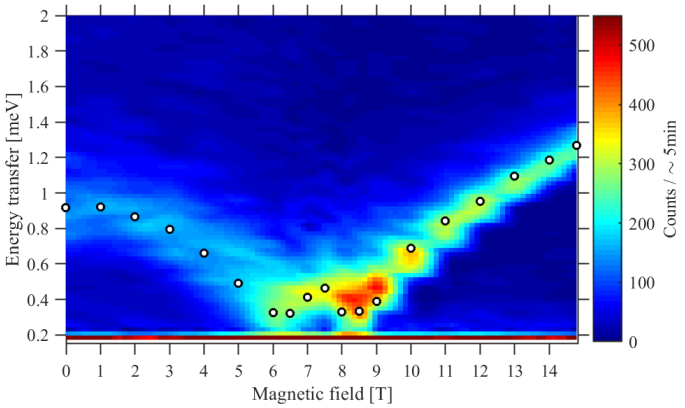

Figure 8.22: *Color plot of the measured neutron intensities at* $\mathbf{Q}$ *=(0, 1, 0) as a function of field and energy transfer measured with* $k_f = 1.3\,\text{Å}^{-1}$*. The plot is formed from the 2D line plots shown in Fig. 8.21. Fitted peak positions are shown with the open circles.*

energy transfers. The tail becomes more pronounced above 6 T compared to below. This asymmetry may be explained by resolution effects (see Appendix D).

Constant **Q** scans at 12 T and at various positions in reciprocal space along $(0, K, 0)$ and $(0, 1, L)$ or $(0, 3, L)$ are shown in Fig. 8.23. The lower limit on the a4 (2θ) motor on FLEXX prevented access to sufficiently high energy transfers at $(0, 1, L)$. Therefore, the spin-wave branch as a function of L was mainly followed at $(0, 3, L)$ despite the lower intensity at this position due to the magnetic form factor. No peaks in the signal were observed at the $(0, 0, L)$ position. Mode positions in Fig. 8.23 are determined by fitting each spectrum to a Gaussian with linear background. The resulting dispersion is plotted in Fig. 8.24 where it is compared to the zero-field dispersion relation determined by Li et al.[74]. At 12 T, the energy gap is coincidencially similar to the zero-field value of ~ 1 meV. Intriguingly, the shape of the dispersion at 12 T and the bandwidth are very similar to the zero-field dispersion too. The major difference between the dispersions at 0 and 12 T appears to be the width of the excitation as a function of energy with a more well-defined excitation at 12 T compared to at 0 T [see Fig. 8.21]. Hence, the zero-field spin-waves are shorter lived and the corresponding magnetic structure is possibly less ordered than at 12 T.

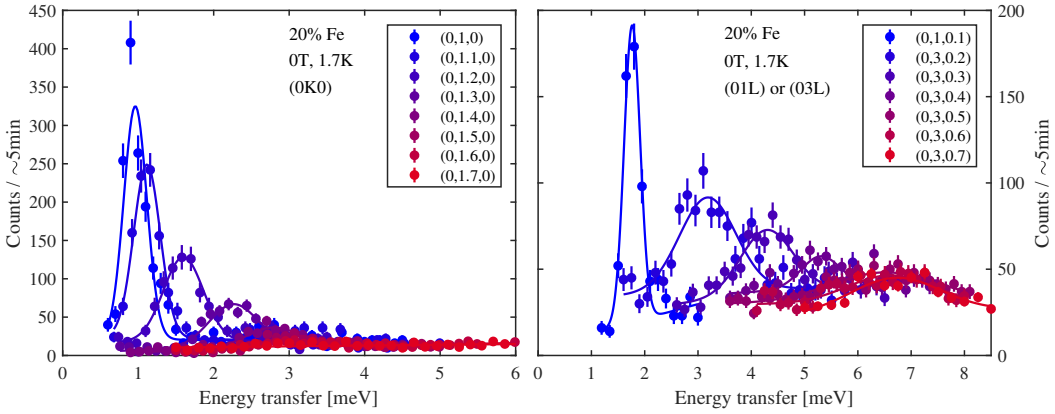

Figure 8.23: *Neutron counts as a function of energy transfer along (0,K,0) and (0,1,L) or (0,3,L) in $LiNi_{0.8}Fe_{0.2}PO_4$. A fixed final energy of $k_f = 1.55$ Å^{-1} was used for scans at (0,K,0) and (0,1,L) and $k_f = 1.7$ Å^{-1} for (0,3,L). Peak positions are determined by fitting curves to a Gaussian function with linear background.*

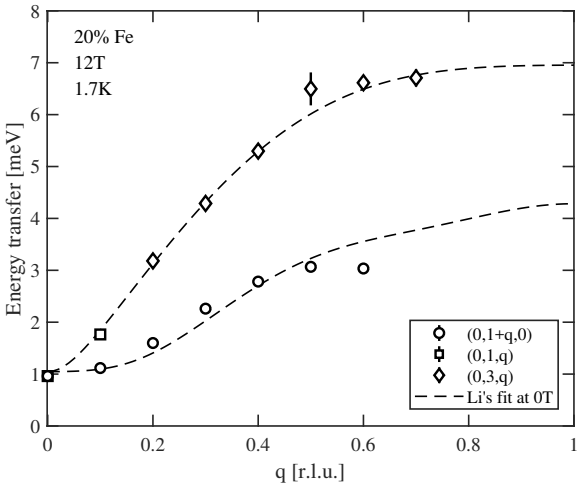

Figure 8.24: *Spin-wave dispersion along (0,K,0) and (0,1,L) or (0,3,L) for $LiNi_{0.8}Fe_{0.2}PO_4$. The dashed lines show the fit to the 0 T dispersion as found in Ref. 74 and with parameters given in Table 8.2.*

.

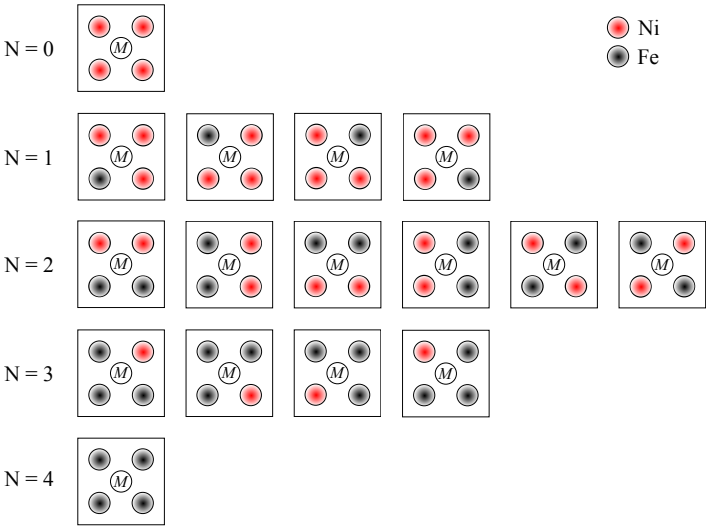

Figure 8.25: *Sketch of the different ways to place N nearest Fe neighbors in the (b, c)-plane for a given magnetic ion, M.*

Table 8.6: *Probability for having N nearest Fe neighbors.*

N	Probability (%)
0	40.96
1	40.96
2	15.36
3	2.56
4	0.16

As just described, the spin-waves at 0 and 12 T are remarkably similar which leads to the conclusion that the magnetic structures in the zero-field and high-field phases must also be very similar. This was also the conclusion based on neutron diffraction measurements. However, one big question remains: what is going on in the field interval $\sim 6 - 9$ T? The observed "W" field-dependency or double minimum of the gap energy at $(0, 1, 0)$ may point towards two phase transitions as previously mentioned. Diffraction measurements also showed abnormal behavior in the transition region and it was proposed that either structural changes or non-equilibrium effects are responsible. We may speculate that because of disorder in the system, one or several intermediate phases are entered before reaching the commensurate high-field phase above 9 T. In this regard, it is perhaps useful to consider the $LiNi_{0.8}Fe_{0.2}PO_4$ system on a microscopic level. With magnetic sites occupied by 80% Ni and 20% Fe one may calculate the probability that a magnetic ion, M, has a certain combination of Ni and Fe neighbors in the (b, c)-plane. This probability can be calculated as $P = 0.8^{4-N}\, 0.2^N \times$ (# of ways to place N Fe neighbors). There is 1 way to place 0 Fe neighbor, 4 ways to place 1 Fe neighbor etc. [see Fig. 8.25]. The corresponding probabilities are listed in Table 8.6. Interestingly, it is equally likely to have 0 or 1 nearest Fe neighbors. Therefore, two quite different magnetic environments occur with the same frequency. Is this possibly connected to the double transition in the field-dependency of the energy gap at $(0, 1, 0)$? Could it be that what we see is first a transition for the $N = 0$ environment and then a transition for the $N = 1$ environment? Speculations aside, there is still much to be done before a complete understanding of the magnetic interactions in $LiNi_{0.8}Fe_{0.2}PO_4$ is obtained. In that regards it would be interesting to look into the local crystal fields.

To conclude this section on $LiNi_{0.8}Fe_{0.2}PO_4$ some of the main findings are restated before moving on to the Monte Carlo simulations in the next section. The easy axis is along a in contrast to the parent compounds, $LiNiPO_4$ and $LiFePO_4$, with easy axes c and b respectively. Two commensurate zero-field phases were identified. For temperatures in the interval $\sim 20 - 25$ K, the spins are aligned along b and have symmetry $(\uparrow\uparrow\downarrow\downarrow)$. Below ~ 20 K, the spins orient in the (a, b)-plane with the major

component along a. Upon applying a magnetic field along a, a spin re-orientation takes place at around $\sim 8\,\mathrm{T}$. The transition is accompanied by anomalous behavior of the energy gap at $(0, 1, 0)$ in the spin-wave dispersion. All observed magnetic phases display the magnetoelectric effect with complicated temperature and field dependencies of the tensor elements.

8.3 Monte Carlo simulations

Although magnetization, pyrocurrent and neutron diffraction measurements together draw a reasonably clear picture of the magnetic states in $LiNi_{0.8}Fe_{0.2}PO_4$, there are still a number of open questions and puzzling features. For instance, which physical mechanism is responsible for the observed zero-field structures? Or why is the system with 20% Fe so different from the parent compound, $LiNiPO_4$, whereas the system with 6% Fe is not? In order to assist in the interpretation of our experimental data and to obtain an overall better understanding of the physics involved, Monte Carlo simulations were performed on the general $LiNi_{1-x}Fe_xPO_4$ system. Simulations allow for singling out individual mechanisms as well as shining a light on their collective behavior. The model and implementation were described earlier on in Chapter 5 and the results are presented in the following.

Single-ion anisotropy energy landscape. Before starting any simulations on the mixed systems it is worth giving some thoughts to the general $LiNi_{1-x}Fe_xPO_4$ spin system. Considering only a single nearest-neighbor exchange interaction all spins will align collinearly regardless of flavor if said interaction is sufficiently strong. The spin orientation then only depends on the lowest single-ion anisotropy energy direction. For Ni and Fe the single-ion anisotropy constants are given in Table 8.7. Assuming that the spins align along one of the crystallographic axes the anisotropy energy as a function of Fe concentration, x, can be found as follows:

$$\begin{aligned} a: &\quad (1-x)\,\mathfrak{D}^a_{\mathrm{Ni}} + 4\,x\,\mathfrak{D}^a_{\mathrm{Fe}}, \\ b: &\quad (1-x)\,\mathfrak{D}^b_{\mathrm{Ni}}, \\ c: &\quad 4\,x\,\mathfrak{D}^c_{\mathrm{Fe}}, \end{aligned}$$

where the factor 4 originates from squaring the Fe spin, $S_{\mathrm{Fe}} = 2$. These three equations are plotted as a function of x in Fig. 8.26. For $x < 0.08$ the c-axis is preferred – corresponding well with our 6% Fe sample which behaves more or less like the stoichiometric $LiNiPO_4$. For $0.08 < x < 0.37$ the a-direction has lowest single-ion anisotropy energy. Again this agrees fairly well with our observations for the 20% Fe sample where the spins mostly align along a. For $x > 0.37$ the b-axis is preferred, corresponding to $LiFePO_4$.

In the above calculation it is assumed that the spins align along one of the principal axes, but what if they do not? In fact we know from polarized neutron diffraction that they align in the (a, b)-plane and in the following we consider the full single-ion anisotropy energy hypersurface as a function of the general spin direction, $\mathbf{S} = (S^a, S^b, S^c)$. It is still assumed that the spins align, i.e. they are collinear such that $\mathbf{S}_{\mathrm{Ni}} || \mathbf{S}_{\mathrm{Fe}}$ and with lengths $S_{\mathrm{Ni}} = \frac{1}{2} S_{\mathrm{Fe}} = S = 1$. The total anisotropy energy is then a function of the three spin components and the Fe substitution level, x:

$$E(S^a, S^b, S^c, x) = (1-x)\mathfrak{D}^a_{\mathrm{Ni}}(S^a)^2 + 4x\mathfrak{D}^a_{\mathrm{Fe}}(S^a)^2 + (1-x)\mathfrak{D}^b_{\mathrm{Ni}}(S^b)^2 + 4x\mathfrak{D}^c_{\mathrm{Fe}}(S^c)^2.$$

Table 8.7: *Single-ion anisotropy constants in meV as given in Refs. 53 and 54.*

	$\mathfrak{D}^a$	$\mathfrak{D}^b$	$\mathfrak{D}^c$
Ni	0.339	1.82	0
Fe	0.62	0	1.56

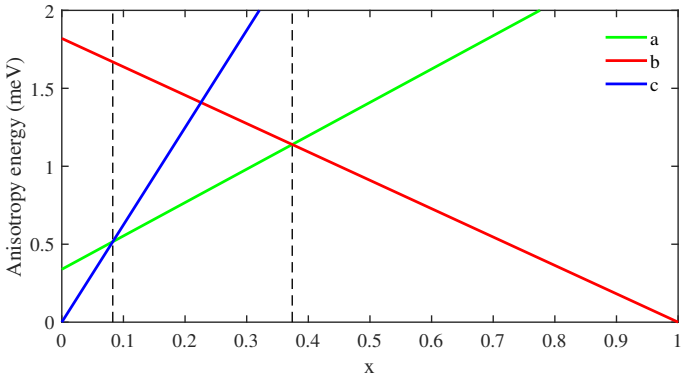

Figure 8.26: *Single-ion anisotropy energies as a function of Fe concentration, x, for the three different crystallographic axes. The vertical dashed lines show the cross-over of lowest-energy directions from c to a at $x = 0.08$ and from a to b at $x = 0.37$.*

Furthermore, the spin length is assumed constant such that $(S^a)^2 + (S^b)^2 + (S^c)^2 - 1 = 0$. The expression for the energy can then be simplified by eliminating S^c:

$$E(S^a, S^b, x) = (1-x)\mathfrak{D}^a_{\mathrm{Ni}}(S^a)^2 + 4x\mathfrak{D}^a_{\mathrm{Fe}}(S^a)^2 + (1-x)\mathfrak{D}^b_{\mathrm{Ni}}(S^b)^2 + 4x\mathfrak{D}^c_{\mathrm{Fe}}\left[1 - (S^a)^2 - (S^b)^2)\right].$$

In order to find the extrema of the energy hypersurface we need to differentiate with respect to each variable and equate to zero as follows:

$$\frac{\partial E}{\partial S^a} = 2\left[(1-x)\mathfrak{D}^a_{\mathrm{Ni}} + 4x\mathfrak{D}^a_{\mathrm{Fe}} - 4x\mathfrak{D}^c_{\mathrm{Fe}}\right] S^a = 0, \tag{8.4}$$

$$\frac{\partial E}{\partial S^b} = 2\left[(1-x)\mathfrak{D}^b_{\mathrm{Ni}} - 4x\mathfrak{D}^c_{\mathrm{Fe}}\right] S^b = 0, \tag{8.5}$$

$$\frac{\partial E}{\partial x} = \left[-\mathfrak{D}^a_{\mathrm{Ni}} + 4\mathfrak{D}^a_{\mathrm{Fe}} - 4\mathfrak{D}^c_{\mathrm{Fe}}\right](S^a)^2 + \left[-\mathfrak{D}^b_{\mathrm{Ni}} - 4\mathfrak{D}^c_{\mathrm{Fe}}\right](S^b)^2 + 4\mathfrak{D}^c_{\mathrm{Fe}} = 0. \tag{8.6}$$

The above set of equations have several solutions. For Eq. (8.4), $S^a = 0$ is a trivial solution. Plugging $S^a = 0$ into Eq. (8.6) yields the spin components S^b and S^c:

$$S^b = \pm\sqrt{\frac{4\mathfrak{D}^c_{\mathrm{Fe}}}{\mathfrak{D}^b_{\mathrm{Ni}} + 4\mathfrak{D}^c_{\mathrm{Fe}}}} = \pm 0.8799, \qquad S^c = \pm\sqrt{1 - (S^b)^2} = \pm 0.4752.$$

The corresponding value of x is then found from Eq. (8.5):

$$x = \frac{\mathfrak{D}^b_{\mathrm{Ni}}}{\mathfrak{D}^b_{\mathrm{Ni}} + 4\mathfrak{D}^c_{\mathrm{Fe}}} = 0.2258.$$

Hence, the coordinate set $(S^a, S^b, S^c, x) = (0, \pm 0.8799, \pm 0.4752, 0.2258)$ is a solution. Similarly, by setting $S^b = 0$ or $S^c = 0$ we get the solutions $(S^a, S^b, S^c, x) = (\pm 1.2338, 0, \pm 0.7227i, 0.0827)$ and $(S^a, S^b, S^c, x) = (\pm 0.6778, \pm 0.7352, 0, 0.3739)$ where the former is clearly not valid since the spin components must be real and less than one. Contour plots of the energy surfaces for $S^a = 0$, $S^b = 0$ and $S^c = 0$ are shown in Fig. 8.27 and it is clear that the obtained solutions are saddle points.

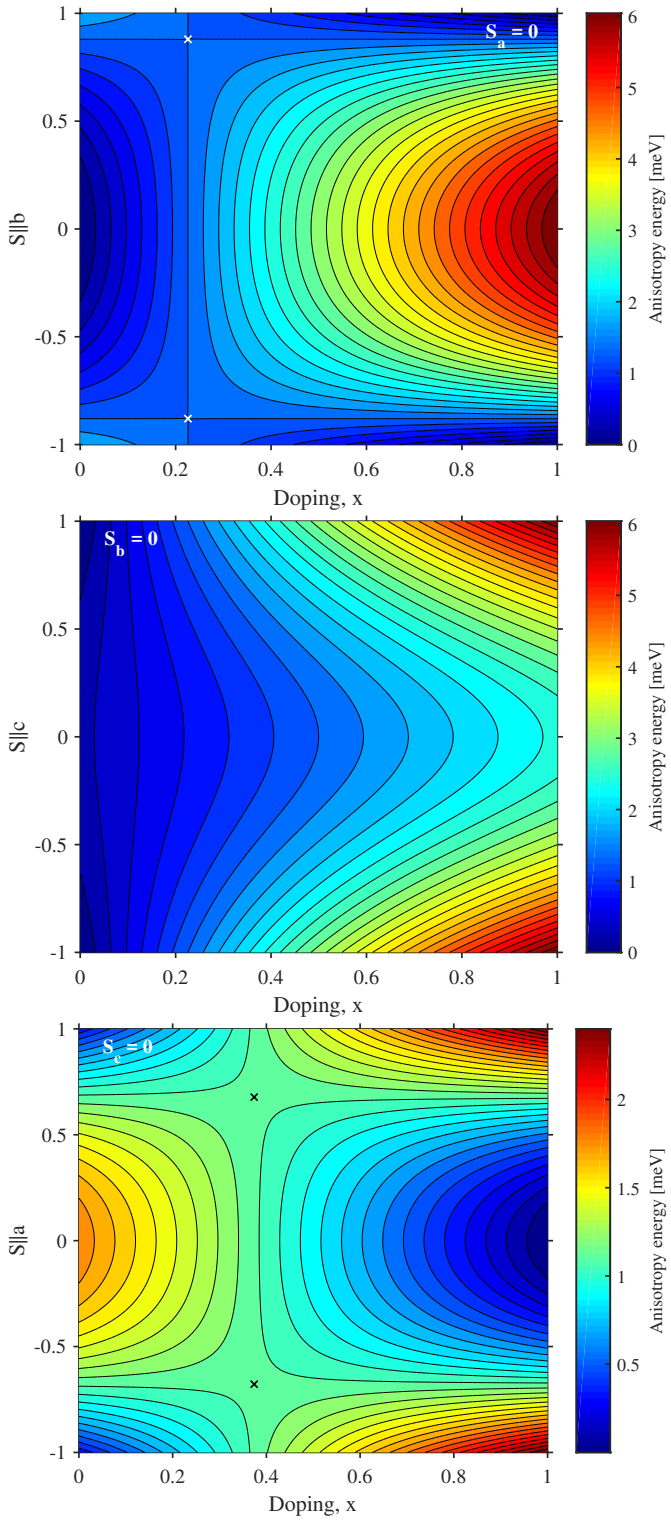

Figure 8.27: *Single-ion anisotropy energy landscape as a function of, x, and* $\mathbf{S}||\mathbf{b}$, $\mathbf{S}||\mathbf{c}$ *and* $\mathbf{S}||\mathbf{a}$ *for* $S^a = 0$, $S^b = 0$ *and* $S^c = 0$ *respectively. Saddle points are marked with crosses.*

Finally, before moving on to the real $LiNi_{1-x}Fe_xPO_4$ system, simulations were performed to imitate the above purely analytical scenario. These were run with

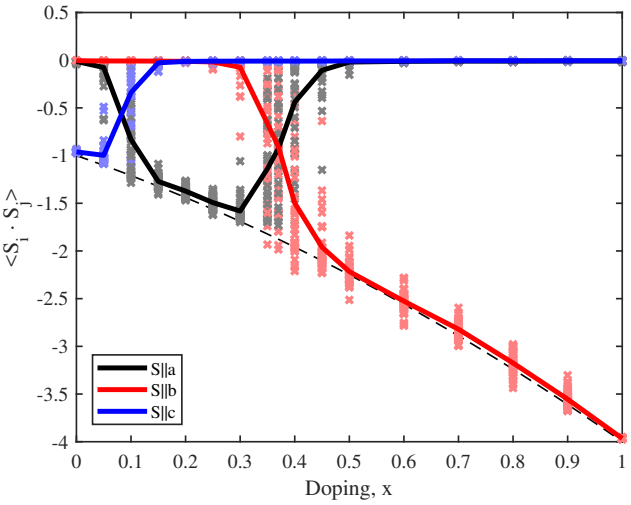

Figure 8.28: *Simulation of optimal spin direction in case of a single* $J_{bc}^{\mathrm{Ni-Ni}} = J_{bc}^{\mathrm{Ni-Fe}} = J_{bc}^{\mathrm{Fe-Fe}} = 10\,meV$. *Simulations were run with* $L = 10$, $10^5\,MCS$, $T = 5$-$600\,K$ *with* $5\,K$ *steps, decreasing temperature and simulated annealing. 5 simulations were run for each value of x. With 20 decoupled* (b, c)*-planes it results in 100 simulations with a 2D grid of* 10×10 *spins. The crosses denote the results for each individual 2D simulation and the solid line shows the average result.*

$J_{bc}^{\mathrm{Ni-Ni}} = J_{bc}^{\mathrm{Ni-Fe}} = J_{bc}^{\mathrm{Fe-Fe}} = 10\,\mathrm{meV}$ and the rest of the exchange interactions put to zero. The value of the exchange constant is chosen such that the energy gain by having antiparallel spins is larger that the gain from orienting spins along their respective easy directions. However, the exchange constant should not be several orders of magnitudes larger than the single-ion anisotropies since then the spin direction would become insignificant. The simulation results are shown in Fig. 8.28. The comparison with the naïve results in Fig. 8.26 is pretty convincing and around $x = 0.37$ multiple solutions with various spin directions in the (a, b)-plane appear.

Using both analytical calculations and simulations this minimalistic model considering only single-ion anisotropy energies already produces magnetic phases with spin orientations compatible with those observed experimentally. Thus encouraged we now look at simulations on $\mathrm{LiNi}_{1-x}\mathrm{Fe}_x\mathrm{PO}_4$ using real parameters.

Simulations on the $\mathrm{LiNi}_{1-x}\mathrm{Fe}_x\mathrm{PO}_4$ system. Monte Carlo simulations were carried out on the $\mathrm{LiNi}_{1-x}\mathrm{Fe}_x\mathrm{PO}_4$ system with exchange and single-ion anisotropy constants as found in Refs. 53 and 54 for the stoichiometric compounds LiNiPO_4 and LiFePO_4 respectively [see Table 8.8]. Interactions between Ni and Fe ions are here computed as the average of the Ni-Ni and Fe-Fe interactions. Note that this assumption on the Ni-Fe interaction may be invalid. In fact, the interaction may be weaker or stronger or even have opposite sign compared to the Ni-Ni and Fe-Fe interactions. This assumption is therefore challenged later but for now an average will do. Single-ion anisotropy constants were listed in Table 8.7. It turns out that for $x = 0.3$, the simulation results correspond well with our experimental observations on $\mathrm{LiNi}_{0.8}\mathrm{Fe}_{0.2}\mathrm{PO}_4$. Therefore, in the presentation of the outcome of the simulations, results for $x = 0.3$ – rather than $x = 0.2$ – are highlighted.

Temperature scans of the energy of the full Hamiltonian and the corresponding heat capacity are shown in the top row of Fig. 8.29 for simulations with $x = 0.0, 0.3$ and 1.0. Phase transitions are identified as peaks in the heat capacity. For $x = 0.0$ and 1.0 there is a single clear transition whereas for $x = 0.3$ there are three transitions. The bottom row of Fig. 8.30 shows the corresponding measure for magnetic order of type C as calculated from Eq. (5.2). Again, for $x = 0.0$ and 1.0 there is a single clear transition where the spins order in a C_z and C_y structure for LiNiPO_4

	J_{bc}	J_b	J_c	J_{ab}	J_{ac}
Ni-Ni	1.04	0.67	-0.05	0.30	-0.11
Ni-Fe	0.905	0.485	0.045	0.22	-0.03
Fe-Fe	0.77	0.30	0.14	0.14	0.05

Table 8.8: *Parameters for echange bonds as used in the Monte Carlo simulations. The parameters for Ni-Ni are found in Ref. 53 and the ones for Fe-Fe are found in Ref. 54. The Ni-Fe parameters are taken as an average.*

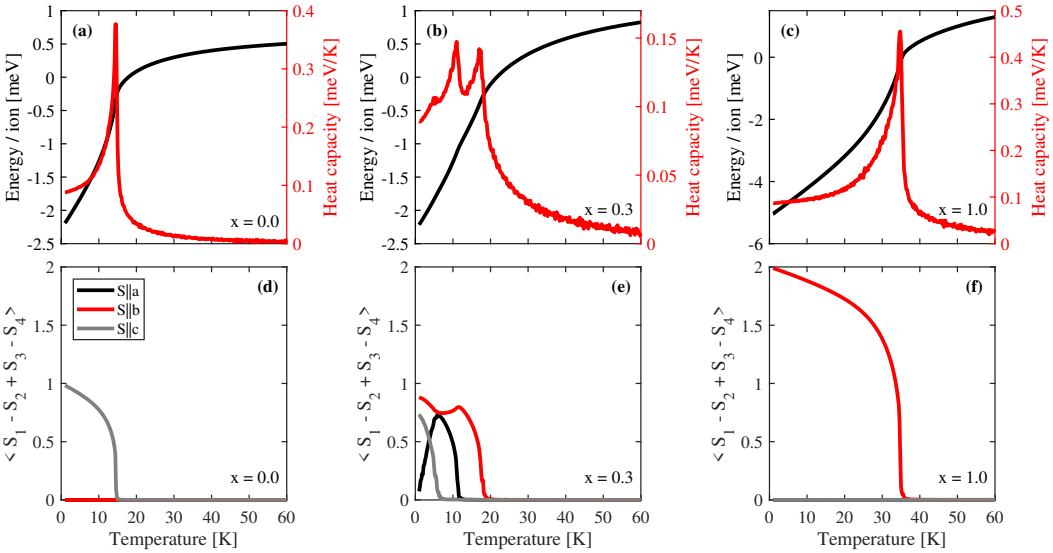

Figure 8.29: *Temperature scans averaged over 5 runs, each performed with $L = 10$, 10^5 MCS, temperature range 1-60 K, temperature step 0.2 K, decreasing temperature and simulated annealing. Exchange parameters are given in Table. 8.8. (a)-(c): energy (black curve) and heat capacity (red curve) are shown for $x = 0.0$, 0.3 and 1.0 as a function of temperature. (d)-(f): measure for magnetic order of type C along a, b and c (black, red and grey curves respectively), shown for $x = 0.0$, 0.3 and 1.0 as for (a)-(c).*

and $LiFePO_4$ respectively. For the mixed compound, $x = 0.3$, three transitions are observed: at ~ 20, ~ 12 and ~ 7 K upon decreasing the temperature. At the first transition, the spins order in a C_y structure which then has a dip at the second transition accompanied by an emerging C_x component. At the last transition, a C_z type structure appears, the C_x structure subsides and the C_y component increases in size. This last transition at ~ 7 K is not as distinct in the heat capacity as compared to the other two transitions.

A series of such temperature scans of the heat capacity and basis vector C for various values of x are stacked to form the color plots in Fig. 8.30 and 8.31. The transitions marked in Fig. 8.30 are combined observations from the heat capacity and the order parameter of the C type structures. From Fig. 8.31 it is clear that a pocket of C_x order exists for $x \approx 0.2 - 0.5$ and that in this phase the spin has components along all three principal directions depending on exact position in the (x, T) phase diagram.

Corresponding measures for A, G and F type structures are zero at low temperatures for $x = 0.0$ and 1.0. For $x = 0.3$, the A component is about 3 orders of magnitude smaller than the C component whereas the G and F type structures are only about 2 orders of magnitude smaller at low temperatures. In all cases,

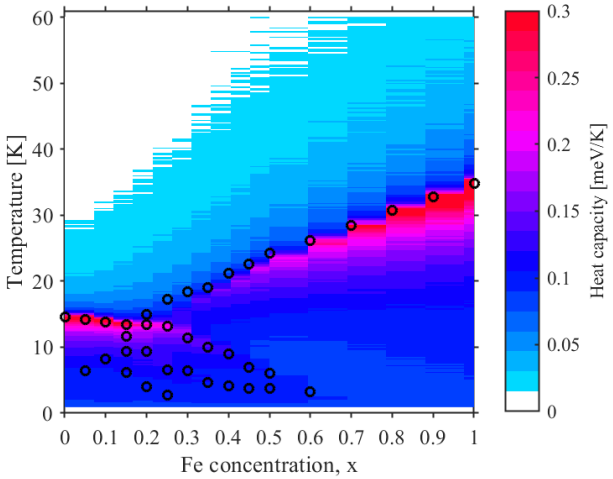

Figure 8.30: *Color plot of the heat capacity as a function of x and T as simulated with $L = 10$, 10^5 MCS, temperature range 1-60 K, temperature step 0.2 K, decreasing temperature and simulated annealing. This plot is created by stacking temperature scans such as shown in the top row of Fig. 8.29. Data is averaged over 5 runs for each value of x. Identified phase transitions are indicated with open circles.*

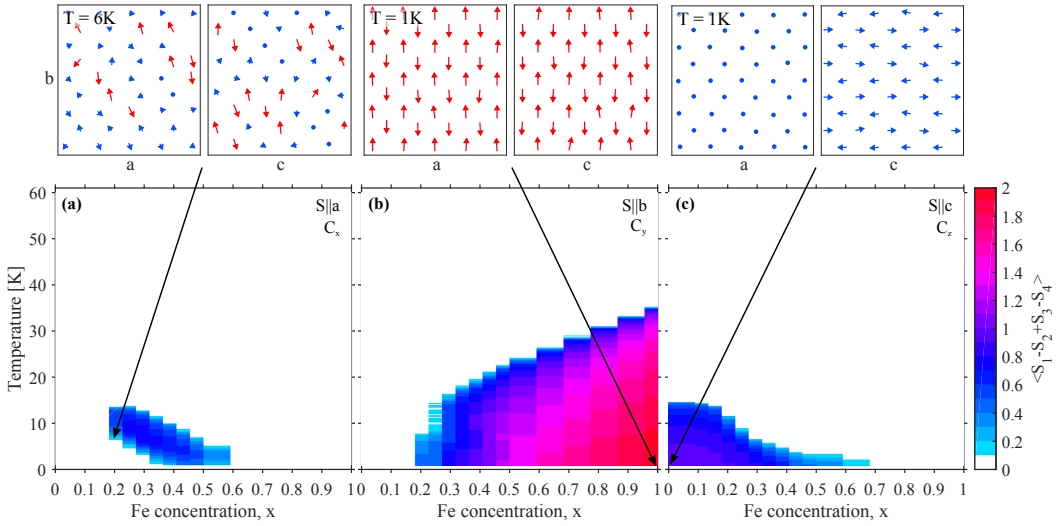

Figure 8.31: *Color plots of the C type order parameter as a function of x and T as simulated with $L = 10$, 10^5 MCS, temperature range 1-60 K, temperature step 0.2 K, decreasing temperature and simulated annealing. These plots are created by stacking temperature scans such as shown in the bottom row of Fig. 8.29. Data is averaged over 5 runs for each value of x. A pocket with a finite spin component along a is present for $x \approx$ 0.2-0.5. The top panels show projections of snapshots of the spin configurations in the (a, b)- and (b, c)-planes for $x = 0.3$, 1.0 and 0.0 at 6, 1 and 1 K from left to right respectively. Red (blue) arrows denote Fe (Ni) ions and dots indicate spins with neglible components in a given plane.*

however, the A, G and F type structures have negligible contributions compared to the C component. Temperature scans of the measures for all four structure types are shown in Appendix A.

When comparing the simulated temperature curves of C_y and C_x above ~ 7 K [Fig. 8.29(e)], they have remarkably similar shape to the polarized neutron intensity curves measured at 4F1 [re-visit Fig. 8.18(h) or (i)]. The interpretation of the 4F1 data is thus solidified with the system ordering in a C_y type structure at T_{N1} and with a C_x component introduced at T_{N2}.

Explorations of parameter space. In order to test the robustness of the above

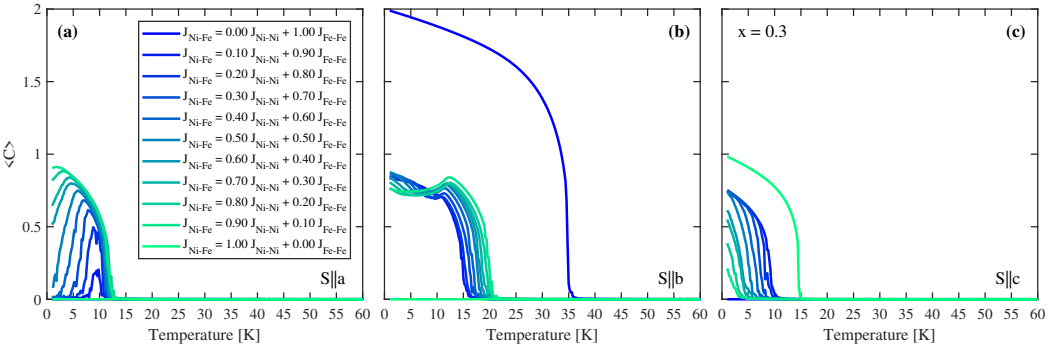

Figure 8.32: *Temperature scans with different Ni-Fe interaction strengths for $x = 0.3$ as defined in Eq. (8.7). Simulations were performed with $L = 10$, 10^5 MCS, temperature range 1-60 K, temperature step 0.2 K, decreasing temperature and simulated annealing. Results were averaged over 5 runs. The dark blue curve shows results for $J_{\mathrm{Ni-Fe}} = J_{\mathrm{Fe-Fe}}$, the light green curve shows results for $J_{\mathrm{Ni-Fe}} = J_{\mathrm{Ni-Ni}}$ and curves of shades in between show simulations where $J_{\mathrm{Ni-Fe}}$ is a mix of $J_{\mathrm{Fe-Fe}}$ and $J_{\mathrm{Ni-Ni}}$.*

Table 8.9: *Exchange parameters for all bonds as used in the simplified model. All values are given in meV.*

J_{bc}	J_b	J_c	J_{ab}	J_{ac}
1	0-1	0	0.3	0

Table 8.10: *Single-ion anisotropy constants in meV for Ni and Fe as used in the simplified model.*

	$\mathfrak{D}^a$	$\mathfrak{D}^b$	$\mathfrak{D}^c$
Ni	0.3	1.8	0
Fe	0.6	0	1.6

results, parts of exchange parameter space was explored. Where in the previous simulations a plain average of the Ni-Ni and Fe-Fe interaction parameters were used for the Ni-Fe interactions, we now perform a series of simulations with different Ni-Fe exchange constants according to the following weighted mean:

$$J_{\mathrm{Ni-Fe}} = p\ J_{\mathrm{Ni-Ni}} + (1-p)\ J_{\mathrm{Fe-Fe}}, \tag{8.7}$$

where $p \in [0,1]$. The order parameter for the C type structure as a function of temperature is shown in Fig. 8.32 for spins along a, b and c. As may be expected, for $p = 0$ and $p = 1$, only the C_y and C_z components are obtained respectively. For $p = 0.2 - 0.9$, i.e. almost the entire interval, the temperature curves for the C order parameters are qualitatively similar to the simple case with $p = 0.5$ as was first simulated. This means that the character of the simulated ground state is remarkably robust and does not depend significantly on the choice of Ni-Fe interaction strength as long as it is some mix of the Ni-Ni and Fe-Fe exchange constants. A better idea as to what the Ni-Fe interaction is like might be possible to obtain from *ab initio* calculations.

Simplified model. Naïvely employing experimentally determined values for exchange and single-ion anisotropy constants yielded simulation results for the mixed $LiNi_{1-x}Fe_xPO_4$ compounds that corresponded well with the observed neutron scattering data. Furthermore, as seen in the previous paragraph, the character of the ground state spin configuration is not sensitive to exactly how the exchange interactions between magnetic ions of different flavor, Ni and Fe, are chosen. However, when using a different set of parameters for $LiFePO_4$ – those found in Ref. 8 rather

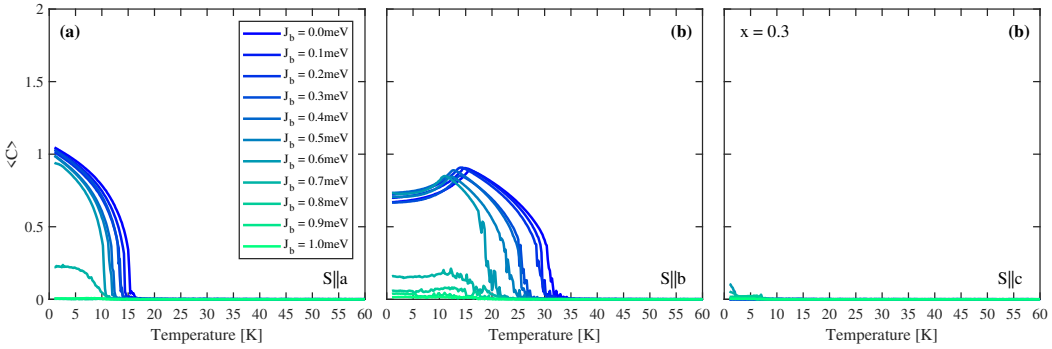

Figure 8.33: *Temperature scans of the C order parameter for the simplified model for $x = 0.3$ and with different values of J_b. Simulations were performed with $L = 10$, 10^5 MCS, temperature range 1-60 K, step 0.2 K, decreasing temperature and simulated annealing. Curves are averaged over 5 runs. For $J_b \leq 0.6$ meV, the curves are qualitatively similar to those in Fig. 8.29(d)-(f).*

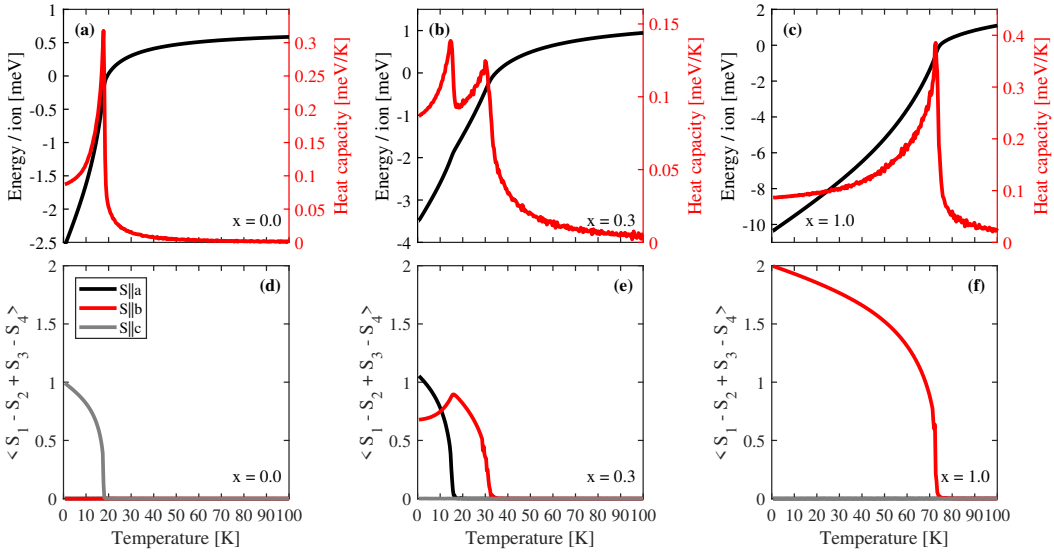

Figure 8.34: *Temperature scans for simulations with $x = 0.0$, 0.3 and 1.0 for the simple model averaged over 5 runs. Each simulation is performed with $L = 10$, 10^5 MCS, temperature range 0.6-100 K, temperature step 0.35 K, decreasing temperature and simulated annealing. Exchange and single-ion parameters are given in Tables 8.9 and 8.10. (a)-(c) Energy (black curve) and heat capacity (red curve) are shown for $x = 0.0$, 0.3 and 1.0 as a function of temperature. (d)-(f) Measure for magnetic order of type C along a, b and c (black, red and grey curves respectively), shown for $x = 0.0$, 0.3 and 1.0 as for (a)-(c).*

than Ref. 54 – the simulations fail to produce a spin component along a for all probed values of x and T. The details of simulations with this set of parameters are given in Appendix A but the conclusion is clear and actually quite obvious: the obtained ground state configuration depends entirely on which parameters are used as input in a simulation.

One important difference between the parameters given in Ref. 54 and 8 is the competition between J_{bc} and J_b. The ratio is $J_{bc}/J_b \approx 2.5$ in Ref. 54 compared to $J_{bc}/J_b \approx 5$ in Ref. 8. This means that the former set of parameters describes

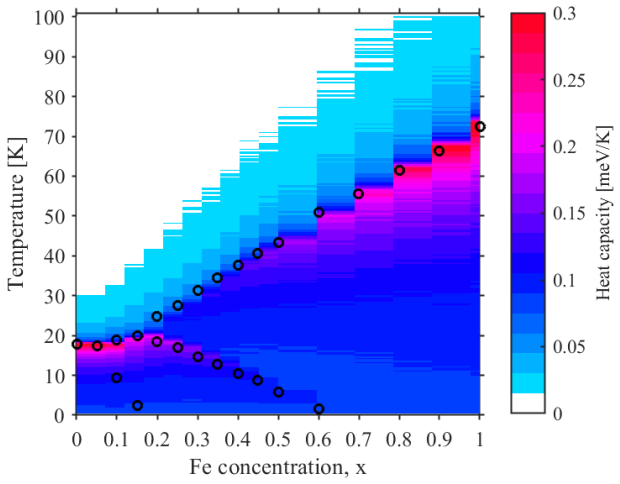

Figure 8.35: *Color plot of the heat capacity as a function of x and T for the simple model as simulated with $L = 10$, 10^5 MCS, temperature range 0.6-100 K, temperature step 0.35 K, decreasing temperature and simulated annealing. Data is averaged over 5 runs for each value of x. Identified phase transitions are indicated with open circles.*

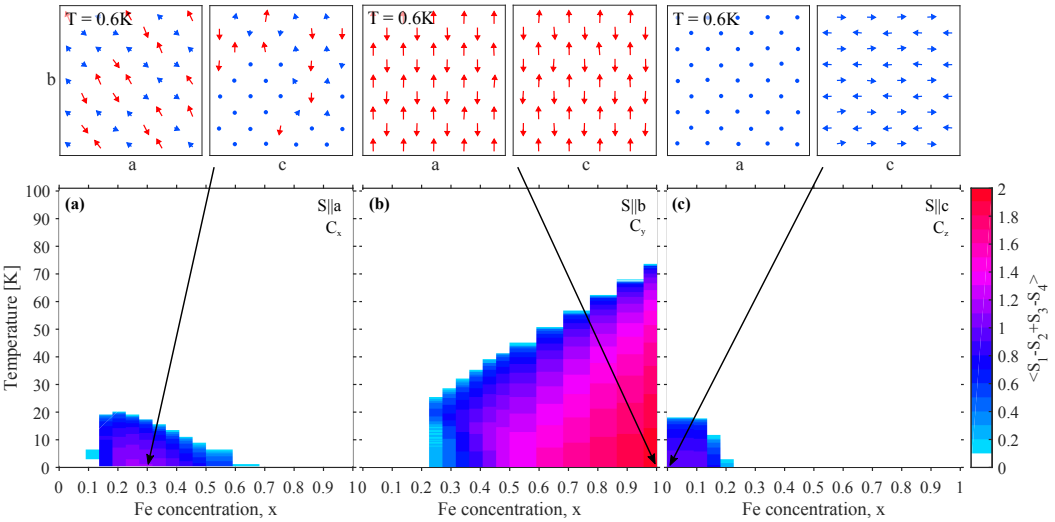

Figure 8.36: *Color plots of the C type order parameter as a function of x and T for the simple model as simulated with $L = 10$, 10^5 MCS, temperature range 0.6-100 K, temperature step 0.35 K, decreasing temperature and simulated annealing. Data is averaged over 5 runs for each value of x. A pocket with a finite spin component along a is present for $x \approx 0.1$-0.6. The top panels show projections of the spin configurations in the (a, b)- and (b, c)-planes at 0.6 K for x =0.3, 1.0 and 0.0 from left to right respectively. Red (blue) arrows denote Fe (Ni) and dots indicate spins with neglible components in a given plane.*

a more frustrated system than the latter. Another difference is the strength of the single-ion anisotropy constants with those in Ref. 8 being ~ 1.4 times stronger. With $S = 2$ for Fe^{2+} and the single-ion anisotropy term in the Hamiltonian being quadratic in S [Eq. (5.1)], a small increase in the anisotropy constant may yield a relatively large change in the energy. In addition, apart from less frustration in the J_{bc}/J_b pair, the overall strength of the exchange parameters are lowered with a factor of ~ 1.5 in Ref. 8 compared to Ref. 54.

In order to achieve a better understanding of the mechanisms in the $LiNi_{1-x}Fe_xPO_4$ system, a simplified model which displays the correct ground state is sought. A key element is believed to be the complementary single-ion anisotropy constants that

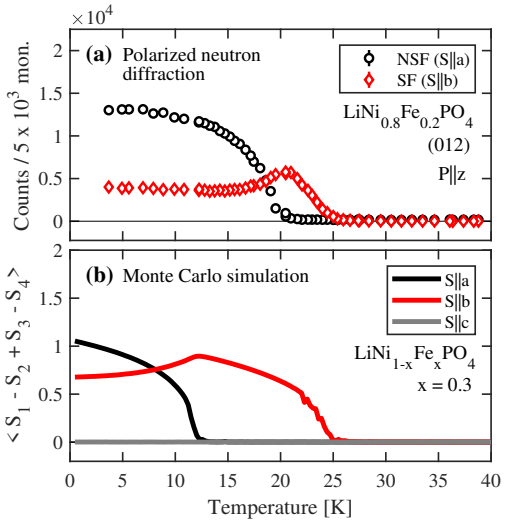

Figure 8.37: *Comparison of polarized neutron diffraction data from 4F1 and Monte Carlo simulations. Note that the temperature has been scaled for the simulation results such that the first transition coincides with the experimental result at* $\sim 25\,\mathrm{K}$.

allow for spin components along a for both Ni and Fe. It is also possible that frustration plays a role. These considerations lead to proposing the model parameters shown in Table 8.9 and 8.10. Note that Ni-Ni, Fe-Fe and Ni-Fe interactions all have the same values, but when calculating the Heisenberg exchange energy the different spin values of Ni and Fe are still taken into account.

Temperature scans of the measure for C type order from simulations with various values of J_b are shown in Fig. 8.33. For $J_b \leq 0.6\,\mathrm{meV}$, the curves are qualitatively similar to those in Fig. 8.29(d)-(f). As expected, the ordering temperature is suppressed as the frustation is increased and as J_b is increased further still, order is eventually destroyed. Consequently, frustration is *not necessary* to obtain a ground state with C_x structure and the model may be further simplified by setting $J_b = 0$. Simulation results for this case are shown in Figs. 8.34-8.36 and the similarities to the original and more complex model shown in Figs. 8.29-8.31 are striking. The most significant difference is the increased transition temperatures due to the removal of frustration by setting $J_b = 0$. Moreover, the pocket with a finite C_x component is slightly wider for the simple model, $x = 0.1 - 0.6$.

Thus, the complex Hamiltonian of the $LiNi_{1-x}Fe_xPO_4$ system may be simplified to a model that still captures the essential elements and produces an intermediate-temperature phase with a C_y type spin structure for $x = 0.3$. Subsequently for decreasing temperature, a C_x component emerges in superposition with the C_y structure. When emplying the complex full Hamiltonian, an additional C_z type order develops and suppresses the C_x type order at low temperatures. In the simplified model, however, no C_z component appears in the simulated temperature interval. The simulated temperature depedencies of the C_x and C_y order parameters as obtained with the simplified model correspond well to the ones measured with polarized neutrons at 4F1. A comparison of the temperature scan of $(0, 1, 2)$ perfomed at 4F1 and the corresponding simulation is shown in Fig. 8.37.

In summary, it was shown that frustration is not necessary in order to obtain a C_x spin component for $x = 0.3$. Instead, the interplay between the single-ion anisotropies of the Fe and Ni ions is believed the key factor and future simulations are planned to investigate this issue.

8.4 Summary and outlook

All results on the $LiNi_{1-x}Fe_xPO_4$ system presented in this chapter are summarized here – both with regards to experiments and simulations. As is apparent from our investigations, there are still a number of open questions and future experiments, simulations and theoretical studies are also suggested in the following.

The magnetic phase diagram of $LiNi_{0.94}Fe_{0.06}PO_4$ was characterized using magnetization measurements and neutron diffraction. At zero field a transition is observed as a function of temperature at $\sim 20\,\mathrm{K}$ where the spins order in a commensurate structure of $(\uparrow\uparrow\downarrow\downarrow)$ symmetry with spins along c. An incommensurate phase exists in a $\sim 1\,\mathrm{K}$ wide interval between the paramagnetic and the commensurate antiferromagnetic phase. These phases are very similar to those in $LiNiPO_4$[42,48,61]. For fields applied along c, there is additionally an field-induced phase transition at $\sim 10\,\mathrm{T}$. Based on the continued existence of the $(0,1,0)$ magnetic Bragg peak and a higher magnetic susceptibility, it is suggested that the spins re-orient in the high-field phase but that the structure remains commensurate. This is different to $LiNiPO_4$ where the field-induced transition leads to an incommensurate spiral structure[48,61]. Finally, spin-wave measurements enabled the determination of exchange and single-ion anisotropy constants. The fitted parameters proved very similar to those of the parent compound, $LiNiPO_4$[53], except for a ~ 7 times lower single-ion anisotropy constant for spins along a.

Likewise, the magnetic phase diagram of $LiNi_{0.8}Fe_{0.2}PO_4$ was investigated using magnetization measurements, pyrocurrent measurements as well as diffraction with and without polarized neutrons. In this compound two transitions are observed at $T_{N1} \approx 25\,\mathrm{K}$ and $T_{N2} \approx 20\,\mathrm{K}$ in zero field. A polarized neutron diffraction experiment revealed that the magnetic structure in the intermediate phase, $T_{N2} < T < T_{N1}$, is of $(\uparrow\uparrow\downarrow\downarrow)$ symmetry and with spins along b. For $T < T_{N2}$, the spins order with the same symmetry but oriented in the (a,b)-plane with major component along a. Pyrocurrent measurements showed that the magnetoelectric tensor elements $\alpha_{ab}, \alpha_{bb} \neq 0$ are active for $T_{N2} < T < T_{N1}$. For $T < T_{N2}$, the additional elements $\alpha_{aa}, \alpha_{ba} \neq 0$ emerge. Note that only tensor elements with $\mathbf{E}||\mathbf{a}$ and $\mathbf{E}||\mathbf{b}$ were probed. $LiNi_{0.8}Fe_{0.2}PO_4$ therefore displays the magnetoelectric effect and with more finite tensor elements than the parent compounds, $LiNiPO_4$ ($\alpha_{ac}, \alpha_{ca} \neq 0$) and $LiFePO_4$ ($\alpha_{ab}, \alpha_{ba} \neq 0$). Results from neutron diffraction and magnetization measurements suggest a spin re-orientation above a field-induced transition at $\sim 8\,\mathrm{T}$ applied along a. It is noteworthy that the strongest response in the electric polarization for $\mathbf{E}||\mathbf{a}$, $\mathbf{H}||\mathbf{a}$ is found precisely at this transition. Similarly, the largest signal in the electric polarization for $\mathbf{E}||\mathbf{b}$, $\mathbf{H}||\mathbf{b}$ coincides with a very subtle transition observed in the magnetization at $4\,\mathrm{T}$. The temperature and magnetic field dependencies of the obtained electric polarizations are highly complex and by far understood yet. Finally, inelastic neutron scattering measurements revealed that for magnetic fields applied along a the energy gap at $\mathbf{Q} = (0,1,0)$ describes a "W" shaped double transition at $6 - 9\,\mathrm{T}$ and the spin-wave spectrum at $12\,\mathrm{T}$ is remarkably similar to that in zero field.

For both systems studied here, the field-induced phase transition for fields applied along their respective easy axes displays anomalous behavior. The curve shape of the intensity of the $(0,1,0)$ magnetic Bragg peak as a function of applied field

depends heavily on the field ramp direction. Moreover, the intensity does not recover the same level above the phase transition after ramping the field down and back up. The observed behavior may be due to non-equilibrium effects although more investigations are needed in order to confirm or falsify this hypothesis.

Overall, substituting 6% Fe onto the magnetic site in $LiNiPO_4$ preserves the magnetic behavior but with a couple of twists. Substituting 20% Fe, however, creates a system with a strong competition between the mixed magnetic anisotropies and the exchange field. Both systems were investigated in zero field and for magnetic fields applied along their respective easy axes. However, it would be interesting to look more into the response to magnetic fields applied along b since this is the local easy axis for the Fe ions.

That the Ni and Fe ions order magnetically together in $LiNi_{0.8}Fe_{0.2}PO_4$ is supported by all experimental and simulated data recorded during this project. Nevertheless, it would no doubt be enlightening to perform a resonant synchrotron X-ray diffraction experiment. Tuning the X-ray energy onto a Ni or Fe absorption edge would allow for the separation of magnetic signals from the two different ions.

Monte Carlo simulations using the Metropolis algorithm were performed in order to gain a better insight into the general $LiNi_{1-x}Fe_xPO_4$ system and to assist in the interpretation of experimental data. For $x = 0.3$, the simulated temperature dependencies of the C_y and C_x symmetry components reproduce the observed behavior in $LiNi_{0.8}Fe_{0.2}PO_4$. This was done using the full spin Hamiltonian and parameters for $LiNiPO_4$ and $LiFePO_4$ as found in Refs. 53 and 54 respectively. Interaction between different ion flavors, Ni-Fe, were calculated as an average of the Ni-Ni and Fe-Fe interactions. Using a model with a much simplified spin Hamiltonian sufficed to yield temperature-dependent behavior of the C_x and C_y magnetic structure components in good agreement with that observed in the polarized neutron experiment.

As a last remark, the Monte Carlo approach opens up for simulating endless different configurations including other magnetic ions, vacancies or clustered configurations as well as exploring the system's response to external variables such as magnetic field. Furthermore, the code is not limited to the $LiA_{1-x}B_xPO_4$ system but merely takes parameters for any orthorhombic system with a face-centered or basic magnetic unit cell.

Conclusions

Throughout this work, magnetic and magnetoelectric properties of $LiCoPO_4$, $LiNiPO_4$ and $LiNi_{1-x}Fe_xPO_4$ were characterized by means of magnetization measurements, pyrocurrent measurements, heat capacity measurements, neutron diffraction, inelastric neutron scattering and Monte Carlo simulations. Conclusions and remarks regarding all results are presented below.

For $\mathbf{LiCoPO_4}$, magnetic ordering was investigated up to 25.9 T applied along the easy b-axis, i.e. close to the saturation field at 28.3 T. The zero-field magnetic structure was refined to be a $(\uparrow\uparrow\downarrow\downarrow)$ arrangement with spins along b and with an additional component along c of symmetry $(\uparrow\downarrow\downarrow\uparrow)$. Consequently, the magnetic point group is reduced to m'_z which is also consistent with the observed magnetoelectric effect and a weak ferromagnetic moment. Upon applying a magnetic field along b, a series of phase transitions are observed at 11.9, 20.5 and 21.0 T. For fields greater than 11.9 T, the magnetic unit cell triples in size with propagation vector $\mathbf{Q} = (0, \frac{1}{3}, 0)$. A magnetized elliptic cycloid is formed with spins in the (b, c) plane and the major axis oriented along b. In the transition region, $11.4 - 11.9$ T, additional ordering vectors $\mathbf{Q} \approx (0, \frac{1}{4}, 0)$ and $\mathbf{Q} \approx (0, \frac{1}{2}, 0)$ appear and a simple model is proposed in order to explain these. The model suggests the existence of even more ordering vectors of the type $\mathbf{Q} = (0, \frac{1}{n}, 0)$ at lower temperatures. In the field interval $20.5 - 21.0$ T, the propagation vector $\mathbf{Q} = (0, \frac{1}{3}, 0)$ remains but the spins orient differently compared to the cycloid phase. Above 21.0 T and for fields up to saturation, a commensurate magnetic structure exists with a ferromagnetic component along b and an antiferromagnetic component along c. Studies with magnetic fields up to 16 T applied along a, show that the induced ferromagnetic moment couples via the Dzyaloshinskii-Moriya interaction to yield an additional, field-induced spin canting. The maximum strength of the Dzyalonshinskii-Moriya interaction was estimated based on the induced canting angle to be approximately as large as the single-ion anisotropy constant along c. Hence, it is clear that the Dzyaloshinskii-Moriya interaction may play an important role in describing the spin Hamiltonian in $LiCoPO_4$.

The magnetic phase diagram of $\mathbf{LiNiPO_4}$ was studied up to a staggering 42 T applied along the easy c-axis. Phase transitions were observed at 12.0, 16.0, 19.1, 20.9, 37.6 and 39.4 T. The magnetic ordering vectors in previously observed phases at $19.1 - 20.9$ T and $20.9 - 37.6$ T were confirmed. In the latter phase the magnetic structure is likely a spiral propagating along b with spins in the transverse plane.

The ordering in the field range $37.6 - 39.4\,\mathrm{T}$ is similar to the previous phase but the structure displays an increased magnetic susceptibility. For fields greater than $39.4\,\mathrm{T}$, a commensurate phase is established and the proposed spin structure is similar to the structures found in the other commensurate phases at $0 - 12\,\mathrm{T}$ and $19.1 - 20.9\,\mathrm{T}$. Moreover, this high-field phase also exhibits the magnetoelectric effect and an extended version of the microscopic model explaining the effect in previous magnetoelectric phases also succeeds in describing the effect here.

The mixed compounds, $\mathbf{LiNi}_{1-x}\mathbf{Fe}_x\mathbf{PO}_4$, were investigated experimentally for $x = 0.06, 0.2$ and by using Monte Carlo simulations for the full range, $x \in [0, 1]$. For low concentrations of Fe, the system behaves like the parent compound, $LiNiPO_4$: c remains the easy axis and an incommensurate phase exists in a $\sim 1\,\mathrm{K}$ interval between the paramagnetic and the commensurate antiferromagnetic phase. For $x = 0.06$, a field-induced phase transitions appears at $\sim 10\,\mathrm{T}$ applied along c and it is suggested a spin re-orientation takes place here. For higher concentrations of Fe, $x = 0.2$, the easy direction changes and two commensurate phases are observed as a function of temperature starting at $T_{N1} \approx 25\,\mathrm{K}$ and $T_{N2} \approx 20\,\mathrm{K}$ in zero field. For $T_{N2} < T < T_{N1}$, spins order entirely along b whereas for $T < T_{N2}$, they order in the (a, b)-plane with major component along a. Therefore, this material behaves neither like $LiNiPO_4$ nor like $LiFePO_4$. Moreover, it does not exhibit a simple mixed phase as predicted by mean-field theory in systems with random magnetic anisotropy[79] and observed e.g. in $Fe_{1-x}Co_xCl_2$[83]. Nor does it display a glassy phase like $Fe_xNi_{1-x}F_2$[85]. For magnetic fields applied along a, a phase transition appears around $\sim 8\,\mathrm{T}$ where again a spin re-orientation is suggested. Pyrocurrent measurements showed that the magnetoelectric tensor elements $\alpha_{ab}, \alpha_{bb} \neq 0$ are finite for $T_{N2} < T < T_{N1}$. For $T < T_{N2}$, the additional elements $\alpha_{aa}, \alpha_{ba} \neq 0$ emerge. Hence, there are more active tensor elements for $x = 0.2$ than for $x = 0.00$ ($\alpha_{ac}, \alpha_{ca} \neq 0$) and $x = 1.00$ ($\alpha_{ab}, \alpha_{ba} \neq 0$). The temperature and magnetic field dependencies of the various elements are complex and by far understood. Finally, spin-wave measurements on both samples enabled probing of the spin Hamiltonian. For $x = 0.06$, the fitted exchange and single-ion anisotropy parameters are very similar to those of the parent compound, $LiNiPO_4$, except for a lower single-ion anisotropy constant for spins along a. For $x = 0.2$, a peculiar "W" behavior of the excitation at $\mathbf{Q} = (0, 1, 0)$ as a function of magnetic field applied along a was discovered. Furthermore, at $12\,\mathrm{T}$ the spin-wave spectrum is remarkably similar to that in zero field. Monte Carlo simulations reproduce the zero-field results using a simplified spin Hamiltonian for the $LiNi_{1-x}Fe_xPO_4$ system and the (x, T) magnetic phase diagram is constructed. A mixed phase with spin components mainly in the (a, b)-plane exists in the interval $x \approx 0.1 - 0.6$ and the simulated temperature dependencies of the C_y and C_x symmetry components for $x = 0.3$ correspond well with the ones observed using polarized neutron diffraction for $x = 0.2$.

The lithium orthophoshates were here studied in order to understand their magnetic phases and spin dynamics but also in order to cast light on the mechanism(s) causing the magnetoelectric effect displayed by these compounds. All previously known magnetoelectric phases in these materials are commensurate and this also holds for the new magnetoelectric phases identified during this thesis work – both for stoichiometric and mixed compounds. The microscopic origin for the effect in $LiNiPO_4$ and $LiFePO_4$ are found in field-induced changes in the exchange and Dzyloshinskii-Moriya interactions respectively. In both cases, a non-collinear albeit

commensurate zero-field structure forms the basis for the suggested models. Hence, it seems that we are close to an all-embracing understanding of the magnetoelectric effect in these materials. However, a succesful model for the mechanism(s) in $LiCoPO_4$ is still to be established and only preliminary investigations of the effect in the mixed compounds, $LiNi_{1-x}Fe_xPO_4$, were carried out.

Although intensively studied for half a century, the lithium orthophosphates still hold interesting physical phenomena to be explored. Especially understanding the magnetoelectric effect carries the promise of tayloring materials functional at room temperature for future applications. Thus, drawing a thread back to the introduction, this thesis comes to an end.

Appendix A

Monte Carlo code testing and additional simulations

The Monte Carlo code has been subject to various kinds of tests before attempting to run simulations describing the real $LiA_{1-x}B_xPO_4$ systems. Among the test models are a number of simple cases which are possible to evaluate analytically or numerically directly from statistical mechanics. Further tests regard symmetry equivalent configurations. Simulation results on the $LiNi_{1-x}Fe_xPO_4$ system supplementing Section 8.3 are found in the last section of this appendix.

A.1 Comparison with analytical results

Four analytically or numerically evaluable models were used for testing the Monte Carlo code. The simple Heisenberg case with just a single nearest neighbor coupling was described in Section 5.3. Here, the energy calculations for three other simple models are shown. Test results for all four models and different values of β/J are shown in Fig. 5.3 in Section 5.3. There is a very good agreement between the simulated and exact or numerical values.

Single-ion anisotropy. A system where only one of the anisotropies is finite, e.g. $\mathfrak{D}^x = \mathfrak{D}$, and all other parameters are zero, may be calculated exact. It is sufficient to regard just a single spin since, in the absence of exchange and DM interactions, they all are independent. The partition function is then:

$$Z = \int_0^\pi d\theta \, \sin\theta \int_0^{2\pi} d\varphi \, e^{-\mathfrak{D}\beta\cos^2\theta},$$

where θ and φ are the usual polar and azimuthal angles in a spherical coordinate system. Changing variable, $x = \cos\theta$, yields:

$$Z = 2\pi \int_{-1}^{1} dx \, e^{-\mathfrak{D}\beta x^2} = 2\pi\sqrt{\frac{\pi}{\mathfrak{D}\beta}} \, \mathrm{erf}\left(\sqrt{\mathfrak{D}\beta}\right),$$

where $\mathrm{erf}(x)$ is the error function. Differentiating with respect to β leads to the

energy as follows:

$$E = -\frac{\partial}{\partial\beta}\ln Z = -\frac{1}{Z}\frac{\partial Z}{\partial\beta} = \frac{1}{2\beta} - \sqrt{\frac{\mathfrak{D}}{\beta\pi}}\,\frac{e^{-\mathfrak{D}\beta}}{\operatorname{erf}\left(\sqrt{\mathfrak{D}\beta}\right)}.$$

With 4 ions in the unit cell, the above energy needs multiplication by a factor of 4 when comparing with simulation results. This model was also tested with $\mathfrak{D} = -1\,\text{meV}$ and with two finite anisotropies, i.e. $\mathfrak{D}^x = \mathfrak{D}^y = \mathfrak{D} = 1\,\text{meV}$. The latter case is symmetry-wise equal to the $\mathfrak{D} = -1\,\text{meV}$ case but the energy is displaced $4\mathfrak{D}$.

Exchange and anisotropy. The Hamiltonian for two interacting spins with one single-ion anisotropy taken into account ($J_{bc} = J = 1$, $\mathfrak{D}^x = \mathfrak{D} = 1$) looks a bit more complicated:

$$\hat{\mathcal{H}}_{\text{ex+ani}} = J\,\mathbf{S}_1\cdot\mathbf{S}_2 + \mathfrak{D}\left((S_1^z)^2 + (S_2^z)^2\right) = J\cos(\theta) + \mathfrak{D}\left(\cos^2(\theta_1) + \cos^2(\theta_2)\right),$$

where θ is now the relative angle between spin 1 and 2 depending on all four spin coordinates: θ_1, θ_2, φ_1 and φ_2 [see Fig. A.1]. The spin orientations in Cartesian coordinates are given as:

$$\begin{aligned} x_1 &= \cos(\varphi_1)\sin(\theta_1), \quad y_1 = \sin(\varphi_1)\sin(\theta_1), \quad z_1 = \cos(\theta_1)\\ x_2 &= \cos(\varphi_2)\sin(\theta_2), \quad y_2 = \sin(\varphi_2)\sin(\theta_2), \quad z_2 = \cos(\theta_2). \end{aligned}$$

With these, the relative angle is found via the scalar product as follows:

$$\begin{aligned} &\mathbf{S}_1\cdot\mathbf{S}_2 = S_1S_2\cos(\theta) \quad \Rightarrow\\ &\cos(\theta) = \cos(\varphi_1)\sin(\theta_1)\cos(\varphi_2)\sin(\theta_2) + \sin(\varphi_1)\sin(\theta_1)\sin(\varphi_2)\sin(\theta_2) + \cos(\theta_1)\cos(\theta_2)\\ &\quad = \Big(\cos(\varphi_1)\cos(\varphi_2) + \sin(\varphi_1)\sin(\varphi_2)\Big)\sin(\theta_1)\sin(\theta_2) + \cos(\theta_1)\cos(\theta_2)\\ &\quad = \frac{1}{2}\Big(\cos(\varphi_1-\varphi_2) + \cos(\varphi_1+\varphi_2) + \cos(\varphi_1-\varphi_2) - \cos(\varphi_1+\varphi_2)\Big)\sin(\theta_1)\sin(\theta_2)\\ &\qquad\qquad + \cos(\theta_1)\cos(\theta_2)\\ &\quad = \cos(\varphi_1-\varphi_2)\sin(\theta_1)\sin(\theta_2) + \cos(\theta_1)\cos(\theta_2), \end{aligned}$$

where the identities $2\cos(a)\cos(b) = \cos(a-b) + \cos(a+b)$ and $2\sin(a)\sin(b) = \cos(a-b) - \cos(a+b)$ were used. The Hamitonian now becomes:

$$\hat{\mathcal{H}}_{\text{ex+ani}} = J\big[\cos(\varphi_1-\varphi_2)\sin(\theta_1)\sin(\theta_2) + \cos(\theta_1)\cos(\theta_2)\big] + \mathfrak{D}\big[\cos^2(\theta_1) + \cos^2(\theta_2)\big],$$

and hence the partition function is:

$$Z = \int_0^\pi d\theta_1\ \sin(\theta_1)\int_0^{2\pi} d\varphi_1\int_0^\pi d\theta_2\ \sin(\theta_2)\int_0^{2\pi} d\varphi_2 \times e^{-J\beta[\cos(\varphi_1-\varphi_2)\sin(\theta_1)\sin(\theta_2)+\cos(\theta_1)\cos(\theta_2)] - \mathfrak{D}\beta\left(\cos^2(\theta_1)+\cos^2(\theta_2)\right)}.$$

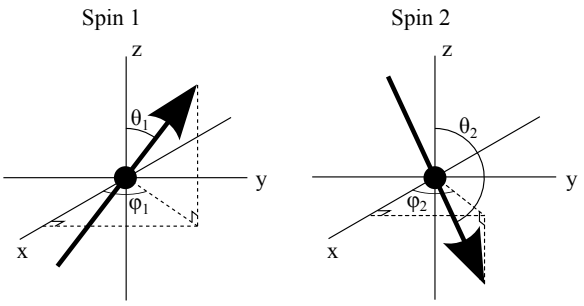

Figure A.1: *Coordinates of spins 1 and 2 as considered for the system with both exchange interaction and single-ion anisotropy as well as for the DM interaction.*

This is a rather nasty integral. However, it only depends on the difference in the coordinates, $\varphi_1 - \varphi_2$, and hence effectively the number of variables is reduced. Using $x = \varphi_1 - \varphi_2$ we have $dx = -d\varphi_2$ together with $x(\varphi_2 = 0) = \varphi_1$ and $x(\varphi_2 = 2\pi) = \varphi_1 - 2\pi$. The partition function can then be written:

$$\begin{aligned} Z &= \int_0^\pi d\theta_1 \ \sin(\theta_1) \int_0^\pi d\theta_2 \ \sin(\theta_2)\, e^{-J\beta\cos(\theta_1)\cos(\theta_2)}\, e^{-\mathfrak{D}\beta\left[\cos^2(\theta_1)+\cos^2(\theta_2)\right]} \\ &\qquad \times \int_0^{2\pi} d\varphi_1 \int_0^{2\pi} d\varphi_2 \ e^{-J\beta\cos(\varphi_1-\varphi_2)\sin(\theta_1)\sin(\theta_2)} \\ &= \int_0^\pi d\theta_1 \ \sin(\theta_1) \int_0^\pi d\theta_2 \ \sin(\theta_2)\, e^{-J\beta\cos(\theta_1)\cos(\theta_2)}\, e^{-\mathfrak{D}\beta\left[\cos^2(\theta_1)+\cos^2(\theta_2)\right]} \\ &\qquad \times \int_0^{2\pi} d\varphi_1 \int_{\varphi_1}^{\varphi_1-2\pi} (-dx)\ e^{-J\beta\cos(x)\sin(\theta_1)\sin(\theta_2)}. \end{aligned}$$

Performing the integral over φ_1 yields a factor of 2π and without loss of generality we can choose $\varphi_1 = 0$ for performing the integral over x. We then get:

$$\begin{aligned} Z &= 2\pi \int_0^\pi d\theta_1 \ \sin(\theta_1) \int_0^\pi d\theta_2 \ \sin(\theta_2)\, e^{-J\beta\cos(\theta_1)\cos(\theta_2)}\, e^{-\mathfrak{D}\beta\left[\cos^2(\theta_1)+\cos^2(\theta_2)\right]} \\ &\qquad \times \int_0^{-2\pi} (-dx)\ e^{-J\beta\cos(x)\sin(\theta_1)\sin(\theta_2)} \\ &= 2\pi \int_0^\pi d\theta_1 \ \sin(\theta_1) \int_0^\pi d\theta_2 \ \sin(\theta_2)\, e^{-J\beta\cos(\theta_1)\cos(\theta_2)}\, e^{-\mathfrak{D}\beta\left[\cos^2(\theta_1)+\cos^2(\theta_2)\right]} \\ &\qquad \times \int_{-2\pi}^{0} dx\ e^{-J\beta\cos(x)\sin(\theta_1)\sin(\theta_2)} \\ &= 4\pi^2 \int_0^\pi d\theta_1 \ \sin(\theta_1) \int_0^\pi d\theta_2 \ \sin(\theta_2)\, e^{-J\beta\cos(\theta_1)\cos(\theta_2)}\, e^{-\mathfrak{D}\beta\left[\cos^2(\theta_1)+\cos^2(\theta_2)\right]} \\ &\qquad \times I_0\left(J\beta\sin(\theta_1)\sin(\theta_2)\right), \end{aligned}$$

where I_0 is the zeroth order modified Bessel function of the first kind. To optain the energy, we have to differentiate with respect to β as usual:

$$\begin{aligned} \frac{\partial Z}{\partial\beta} &= \frac{\partial}{\partial\beta}\Bigg[4\pi^2 \int_0^\pi d\theta_1 \ \sin(\theta_1) \int_0^\pi d\theta_2 \ \sin(\theta_2)\, e^{-J\beta\cos(\theta_1)\cos(\theta_2)}\, e^{-\mathfrak{D}\beta\left[\cos^2(\theta_1)+\cos^2(\theta_2)\right]} \\ &\qquad \times I_0\left(J\beta\sin(\theta_1)\sin(\theta_2)\right)\Bigg] \\ &= 4\pi^2 \int_0^\pi d\theta_1 \ \sin(\theta_1) \int_0^\pi d\theta_2 \ \sin(\theta_2)\, e^{-J\beta\cos(\theta_1)\cos(\theta_2)}\, e^{-\mathfrak{D}\beta\left[\cos^2(\theta_1)+\cos^2(\theta_2)\right]} \\ &\qquad \times \Bigg(-\Big[J\cos(\theta_1)\cos(\theta_2) + \mathfrak{D}(\cos^2(\theta_1)+\cos^2(\theta_2))\Big] I_0\left(J\beta\sin(\theta_1)\sin(\theta_2)\right) \\ &\qquad\qquad + J\sin(\theta_1)\sin(\theta_2) I_1\left(J\beta\sin(\theta_1)\sin(\theta_2)\right)\Bigg), \end{aligned}$$

where I_1 is the first order modified Bessel function of the first kind. From here on the remaining integrals are evaluated numerically for both Z and $\frac{\partial Z}{\partial\beta}$. This was done in MATLAB using the function `quad2d()`. Like described in Section 5.3, the exchange bond in a single unit cell simulation is actually $J \to 4J$ due to the periodic boundary conditions and with two ion layers in a unit cell $E \to 2E$.

It was confirmed that both the simple Heisenberg and the single-ion anisotropy models are recovered in the limits $J = 1$, $\mathfrak{D} = 0$ and $J = 0$, $\mathfrak{D} = 1$. This is indeed the case and the agreement between the exact and numerical results is very good.

Dzyaloshinskii-Moriya interaction. Finally, a unit cell with a single active DM interaction is considered. For the lithium orthophosphates the allowed DM interaction vector has the form $\mathbf{D} = (0, D, 0)$[48] yielding an interaction energy of:

$$\hat{\mathcal{H}}_{\mathrm{DM}} = \mathbf{D} \cdot (\mathbf{S}_1 \times \mathbf{S}_2) = D \left(\cos\varphi_2 \cos\theta_1 \sin\theta_2 - \cos\varphi_1 \sin\theta_1 \cos\theta_2\right),$$

and the partition function becomes:

$$\begin{aligned} Z &= \int_0^{2\pi} d\varphi_1 \int_0^{\pi} d\theta_1 \, \sin\theta_1 \int_0^{2\pi} d\varphi_2 \int_0^{\pi} d\theta_2 \, \sin\theta_2 \; e^{-\beta D(\cos\varphi_2 \cos\theta_1 \sin\theta_2 - \cos\varphi_1 \sin\theta_1 \cos\theta_2)} \\ &= \int_0^{\pi} d\theta_1 \, \sin\theta_1 \int_0^{\pi} d\theta_2 \, \sin\theta_2 \int_0^{2\pi} d\varphi_2 \; e^{-\beta D \cos\varphi_2 \cos\theta_1 \sin\theta_2} \int_0^{2\pi} d\varphi_1 \; e^{\beta D \cos\varphi_1 \sin\theta_1 \cos\theta_2} \\ &= 4\pi^2 \int_0^{\pi} d\theta_1 \int_0^{\pi} d\theta_2 \; \sin\theta_1 \, \sin\theta_2 \, I_0\left(\beta D \cos\theta_1 \sin\theta_2\right) \, I_0\left(\beta D \sin\theta_1 \cos\theta_2\right), \end{aligned}$$

where again I_0 denotes the zeroth order modified Bessel function of the first kind. The derivative of Z with respect β is:

$$\begin{aligned} \frac{\partial Z}{\partial \beta} = 4\pi^2 D \int_0^{\pi} d\theta_1 \int_0^{\pi} d\theta_2 \; \sin\theta_1 \, \sin\theta_2 \\ \times \Big(\cos\theta_1 \sin\theta_2 \, I_1\left(\beta D \cos\theta_1 \sin\theta_2\right) \, I_0\left(\beta D \sin\theta_1 \cos\theta_2\right) \\ + \sin\theta_1 \cos\theta_2 \, I_0\left(\beta D \cos\theta_1 \sin\theta_2\right) \, I_1\left(\beta D \sin\theta_1 \cos\theta_2\right) \Big). \end{aligned}$$

The integrals are again evaluated numerically in MATLAB using the `quad2d()` function and the energies are calculated as usual, $E = -\frac{1}{Z}\frac{\partial Z}{\partial \beta}$.

A.2 Symmetry checks

Simulations sporting combinations of interactions which should yield the same results from a symmetry point of view are run. For example, a configuration with only J_{bc} active and all other parameters set to zero is equivalent to having only J_{ab} or J_{ac} active. This scenario is illustrated in Fig. A.2. Hence, in the first set of runs all parameters are put to zero except one. The resulting energies for different values of β are shown in Table A.1. Relatively good agreement between the symmetry equivalent interactions (J_{bc}, J_{ab}, J_{ac}), (J_b, J_c) and $(\mathfrak{D}^a, \mathfrak{D}^b, \mathfrak{D}^c)$ are seen. Note that the DM interaction was deactivated for all symmetry-related test runs.

Likewise, in the next set of runs all parameters are put to 1 meV except one. In order to obtain symmetry between J_{bc}, J_{ab} and J_{ac}, $J_b = J_c = 0$. The results are shown in Table A.2. Here there are some differences for $(\mathfrak{D}^a, \mathfrak{D}^b, \mathfrak{D}^c)$ for $\beta = 10, 50$. It appears that the simulation does not quite relax to the ground state every time and there may be a problem with the implementation of the anisotropies. To investigate this issue, additional runs were performed with two of the anisotropy constants set to 1 meV and the remaining parameters set to zero. The results are listed in Table A.3. For these runs the agreement between symmetry equivalent configurations is good so somehow the discrepancies only occur for a combination of J's and $\mathfrak{D}$'s.

Table A.1: *Total energies for simulations with 4x4x4 unit cells and all parameters set to zero except the one listed in the leftmost column. For the first row* $J_{bc} = 1\,\mathrm{meV}$, $J_{ab} = J_{ac} = J_b = J_c = \mathfrak{D}^a = \mathfrak{D}^b = \mathfrak{D}^c = 0$ *and so on. These runs were with* 10^5 *MCS and quenching.*

β	1/2	1	2	10	50
J_{bc}	-88.7338(838)	-206.1457(2110)	-378.1134(1320)	-486.9846(403)	-507.0543(106)
J_{ab}	-88.8698(840)	-205.9186(2144)	-377.8939(1350)	-486.8985(419)	-507.0740(103)
J_{ac}	-88.5704(808)	-205.7845(2058)	-377.7429(1344)	-486.8851(429)	-507.0314(105)
J_b	-43.0417(470)	-86.4340(570)	-155.1593(650)	-236.6397(272)	-252.142(80)
J_c	-43.0998(464)	-86.4868(590)	-155.1857(637)	-236.5974(268)	-252.1568(79)
$\mathfrak{D}^a$	74.5055(252)	64.9396(238)	49.5187(218)	12.7802(90)	2.5600(27)
$\mathfrak{D}^b$	74.5311(248)	64.9293(246)	49.4950(218)	12.7938(90)	2.5586(27)
$\mathfrak{D}^c$	74.5467(251)	65.0087(234)	49.4808(220)	12.7983(92)	2.5564(28)

Table A.2: *Total energies for simulations with 4x4x4 unit cells and all parameters set to* $1\,\mathrm{meV}$ *except the one in the leftmost column. For the first row* $J_{bc} = 0$, $J_{ab} = J_{ac} = \mathfrak{D}^a = \mathfrak{D}^b = \mathfrak{D}^c = 1\,\mathrm{meV}$ *and so on.* $J_b = J_c = 0$ *always to obtain face-centered symmetry. These runs were with* 10^5 *MCS and quenching.*

β	1/2	1	2	10	50
$-J_{bc}$	-86.3599(7841)	-490.9544(2668)	-636.0875(1608)	-742.4680(459)	-762.8377(122)
$-J_{ab}$	-87.2467(7894)	-491.1140(2643)	-635.8408(1580)	-742.2877(513)	-762.8628(116)
$-J_{ac}$	-86.7313(7933)	-490.8867(2619)	-636.0194(1652)	-742.3254(482)	-762.8895(197)
$-\mathfrak{D}^a$	-6.5544(1023)	-122.7335(1812)	-371.6795(1599)	-486.1290(461)	-506.8519(4466)
$-\mathfrak{D}^b$	-6.7336(993)	-122.2501(1793)	-371.3375(1639)	-485.9986(464)	-506.8379(110)
$-\mathfrak{D}^c$	-6.5321(1010)	-122.3701(1785)	-371.2852(1617)	-454.0532(437)	-500.3510(7477)

Table A.3: *Total energies for simulations with 4x4x4 unit cells and all parameters set to zero except the anisotropy constants given in the leftmost column. For the first row* $\mathfrak{D}^a = \mathfrak{D}^b = 1\,\mathrm{meV}$, $J_{bc} = J_{ab} = J_{ac} = J_b = Jc = \mathfrak{D}^c = 0$ *and so on. These runs were with* 10^5 *MCS and quenching.*

	1/2	1	2	10	50
$\mathfrak{D}^a, \mathfrak{D}^b$	158.7744(273)	146.1994(317)	119.9922(377)	27.4466(264)	5.1882(90)
$\mathfrak{D}^b, \mathfrak{D}^c$	158.7639(285)	146.0126(324)	119.9547(380)	27.4422(262)	5.1610(84)
$\mathfrak{D}^c, \mathfrak{D}^a$	158.7787(286)	146.1420(313)	119.9577(383)	27.4282(276)	5.1789(86)

Table A.4: *These runs are exactly like those in the bottom half of Table A.2 except that these are done with simulated annealing.*

β	1/2	1	2	10	50
$-\mathfrak{D}^a$	-6.5806(1010)	-122.6107(1753)	-371.6155(1592)	-486.0918(459)	-506.8971(106)
$-\mathfrak{D}^b$	-6.5074(1043)	-122.5368(1759)	-371.8058(1662)	-486.0112(438)	-506.8636(110)
$-\mathfrak{D}^c$	-6.6242(981)	-122.4997(1746)	-371.5613(1721)	-485.9964(435)	-506.8767(115)

Finally, the runs in the bottom half of Table A.2 were repeated but this time with simulated annealing to see if the problems with the single-ion anisotropies are related to difficulties with reaching the ground state. The results for these runs are shown in Table A.4 and now there is a better agreement between different equivalent configurations. A comparison of simulations performed with quenching and simulated annealing are shown in Fig. A.3. Clearly, there is a problem with the simulations relaxing to the lowest energy configuration when quenching to low temperatures. It is not immediately obvious whether this exposes a major problem in the code but it certainly means that simulations should generally be run using simulated annealing.

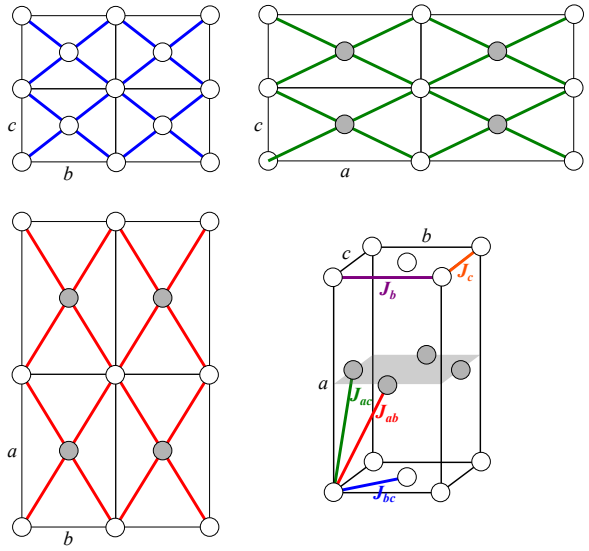

Figure A.2: *Symmetry equivalent configurations for J_{bc}, J_{ab} or $J_{ab} \neq 0$ and all other parameters set to zero. The 3D unit cell shows the different exchange interactions and the projections illustrate face-centered lattices created by J_{bc}, J_{ab} and J_{ab}.*

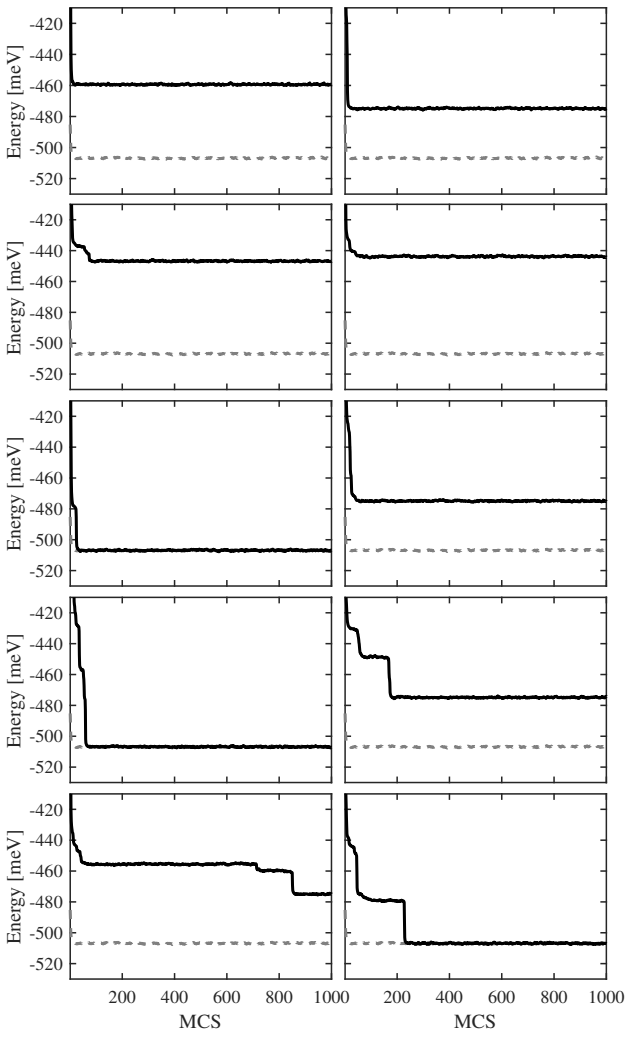

Figure A.3: *Total energy as a function of MCS for 10 different runs with $J_{bc} = J_{ab} = J_{ac} = \mathfrak{D}^b = \mathfrak{D}^c = 1\,meV$ and $\mathfrak{D}^a = 0$ and quenched to $\beta = 50$. The corresponding run performed with simulated annealing is shown with the dashed lines.*

A.3 More Monte Carlo simulations

This section contains additional simulation results to elaborate on and support the conclusions regarding the $LiNi_{1-x}Fe_xPO_4$ system in Section 8.3.

A, G, C and F order parameters. Fig. A.4 shows simulated energy, heat capacity and order parameters for A, G, C and F type structures as a function of temperature for $x = 0.0, 0.3, 1.0$. Note the variable y-axis limits. These simulations were performed with the exchange interactions and single-ion anisotropy constants listed in Tables 8.7-8.8 as found in Section 8.3. Interactions between Ni and Fe ions are defined as a mean of the Ni-Ni and Fe-Fe interactions.

For $x = 0.0$ and $x = 1.0$, the only sizeable temperature-dependent structure components are C_z and C_y respectively. This is expected from the known zero-field structures for the parent compounds, $LiNiPO_4$[48] and $LiFePO_4$[54]. For $x = 0.3$, all three components of C are active. Here, the A, G and F type structures also display temperature dependencies but the size of these components is 2-3 orders of magnitude smaller at low temperatures compared to the C components.

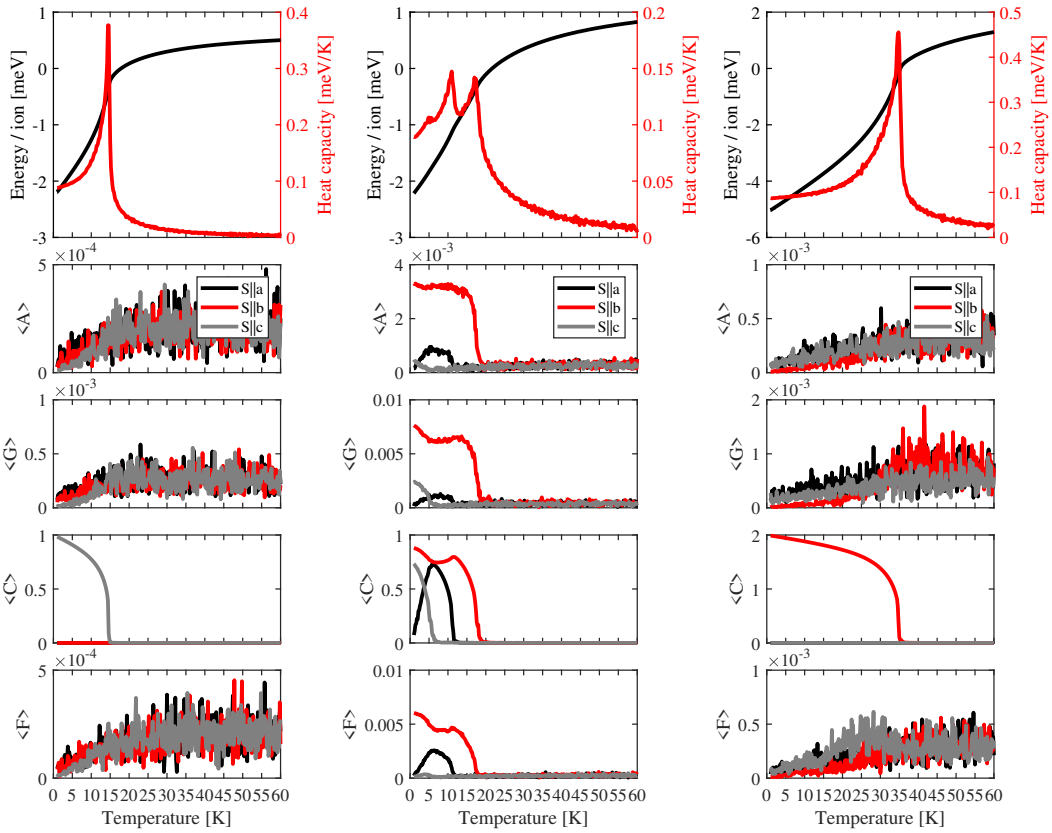

Figure A.4: *Temperature scans averaged over 5 runs, each performed with $L = 10$, 10^5 MCS, temperature range 1-60 K, temperature step 0.2 K, decreasing temperature and simulated annealing. Parameters are given in Tables 8.7-8.8. Top row: energy (black curve) and heat capacity (red curve) are shown for $x = 0.0$, 0.3 and 1.0 as a function of temperature. Four lower rows: measures for magnetic order of type A, G, C and F along a, b and c (black, red and grey curves respectively), shown for $x = 0.0$, 0.3 and 1.0 as above. Note the variable y-axis limits.*

Simulations with a different set of parameters for $LiFePO_4$. Several sets of parameters describing $LiFePO_4$ exist in literature. The ones used in Section 8.3 are from Ref. 54 where low-temperature (1.7 K) spin-wave spectra measured with inelastic neutron scattering are fitted to a dispersion relation [Eq. (8.2)] using the least squares method. The dispersion relation in Ref. 54 is derived from linear spin-wave theory[53]. In a later inelastic neutron study[8], a new low-energy nearly dispersionless mode is discovered at higher temperatures (35 K). This mode is not contained within the linear spin-wave theory and therefore, the authors employ the random phase approximation to determine the interaction parameters as well as single-ion anisotropies.

Using these new parameters [Tables A.5-A.6] in the Monte Carlo simulation yields the (x, T) phase diagrams illustrated in Figs. A.5 and A.6 for the heat capacity and C structures respectively. Again, for $x = 0.0$ and $x = 1.0$ respectively, the C_z and C_y structures are obtained. However, no spin component along a is observed in the intermediate phase at $x \approx 0.2 - 0.5$. Here, only a superposition of spin components along b and c exists.

Since $LiFePO_4$ has easy axis along b and $LiNiPO_4$ has easy axis along c, this is what one may naïvely expect when mixing Ni and Fe on the magnetic site, M, in $LiMPO_4$. However, our magnetization and neutron diffraction experiments show that for $LiNi_{0.8}Fe_{0.2}PO_4$ the major spin component is along a at low temperatures. Clearly, the set of parameters found in Ref. 8 does not reproduce these experimental observations and no further simulations were performed with them.

Now one may ask: why do the parameters in Ref. 54 work better than those found in Ref. 8? One reason may be that the parameters in Ref. 8 are determined such that the weakly dispersive mode observed at 35 K is included in the description of the system. At low temperatures, this mode is not populated and the high-temperature description may not be appropriate. It is pointed out that the ordering temperature of $LiNi_{0.8}Fe_{0.2}PO_4$ is $T_{N1} = 25.6(2)$ K as measured with neutrons.

Comparing the strength of the most important exchange interactions in the (b, c)-plane in Refs. 54 and 8 may hold another clue as to why the ones in Ref. 8 yield magnetic order different to the experimentally observed ones. In Ref. 54 the ratio between the strongest interactions in the (b, c)-plane is $J_{bc}/J_b \approx 2.5$ whereas in Ref. 8 it is $J_{bc}/J_b \approx 5$. This means that the parameters in Ref. 54 describe a more frustrated system than the parameters found in Ref. 8. In $LiNiPO_4$, the ratio is $J_{bc}/J_b \approx 1.5$[53] and in $LiMnPO_4$, the ratio is $J_b/J_{bc} \approx 2.5$[55] and hence, one may expect a similar level of frustration in the sister compound, $LiFePO_4$. However, as

Table A.5: *Exchange parameters for Ni-Ni, Ni-Fe and Fe-Fe bonds as used in the Monte Carlo simulations. The parameters for Ni-Ni are found in Ref. 53 and the ones for Fe-Fe are found in Ref. 8. The Ni-Fe exchange parameters are calculated as the mean.*

	J_{bc}	J_b	J_c	J_{ab}	J_{ac}
Ni-Ni	1.04	0.67	-0.05	0.30	-0.11
Ni-Fe	0.75	0.38	-0.02	0.195	-0.05
Fe-Fe	0.46	0.09	0.01	0.09	0.01

Table A.6: *Single-ion anisotropy constants for Ni and Fe as found in Refs. 53 and 8 respectively. The values for Fe are now larger than in Ref. 54.*

	$\mathfrak{D}^a$	$\mathfrak{D}^b$	$\mathfrak{D}^c$
Ni	0.339	1.82	0
Fe	0.86	0	2.23

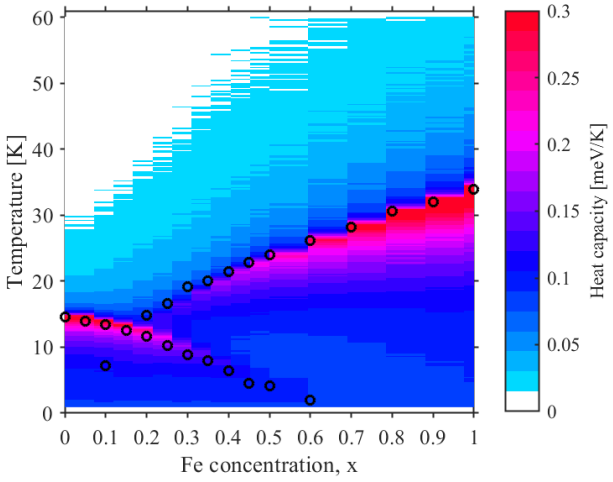

Figure A.5: *Color plot of the heat capacity as a function of x and T using the parameters shown in Tables A.5-A.6. Simulations are run with $L = 10$, 10^5 MCS, temperature range 0.6-100 K, temperature step 0.35 K, decreasing temperature and simulated annealing. Data is averaged over 5 runs for each value of x. Identified phase transitions are indicated with open circles.*

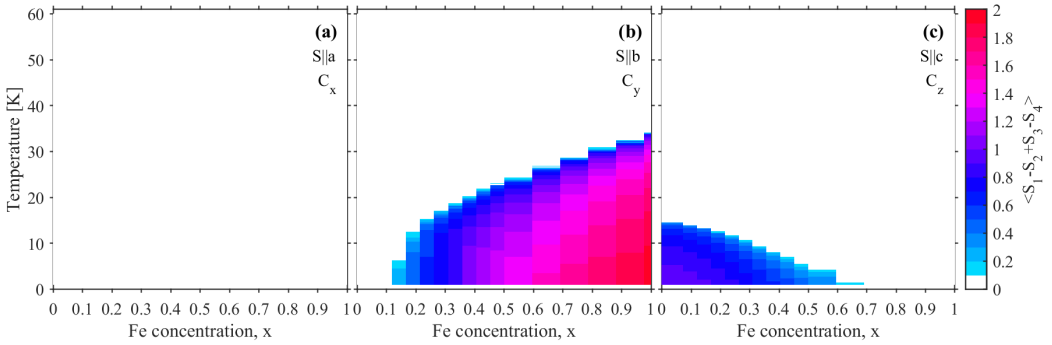

Figure A.6: *Color plots of the C type order parameter as a function of x and T using the parameters shown in Tables A.5-A.6. Simulations are run with $L = 10$, 10^5 MCS, temperature range 0.6-100 K, temperature step 0.35 K, decreasing temperature and simulated annealing. Data is averaged over 5 runs for each value of x. Only spin components along b and c are observed.*

was seen in Section 8.3, the degree of frustration is not important for obtaining a C_x type structure in the simulations. Finally, the overall strength of the exchange interactions found in Ref. 8 is ~ 1.5 smaller than in Ref. 54.

Another difference between the two sets of parameters in Refs. 54 and 8 is the sizes of the single-ion anisotropy constants. In Ref. 54, we have $\mathfrak{D}^a = 0.62\,\text{meV}$ and $\mathfrak{D}^c = 1.56\,\text{meV}$ as compared to $\mathfrak{D}^a = 0.86\,\text{meV}$ and $\mathfrak{D}^c = 2.23\,\text{meV}$ in Ref. 8. Hence, the single-ion anisotropy constants are ~ 1.4 times stronger in Ref. 8 compared to those found in Ref. 54. With the single-ion anisotropy term in the spin Hamiltonian, Eq. (5.1), being quadratic in S and $S = 2$ for Fe, small differences in the $\mathfrak{D}$'s result in relatively large differences in energy. This means that finding a configuration in the $LiNi_{1-x}Fe_xPO_4$ system with a spin component along a is much harder with $\mathfrak{D}^a = 0.86\,\text{meV}$ rather than $\mathfrak{D}^a = 0.62\,\text{meV}$.

Appendix B

Data analysis on the HFM/EXED and NOBORU experiments on $LiNiPO_4$

Some details on the data analysis regarding the HFM/EXED and NOBORU eperiments on $LiNiPO_4$ are presented here.

B.1 Zero-field data and background subtraction on NOBORU

In order to fit Gaussian profiles to the data with magnetic field on shown in Figs. 7.5(b)-(d) the peak widths were fixed to those obtained for the zero-field intensities. How this is done is briefly described in this section.

First of all, the background [Fig. B.1(a)] is fitted to various different functions and for $K \leq 7$ it turns out that a second order polynomial yields the best description. Note that this is an entirely emperical approach focussed on low values of K since magnetic peaks at high fields were observed for $K \approx 0.5 - 2$. Once the background is subtracted, Gaussian profiles are fitted to the observed Bragg peaks [Fig. B.1(b)]. The obtained peak widths are then fitted to a linear dependency, $\sigma(K) = \alpha K + \beta$ with $\alpha = 0.0143(1)$ and $\beta = 0.0022(7)$ r.l.u. [Fig. B.1(c)]. Now, when fitting Gaussian profiles to the field-on data in Figs. 7.5(b)-(d) the peaks widths are fixed according to this linear dependency.

B.2 Integrated peak intensities on HFM/EXED

The analysis for HFM/EXED is done in Mantid[122] and is based on a script written by Maciej Bartkowiak (HFM/EXED, HZB).

Peak positions on the forward scattering detector are indicated in Fig. B.2 for

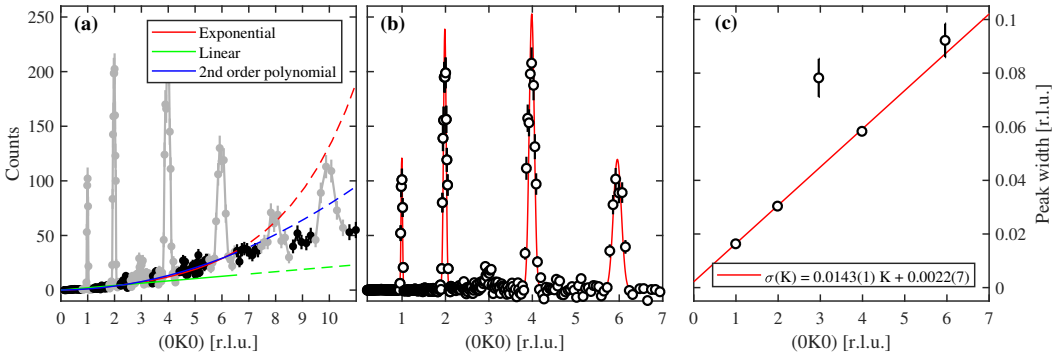

Figure B.1: *Zero-field data from NOBORU. (a) Neutron counts as a function of (0,K,0) up to K = 11 r.l.u. with different curves fitted to the background (black symbols). Bragg peaks (grey symbols) are observed at K = 1,2,3,4,6,8,10. Solid lines show fitted region (K ≤ 7 r.l.u.) and dashed lines are extrapolations. (b) Neutron counts as a function of (0,K,0) with a polynomial background subtracted and Gaussian profiles (red curve) fitted to the observed Bragg peaks. (c) Fitted peak width as a function of (0,K,0) with a linear dependency fitted (red line).*

the data taken at 1.3 K and 23 T. Rectangular masks and relevant TOF intervals are defined manually. The masks are chosen such that all pixels with increased intensity are included in the intensity calculation. The TOF intervals determine what part of the spectrum is part of the background and what part belongs to the peak. These are indicated for $(1, -1, 0)$ in Fig. B.3 and values for all identified peaks are listed in Table B.1. The integrated intensity of each peak is then found by the following steps:

1. TOF intervals are defined for background and peak
2. Mask is loaded
3. Data is corrected for monitor and Vanadium (detector efficiency)
4. A second order polynomial is fitted as background and subsequently subtracted
5. Intensity is calculated directly by summation

Resulting intensities are listed in Table B.2. It is clear that there are some problems with the obtained intensities as discussed in Sections 7.2 and 7.3. For instance, in the paramagnetic phase the intensities of the equivalent pair $(-1, -2, 0)$ and $(1, -2, 0)$ are 2.46(30) and 9.9(1.4) respectively! Moreover, some intensities are negative and for some peaks, e.g. $(0, -2, 0)$, the intensity is lower in phases IV and V compared to in the paramagnetic phase.

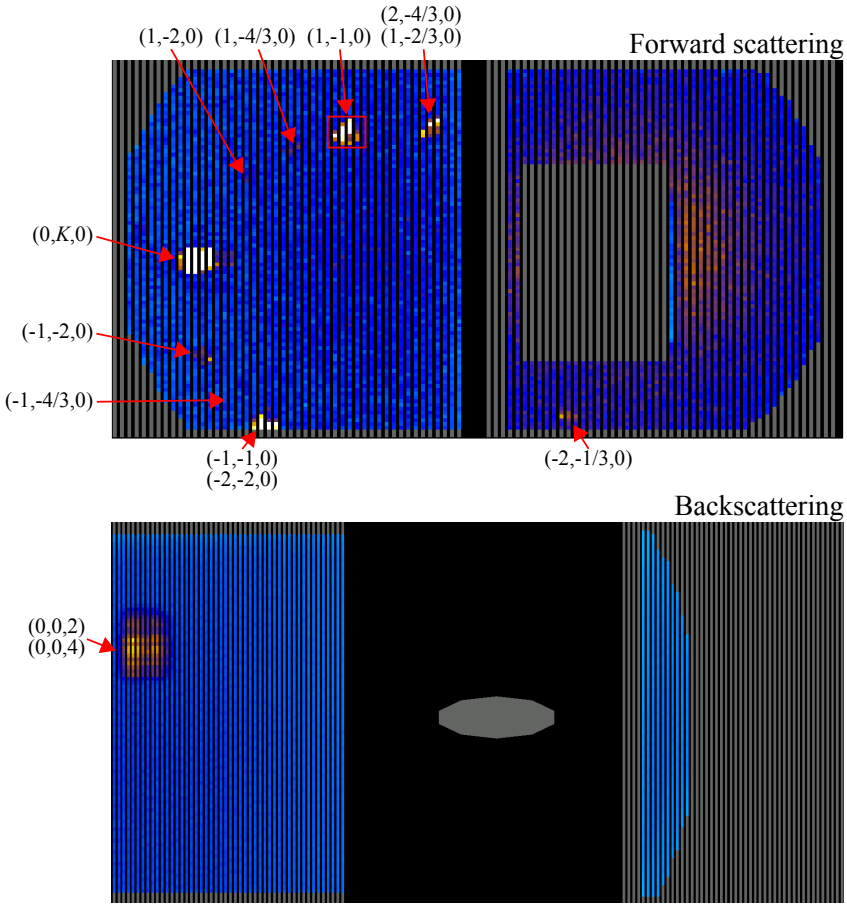

Figure B.2: *Forward scattering and backscattering detector images at 1.3 K and 23 T with various peak positions indicated. The red box on the forward scattering detector shows the rectangular mask for the (1,-1,0) Bragg peak. Images are shown for TOF intervals 10-17 ms and 62-69 ms for forward scattering and backscattering respectively.*

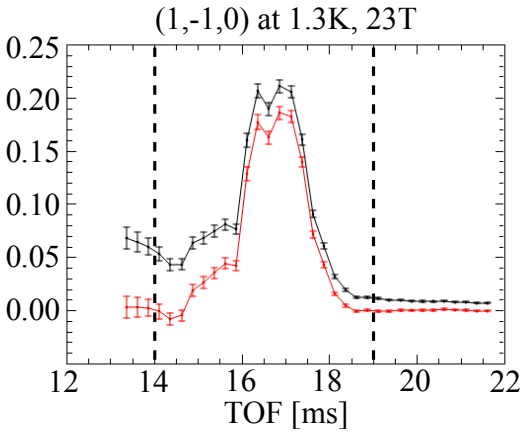

Figure B.3: *Lineshape of (1,-1,0) as a function of TOF without (black curve) and with (red curve) background subtraction. The vertical dashed lines show the TOF interval for which the peak is integrated in accordance with Table B.1.*

Table B.1: *List of TOF intervals for background fitting (first and last number) and for peak integration (two middle numbers) as well as mask detector indices for all identified Bragg peaks in phases IV and V.*

Peak	TOF [ms]	Mask detector indices
$(-1,-2,0)$	11, 12, 14, 16	13218-13224, 13118-13124, 13018-13024
$(-1,-\frac{4}{3},0)$	12, 16, 20, 23	12808-12812, 12708-12712, 12608-12612
$(-1,1,0)$	14, 19, 25, 30	12400-12408, 12300-12308, 12200-12208, 12100-12108, 12000-12008
$(-2,-2,0)$	8, 9.5, 11.5, 15	12400-12407, 12300-12307, 12200-12207, 12100-12107, 12000-12007
$(0,-2,0)$	8, 11, 14.5, 16	13543-13551, 13443-13451, 13343-13351, 13243-13251, 13143-13151, 13043-13051, 12943-12951
$(0,-\frac{4}{3},0)$	15, 17, 22, 23	13438-13450, 13338-13351, 13238-13250, 13138-13150, 13038-13050, 12938-13950
$(0,-1,0)$	22, 24.5, 27.5, 30	13338-13351, 13238-13250, 13138-13150, 13038-13050, 12938-13950
$(0,-\frac{2}{3},0)$	29, 31, 43, 45	13534-13551, 13434-13451, 13334-13351, 13234-31251, 13134-13151, 13034-13051, 12934-12951, 12834-12851, 12734-12751, 12634-12651
$(1,-2,0)$	9, 10.5, 12.5, 14	12666-12671, 12566-12571, 12466-12471
$(1,-\frac{4}{3},0)$	11, 13.5, 17, 19	12070-12076, 11970-11976, 11870-11876, 11770-11776
$(1,-1,0)$	12, 14, 19, 23	11476-11483, 11376-11383, 11276-11283, 11176-11183, 11076-11083
$(2,-\frac{4}{3},0)$	8, 8.2, 10.2, 13	10281-10284, 10181-10184
$(1,-\frac{2}{3},0)$	12, 16, 20, 24	10279-10286, 10179-10186, 10079-10086, 9976-9986
$(-2,-\frac{1}{3},0)$	8, 9.4, 12.5, 14	3704-3708, 3604-3608, 3504-3508
$(0,0,4)$	30, 32, 35, 37	9552-9576, 9452-9476, 9352-9376, 9252-9276, 9152-9176, 9052-9076, 8952-8976, 8852-8876, 8752-8776, 8652-8676, 8552-8576, 8452-8476
$(0,0,2)$	60, 64, 67, 70	9552-9576, 9452-9476, 9352-9376, 9252-9276, 9152-9176, 9052-9076, 8952-8976, 8852-8876, 8752-8776, 8652-8676, 8552-8576, 8452-8476

Table B.2: *Integrated intensities as found in Mantid[122] for the HFM/EXED experiment on $LiNiPO_4$. The four different datasets correspond to the paramagnetic phase, phase I, phase IV and phase V respectively. Colored cells indicate significant magnetic intensities.*

Peak	(43 K, 0 T)	(1.3 K, 0 T)	(1.3 K, 20 T)	(1.3 K, 23 T)
$(-1,-2,0)$	2.46(30)	3.40(22)	4.23(18)	2.71(13)
$(-1,-\frac{4}{3},0)$	0.083(27)	0.038(22)	0.011(11)	0.155(10)
$(-1,1,0)$	0.496(16)	0.536(10)	0.568(7)	0.740(7)
$(-2,-2,0)$	122(7)	121(5)	120(3)	115(3)
$(0,-2,0)$	202(3)	206(2)	191(1)	185(1)
$(0,-\frac{4}{3},0)$	-0.017(26)	0.23(8)	0.18(7)	13.11
$(0,-1,0)$	0.135(7)	10.59(2)	12.54(2)	0.148(3)
$(0,-\frac{2}{3},0)$	-0.054(4)	-0.058(2)	-0.011(3)	11.202(6)
$(1,-2,0)$	9.9(1.4)	7.2(7)	8.0(6)	5.1(4)
$(1,-\frac{4}{3},0)$	-0.05(4)	-0.08(3)	-0.014(25)	0.05(2)
$(1,-1,0)$	1.09(5)	1.13(3)	1.29(2)	1.53(2)
$(2,-\frac{4}{3},0)$	1.98(41)	0.89(62)	1.22(1.05)	24.5(3.1)
$(1,-\frac{2}{3},0)$	0.021(9)	0.010(5)	0.016(4)	0.544(8)
$(-2,-\frac{1}{3},0)$	0.62(32)	0.40(16)	0.31(15)	3.76(33)
$(0,0,4)$	91.7(8)	91.2(5)	87.5(4)	91.0(3)
$(0,0,2)$	10.61(4)	10.67(2)	10.00(2)	10.21(1)

Appendix C

Pyrocurrent background subtraction

A good description of the pyrocurrent background is needed for subtraction. This is important since the electric polarization is obtained by integrating the pyrocurrent and is therefore very sensitive to the choice of background. Any constant offset – or even worse, any temperature-dependent background – would hamper the results. Therefore, various ways of describing the pyrocurrent background are explored:

1. Fitting a 2. order polynomial to datapoints that are picked as belonging to the background. Each dataset is treated individually.
2. Like above, but all datasets are taken into account and the background is fitted collectively.
3. All datasets are considered and all the selected background points are re-binned to a combined background. Background values are then determined by interpolation. This is necessary since all datasets have different lengths and the recorded temperatures vary.
4. Like above, but only the zero-field dataset is used for the background.

All listed methods were implemented and the resulting polarizations compared for the dataset with $\mathbf{E}||\mathbf{a}$, $\mathbf{H}||\mathbf{a}$. Method 4 yields the most satisfactory description of the pyrocurrent background, however still not perfect. Methods 3-4 assume nothing about the shape of the background but use the data directly. Furthermore, methods 1-3 are extremely sensitive to which datapoints are picked as belonging to the background and the background should, in principle, be close to the zero-field curve. Upon applying a magnetic field, the whole curve appears to shift. Said shift is assumed temperature independent and the background is finally determined as the zero-field curve plus a constant offset found as the average difference between the measured datapoints and the zero-field curve for $T > 30\,\mathrm{K}$. The resulting background curves are shown in Figs. C.1-C.3.

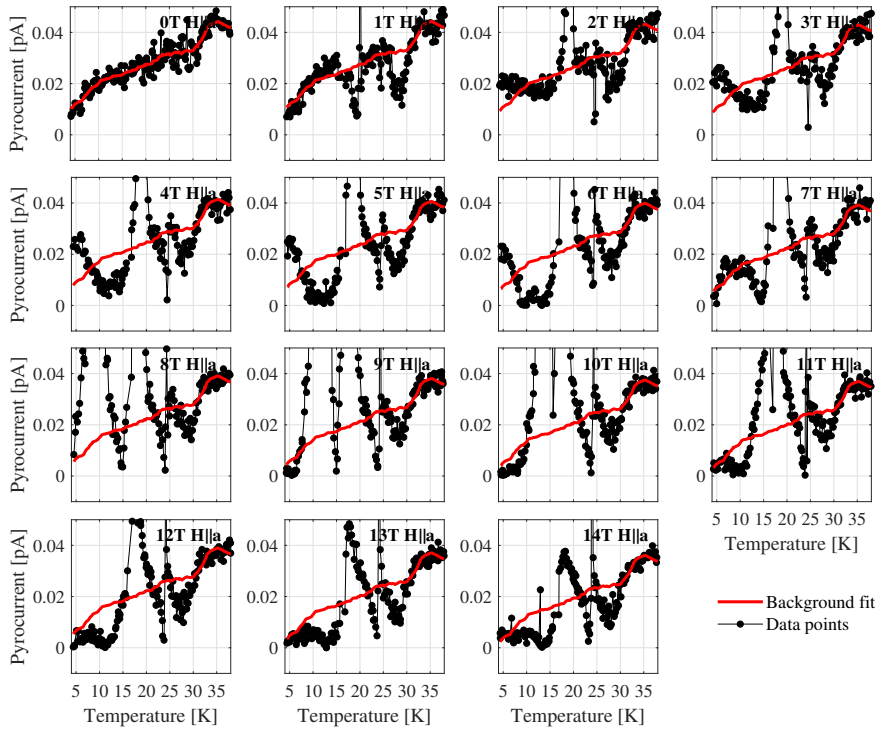

(a) **E**||**a**, **H**||**a**

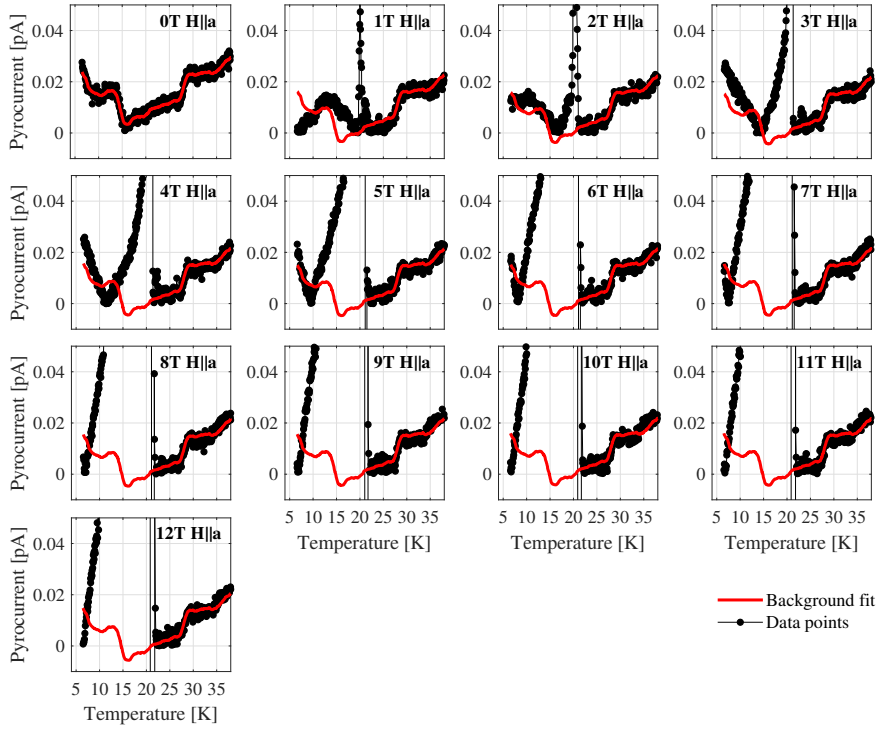

(b) **E**||**b**, **H**||**a**

Figure C.1: *Temperature scans of the pyrocurrent at various magnetic field values for* **H**||**a**. *Black circles show the raw data and red lines are the background as determined by method 4. A constant shift of the entire background curve has been corrected as described in the text.*

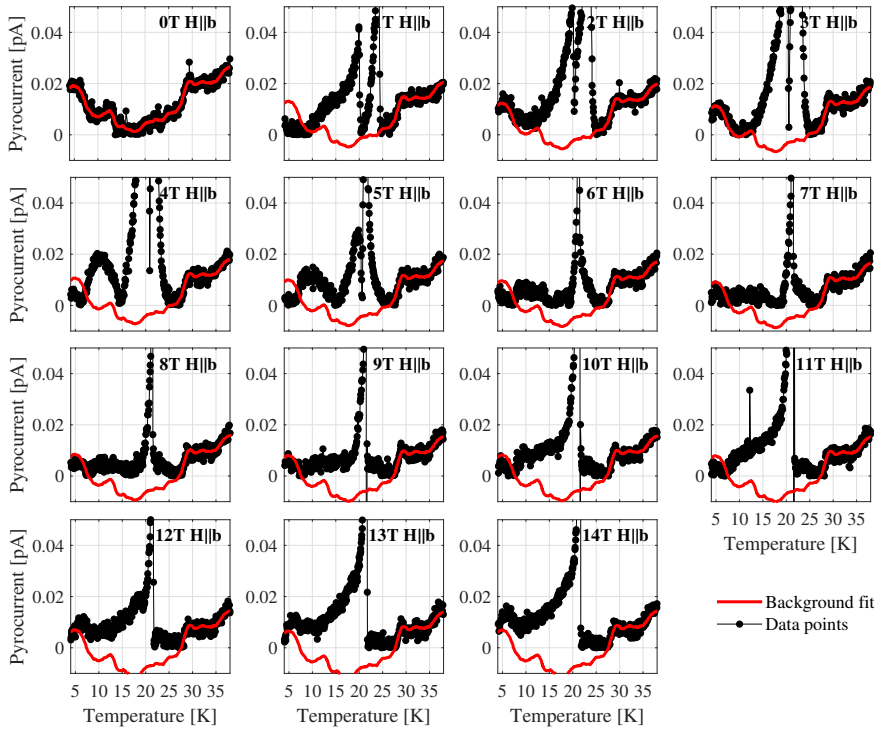

(a) **E**||**a**, **H**||**b**

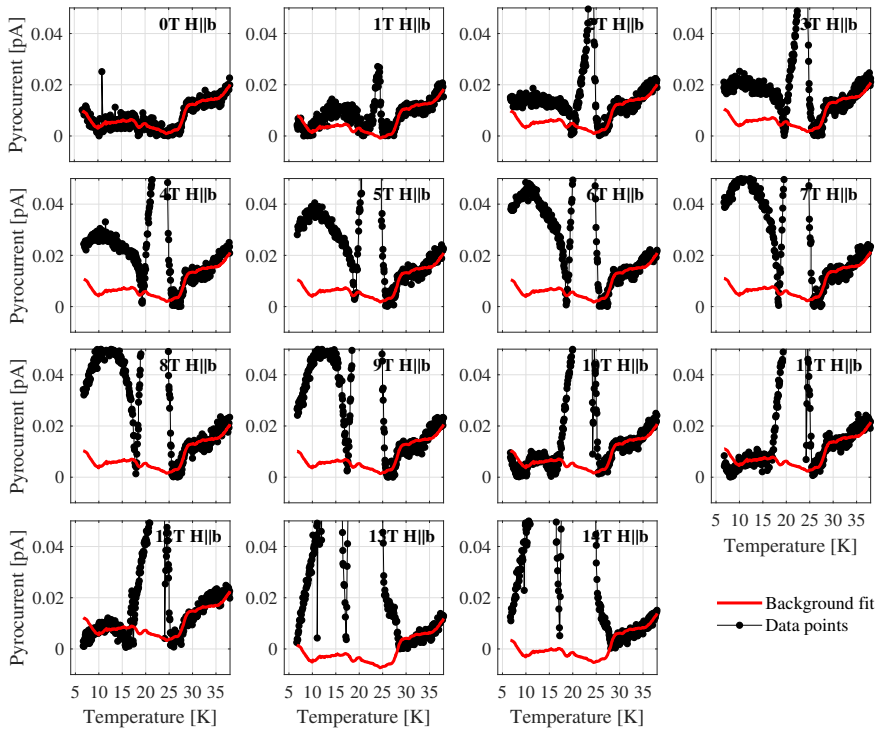

(b) **E**||**b**, **H**||**b**

Figure C.2: *Temperature scans of the pyrocurrent at various magnetic field values for* **H**||**b**. *Black circles show the raw data and red lines are the background as determined by method 4. A constant shift of the entire background curve has been corrected as described in the text.*

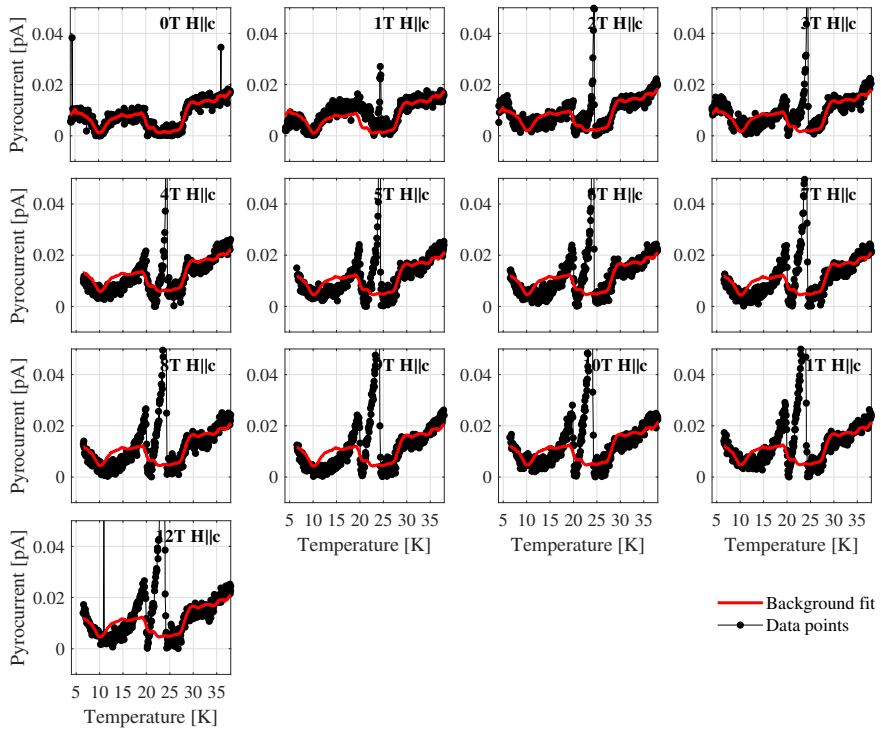

(a) **E**||**a**, **H**||**c**

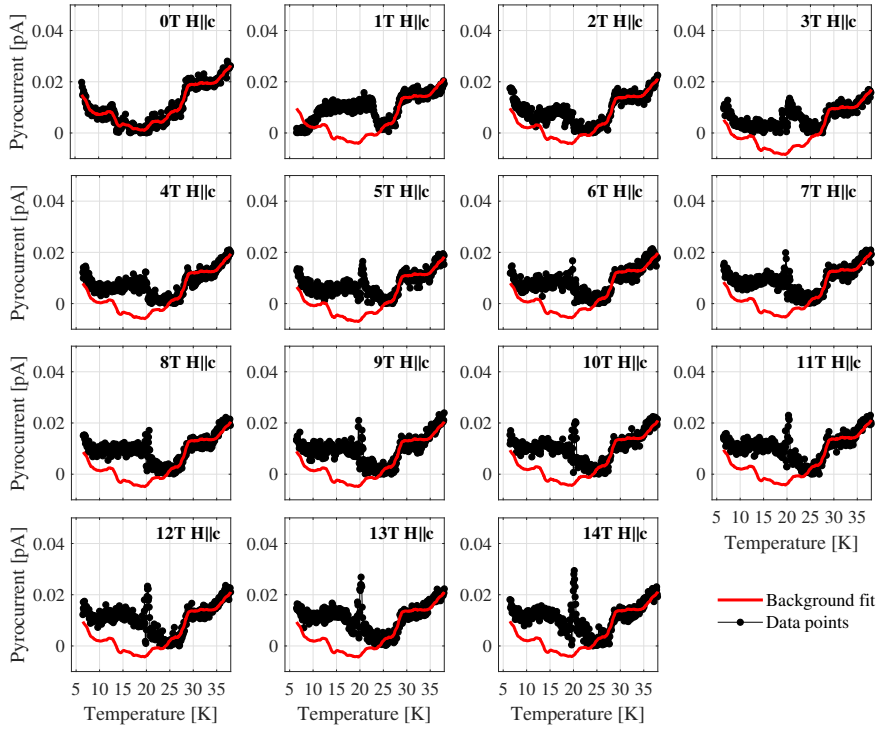

(b) **E**||**b**, **H**||**c**

Figure C.3: *Temperature scans of the pyrocurrent at various magnetic field values for* **H**||**c**. *Black circles show the raw data and red lines are the background as determined by method 4. A constant shift of the entire background curve has been corrected as described in the text.*

Appendix D

Details on the data analysis of the inelastic neutron scattering experiment on $LiNi_{0.8}Fe_{0.2}PO_4$

This Appendix contains details regarding determination of the energy gap size at the zone center at $\mathbf{Q} = (0, 1, 0)$ in $LiNi_{0.8}Fe_{0.2}PO_4$ as well as how resolution effects may cause asymmetric line shapes. A brief description of the inelastic neutron scattering experiment performed on FLEXX at HZB was given in Section 8.2.

Energy gap at the zone center. First of all, data was collected at 40 K, 0 T, i.e. in the paramagnetic phase, in order to ensure that no phonons interfere with our measurements [see Fig. D.1]. The elastic line at $\mathbf{Q} = (0, 1, 0)$ [Fig. D.1(a)] was fitted to both a Gaussian and a Voigt with parameters $\{x_0 = 0.011(2), \sigma = 0.060(1), \}$ and $\{x_0 = 0.012(2), \sigma_G = 0.119(6), \sigma_L = 0.022(5)\}$ respectively. Here x_0 is the peak position, σ is the width of the Gaussian functions and σ_G and σ_L are the widths of the Gaussian and Lorenzian parts of the Voigt function. Both fits describe the measured curve well but the Voigt yields a better fit at the base of the peak.

Energy scans through the elastic line at $(0, 1, 0)$ was performed at every field value as well as a scan for incoherent scattering at $(0, 0.75, 0.25)$ for $5 - 12$ T and 0 T. Furthermore, at 0 T an additional scan was performed at $(0, 0.7, 0.6)$ in order to check whether the incoherent scattering is $\mathbf{Q}$-independent – and indeed, it is (data not shown).

In order to be able to make any sensible fit to the inelastic signal, the elastic line is first investigated [see Fig. D.2]. Different kinds of fits were tried out here too: a Voigt with widths fixed to those found at 40 K, a Gaussian with free parameters and a Voigt with free parameters. Of these, the Gaussian fitted the best and resulting fits are shown in Fig. D.2(a). The fitted intensities, positions and widths are shown as a function of applied field in Fig. D.2(b). The position and width stay roughly constant with field whereas the intensity has a maximum around 8 T.

The incoherent scattering turned out to be field-independent [see Fig. D.3]. Therefore, all the dataset are added up and a Gaussian is fitted to the combined data.

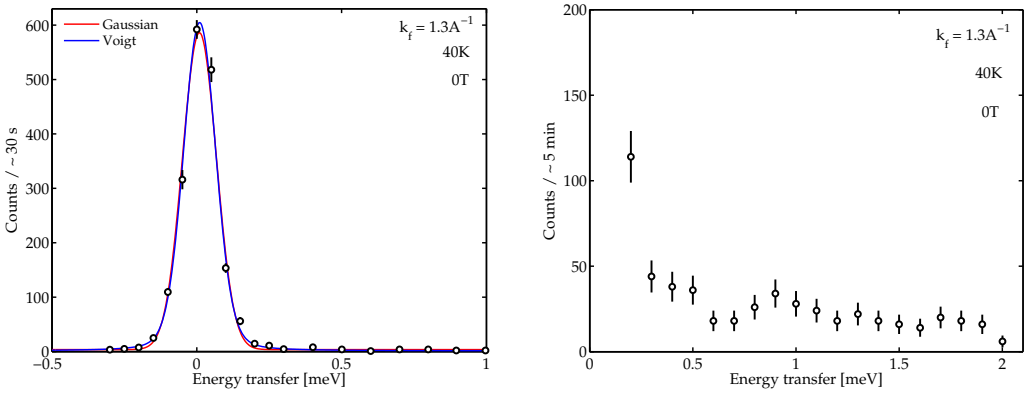

(a) (b)

Figure D.1: *(a) Scan through $\Delta E = 0$ at (0,1,0) at 40 K, 0 T and with $k_f = 1.3\,\text{Å}^{-1}$. Both a Gaussian (red line) and Voigt (blue line) were fitted to see which function yields the best result. The Voigt fits better at the base of the peak. (b) Background scan at (0,1,0) at 40 K, 0 T. The neutron intensity is almost flat as a function of energy transfer – showing that there is no phonon present here.*

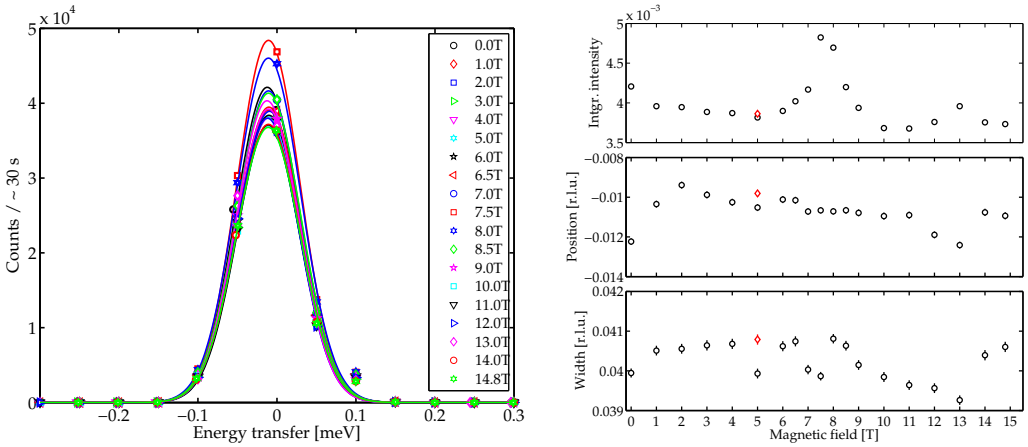

(a) (b)

Figure D.2: *(a) Scans of (0,1,0) through $\Delta E = 0$ at different field values. The solid lines are Gaussian fits to each individual dataset. (b) Integrated intensity, position and width as a function of applied field. The latter two are mostly constant in field whereas the intensity changes as a function of field. The red diamond is a check point at 5 T to see whether something might have changed after collecting data at 5-14.8 T then ramping down, heating up and cooling back down to start collecting again at 0-5 T. Fortunately, nothing appears to have changed significantly.*

This is done in order to be able to subtract the incoherent signal from the inelastic signal. The fitted function and parameters are defined as follows:

$$I = I_0\, e^{-(x-x_0)^2/(2\sigma^2)} + C,$$
$$I_0 = 0.00144(1),\ x_0 = 0.0135(4),\ \sigma = 0.0601(3),\ C = 0\,(\text{fixed}),$$

where the background, $C = 0$, is fixed. This is done because the energy scans have not been performed far enough out on either side of the incoherent peak making it

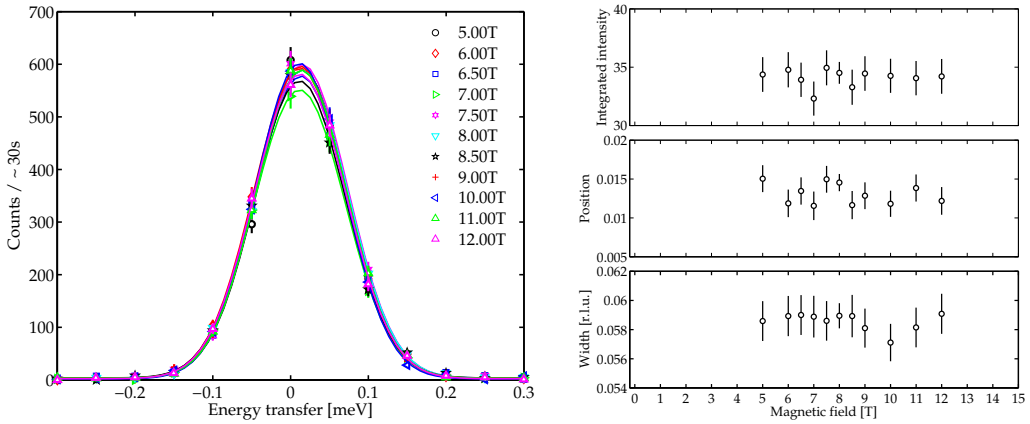

(a) (b)

Figure D.3: *(a) Scans of incoherent scattering at (0,0.75,0.5) through $\Delta E = 0$ at different field values. Evidently, the incoherent scattering in largely field-independent. The solid lines are Gaussian fits. (b) Integrated intensity, position and width as a function of applied field for the incoherent scattering at (0,0.75,0.25).*

difficult to fit the background.

The fits shown in Fig. 8.21 in Section 8.2 are now obtained by performing the following steps for each dataset:

- Subtract the model of the incoherent signal from elastic line and inelastic signal
- Fit the elastic line to a Gaussian with background fixed to zero
- Combine elastic line and inelastic signal and fit them to two Gaussians where the one describing the elastic line has intensity, position and width fixed to the values found in the previous step

The results of this procedure are discussed in Section 8.2.

Asymmetric line shapes and resolution effects. In the analysis above, neutron intensities measured as a function of energy transfer were fitted to a Gaussian or Voigt function and these functions have symmetric line shapes. However, the line shape of the observed inelastic mode along $(0, K, 0)$ is pronouncedly asymmetric close to the zone center and with a tail towards high energy transfers. By performing a more rigorous data treatment and employing the Cooper-Nathans approximation[125] within the ResLib framework[126], it turns out that the asymmetry may be explained by resolution effects. Hence, the asymmetric line shapes do (somewhat disappointingly) not signify any interesting new physics such as less populated multiple modes at higher energies.

The MATLAB-based ResLib software package was developed by Andrey Zheludev at Brookhaven National Laboratory, Oak Ridge National Laboratory and Eidgenössische Technische Hochschule Zürich[126]. The FLEXX instrument is defined with relevant quantities such as final neutron energy, collimation sequence, monochromator and analyzer mosaicities and dimensions, beam size and various distances.

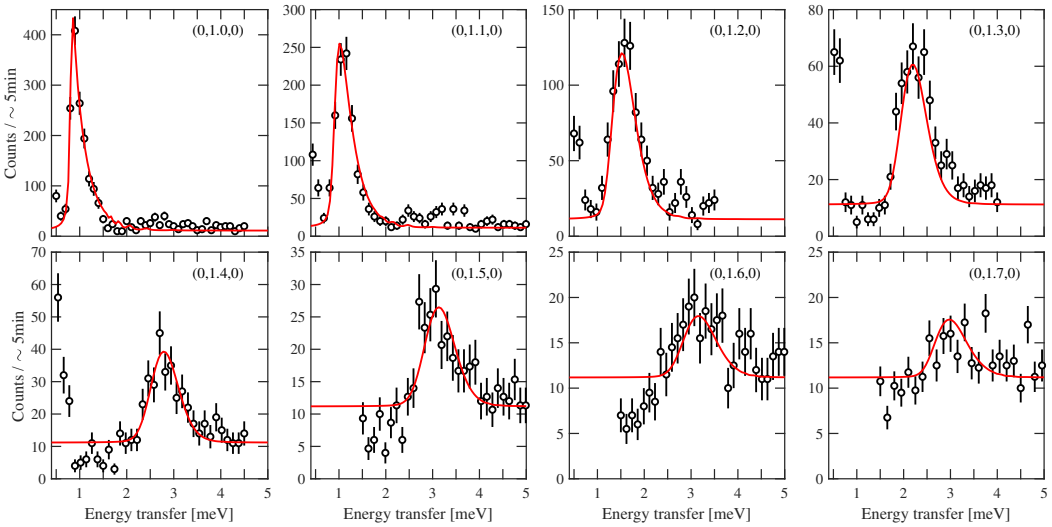

Figure D.4: *Individual plots of neutron intensities as a function of energy transfer for measurements performed with k_f =1.55 Å^{-1} along (0,K,0) with K = 1,1.1,...,1.7 and at 12 T, 1.7 K. The red lines show fits obtained within the ResLib framework[126] as described in the text.*

Likewise, the $LiNi_{0.8}Fe_{0.2}PO_4$ sample is defined with unit cell, geometry and orientation. All datasets may then be simultaneously fitted by using the desired dispersion relation which is then convoluted with the resolution function for each point in $(\mathbf{Q}, \Delta E)$.

The dispersion relation used here was derived in Ref. 123 using linear spin-wave theory. The Hamiltonian and resulting dispersion relation were listed in Eqs. (8.1) and (8.2) but for convenience, they are repeated here:

$$\hat{\mathcal{H}} = \sum_{i,j} J_{ij} \mathbf{S}_i \cdot \mathbf{S}_j + \sum_{i,\alpha} \mathfrak{D}^\alpha \left(S_i^\alpha\right) \quad \text{with eigenvalues} \quad \hbar\omega = \sqrt{A^2 - (B \pm C)^2},$$

where

$$\begin{aligned} A &= 4S\left(J_{bc} + J_{ab}\right) - 2S\Big(J_b\left[1 - \cos\left(\mathbf{Q}\cdot\mathbf{r}_5\right)\right] + J_c\left[1 - \cos\left(\mathbf{Q}\cdot\mathbf{r}_6\right)\right] \\ &\quad + J_{ac}\left[2 - \cos\left(\mathbf{Q}\cdot\mathbf{r}_7\right) - \cos\left(\mathbf{Q}\cdot\mathbf{r}_8\right)\right]\Big) + (S - 1/2)\left(\mathfrak{D}^a + \mathfrak{D}^b\right), \\ B &= (S - 1/2)\left(\mathfrak{D}^a - \mathfrak{D}^b\right)/2, \\ C &= 2S\Big(J_{bc}\left[\cos\left(\mathbf{Q}\cdot\mathbf{r}_1\right) + \cos\left(\mathbf{Q}\cdot\mathbf{r}_2\right)\right] + J_{ab}\left[\cos\left(\mathbf{Q}\cdot\mathbf{r}_3\right) + \cos\left(\mathbf{Q}\cdot\mathbf{r}_4\right)\right]\Big), \end{aligned}$$

with ion positions

$$\begin{aligned} \mathbf{r}_{1,2} &= (0, b/2, \pm c/2), \quad \mathbf{r}_{3,4} = (a/2, \pm b/2, 0), \\ \mathbf{r}_5 &= (0, b, 0), \quad \mathbf{r}_6 = (0, 0, c), \quad \mathbf{r}_{7,8} = (a/2, 0, \pm c/2). \end{aligned}$$

It should be mentioned that the above model is not entirely appropriate since the applied magnetic field was not included in the Hamiltonian. Some efforts were put into including the field, although within the time frame of the project, the calculations were not completed. The ResLib fitting results are shown in Fig. D.4

for data collected along the $(0, K, 0)$ direction. Here $J_c = J_{ab} = J_{ac} = 0$ were fixed. The asymmetric curve shape is nicely reproduced and may hence be subscribed to resolution effects.

Bibliography

[1] R. T. Merrill and M. W. McElhinny. *The Earth's Magnetic Field – It's History, Origin and Planetary Perspective.* Academic Press 1983.

[2] N. Ekker, T. Coughlin, and J. Handy. *An Introduction to Solid State Storage.* Solid State Storage Initiative 2009.

[3] C. Chappert, A. Fert, and F. Nguyen Van Dau. The emergence of spin electronics in data storage. *Nature Materials* **6**, 813–823 (2007).

[4] S. Blundell. *Magnetism in Condensed Matter.* Oxford University Press 2001.

[5] K. Yosida. *Theory of Magnetism.* Springer 2010.

[6] T. Kimura. Spiral magnets as magnetoelectrics. *Annu. Rev. Mater. Res.* **37**, 387 (2007).

[7] J.-P. Rivera. A short review of the magnetoelectric effect and related experimental techniques on single phase (multi-) ferroics. *The European Physical Journal B* **71**, 299–313 (2009).

[8] Y Yiu, M. D. Le, R. Toft-Petersen, G. Ehlers, R. J. McQueeney, and D. Vaknin. Hybrid excitations due to crystal field, spin-orbit coupling, and spin waves in $LiFePO_4$. *Phys. Rev. B* **95**, 104409 (2017).

[9] I. E. Dzyaloshinskii. A thermodynamic theory of "weak" ferromagnetism of antiferromagnetics. *J. Phys. Chem. Solids* **4**, 241–255 (1958).

[10] Tôru Moriya. New mechanism of anisotropic superexchange interaction. *Phys. Rev. Lett.* **4**, 228–230 (1960).

[11] A. P. Ramirez. Strongly geometrically frustrated magnets. *Annu. Rev. Mater. Sci.* **24**, 453–480 (1994).

[12] S.-W. Cheong and M. Mostovoy. Multiferroics: a magnetic twist for ferroelectricity. *Nature Materials* **6**, 13–20 (2007).

[13] W. Eerenstein, N. D. Mathur, and J. F. Scott. Multiferroic and magnetoelectric materials. *Nature* **442**, 759–765 (2006).

[14] M. Fiebig. Revival of the magnetoelectric effect. *J. Phys. D.* **38**, 123–152 (2005).

[15] R. R. Birss. *Symmetry and magnetism.* North-Holland Pub. Co. 1964.

[16] P. Curie. Sur la symétrie dans les phénomènes physiques, symétrie d'un champ électrique et d'un champ magnétique. *J. Phys. Theor. Appl.* **3**, 393–415 (1894).

[17] I. E. Dzyaloshinskii. On the magneto-electrical effect in antiferromagnets. *Soviet Physics JETP* **10**, 628–629 (1959).

[18] D. N. Astrov. The magnetoelectric effect in antiferromagnetics. *J. Exp. Theor. Phys.* **38**, 984–985 (1960).

[19] H. Schmid. Some symmetry aspects of ferroics and single phase multiferroics. *J. Phys.: Condens. Matter* **20**, 434201 (2008).

[20] N. A. Spaldin, M. Fiebig, and M. Mostovoy. The toroidal moment in condensed-matter physics and its relation to the magnetoelectric effect. *J. Phys. Cond. Matt.* **20**, 434203 (2008).

[21] J. Goodenough. *Magnetism and the Chemical Bond.* New York: Wiley (1963).

[22] G. A. Gehring. On the microscopic theory of the magnetoelectric effect. *Ferroelectrics* **161**, 275–285 (1994).

[23] R. Ramesh and N. A. Spaldin. Multiferroics: progress and prospects in thin films. *Nature Materials* **6**, 21–29 (2007).

[24] M. Gajek, M. Bibes, S. Fusil, K. Bouzehouane, J. Fontcuberta, A. Barthélémy, and A. Fert. Tunnel junctions with multiferroic barriers. *Nature Materials* **6**, 296–302 (2007).

[25] M. Bibes and A. Barthélémy. Multiferroics: Towards a magnetoelectric memory. *Nature Materials* **7**, 425–426 (2008).

[26] Y.-H. Chu, L. W. Martin, M. B. Holcomb, M. Gajek, S.-J. Han, Q. He, N. Balke, C.-H. Yang, D. Lee, W. Hu, Q. Zhan, P.-L. Yang, A. Fraile-Rodríguez, A. Scholl, S. X. Wang, and R. Ramesh. Electric-field control of local ferromagnetism using a magnetoelectric multiferroic. *Nature Materials* **7**, 478–782 (2008).

[27] W. Chen and M. Sigrist. Dissipationless multiferroic magnonics. *Phys. Rev. Lett.* **114**, 157203 (2015).

[28] V. Laukhin, V. Skumryev, X. Martí, D. Hrabovsky, F. Sánchez, M. V. García-Cuenca, C. Ferrater, M. Varela andU. Lüders, J. F. Bobo, and J. Fontcuberta. Electric-field control of exchange bias in multiferroic epitaxial heterostructures. *Phys. Rev. Lett.* **97**, 227201 (2006).

[29] F. A. Cuellar, Y. H. Liu, J. Salafranca, N. Nemes, E. Iborra, G. Sanchez-Santolino, M. Varela, M. Garcia Hernandez, J. W. Freeland, M. Zhernenkov, M. R. Fitzsimmons, S. Okamoto, S. J. Pennycook, M. Bibes, A. Barthélémy, S. G. E. te Velthuis, Z. Sefrioui, C. Leon, and J. Santamaria. Reversible electric-field control of magnetization at oxide interfaces. *Nature Communications* **5**, 4215 (2014).

[30] T. H. Kim, P. Grünberg, S. H. Han, and B. K. Cho. Precessional switching of antiferromagnets by electric field induced dzyaloshinskii-moriya torque. *Phys. Rev. B* **97**, 184427 (2018).

[31] G. L. Squires. *Introduction to the theory of thermal neutron scattering.* Cambridge University Press 2012.

[32] S. W. Lovesey. *Theory of neutron scattering from condensed matter.* Oxford University Press 1984.

[33] A. Furrer, J. Mesot, and T. Strässle. *Neutron Scattering in Condensed Matter Physics.* World Scientific 2009.

[34] B. N. Brockhouse. Slow neutron spectroscopy: an historical account over the years 1950 – 1977. In *The Neutron and its Applications* pages 193–198 London and Bristol 1982. The Institute of Physics.

[35] O. Halpern and M. H. Johnson. On the magnetic scattering of neutrons. *Phys. Rev.* **55**, 898–923 (1939).

[36] K. Lefmann. *Neutron Scattering: Theory, Instrumentation, and Simulation.* Niels Bohr Institute 2014.

[37] R. M. Moon, T. Riste, and W. C. Koehler. Polarization analysis of thermal-neutron scattering. *Phys. Rev.* **181**, 920–931 (1969).

[38] J. R. Stewart, P. P. Deen, K. H. Andersen, H. Schober, J.-F. Barthélémy, J. M. Hillier, A. P. Murani, T. Hayesb, and B. Lindenau. Disordered materials studied using neutron polarization analysis on the multi-detector spectrometer, d7. *J. Appl. Cryst.* **42**, 69–84 (2009).

[39] M. Mercier. *Étude de l'effet magnetoelectrique sur de composés de type olivine, perovskite et grenat.* PhD thesis Université de Grenoble 1969.

[40] R. E. Newnham, R. P. Santoro, and M. J. Redman. Neutron-diffraction study of $LiMnPO_4$. *J. Phys. Chem. Solids* **26**, 445–447 (1965).

[41] R. E. Newnham and M. J. Redman. Crystallographic data for $LiMgPO_4$, $LiCoPO_4$ and $LiNiPO_4$. *J. Am. Ceram. Soc.* **48**, 547 (1965).

[42] R. P. Santoro, D. J. Segal, and R. E. Newnham. Magnetic properties of $LiCoPO_4$ and $LiNiPO_4$. *J. Phys. Chem. Solids* **27**, 1192–1193 (1966).

[43] R. P. Santoro and R. E. Newnham. Antiferromagnetism in $LiFePO_4$. *Acta Cryst.* **22**, 344–347 (1967).

[44] R. M. Bozorth and V. Kramer. Some ferrimagnetic and antiferromagnetic materials at low temperatures. *J. Phys. Radium* **20**, 393–401 1959.

[45] I. Abrahams and K. S. Easson. Structure of lithium nickel phosphate. *Acta Crystallographica Section C* **49**(5), 925–926 (1993).

[46] S. Geller and J. L. Durand. Refinement of the structure of $LiMnPO_4$. *Acta Cryst.* **13**, 325–331 (1960).

[47] D. Vaknin, J. L. Zarestky, L. L. Miller, J.-P. Rivera, and H. Schmid. Weakly coupled antiferromagnetic planes in single-crystal $LiCoPO_4$. *Phys. Rev. B* **65**, 224414 (2002).

[48] T. B. S. Jensen, N. B. Christensen, M. Kenzelmann, H. M. Rønnow, C. Niedermayer, N. H. Andersen, K. Lefmann, J. Schefer, M. Zimmermann, J. Li, J. L. Zarestky, and D. Vaknin. Field-induced magnetic phases and electric polarization in $LiNiPO_4$. *Phys. Rev. B* **79**, 092412 (2009).

[49] D. Vaknin, J. L. Zarestky, J.-P. Rivera, and H. Schmid. Commensurate-incommensurate magnetic phase transition in magnetoelectric single crystal $LiNiPO_4$. *Phys. Rev. Lett.* **92**(10), 207201 (2004).

[50] J. M. Mays. Nuclear magnetic resonances and mn-0-p-0-mn superexchange linkages in paramagnetic and antiferromagnetic $LiMnP0_4$. *Phys. Rev.* **131**, 38–53 (1963).

[51] J.-P. Rivera. The linear magnetoelectric effect in $LiCoPO_4$ revisited. *Ferroelectrics* **161**, 147–164 (1994).

[52] W. S. Wieglhofer and A. Lakhtakia. *Introduction to Complex Mediums for Optics and Electromagnetics*. SPIE Press 2003.

[53] T. B. S. Jensen, N. B. Christensen, M. Kenzelmann, H. M. Rønnow, C. Niedermayer, N. H. Andersen, K. Lefmann, M. Jiménez-Ruiz, F. Demmel, J. Li, J. L. Zarestky, and D. Vaknin. Anomalous spin waves and the commensurate-incommensurate magnetic phase transition in $LiNiPO_4$. *Phys. Rev. B* **79**, 092413 (2009).

[54] R. Toft-Petersen, M. Reehuis, T. B. S. Jensen, N. H. Andersen J. Li, M. D. Le, M. Laver, C. Niedermayer, B. Klemke, K. Lefmann, and D. Vaknin. Anomalous magnetic structure and spin dynamics in magnetoelectric $LiFePO_4$. *Phys. Rev. B* **92**, 024404 (2015).

[55] J. Li, W. Tian, Y. Chen, J. L. Zarestky, J. W. Lynn, and D. Vaknin. Antiferromagnetism in the magnetoelectric effect single crystal $LiMnPO_4$. *Phys. Rev. B* **79**, 144410 (2009).

[56] G. Liang, K. Park, J. Li, R. E. Benson, D. Vaknin, J. T. Markert, and M. C. Croft. Anisotropy in magnetic properties and electronic structure of single-crystal $LiFePO_4$. *Phys. Rev. B* 77, 064414 (2008).

[57] R. Toft-Petersen. Personal communication.

[58] N. F. Kharchenko, V. M. Khrustalev, and V. N. Savitskii. Magnetic field induced spin reorientation in the strongly anisotropic antiferromagnetic crystal $LiCoPO_4$. *Low Temp. Phys.* **36**, 558–564 (2010).

[59] H. Wiegelmann. *Magnettoelectic effects in strong magnetic fields.* PhD thesis Universität Konstanz 1994.

[60] V.M. Khrustalyov, V.N. Savitsky, and N.F. Kharchenko. Multi-step-like magnetization of $LiNiPO_4$ in a pulse magnetic field. *Czechoslovak Journal of Physics* **54** (2004).

[61] R. Toft-Petersen, J. Jensen, T. B. S. Jensen, N. H. Andersen, N. B. Christensen, C. Niedermayer, M. Kenzelmann, M. Skoulatos, M. D. Le, K. Lefmann, S. R. Hansen, J. Li, J. L. Zarestky, and D. Vaknin. High-field magnetic phase transitions and spin excitations in magnetoelectric $LiNiPO_4$. *Phys. Rev. B* **84**, 054408 (2011).

[62] R. Toft-Petersen, N. H. Andersen, H. Li, J. Li, W. Tian, S. L. Bud'ko, T. B. S. Jensen, C. Niedermayer, M. Laver, O. Zaharko, J. W. Lynn, and D. Vaknin. Magnetic phase diagram of magnetoelectric $LiMnPO_4$. *Phys. Rev. B* **85**, 224415 (2012).

[63] Yu. Kharchenko, N. Kharchenko, L. Hiltunen, M. Baran, and R. Szymczak. Weak ferromagnetism in magnetoelectrics $LiCoPO_4$ and $LiNiPO_4$. (2003).

[64] C. Ederer and N. A. Spaldin. Towards a microscopic theory of toroidal moments in bulk periodic crystals. *Phys. Rev. B* **76**, 214404 (2007).

[65] B. B. Van Aken, J.-P. Rivera, H. Schmid, and M. Fiebig. Observation of ferrotoroidic domains. *Nature Letters* **449**, 702–705 (2007).

[66] A. S. Zimmermann, D. Meier, and M. Fiebig. Ferroic nature of magnetic toroidal order. *Nature Communications* **5**, 4796 (2014).

[67] V. M. Khrustalyov, V. M. Savytsky, and M. F. Kharchenko. Magnetoelectric effect in antiferromagnetic $LiCoPO_4$ in pulsed magnetic fields. *Low Temp. Phys.* **42**, 280–285 (2016).

[68] V. M. Khrustalyov, V. M. Savytsky, and M. F. Kharchenko. (H, T_i)-diagram of magnetic transformations induced by a pulsed magnetic field in antiferromagnetic $LiCoPO_4$. *Low Temp. Phys.* **43**, 1332–1337 (2017).

[69] R. Toft-Petersen, E. Fogh, T. Kihara, J. Jensen, K. Fritsch, J. Lee, G. E. Granroth, M. B. Stone, D. Vaknin, H. Nojiri, and N. B. Christensen. Field-induced reentrant magnetoelectric phase in $LiNiPO_4$. *Phys. Rev. B* **95**, 064421 (2017).

[70] E. Fogh. Magnetic high-field phases of magnetoelectric $LiNiPO_4$. Master's thesis Technical University of Denmark 2014.

[71] G. Rousse, J. Rodriguez-Carvajal, S. Patoux, and C. Masquelier. Magnetic structures of the triphylite $LiFePO_4$ and of its delithiated form $FePO_4$. *Chem. Mater.* **15**, 4082–4090 (2003).

[72] W. Kim, C. H. Rhee, H. J. Kim, S. J. Moon, and C. S. Kim. Strong crystalline field at the fe site and spin rotation in olivine $LiNi_{0.99}{}^{57}Fe_{0.01}PO_4$ material by mössbauer spectroscopy. *Appl. Phys. Lett.* **96**, 242505 (2010).

[73] A. S. Zimmermann, E. Sondermann, J. Li, D. Vaknin, and M. Fiebig. Antiferromagnetic order in $Li(Ni_{1-x}Fe_x)PO_4$ ($x = 0.06$, 0.20). *Phys. Rev. B* **88**, 014420 (2013).

[74] J. Li, T. B. S. Jensen, N. H. Andersen, J. L. Zarestky, R. W. McCallum, J.-H. Chung, J. W. Lynn, and D. Vaknin. Tweaking the spin-wave dispersion and supressing the incommensurate phase in $LiNiPO_4$ by iron substitution. *Phys. Rev. B* **79**, 174435 (2009).

[75] K. Mizushima, P. C. Jones, P. J. Wiseman, and J. B. Goodenough. Li_xCoO_2 ($0 < x \leq 1$): a new cathode material for batteries of high energy density. *Mat. Res. Bull.* **15**, 783–789 (1980).

[76] M. G. S. R. Thomas, W. I. F. David, and J. B. Goodenough. Synthesis and structural characterization of the normal spinel $Li[Ni_2]O_4$. *Mat. Res. Bull* **20**, 1137–1146 (1985).

[77] A. R. Armstrong and P. G. Bruce. Synthesis of layered $LiMn_2$ as an electrode for rechargeable lithium batteries. *Nature* **381**, 499–500 (1996).

[78] N. Nitta, F. Wu, J. T. Lee, and G. Yushin. Li-ion battery materials: present and future. *Materials Today* **18**, 252–264 (2015).

[79] S. Fishman and A. Aharony. Phase diagrams of multicritical points in randomly mixed magnets. i. mixed anisotropies. *Phys. Rev. B* **18**, 3507–3520 (1978).

[80] J. M. Kosterlitz, D. R. Nelson, and M. E. Fisher. Bicritical anfl tetracritical points in anisotropic antiferromagnetic systems. *Phys. Rev. B* **13**, 412–432 (1976).

[81] F. Wegner. On the magnetic phase diagram of (Mn,Fe)WO_4. *Solid State Comm.* **12**, 785–787 (1973).

[82] L. Bevaart, E. Frikkee, J. Lebesque, and L. J. de Jongh. Magnetic and neutron scattering experiments on the antiferromagnetic layer-type compounds $K_2Mn_{1-x}M_xF_4$ (M = Fe,Co). *Phys. Rev. B* **18**, 3376–3392 (1978).

[83] P. Wong, P. M. Horn, H. J. Birgeneau, C. H. Safinya, and G. Shirane. Competing order parameters in quenched random alloys: $Fe_{1-x}Co_xCl_2$. *Phys. Rev. Lett.* **45**, 1974–1977 (1980).

[84] T. Tawaraya, K. Katsumata, and H. Yoshizawa. Neutron diffraction experiment on a randomly mixed antiferromagnet with competing spin anisotropies. *J. Phys. Soc. Jpn.* **49**, 1299–1305 (1980).

[85] F. A. Perez, P. Borisov, T. A. Johnson, T. D. Stanescu, and D. Lederman R. Trappen abd M. B. Holcomb, M. R. Fitzsimmons, A. A. Aczel, and T. Hong. Phase diagram of a three-dimensional antiferromagnet with random magnetic anisotropy. *Phys. Rev. Lett.* **114**, 097201 (2015).

[86] K. Katsumata, M. Kobayashi, T. Sato, and Y. Miyako. Experimental phase diagram of a randum mixture of two anisotropic antiferromagnets. *Phys. Rev. B* **19**, 2700–2703 (1979).

[87] R. B. Griffiths. Nonanalytic behavior above the critical point in a random ising ferromagnet. *Phys. Rev. Lett.* **23**, 17–19 (1969).

[88] S. Zherlitsyn, A. D. Bianchi, T. Herrmannsdoefer, F. Pobell, Yu. Skourski, A. Sytcheva, S. Zyvagin, and J. Wosnitza. Coil design for non-destructive pulsed-field magnets targeting 100 t. *IEEE. Trans. Appl. Supercond.* **16**, 1660–1663 (2006).

[89] Y. Skourski, M. D. Kuz'min, K. P. Skokov, A. V. Andreev, and J. Wosnitza. High-field magnetization of Ho_2Fe_17. *Phys. Rev. B* **83**, 214420 (2011).

[90] M. Akaki, H. Iwamoto, T. Kihara, M. Tokunaga, and H. Kuwahara. Multiferroic properties of an åkermanite $Sr_2CoSi_2O_7$ single crystal in high magnetic fields. *Phys. Rev. B* **86**, 060413(R) (2012).

[91] H. Mitamura, S. Mitsuda, S. Kanetsuki, H. A. Katori, T. Sakakibara, and K. Kindo. Dielectric polarization measurements on the antiferromagnetic triangular lattice system $CuFeO_2$ in pulsed high magnetic fields. *J. Phys. Soc. Jpn.* **76**, 094709 (2007).

[92] Quantum Design. *Physical Property Measurement System - Heat Capacity Option User's Manual.*

[93] S. Paeckel. Setup of a measurement system to determine the electric polarization. Bachelor's thesis Technische Universität Berlin 2010.

[94] A. G. Chynoweth. Dynamic method for measuring the pyroelectric effect with special reference to barium titanate. *J. Appl. Phys.* **27**, 78–84 (1956).

[95] R. Pynn. Lorentz factor for triple-axis spectrometers. *Acta. Cryst. B* **31**, 2555–2556 (1975).

[96] D. P. Landau and K. Binder. *A Guide to Monte Carlo Simulations in Statistical Physics.* Cambridge University Press 2015.

[97] N. Metropolis, A. W. Rosenbluth, M. N. Rosenbluth, A. H. Teller, and E. Teller. Equation of state calculations by fast computing machines. *J. Chem. Physics* **21**, 1087–1092 (1953).

[98] G. Marsaglia. Choosing a point from the surface of a sphere. *Ann. Math. Stat.* **43**, 645–646 (1972).

[99] M. S. Green, editor. *Critical Phenomena.* Academic Press, London 1971.

[100] V. Privman. *Finite Size Scaling and Numerical Simulations of Statistical Systems.* World Scientific, Singapore 1990.

[101] C. B. Lang and H. Gausterer, editors. *Computational Methods in Field Theory.* Springer, Berlin 1992.

[102] E. Fogh, R. Toft-Petersen, E. Ressouche, C. Niedermayer, S. L. Holm, M. Bartkowiak, O. Prokhnenko, S. Sloth, F. W. Isaksen, D. Vaknin, and N. B. Christensen. Magnetic order, hysteresis, and phase coexistence in magnetoelectric $LiCoPO_4$. *Phys. Rev. B* **96**, 104420 (2017).

[103] J. Rodriguez-Carvajal. Recent advances in magnetic structure determination by neutron powder diffraction. *Physica B* 192(55-69) (1993).

[104] F. Kubel. Crystal structure of lithium cobalt double orthophosphate, $LiCoPO_4$. *Zeitschrift für Kristallographie* **209**, 755 (1994).

[105] B. B. Van Aken, J.-P. Rivera, H. Schmid, and M. Fiebig. Anisotropy of antiferromagnetic 180° domains in $LiCoPO_4$ and $LiNiPO_4$. *Phys. Rev. Lett.* **101**, 157202 (2008).

[106] A. S. Zimmermann, B. B. Van Aken, H. Schmid, J.-P. Rivera, J. Li, D. Vaknin, and M. Fiebig. Anisotropy of antiferromagnetic 180° domains in magnetoelectric LiMPO$_4$ (M = Fe, Co, Ni). *Eur. Phys. J. B* **71**, 355–360 (2009).

[107] N. F. Kharchenko, Yu. N. Kharchenko, R. Szymczak, M. Baran, and H. Schmid. Weak ferromagnetism in the antiferromagnetic magnetoelectric crystal $LiCoPO_4$. *Low Temp. Phys.* **27**, 895 (2001).

[108] I. Kornev, M. Bichurin, J.-P. Rivera, S. Gentil, H. Schmid, A. G. M. Jansen, and P. Wyder. Magnetoelectric properties of $LiCoPO_4$ and $LiNiPO_4$. *Phys. Rev. B* **62**(18), 12247–12253 (2000).

[109] J. G. Creer and G. J. Troup. The magnetic susceptibility of $LiFePO_4$ and $LiCoPO_4$. *Phys. Lett. A* **32**, 439 (1970).

[110] K. Yamauchi and S. Picozzi. Magnetic anisotropy in liphosphates and origin of magnetoelectricity in $LiNiPO_4$. *Phys. Rev. B* **81**, 024110 (2010).

[111] P. Bak. One-dimensional ising model and the complete devil's staircase. *Phys. Rev. Lett.* **49**, 249 (1982).

[112] P. Bak. The devil's staircase. *Phys. Today* **39**, 38 (1986).

[113] W. Tian, J. Li, J. W. Lynn, J. L. Zarestky, and D. Vaknin. Spin dynamics in the magnetoelectric effect compound $LiCoPO_4$. *Phys. Rev. B* **78**, 184429 (2008).

[114] P. Smeibidl, M. Bird, H. Ehmler, I. Dixon, J. Heinrich, M. Hoffmann, S. Kempfer, S. Bole, J. Toth, O. Prokhnenko, and B. Lake. First hybrid magnet for neutron scattering at helmholtz-zentrum berlin. *IEEE Trans. Appl. Supercond.* **26**, 4301606 (2016).

[115] O. Prokhnenko, W.-D. Stein, H.-J. Bleif, M. Fromme, M. Bartkowiak, and T. Wilpert. Time-of-flight extreme environment diffractometer at the helmholtz-zentrum berlin. *Rev. Sci. Instrum.* **86**, 033102 (2015).

[116] O. Prokhnenko, M. Bartkowiak, W.-D. Stein, N. Stuesser, H.-J. Bleif, M. Fromme, K. Prokes, P. Smeibidl, M. Bird, and B. Lake. HFM-EXED - the high field facility for neutron scattering at HZB. *Proceedings of ICANS-XXI* pages 278–285 (2016).

[117] V. M. Khrustalyov, V. M. Savytsky, and M. F. Kharchenko. Magnetoelectric effect in antiferromagnetic $LiNiPO_4$ in pulsed magnetic fields. *Low Temp. Phys.* **42**, 1126–1129 (2016).

[118] R. E. Newnham, J. J. Kramer, W. A. Schulze, and L. E. Cross. Magnetoferroelectricity in Cr_20_4. *J. Appl. Phys.* **49**, 6088 (1978).

[119] H. Nakamura and K. Kohn. Magnetoelectric effect of rare earth manganese oxide RMn_2O_5. *Ferroelectric* **204**, 107–114 (1997).

[120] A. Szewczyk, M. U. Gutowska, J. Wieckowski, A. Wisniewski, R. Puzniak, R. Diduszko, Yu. Kharchenko, M. F. Kharchenko, and H. Schmid. Phase transitions in single-crystalline magnetoelectric $LiCoPO_4$. *Phys. Rev. B* **84**, 104419 (2011).

[121] S. Yoshii, K. Ohoyama, K. Kurosawa, H. Nojiri, M. Matsuda, P. Frings, F. Duc, B. Vignolle, G. L. J. A. Rikken, L.-P. Regnault, S. Michimura, and F. Iga. Neutron diffraction study on the multiple magnetization plateaus in TbB_4 under pulsed high magnetic field. *Phys. Rev. Letters* **103**, 077203 (2009).

[122] O. Arnold, J. C. Bilheux, J. M. Borreguero, A. Buts, S. I. Campbell L. Chapon, M. Doucet, N. Draper, R. Ferraz Leal, M. A. Gigg, V. E. Lynch, A. Markvardsen, D. J. Mikkelson, R. L. Mikkelson, R. Miller, K. Palmen, P. Parker, G. Passos, T. G. Perring, P. F. Peterson, S. Ren, M. A. Reuter, A. T. Savici, J. W. Taylor, R. J. Taylor, R. Tolchenov, W. Zhou, and J. Zikovsky. Mantid – data analysis and visualization package for neutron scattering and μsr experiments. *Nucl. Instrum. Methods Phys. Res.* **764**, 156 – 166 (2014).

[123] T. B. S. Jensen. *Magnetic structures, phase diagram and spin waves of magneto-electric $LiNiPO_4$*. PhD thesis Risø National Laboratory, DTU 2007.

[124] H. Grimmer. The forms of tensors describing magnetic, electric and toroidal properties. *Ferroelectrics* **161**, 181–189 (1994).

[125] M. J. Cooper and R. Nathans. The resolution function in neutron diffractometry i. the resolution function of a neutron diffractometer and its application to phonon measurements. *Acta Cryst.* **23**, 357–367 (1967).

[126] A. Zheludev. *ResLib 3.4*. Oak Ridge National Laboratory.

Paper I

Field-induced reentrant magnetoelectric phase in $LiNiPO_4$
R. Toft-Petersen, E. Fogh, T. Kihara, J. Jensen, K. Fritsch, J. Lee, G. E. Granroth, M. B. Stone, D. Vaknin, H. Nojiri and N. B. Christensen
Physical Review B **95**, 064421 (2017)

The work leading to this paper was initiated during my Master's project where we conducted a pulsed-field neutron Laue diffraction experiment with fields up to 30 T, the analysis of which made up my project. The final data analysis, interpretation of the results, modelling of the magnetoelectric effect as well as writing up the manuscript were carried out in the first half of my PhD.

Field-induced reentrant magnetoelectric phase in $LiNiPO_4$

Rasmus Toft-Petersen,[1,*] Ellen Fogh,[2] Takumi Kihara,[3] Jens Jensen,[4] Katharina Fritsch,[1] Jooseop Lee,[5] Garrett E. Granroth,[6] Matthew B. Stone,[5] David Vaknin,[7] Hiroyuki Nojiri,[3] and Niels Bech Christensen[2]

[1]*Helmholtz Zentrum Berlin für Materialien und Energie, D-14109 Berlin, Germany*

[2]*Department of Physics, Technical University of Denmark, DK-2880 Kongens Lyngby, Denmark*

[3]*Institute for Materials Research, Tohoku University, Sendai 980-8577, Japan*

[4]*Niels Bohr Institute, Universitetsparken 5, DK-2100 Copenhagen, Denmark*

[5]*Quantum Condensed Matter Division, Oak Ridge National Laboratory, Oak Ridge, Tennessee 37831, USA*

[6]*Neutron Data Analysis and Visualization Division, Oak Ridge National Laboratory, Oak Ridge, Tennessee 37831, USA*

[7]*Ames Laboratory and Department of Physics and Astronomy, Iowa State University, Ames, Iowa 50011, USA*

(Received 1 April 2016; revised manuscript received 20 January 2017; published 21 February 2017)

Using pulsed magnetic fields up to 30 T we have measured the bulk magnetization and electrical polarization of $LiNiPO_4$ and have studied its magnetic structure by time-of-flight neutron Laue diffraction. Our data establish the existence of a reentrant magnetoelectric phase between 19 T and 21 T. We show that a magnetized version of the zero field commensurate structure explains the magnetoelectric response quantitatively. The stability of this structure suggests a field-dependent spin anisotropy. Above 21 T, a magnetoelectrically inactive, short-wavelength incommensurate structure is identified. Our results demonstrate the combination of pulsed fields with epithermal neutron Laue diffraction as a powerful method to probe even complex phase diagrams in strong magnetic fields.

DOI: 10.1103/PhysRevB.95.064421

I. INTRODUCTION

The coupling between magnetization and ferroelectricity in magnetoelectric (ME) materials [1–3] suggests a wide range of prospects for applications [4]. Low-power ME memory devices are currently being realized [5–9] and electrically manipulating spin waves to process information has far-reaching perspectives [10–12]. These low-symmetry materials offer a menagerie of possible microscopic origins for the ME coupling, including incommensurate (IC) magnetic structures in frustrated magnets [13] and transition metal orbital magnetism [14]. For instance, $TbMnO_3$ has a complex magnetic phase diagram with two distinct multiferroic phases [15,16], where a cycloid IC structure produces ferroelectric polarization [17]. Another example is $MnWO_4$, where electric polarization is generated by an elliptical spiral [18], the chirality of which can be controlled by an electric field [19]. In Cr_2O_3, multiple coexisting mechanisms may even be possible [20,21].

The $S = 1$ Ni^{2+} ions in orthorhombic $LiNiPO_4$ (space group $Pnma$ with lattice parameters $a = 10.02$ Å, $b = 5.83$ Å, and $c = 4.66$ Å) [22–25] form a frustrated 3D antiferromagnetic network. Its spin dynamics is dominated by the competition between nearest (J_1) and next-nearest (J_2) neighbor interactions in the bc plane [26,27]. The c axis is the easy axis, but the anisotropy within the ac plane is weak. The combination of spin anisotropy and a prominent Dzyaloshinskii-Moriya (DM) interaction results in commensurate magnetic order below $T_N = 20.7$ K and—for magnetic fields along the easy c-axis—in a ME response P_x caused by field-induced canting of the spins [28]. The ratio of J_1 to J_2 leaves $LiNiPO_4$ near an instability to IC magnetic order. Indeed, the low-temperature commensurate phase is bordered by IC phases (with collinear and spiral spin structures, respectively) above T_N in zero field [29] and above 12 T parallel to c at 1.5 K [28,30]. Both of these phases are magnetoelectrically inactive. At 16 T the IC modulation of the spiral locks into a quintupling of the crystallographic unit cell along b. Pulsed field magnetization measurements at 4.2 K indicate the existence of additional magnetic phase transitions for fields in the range 14–22 T [31]. The ME properties and magnetic structures of the higher-field phases are unknown, but recent advances in pulsed-field diffraction [32–35] imply that the latter can now be investigated using neutron scattering.

We use pulsed magnetic fields to study the magnetization, electrical polarization, and magnetic structures of $LiNiPO_4$ up to 30 T along the c axis. Our results demonstrate how epithermal neutron Laue diffraction in pulsed fields allows an efficient and exhaustive identification of propagation vectors characterizing a complex sequence of magnetic phases. We show that magnetoelectricity reemerges in the field range 19–21 T and is accompanied by commensurate antiferromagnetic order with spins polarized along the applied field axis. This phase is supplanted by a magnetoelectrically inactive, short-wavelength IC structure above 21 T. Combining the bulk and neutron diffraction data, a quantitative model connecting the magnetic structures, magnetization process, and magnetoelectric response of $LiNiPO_4$ is developed. Finally, we discuss whether a drastic field dependence of the spin-anisotropy can explain the observed magnetic structure. Our results establish $LiNiPO_4$ as a model system with a complex phase diagram that is directly impacted by the spin-lattice coupling.

II. EXPERIMENTAL DETAILS

The neutron diffraction experiment was performed on the SEQUOIA direct time-of-flight spectrometer [36] at the Spallation Neutron Source, Oak Ridge National Laboratory. The instrument was operated in Laue mode with an epithermal neutron wavelength band $\lambda = 0.1$–0.8 Å. The pulsed magnetic field was generated by a solenoid coil, mounted in an insert for a standard ^{4}He -flow cryostat, and connected to a capacitor

*Present address: Department of Physics, Technical University of Denmark, DK-2880 Kongens Lyngby, Denmark.

bank delivering 4–5 ms pulses and a maximum field of 30 T. This setup [32,33] allows the sample temperature to be controlled by the cryostat, while the solenoid is immersed in liquid nitrogen. A high-quality single crystal ($m \approx 400$ mg [29]) was mounted inside the 12 mm magnet bore with its crystallographic a axis vertical and the c axis at an angle $\theta = 2.8^\circ$ away from the field axis, which in turn was parallel to the incident beam. With this crystal orientation, momentum transfers parallel to $(0,1,0)$ are probed at a horizontal scattering angle 2θ.

The existence of specific Bragg peaks $\mathbf{Q} = (0,K,0)$ can now be investigated by adjusting the maximum field $\mu_0 H_{\max}$ and the time delay Δt between the magnet pulse and the neutron pulse emanating from the spallation target (see Appendix A and Fig. 4). Neutrons fulfilling the condition $Q = (2\pi/b)K = (4\pi/\lambda)\sin(\theta)$ then arrive at the sample position while the field takes on a value in the range of interest. Employing the time-of-flight method, the neutron wavelength λ, and therefore K, depends on time. With each setting, Bragg peaks are probed along a curve in a $\mu_0 H_z$ versus K plane [see Fig. 2(a)].

The advantage of using epithermal neutrons is that the momentum range probed near the field maximum is comparable to typical Brillouin zone dimensions. Further, the decrease in Bragg peak reflectivity associated with the use of short-wavelength neutrons is partially compensated by a reduction in absorbtion and extinction losses [37]. The cooling requirements of the coil limit the number of pulses to 6–10 per hour, leaving only the strongest Bragg peaks observable.

In addition to the diffraction experiment, the magnetization and electrical polarization were measured in pulsed fields up to 30 T applied along the c axis. The pulse durations (FWHM) were 5 ms and 2 ms, respectively. The absolute value of the magnetization m was scaled to previous results obtained with static fields [30]. The electrical polarization was measured using a procedure similar to that described in Refs. [38,39]. All measurements presented in this paper were obtained at $T = 4.2$ K.

III. RESULTS

The bulk magnetization shown in Fig. 1(a) indicates the existence of five phases at 4.2 K (enumerated I–V with increasing field) up to 30 T where the magnetization approaches $(1/3)m_S$, with the expected saturation magnetization per ion given by $m_S \simeq 2.2\mu_B$. The associated critical fields are in rough agreement with those reported in Ref. [31]. The two lowest transition fields at 12 and 16 T are in agreement with our previous studies [28,30]. The ME response $P_x = \alpha_{xz} H_z$ of the five phases is shown in Fig. 1(b). At low fields in phase I, the known linear ME effect of $LiNiPO_4$ [22,28], is observed. At fields larger than ~ 6.5 T, a quadratic component develops before the polarization drops to zero at the transition from the commensurate phase I to the IC screw spiral phase II. P_x remains zero as the spiral structure reestablishes commensuration with the lattice [30] in phase III. In phase IV a dramatic reentrance of ME effect is observed, with P_x increasing linearly with field before disappearing at the transition to phase V.

We note that there are slight variations between the transition fields seen in the magnetization and polarization measurements. These are likely due to the differences in pulse duration and shape. Furthermore, phase coexistence and demagnetization effects are expected to be more pronounced for pulsed fields as compared to static fields. Additionally, both data sets display hysteresis as is typical for first-order transitions.

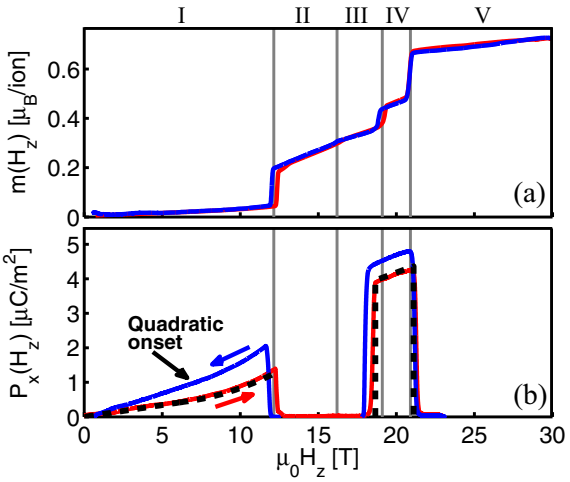

FIG. 1. Magnetization m (a) and electrical polarization P_x (b) at 4.2 K versus $\mu_0 H_z$. The solid vertical lines at $\mu_0 H_z \simeq 12$ T, 16 T, 19 T, and 21 T are approximate transition fields deduced from the magnetization and its derivative. The polarization data indicate a finite ME response in phases I ($\mu_0 H_z \leqslant 12$ T) and IV (19 T $\leqslant \mu_0 H_z \leqslant$ 21 T). The dashed line corresponds to the model calculation described in the text.

Next, we describe the pulsed field neutron diffraction results. Figure 2(a) shows all data obtained for $\mu_0 H_z > 10$ T. Each circle represents a single neutron recorded by a small number of detector pixels near the horizontal scattering angle 2θ (see Appendix A for details). The curved, solid lines represent corresponding values of $(0,K,0)$ and $\mu_0 H_z$ for each field pulse setting. A clustering of neutrons near specific values of K is evident in each of the magnetic phases. Note in particular that the nuclear $(0,2,0)$ reflection is observed for all magnet pulses, in the field interval 0–21 T, demonstrating that the sample maintains its orientation throughout the experiment. In Figs. 2(b)–2(d) we integrate the detected neutron counts over the field ranges of phases III, IV, and V. The peak positions are then extracted by fitting the resulting curves to Gaussian line shapes. The peak widths were fixed to values obtained by extrapolation from high-statistics measurements of the $(0,1,0)$ and $(0,2,0)$ Bragg peaks performed in zero field (see Appendix A).

From the data in Fig. 2(b), we verify the known propagation vector $(0,0.8,0)$ of phase III. Figure 2(c) shows a main result of our work: the novel magnetoelectric phase IV is characterized by a single propagation vector $(0,0.99(1),0)$ which is equal to $(0,1,0)$ within error. Therefore, the two magnetoelectric phases I and IV of $LiNiPO_4$ are characterized by identical propagation vectors. Finally, Fig. 2(d) indicates the presence of two Bragg reflections, $(0,0.99(1),0)$ and $(0,1.33(1),0)$, in phase V. Due to the possibility of phase coexistence near phase boundaries, the existence of the former peak should be treated with caution and is subject to further investigation.

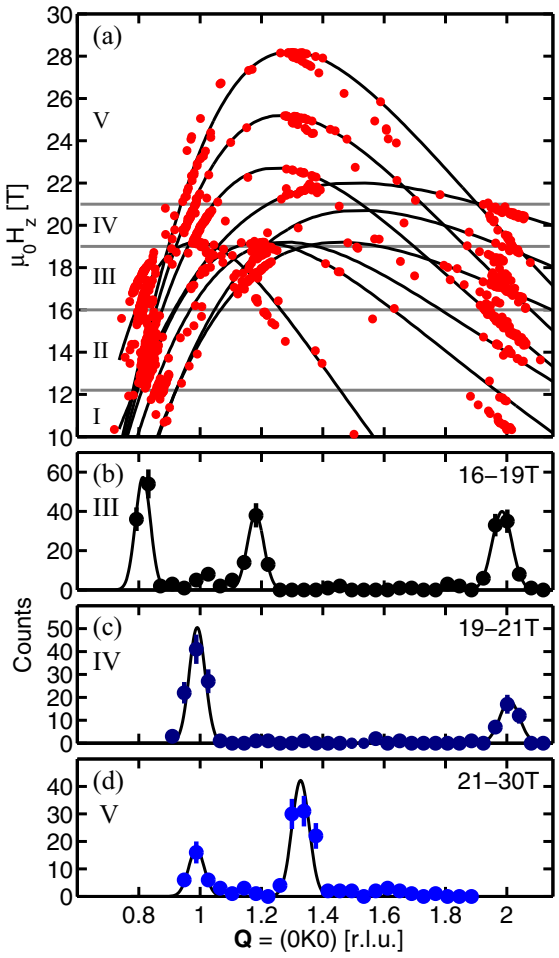

FIG. 2. (a) Raw neutron Laue diffraction data. Each marker represents a single detected neutron. The neutrons probe Bragg peaks on the $(\mu_0 H_z, K)$ curves (solid lines) depending on the maximum field and pulse timing. The horizontal lines represent the transition fields obtained from the magnetization data. Panels (b)–(d) show integrated neutron counts in the field intervals of phases III, IV, and V, normalized to 100 neutron pulses. The Q range is limited to wave vector transfers covered by one or more pulses in the respective magnetic phases.

IV. DISCUSSION

A. Magnetic structure in phase IV

The measured magnetization and propagation vector allow us to establish a quantitative model for the electric polarization in phase IV. In this section we show how the most probable magnetic structure consistent with the measured magnetization and electric polarization in Fig. 1 can be identified.

We start by providing an argument showing that the propagation vector in phase IV is commensurate and not incommensurate. The hard axis in $LiNiPO_4$ is along b due to a single-ion anisotropy energy $D_y S_y^2$ with a large $D_y = 1.423$ meV (see Ref. [30] and Appendix C). This serves to confine the magnetic moments to the ac plane. Hence, any magnetic structure characterized by $(0,K,0) = (0,1 \pm k,0)$ has ordered moments perpendicular to the propagation vector. This is the case for the screw spiral structures observed in phases II and III, as well as the sinusoidally modulated structure observed in zero field just above T_N [29,30]. Neither of these structures support the linear ME effect [40]. On the other hand, the commensurate structure in phase I does support the ME effect. This suggests that because a finite electrical polarization is observed in phase IV, its propagation vector is truly commensurate and equal to $(0,1,0)$. The neutron diffraction data give rise to the same conclusion.

We proceed to determine the most probable structure by help of symmetry analysis [28,30]. The four Ni^{2+} ions reside in a nearly face-centered orthorhombic arrangement at $\mathbf{r}_1 = (0.275,0.25,0.98)$, $\mathbf{r}_2 = (0.775,0.25,0.52)$, $\mathbf{r}_3 = (0.725,0.75,0.02)$, and $\mathbf{r}_4 = (0.225,0.75,0.48)$. The magnetic reflections $(0,1 \pm k,0)$ exclusively reflect magnetic ordering of the four ions according to the pattern $C_\gamma = (+,+,-\beta,-\beta)$, where γ denotes the moment direction and $\beta = e^{i\pi k}$ is a phase factor. Here k can be a rational number, corresponding to commensurate propagation vectors, or an irrational number corresponding to an IC propagation vector. In the case of phase IV we have $k = 0$. Other possible symmetry components are $G_\gamma = (+,-,+\beta,-\beta)$, $A_\gamma = (+,-,-\beta,+\beta)$, and $F_\gamma = (+,+,+\beta,+\beta)$. For the momenta $(0,1 \pm k,0)$ probed in our experiment (see Fig. 2), the neutron scattering selection rules imply vanishing intensity contributions from any spin component parallel to b. Thus, $(0,1 \pm k,0)$ peaks reflect *only* C_x and C_z components of the magnetic structure. As shown in Appendix A, the full $\mathbf{Q}$ range probed in the neutron scattering experiment included $(1,1,0)$ and $(1,2,0)$ reflecting G and A symmetry components, respectively. No intensity was observed at these positions and hence we can exclude any major components of these types. Based on the data shown in Figs. 2(b)–2(d) it is estimated that Bragg peaks of ~ 10 times less intensity than the $(0,1,0)$ peak would be impossible to observe in the pulsed-field experiment. On the other hand, the finite magnetization [see Fig. 1(a)] is represented by an F_z component, coexisting with the C_x or C_z component.

We can now exploit the symmetry constraints on the ME effect to choose between these two possibilities, C_x and C_z, for the main magnetic structure components. These constitute two distinct magnetic point groups with two different magnetoelectric tensor components. Thus, a C_x component would lead to the absence of an α_{xz} ME tensor component [2,22,41], in contrast to the observations. On the other hand, a C_z component allows a nonzero α_{xz} element as indeed observed in phase IV. Therefore, we conclude that the main magnetic structure component in phase IV is C_z, just as is the case for the zero-field structure. In zero field, an additional symmetry component, A_x, was observed, resulting in a canting of spin pairs (1, 2) and (3, 4); see Fig. 3(a). In Ref. [28], a small applied field was shown to introduce an asymmetry in this canting angle—represented by a G_x component—in addition to a component F_z reflecting the field-induced magnetization. For phase IV, we propose the version of this structure shown in Fig. 3(b). Here, the spins on sites 1 and 2 are nearly parallel to the applied magnetic field, while those on sites 3 and 4 are rotated away from the c axis. This corresponds to the presence of two additional antiferromagnetic symmetry components of similar magnitude, $A_x \sim G_x$, in addition to the C_z and F_z components deduced from the neutron diffraction and magnetization data, respectively. The squared structure factors for the Bragg peaks

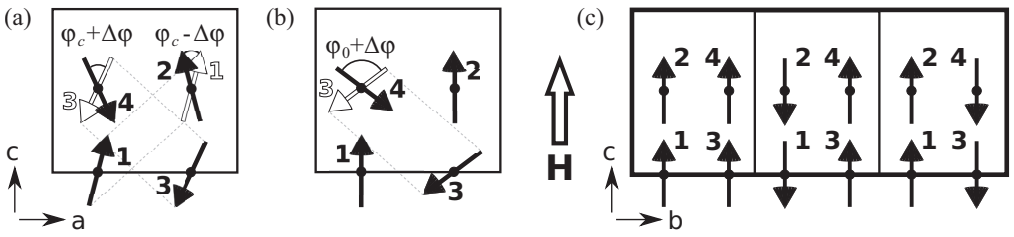

FIG. 3. (a) The magnetic structure in small applied fields in phase I; the difference in spin canting between spin pairs (1, 2) and (3, 4) produces the ME effect [28]. (b) The proposed magnetic structure in phase IV producing the reentrant polarization. The open arrows in (a) and (b) are translated copies of the moments on sublattices 1 and 3, illustrating the relative angles ϕ_c, ϕ_0, and $\Delta\phi(H)$ described in the text. (c) The calculated c components of the IC structure in phase V with $k = 1/3$.

reflecting the A_x and G_x symmetry components correspond to peak intensities about an order of magnitude smaller than the intensity of the observed (0,1,0) peak, and are thus too weak to be observed directly in pulsed fields. However, the existence of these symmetry components is made plausible by the quantitative model for the ME response in both phases I and IV as described in the next section.

Generally, in simple Heisenberg antiferromagnets a spin-flop transition is expected for magnetic fields applied along the easy axis [42,43]. The magnitude of the easy-axis anisotropy determines the spin-flop transition field at which the spins reorient from configurations parallel and antiparallel to the field, to one in which they are transverse to the field. In the transverse configurations spins may gradually turn towards the field direction whereas in a longitudinal structure Zeeman energy can only be gained at $T = 0$ by flipping a spin. With weak ac-plane anisotropy the transverse configuration is therefore favorable in terms of the balance between Zeeman and exchange energy. In addition, the C_x component is experimentally observed to increase in the elliptical (C_z, C_x) spiral structures in phase II and III. Consequently, the observation of a C_z structure in phase IV instead of a C_x structure is surprising. Indeed, the mean-field model that explains the susceptibility, magnetic structure, and dynamics below 17.3 T [30] predicts a C_x-type structure in phase IV. However, as argued above, the only structure consistent with the observed nonzero α_{xz} ME tensor component is C_z. As we shall show below, the C_z structure is further substantiated by providing a canvas for a quantitative model explaining the field dependence of the ME effect in phase IV.

Within the mean-field model [30], the single-ion anisotropy term (providing a preference for spins being oriented along c within the easy ac plane), $D_x S_x^2$ with $D_x = 0.413$ meV, is far too weak to energetically favor a structure with spins along c in phase IV. Nearly a doubling of D_x is required for the system to prefer a longitudinal C_z structure over a C_x-type spin-flop structure in phase IV. Such a dramatic change of anisotropy can hardly be produced by the perturbation of the crystal field levels by the applied magnetic field. Instead, a change of the crystal field itself is probable. This is due to the low symmetry of the crystal field in $LiNiPO_4$ [44], allowing the spin-orbit interaction to introduce a significant orbital contribution to the otherwise quenched ground state, resulting in relatively strong DM interactions and single-ion anisotropy [28]. Even minor changes in the crystal field could have an important impact on the spin anisotropy. Such a field-induced change in spin anisotropy could be produced by a strong magnetostrictive effect, possibly associated with the shift of PO_4 tetrahedra. When the orbital contribution to the ground state is significant, the magnetic field can even alter the crystal field via orbital magnetism coupled directly to the lattice. Such orbitally induced distortions of the crystal field in applied magnetic fields were calculated for the isostructural compound $LiFePO_4$ in Ref. [14].

B. Magnetoelectric effect in phase IV

Our starting point for modeling the magnetoelectric effect in phase IV is inspired by the model previously developed for phase I in Ref. [28] and the similarities between the magnetic structures in phases I and IV. The magnetic structure in phase I, see Fig. 3(a), is predominantly described by C_z with an additional minor symmetry component A_x causing a small canting angle $\phi_c = 15.5^\circ = 0.27$ rad in zero magnetic field. The magnetic structure in phase IV is similar but with a much more pronounced canting angle; see Fig. 3(b). This canting of predominantly the spins on sites 3 and 4 is described by two distinct and similar antiferromagnetic components $A_x \sim G_x \sim \frac{1}{3}C_z$. While these components are too small to be observable in the neutron data directly, their existence can be deduced from the following model encompassing the ME response in both phases I and IV. At the onset field $\mu_0 H \simeq 19$ T the magnetization in phase IV is $m = 0.45\mu_B \simeq (1/5)m_S$ corresponding to an angle between spins 3 and 4 of $\phi_0 \simeq 105^\circ$. In both phases the applied field along c changes the canting angles by $\Delta\phi$, creating an asymmetry in the superexchange (SE) energy of the two spin pairs (1,2) and (3,4). As a result, the SE energy can be lowered by translating the exchange-mediating PO_4 tetrahedra by a distance x along the a axis, leading to an increase (reduction) of the J_{34} (J_{12}) exchange couplings [28]. The corresponding SE energy of the two spin pairs in phase IV is $\mathcal{H}^{\rm SE}_{12,34} = J_{34}\langle S\rangle^2\cos[\phi_0 + \Delta\phi(H)] + J_{12}\langle S\rangle^2 \approx J_{34}\langle S\rangle^2[-0.26 - 0.97\Delta\phi(H)] + J_{12}\langle S\rangle^2$, where the last part is obtained by a Taylor expansion around ϕ_0. $\Delta\phi(H)$ is the field-induced rotation of the moments on sites 3 and 4 in the ac plane. The PO_4 tetrahedra displacement x introduces an asymmetry in the exchange paths increasing $J_{34} \to J + \lambda x$ and decreasing $J_{12} \to J - \lambda x$ (λ is a proportionality constant). This leads to a reduction of the SE energy $\Delta\mathcal{E} =$

$\langle S\rangle^2[-1.26\lambda x - 0.97\lambda x\Delta\phi(H)]$. The displacement of the PO_4 tetrahedra in the lattice is associated with an elastic energy $\epsilon_x x^2$. Minimizing the sum of the SE and elastic energy yields the equilibrium tetrahedral displacement x, proportional to the bulk polarization via $P_x = \mathcal{K}x$:

$$P_x = \frac{\mathcal{K}\langle S\rangle^2\lambda}{\epsilon_x}[0.63 + 0.48\Delta\phi(H)],$$

where $\mathcal{K}$ connects the microscopic charge displacement of the PO_4 tetrahedra to bulk electric polarization. Since this model applies for both phases I and IV, we proceed to use the measured ME response in phase I to estimate the ratio $\frac{\mathcal{K}\lambda}{\epsilon_x}$, enabling us to predict the ME response in phase IV. In phase I, the polarization is described by $P_x = \frac{\mathcal{K}\lambda}{\epsilon_x}\langle S\rangle^2\phi_c\Delta\phi$ [28]. A quadratic onset of $P_x(H_z)$ is evident in Fig. 1. This is due to a constant angle between moments on sites 1 and 2 when $\Delta\phi \to \phi_c$ where the low-angle quadratic terms of an expansion of the SE energy for the two ion pairs (3,4) and (1,2) no longer cancel out (see Appendix B). The quadratic response was fitted to set in at 6.5 T with increasing field, where the measured polarization is $P_x = \mathcal{K}x = 4.6 \times 10^{-7}\frac{\mu C}{cm^2}$. At $\Delta\phi = \phi_c = 0.27$ rad [28], we estimate $\frac{\mathcal{K}\lambda\langle S\rangle^2}{\epsilon_x} \approx 6.2 \times 10^{-6}\frac{\mu C}{cm^2}$. In phase IV, the magnetization increases from $0.45\mu_B$ to $0.5\mu_B$ representing a change in canting angle of $\Delta\phi = 0.13$ rad for ions 3 and 4. Using the estimate for $\frac{\mathcal{K}\lambda\langle S\rangle^2}{\epsilon_x}$, a linear change in the polarization in the interval $P_x = 3.9$–$4.3 \times 10^{-6}\frac{\mu C}{cm^2}$ going through phase IV is predicted. This corresponds well with the observed polarization in phase IV as evident in Fig. 1, strongly supporting the establishment of a longitudinal C_z structure in phase IV.

C. Magnetic structure in phase V

The data shown in Fig. 1(a) indicate that the magnetization is $m \simeq (1/3)m_S$ and slowly varying with field. The neutron diffraction data in Fig. 2(d) display two Bragg peaks at (0,1,0) and (0,4/3,0). As shown in Appendix A, no additional peaks were observed. It is therefore likely that the structure is a longitudinal spin-flip type structure, mainly composed of a $k = 0$ ferromagnetic F_z component (the magnetization) and a C_z component with a commensurate ordering wave vector $k = 1/3$. Note that a C_z component $(+, +, -\beta, -\beta)$ with $k = 1/3$ is equivalent to an F_z component $(+, +, +\beta, +\beta)$ with $k = 2/3$, both being fully compensated AFM structures. The DM interaction is expected to produce weak components transverse to the c axis, but the resulting low-intensity Bragg peaks reflecting these minor components are not observable. When using the weak $D_x = 0.413$ meV anisotropy in a mean-field calculation similar to that presented in Ref. [30], a $k = 1/3$ C_z magnetic structure with spins almost entirely aligned along the c axis is stabilized. The spin components in the bc plane are shown in Fig. 3(c) (see also Appendix C). Phase V does not display the ME effect and the calculated structure obeys this constraint. However it does not produce the observed (0,1,0) reflection. As mentioned earlier, this peak is probed only near the phase boundary between phases IV and V and could have its origin in phase coexistence. The existence of a (0,1,0) Bragg peak in phase V is therefore subject to further investigation. We emphasize that the zero-field Hamiltonian is unable to predict the magnetic structure in phase IV, and therefore the mean-field predictions for phase V should be treated with caution. Clarifying the magnetic structure in phase V requires additional neutron scattering studies.

V. CONCLUSION

To conclude, we have discovered the reentrance of a magnetoelectric response between 19 T and 21 T in $LiNiPO_4$ for fields applied along the c axis. Pulsed-field neutron Laue diffraction reveals a commensurate magnetic structure in this phase, characterized by the propagation vector (0,1,0). We have shown that a magnetized version of the zero-field structure is consistent with all data. This is confirmed by a quantitative model for $P_x(H_z)$ which is in excellent agreement with the data. For fields in the range between 21 T and 30 T we propose a spin-flip type structure with ordering vector (0,1/3,0) and spins nearly parallel to the c axis. In this phase the magnetoelectric effect is absent. A mean-field model employing the zero-field exchange couplings and single-ion anisotropies fails to predict the magnetic structure in the high-field magnetoelectric phase. This indicates that the couplings between magnetic and structural degrees of freedom have a strong influence on the physical properties of $LiNiPO_4$.

Note Added. A very recent paper [45] reports an experimental study of the magnetoelectric effect in $LiNiPO_4$ in pulsed fields. The paper confirms the existence of a magnetoelectric phase near 20T as well as a nonlinear contribution to the magnetoelectric effect in phase I.

ACKNOWLEDGMENTS

We thank N. H. Andersen for discussions. This work was supported by the Danish Agency for Science, Technology, and Innovation under DANSCATT. Research at Ames Laboratory was supported by the US Department of Energy, Office of Basic Energy Sciences, Division of Materials Sciences and Engineering, under Contract No. DE-AC02-07CH11358. A portion of this research used resources at the Spallation Neutron Source, a DOE Office of Science User Facility operated by the Oak Ridge National Laboratory. H.N. acknowledges support by KAKENHI 23224009, ICC-IMR, and MD program.

R.T.-P. and E.F. contributed equally to this work.

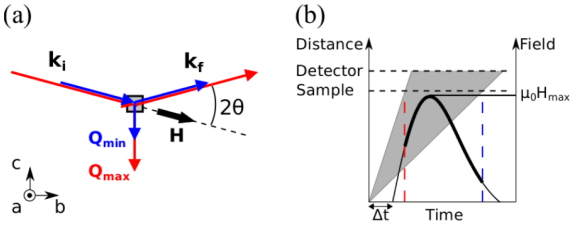

FIG. 4. Experimental setup. (a) Scattering geometry with the magnetic field direction and crystallographic directions indicated. The red (blue) arrows represent the shortest (longest) accessible wavelengths. (b) Neutron travel distance and magnetic field strength as a function of time. The overlap of the neutron pulse (gray area) and magnet pulse (black curve) is determined by the maximum field strength, $\mu_0 H_{max}$, and the time delay, Δt. The red (blue) dashed line corresponds to TOF of the shortest (longest) accessible wavelength.

TABLE I. Magnet settings used in the neutron experiment. The field was generated by a 5.6 mF capacitor bank with a maximum charging level of 1.5 kV corresponding to $\mu_0 H_{\max} = 30$ T.

$\mu_0 H_{\max}$ (T)	19.2	19.2	19.2	19.2	20.7	22.0	22.7	25.2	28.2
Δt (μs)	360	600	750	1200	300	0	700	700	700
No. of pulses	193	73	117	151	119	127	163	202	266

This manuscript has been authored by UT-Battelle, LLC under Contract No. DE-AC05-00OR22725 with the US Department of Energy. The United States Government retains and the publisher, by accepting the article for publication, acknowledges that the United States Government retains a nonexclusive, paid-up, irrevocable, worldwide license to publish or reproduce the published form of this manuscript, or allow others to do so, for United States Government purposes. The Department of Energy will provide public access to these results of federally sponsored research in accordance with the DOE Public Access Plan (http://energy.gov/downloads/doe-public-access-plan).

APPENDIX A: FURTHER EXPERIMENTAL DETAILS

The scattering geometry in the pulsed-field experiment and the principle of controlling the overlap between the magnet and neutron pulses are illustrated in Fig. 4. Table I lists the magnet settings employed as well as the number of magnet pulses discharged for each setting.

In Fig. 5 we show a SEQUOIA detector image in which we have integrated over all field pulses. Only a small detector area around the forward-scattering direction is accessible. This is due to neutron-absorbing boron shielding around the magnet and the sample space. Within the illuminated portion of the detector we only observe Bragg peaks around the expected $(0,K,0)$ position. A careful search for peaks of other forms, e.g., (1,1,0), (1,1.33,0), and (1,2,0), was conducted. No such peaks could be observed in this experiment.

In the interval between the field pulses, the instrument collected zero-field data. Due to the long waiting times, the statistical quality of these data, shown in Fig. 6, is very good.

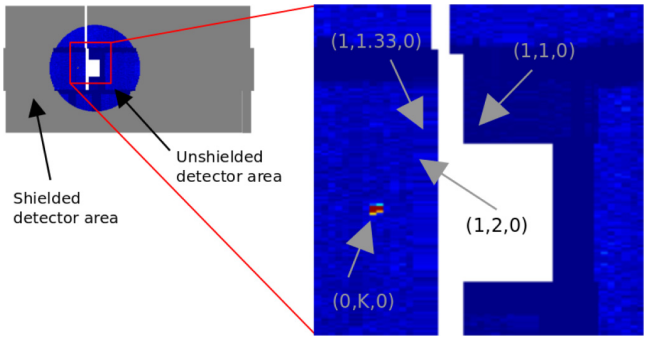

FIG. 5. SEQUOIA detector image integrated over all magnetic field pulses. In the part of the detector not affected by the shielding around the magnet insert, only peaks of the type $(0,K,0)$ were identified.

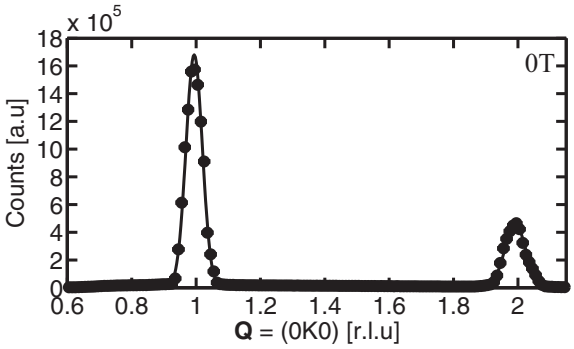

FIG. 6. All neutron counts obtained in zero field as a function of scattering vector $\mathbf{Q} = (0,K,0)$.

As expected, we observe two Bragg peaks in phase I: a nuclear $(0,2,0)$ peak and a magnetic $(0,1,0)$ peak.

The limited statistics of having only counted 1274 neutrons for finite fields exclusively allows for the determination of the Bragg peak positions and not for any quantitative analysis of the intensities. The peak centers are determined by fitting Gaussian line shapes to the data. The peak widths were fixed to values obtained by a linear extrapolation based on the zero-field data shown in Fig. 6.

For each magnet setting, a curve in $(\mu_0 H, K)$ space is probed. The scattered neutrons were recorded in event mode allowing us to assign a corresponding field value (at the sample position) for each individual detected neutron. In Fig. 2 it is evident that some neutron counts occur away from the solid lines representing the corresponding values of $\mathbf{Q} = (0,K,0)$ and magnetic field, $\mu_0 H$. The reason is that the scattered neutrons are spread over two vertical detector tubes, each with signal in 10 pixels. The resulting variation in scattering angle gives rise to a slight difference in flight path. This, in turn, implies that for a given setting of the maximum field strength and delay time, any given value of $\mathbf{Q} = (0,K,0)$ is probed over a small distribution of fields. This is shown in Fig. 7 for the particular case of the data set obtained with $\mu_0 H_{\max} = 28.2$ T and $\Delta t = 700$ μs.

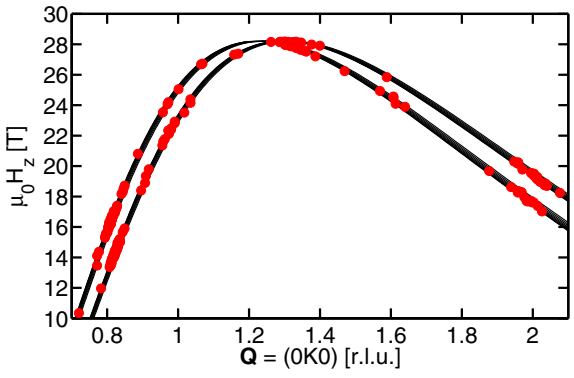

FIG. 7. The effect of having the $(0,K,0)$ Bragg peak signals distributed over multiple pixels in two adjacent detector tubes. The probed curve in $(\mu_0 H, K)$ space is split into two curves which are broadened due to the spread in pixels, as indicated by the curve widths.

TABLE II. The exchange parameters (in units of meV) used in the mean-field model, including the number of neighbors (Z) using the same notation as in Ref. [30].

	J_{bc}^{nn}	J_b'	J_c'	J_{ab}	J_{ac}	J_b^c	J_{bc}^{nnn}
Z	4	2	2	2 + 2	2 + 2	4	4
$J(ij)$	1.002	1.13	0.40	0.321	−0.112	−0.23	−0.08

APPENDIX B: ONSET OF QUADRATIC POLARIZATION IN PHASE I

In phase I, the energy $\mathcal{E}_{12,34}^{\mathrm{SE}}$ of the Hamiltonian $\mathcal{H}_{12,34}^{\mathrm{SE}} = J_{12}\mathbf{S}_1 \cdot \mathbf{S}_2 + J_{34}\mathbf{S}_3 \cdot \mathbf{S}_4$ can be Taylor expanded

$$\mathcal{E}_{\mathrm{SE}} = (J_{12} + J_{34})\langle S\rangle^2\left[1 - \frac{1}{2}(\phi_c^2 + \Delta\phi^2)\right] - (J_{34} - J_{12})\langle S\rangle^2\phi_c\Delta\phi,$$

where $\Delta\phi$ is the field-induced change in canting angle. Assuming that the resulting asymmetry in canting angles changes $J_{12} = J_{34}$ to produce $J_{12} = J - \delta$ and $J_{34} = J + \delta$, only the last term contributes to the resulting change in superexchange energy $\Delta\mathcal{E}_{\mathrm{SE}} = -2\delta\langle S\rangle^2\phi_c\Delta\phi$. This linear dependence on $\Delta\phi$ is shown in Ref. [28] to produce a linear ME response at low fields. However, if the field is strong enough, $\Delta\phi \to \phi_c$, resulting in constant alignment of spins 1 and 2. This activates the first term in the Taylor expansion as a source of ME response. Using the same procedure as in the main text, a Taylor expansion of the superexchange energy around $2\phi_c$ now yields

$$\mathcal{E}_{\mathrm{SE}} = J_{34}\langle S\rangle^2\left[\cos(2\phi_c) - 2\phi_c\Delta\phi - \frac{\cos(2\phi_c)}{2}\Delta\phi^2\right] + J_{12}\langle S\rangle^2$$

using the small-angle approximation for $\sin(2\phi_c)$. Assuming the linear change in exchange constants the energy difference now becomes

$$\Delta\mathcal{E}_{\mathrm{SE}} = \langle S\rangle^2\left(-0.15 - 2\delta\phi_c\Delta\phi - \frac{\delta\cos(2\phi_c)}{2}\Delta\phi^2\right). \tag{B1}$$

Using the same assumptions as in the main text, this gives rise to a continuation of the lower-field ME response through the linear term, with an additional quadratic component as $\Delta\phi > \phi_c$, with tetrahedra displacement given by $x = \frac{\langle S\rangle^2\lambda}{2\epsilon_x}(0.15 + \phi_c\Delta\phi + \frac{\cos(2\phi_c)}{2}\Delta\phi^2)$. Assuming $\Delta\phi \propto M = \chi_c H_z$, we can fit P_x vs H_z in phase I to the function $P_x = c_1 H_z + c_2 S_{c_3}(H_z)(H_z - c_3)^2$, where the c_i are variables and $S_{c_3}(H_z)$ is a Heaviside step function centered at $H_z = c_3$. The step function roughly represents the crossover regime between the two cases described. The quadratic onset thus has a clear justification using the employed model, and can be said to arise from $\Delta\phi \to \phi_c$.

TABLE III. The stabilized $\mathbf{Q} = (0,1/3,0)$ structure at $\mu_0 H \geqslant 23$ T. Due to the spin anisotropy $S_y = 0$ for all ions.

Unit cell 1	ion 1	ion 2	ion 3	ion 4
S_x	0.042	−0.042	0.042	−0.042
S_z	0.985	0.985	0.985	0.985
Unit cell 2	ion 5	ion 6	ion 7	ion 8
S_x	0.236	−0.236	0.042	−0.042
S_z	−0.962	−0.962	0.985	0.985
Unit cell 3	ion 9	ion 10	ion 11	ion 12
S_x	0.042	−0.042	0.236	−0.236
S_z	0.985	0.985	−0.962	−0.962

APPENDIX C: ELABORATION ON THE MEAN-FIELD MODEL

The mean-field model employed in this work was originally introduced in Ref. [30]. The Hamiltonian is assumed to be

$$\mathcal{H} = \frac{1}{2}\sum_{ij} J(ij)\mathbf{S}_i \cdot \mathbf{S}_j + \mathcal{H}_{\mathrm{DM}} + \sum_{\alpha,i} D_\alpha S_{\alpha i}^2 - g\mu_B\sum_i \mathbf{H}\cdot\mathbf{S}_i$$

with $g = 2.2$. Assuming only nearest neighbors to contribute, the DM interaction allowed by symmetry is [28]

$$\mathcal{H}_{\mathrm{DM}} = D_{14}\sum_{ij\in\mathrm{n.n.}}[S_z(1i)S_x(4j) - S_x(1i)S_z(4j) + S_z(3i)S_x(2j) - S_x(3i)S_z(2j)],$$

where, e.g., $S_z(1i)$ only contributes to the sum if the ith site belongs to sublattice 1 consisting of ions on position $\mathbf{r}_1$. The exchange constants used in the Hamiltonian are given in Table II. In order to stabilize structures with short modulation wavelengths, a weak next-nearest neighbor interaction along the b axis between sublattices 1 and 4 in the bc plane, J_{bc}^{nnn}, is introduced. For calculating the structure in phase V, the modulation period along the b axis was fixed to 3 unit cells ($K = 1/3$), which was also found to be the most stable modulation above approximately 23 T in the model with $J_{bc}^{nnn} = -0.08$ meV. The resulting components (thermal mean values) of S_x and S_z on each of the 12 sites are given in Table III. The S_y components of the spins have been omitted as they are all zero, due to the strong D_y term.

[1] W. Eerenstein, N. D. Mathur, and J. F. Scott, Nature (London) **442**, 759 (2006).

[2] H. Schmidt, Ferroelectrics **162**, 317 (1994).

[3] G. A. Smolenskii and I. E. Chapuis, Sov. Phys. Usp. **25**, 475 (1983).

[4] C. Israel, N. D. Mathur, and J. F. Scott, Nat. Mater. **7**, 93 (2008).

[5] Y. Geng, Hena Das, Aleksander L. Wysocki, Xueyun Wang, S.-W. Cheong, M. Mostovoy, Craig J. Fennie, and Weida Wu, Nat. Phys. **13**, 163 (2014).

[6] M. Bibe and A. Barthelemy, Nat. Mater. **7**, 425 (2008).

[7] Claude Chappert, Albert Fert, and Frederic Nguyen Van Dau, Nat. Mater. **6**, 813 (2007).

[8] N. Hur, S. Park, P. A. Sharma, J. S. Ahn, S. Guha, and S-W. Cheong, Nature (London) **429**, 392 (2004).

[9] J. T. Heron, J. L. Bosse, Q. He, Y. Gao, M. Trassin, L. Ye, J. D. Clarkson, C. Wang, Jian Liu, S. Salahuddin, D. C. Ralph, D. G. Schlom, J. Iniguez, B. D. Huey, and R. Ramesh, Nature (London) **516**, 370 (2014).

[10] V. V. Kruglyak, S. O. Demokritov, and D. Grundler, J. Phys. D **43**, 264001 (2010).

[11] Wei Chen and Manfred Sigrist, Phys. Rev. Lett. **114**, 157203 (2015).

[12] A. Pimenov, A. A. Mukhin, V. Yu. Ivanov, V. D. Travkin, A. M. Balbashov, and A. Loid, Nat. Phys. **2**, 97 (2006).

[13] S. W. Cheong and M. Mostovoy, Nat. Mater. **6**, 13 (2007).

[14] A. Scaramucci, E. Bousquet, M. Fechner, M. Mostovoy, and N. A. Spaldin, Phys. Rev. Lett. **109**, 197203 (2012).

[15] T. Kimura, T. Goto, H. Shintani, K. Ishizaka, T. Arima, and Y. Tokura, Nature (London) **426**, 55 (2003).

[16] Masakazu Matsubara, Sebastian Manz, Masahito Mochizuki, Teresa Kubacka, Ayato Iyama, Nadir Aliouane, Tsuyoshi Kimura, Steven L. Johnson, Dennis Meier, and Manfred Fiebig, Science **348**, 1112 (2015).

[17] M. Kenzelmann, A. B. Harris, S. Jonas, C. Broholm, J. Schefer, S. B. Kim, C. L. Zhang, S.-W. Cheong, O. P. Vajk, and J. W. Lynn, Phys. Rev. Lett. **95**, 087206 (2005).

[18] K. Taniguchi, N. Abe, T. Takenobu, Y. Iwasa, and T. Arima, Phys. Rev. Lett. **97**, 097203 (2006).

[19] M. Baum, J. Leist, Th. Finger, K. Schmalzl, A. Hiess, L. P. Regnault, P. Becker, L. Bohaty, G. Eckold, and M. Braden, Phys. Rev. B **89**, 144406 (2014).

[20] Andrei Malashevich, Sinisa Coh, Ivo Souza, and David Vanderbilt, Phys. Rev. B **86**, 094430 (2012).

[21] Maxim Mostovoy, Andrea Scaramucci, Nicola A. Spaldin, and Kris T. Delaney, Phys. Rev. Lett. **105**, 087202 (2010).

[22] M. Mercier, Ph.D. thesis, Université de Grenoble, 1969.

[23] I. Kornev, M. Bichurin, J.-P. Rivera, S. Gentil, H. Schmid, A. G. M. Jansen, and P. Wyder, Phys. Rev. B **62**, 12247 (2000).

[24] V. I. Fomin, V. P. Gnezdilov, V. S. Kurnosov, A. V. Peschanskii, A. V. Yeremenko, H. Schmid, J.-P. Rivera, and S. Gentil, Low Temp. Phys. **28**, 203 (2002).

[25] Yu. N. Kharchenko, N. F. Kharcheno, M. Baran, and R. Szymczak, Low Temp. Phys. **29**, 579 (2003).

[26] T. B. S. Jensen, N. B. Christensen, M. Kenzelmann, H. M. Rønnow, C. Niedermayer, N. H. Andersen, K. Lefmann, M. Jiménez-Ruiz, F. Demmel, J. Li, J. L. Zarestky, and D. Vaknin, Phys. Rev. B **79**, 092413 (2009).

[27] K. Yamauchi and S. Picozzi, Phys. Rev. B **81**, 024110 (2010).

[28] Thomas Bagger Stibius Jensen, Niels Bech Christensen, Michel Kenzelmann, Henrik Moodysson Rønnow, Christof Niedermayer, Niels Hessel Andersen, Kim Lefmann, Jürg Schefer, Martin v. Zimmermann, Jiying Li, Jerel L. Zarestky, and David Vaknin, Phys. Rev. B **79**, 092412 (2009).

[29] D. Vaknin, J. L. Zarestky, J.-P. Rivera, and H. Schmid, Phys. Rev. Lett. **92**, 207201 (2004).

[30] Rasmus Toft-Petersen, Jens Jensen, Thomas Bagger Stibius Jensen, Niels Hessel Andersen, Niels Bech Christensen, Christof Niedermayer, Michel Kenzelmann, Markos Skoulatos, Manh Duc Le, Kim Lefmann, Sonja Rosenlund Hansen, Jiying Li, Jerel L. Zarestky, and David Vaknin, Phys. Rev. B **84**, 054408 (2011).

[31] V. M. Khrustalyov, V. N. Savitsky, and N. F. Kharchenko, Czech. J. Phys. **54**, 27 (2004).

[32] H. Nojiri, S. Yoshii, M. Yasui, K. Okada, M. Matsuda, J.-S. Jung, T. Kimura, L. Santodonato, G. E. Granroth, K. A. Ross, J. P. Carlo, and B. D. Gaulin, Phys. Rev. Lett. **106**, 237202 (2011).

[33] S. Yoshii, K. Ohoyama, K. Kurosawa, H. Nojiri, M. Matsuda, P. Frings, F. Duc, B. Vignolle, G. L. J. A. Rikken, L.-P. Regnault, S. Michimura, and F. Iga, Phys. Rev. Lett. **103**, 077203 (2009).

[34] J. P. C. Ruff, Z. Islam, J. P. Clancy, K. A. Ross, H. Nojiri, Y. H. Matsuda, H. A. Dabkowska, A. D. Dabkowski, and B. D. Gaulin, Phys. Rev. Lett. **105**, 077203 (2010).

[35] S. Gerber, H. Jang, H. Nojiri, S. Matsuzawa, H. Yasumura, D. A. Bonn, R. Liang, W. N. Hardy, Z. Islam, A. Mehta, S. Song, M. Sikorski, D. Stefanescu, Y. Feng, S. A. Kivelson, T. P. Devereaux, Z.-X. Shen, C.-C. Kao, W.-S. Lee, D. Zhu, and J.-S. Lee, Science **350**, 949 (2015).

[36] G. E. Granroth, A. I. Kolesnikov, T. E. Sherline, J. P. Clancy, K. A. Ross, J. P. C. Ruff, B. D. Gaulin, and S. E. Nagler, J. Phys.: Conf. Ser. **251**, 012058 (2010).

[37] Rasmus Toft-Petersen, Manfred Reehuis, Thomas B. S. Jensen, Niels H. Andersen, Jiying Li, Manh Duc Le, Mark Laver, Christof Niedermayer, Bastian Klemke, Kim Lefmann, and David Vaknin, Phys. Rev. B **92**, 024404 (2015).

[38] M. Akaki, H. Iwamoto, T. Kihara, M. Tokunaga, and H. Kuwahara, Phys. Rev. B **86**, 060413(R) (2012).

[39] Hiroyuki Mitamura, Setsuo Mitsuda, Shunsuke Kanetsuki, Hiroko Aruga Katori, Toshiro Sakakibara, and Koichi Kindo, J. Phys. Soc. Jpn. **76**, 094709 (2007).

[40] T. Kimura, Annu. Rev. Mater. Res. **37**, 387 (2007).

[41] J. P. Rivera, Eur. Phys. J. B **71**, 299 (2009).

[42] L. Neel, Ann. Phys. (Paris) **18**, 5 (1932).

[43] M. Fischer and D. R. Nelson, Phys. Rev. Lett. **32**, 1350 (1974).

[44] I. Abrahams and K. S. Easson, Acta Crystallogr., Sect. C: Cryst. Struct. Commun. **49**, 925 (1993).

[45] V. M. Khrustalyov, V. M. Savytsky and M. F. Kharchenko, Low Temp. Phys. **42**, 1126 (2016).

Paper II

Magnetic order, hysteresis and phase coexistence in magnetoelectric $LiCoPO_4$
E. Fogh, R. Toft-Petersen, E. Ressouche, C. Niedermayer, S. L. Holm, M. Bartkowiak, O. Prokhnenko, S. Sloth, F. W. Isaksen, D. Vaknin and N. B. Christensen
Physical Review B **96**, 104420 (2017)

This paper is the culmination following several experiments and data analysis with key input from Eric Ressouche (D23, ILL) and Maciej Bartkowiak (HFM/EXED, HZB).

PHYSICAL REVIEW B **96**, 104420 (2017)

Magnetic order, hysteresis, and phase coexistence in magnetoelectric $LiCoPO_4$

Ellen Fogh,[1,*] Rasmus Toft-Petersen,[1] Eric Ressouche,[2] Christof Niedermayer,[3] Sonja Lindahl Holm,[3,4] Maciej Bartkowiak,[5] Oleksandr Prokhnenko,[5] Steffen Sloth,[1] Frederik Werner Isaksen,[1] David Vaknin,[6] and Niels Bech Christensen[1]

[1]*Department of Physics, Technical University of Denmark, DK-2800 Kongens Lyngby, Denmark*

[2]*INAC-SPSMS, CEA & Universite Grenoble Alpes, 38000 Grenoble, France*

[3]*Laboratory for Neutron Scattering and Imaging, Paul Scherrer Institute, Villigen CH-5232, Switzerland*

[4]*Nano-Science Center, Niels Bohr Institute, University of Copenhagen, DK-2100 Copenhagen Ø, Denmark*

[5]*Helmholtz-Zentrum Berlin für Materialien und Energie, D-14109 Berlin, Germany*

[6]*Ames Laboratory and Department of Physics and Astronomy, Iowa State University, Ames, Iowa 50011, USA*

(Received 10 June 2017; published 15 September 2017)

The magnetic phase diagram of magnetoelectric $LiCoPO_4$ is established using neutron diffraction and magnetometry in fields up to 25.9 T applied along the crystallographic b axis. For fields greater than 11.9 T, the magnetic unit cell triples in size with propagation vector $\mathbf{Q} = (0, \frac{1}{3}, 0)$. A magnetized elliptic cycloid is formed with spins in the (b,c) plane and the major axis oriented along b. Such a structure allows for the magnetoelectric effect with an electric polarization along c induced by magnetic fields applied along b. Intriguingly, additional ordering vectors $\mathbf{Q} \approx (0, \frac{1}{4}, 0)$ and $\mathbf{Q} \approx (0, \frac{1}{2}, 0)$ appear for increasing fields in the hysteresis region below the transition field. Traces of this behavior are also observed in the magnetization. A simple model based on a mean-field approach is proposed to explain these additional ordering vectors. In the field interval 20.5–21.0 T, the propagation vector $\mathbf{Q} = (0, \frac{1}{3}, 0)$ remains but the spins orient differently compared to the cycloid phase. Above 21.0 T and up until saturation, a commensurate magnetic structure exists with a ferromagnetic component along b and an antiferromagnetic component along c.

DOI: 10.1103/PhysRevB.96.104420

I. INTRODUCTION

The rich physics of magnetically frustrated systems, although studied theoretically and experimentally for half a century [1,2], continues to attract interest in condensed matter research. Frustration is imposed either by the geometry of the spin lattice or by competing interactions. In either case, the system can not minimize all interaction energies simultaneously. One possible outcome is a magnetically disordered and highly degenerate state where the system fluctuates between many different configurations down to very low temperatures. In this case, one encounters exotic materials such as spin ices [3] and quantum spin liquids [4] displaying magnetic monopoles and spinon excitations. Alternatively, a frustrated system may find an ordered configuration in which the interaction terms in the spin Hamiltonian are not all minimized. This often brings about noncollinear and/or incommensurate magnetic structures [5]. In turn, these structures are closely linked to multiferroicity, magnetostriction, and magnetoelectricity [5], just to mention a few profound curiosities of technological and fundamental interest. The symmetries of the nuclear and magnetic structures govern how the individual material properties are manifested. Finally, in combination with disorder, frustrated interactions may ultimately result in spin glasses where spin directions are frozen in at random [6].

The lithium orthophosphates, $LiMPO_4$ (M = Co, Ni, Mn, Fe), are a family of compounds with orthorhombic symmetry (space group *Pnma*) which all exhibit commensurate antiferromagnetism as well as the magnetoelectric effect in their ground states [7,8]. In these materials, the coupling between ferroelectricity and antiferromagnetism is governed by the magnetic structure [8,9], the details of which are also believed to explain the effect in $LiCoPO_4$ [10,11]. Previously it has been shown that the magnetoelectric effect in $LiNiPO_4$ is closely related to a field-induced spin canting facilitated by the Dzyaloshinskii-Moriya interaction [12]. The magnetoelectric effect in $LiCoPO_4$ is by far the strongest in the lithium orthophosphate family [13] but the microscopic mechanism behind it is yet to be understood. We also note that in addition to being exciting magnetoelectric materials, the members of the lithium orthophosphate family, and especially $LiFePO_4$, are of significant scientific and technological interest as cathode materials for batteries [14–16].

$LiCoPO_4$ has cell parameters $a = 10.20$ Å, $b = 5.92$ Å, and $c = 4.70$ Å [17] and the four magnetic Co^{2+} ions ($S = \frac{3}{2}$) of the crystallographic unit cell form an almost face-centered structure with the position vectors $\mathbf{r}_1 = (1/4 + \varepsilon, 1/4, 1 - \delta)$, $\mathbf{r}_2 = (3/4 + \varepsilon, 1/4, 1/2 + \delta)$, $\mathbf{r}_3 = (3/4 - \varepsilon, 3/4, \delta)$, and $\mathbf{r}_4 = (1/4 - \varepsilon, 3/4, 1/2 - \delta)$ where $\varepsilon = 0.0286$ and $\delta = 0.0207$ [18]. The displacement ε of the ions gives rise to a toroidal moment as demonstrated both theoretically [19,20] and experimentally [21,22]. The easy axis for the Co^{2+} ions is along b as deduced from magnetic susceptibility data [23] showing that $LiCoPO_4$ is magnetized twice as readily along b as compared to along a and c in the paramagnetic phase. Furthermore, although the susceptibilities along a and c are of similar magnitude, a is the harder axis. *A priori* density functional theory calculations agree with these measurements [24]. Hence, the single-ion anisotropy of the Co^{2+} ions is largely axial and with the easy axis along b. Below $T_N = 21.6$ K, $LiCoPO_4$ orders antiferromagnetically with spins along the easy axis in a commensurate ($\uparrow\uparrow\downarrow\downarrow$) arrangement [7,25]. Here, $\uparrow$ and $\downarrow$ denote spin up and down, respectively, for the ion sites in forthcoming order, i.e., in the above case spins 1 and 2 are up and spins 3 and 4 are down. In addition, a small spin rotation

*Corresponding author: elfogh@fysik.dtu.dk

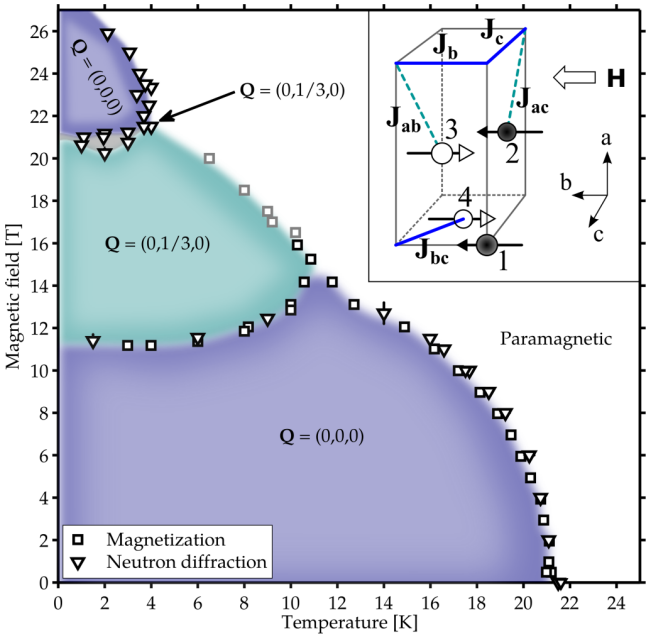

FIG. 1. Magnetic phase diagram of $LiCoPO_4$ for fields up to 25.9 T applied along b as measured by magnetization (square symbols) and neutron diffraction (triangular symbols). The gray symbols are from Ref. [8]. The transition fields and temperatures are determined for increasing fields and upon cooling below 16 T and upon heating above. The propagation vectors identified from neutron diffraction are shown in the respective phases. The zero-field magnetic unit cell with exchange interactions indicated is shown as an inset. Note that only the major spin component along b is shown (see text).

away from the b axis as well as a weak ferromagnetic moment have been reported [10,26,27].

Pulsed-field magnetic susceptibility measurements up to 29 T at liquid He temperatures show a number of phase transitions [28]. At ∼12 T, the magnetization jumps to a plateau of $\frac{1}{3}$ of its saturation value $M_S = 3.6\,\mu_B$/Co ion. Next, at ∼22 T, it gradually increases to $2/3\,M_S$ and then finally increases linearly until saturation is achieved at $\mu_0 H_S = 28.3$ T. The magnetoelectric tensor element α_{ab} was recently probed in a pulsed-field electric polarization experiment ($P_i = \alpha_{ij} H_j$ where $i,j = \{a,b,c\}$, P_i is the induced electric polarization and H_j the applied magnetic field). The measurements show that the phase in the interval 22–28 T supports the magnetoelectric effect but with considerably smaller magnetoelectric coefficient compared to the commensurate low-field phase [29]. The intermediate phase displaying the $\frac{1}{3}$ magnetization plateau does not, on the other hand, exhibit the magnetoelectric effect for the coefficient α_{ab}.

The magnetic exchange interactions of $LiCoPO_4$ are shown in the inset of Fig. 1 together with the magnetic unit cell of the commensurate low-field structure. The interactions in the lithium orthophosphates are generally frustrated leading to a multitude of phases as a function of temperature and applied magnetic field [30–32]. The nearest-neighbor interaction J_{bc} is antiferromagnetic but so are J_b and J_{ab} (terminology adopted from Ref. [33]). The interactions J_c and J_{ac} are weak and may differ in sign depending on the magnetic ion in question [34]. The exchange interactions are mediated via superexchange paths such as M-O-M or M-O-P-O-M [10,11,25]. In Ref. [28], the values of J_{bc}, J_b, and J_c were estimated for $LiCoPO_4$ from the transition field values using a model for the magnetic structures based on magnetization measurements exclusively. Collinear structures with moments along b and propagation vector along c were assumed in all phases. In another study, the spin wave spectrum was measured and although the fitted exchange parameters are subject to large uncertainties, they offer a reasonable estimate for the interactions [35,36].

In this work, we investigate the phase diagram of $LiCoPO_4$ up to 25.9 T for magnetic fields applied along b. We present magnetization and neutron diffraction results for the field-induced transition at 11.9 T. These provide direct evidence that the ordering vector of the phase with $\frac{1}{3}$ magnetization is $\mathbf{Q} = (0,\frac{1}{3},0)$ and the spin arrangement is a superposition of a cycloid structure in the (b,c) plane and a ferromagnetic component. Furthermore, hysteresis is observed as well as pronounced differences in the way the transition occurs depending on field ramp direction. For increasing field, several magnetic Bragg peaks signifying different incommensurate spin structures coexist in the region below the transition, 11.4–11.9 T. For decreasing field, the transition appears abruptly but for a broadening of the commensurate peak at the transition. We also present neutron diffraction results for the phases at 20.5–21.0 T and above 21.0 T. The former has propagation vector $\mathbf{Q} = (0,\frac{1}{3},0)$ too but a different spin orientation compared to the cycloid phase. The latter is commensurate, most likely with a ferromagnetic component along b as well as an antiferromagnetic component along c.

II. EXPERIMENTAL DETAILS

Magnetization measurements were carried out using the vibrating sample method with a standard CRYOGENIC cryogen free measurement system. Magnetic fields of $0 \leqslant \mu_0 H \leqslant 16$ T were applied along the b axis for temperatures in the interval $2\text{ K} \leqslant T \leqslant 300$ K.

Neutron diffraction experiments were performed at the triple-axis spectrometer RITA-II at the Paul Scherrer Institute with a PG(002) vertically focusing monochromator and 80′ collimation between monochromator and sample. The instrument was operated with incoming and outgoing wavelength $\lambda = 4.04$ Å and a cooled Be filter before the analyzer. Vertical magnetic fields up to 15 T were applied along b and momentum transfers were confined to the $(H,0,L)$ plane.

Studies with magnetic fields up to 12 T along the b axis took place at the diffractometer D23 at the Institute Laue-Langevin utilizing neutrons of wavelength $\lambda = 1.279$ Å and with no collimation. A lifting detector and vertical field cryomagnet with asymmetric opening angles allowed for measurements of momentum transfers with significant out-of-plane components. This proved pivotal for identifying the propagation vector in the $\frac{1}{3}$ magnetization phase. For crystal and magnetic structure determination, 86 commensurate peaks were collected at (30 K,0 T), (2 K,0 T), and (2 K,12 T) and 91 incommensurate peaks were collected at (2 K,12 T). Circular diaphragms of 15 and 6 mm were used for peak collection and for high-resolution scans along $(3,K,1)$, respectively.

Further measurements with fields greater than 12 T were performed at the high magnetic field facility for neutron scattering at the Helmholtz-Zentrum Berlin, which consists of the extreme environment diffractometer (EXED) and the high field magnet (HFM) [37–39]. This truly unique horizontal hybrid solenoid magnet allowed for direct probing of all magnetic phases up to 25.9 T dc field. The magnet has 30° conical opening angles, which combined with magnet rotation with respect to the incident neutron beam and the time-of-flight neutron technique implemented on EXED, gives access to a substantial region of reciprocal space. In our case, the crystal was oriented with (0,1,0) and (1,0,1) in the horizontal scattering plane and magnetic fields were applied along the b axis with temperatures in the range 1.1–30 K. Two different magnet and EXED chopper settings were employed for measuring Bragg peaks occurring in the forward scattering and backscattering detectors, respectively: (i) magnet rotation −11.83° with respect to the incoming beam, wavelength band 0.7–1.7 Å (wavelength resolution ∼4%–2%) and (ii) magnet rotation −10.5°, wavelength band 4.8–12.0 Å (wavelength resolution ∼0.6% − 0.2%).

The same high-quality $LiCoPO_4$ single crystal measuring ∼2×2×5 mm^3 (21.4 mg) was used for both magnetization measurements and neutron diffraction experiments. In all cases, the crystal was aligned such that $H \parallel b$ within about 1° except at HFM/EXED where the alignment was within 3°.

III. RESULTS

A. Phase diagram

Using magnetization measurements and by tracking the temperature and field dependencies of selected magnetic Bragg peaks, the magnetic phase boundaries of $LiCoPO_4$ were determined for fields up to 25.9 T applied along b (see Figs. 1 and 2). The phase boundary as a function of temperature for fields in the interval 16–20 T is reproduced from Ref. [8] and fits well with our results. The transition temperature in zero field is found to be $T_N = 21.6(1)$ K in good agreement with literature, and the refined zero-field magnetic structure is consistent with the (↑↑↓↓) configuration of spins along b as previously reported by others [7,10,25]. Field-induced phase transitions were observed at 11.9, 20.5, and 21.0 T at liquid He temperatures. These transition fields correlate reasonably well with features observed in the pulsed-field magnetization data of Ref. [28]. The Curie-Weiss temperature, $\theta_{CW} = 121(1)$ K, was determined from the inverse magnetic susceptibility (not shown) at 0.5 T applied along b. Thus, the frustration parameter [1], $f = \frac{\theta_{CW}}{T_N} \approx 5$, indicates the presence of moderate frustration in the system.

The shape of the phase boundary as a function of temperature is somewhat unusual with the transition temperature being considerably suppressed at 12 T compared to zero field, $T_N(H = 1/3\, H_S) \approx 1/2\, T_N(H = 0)$, and to an even greater extent at 21 T, $T_N(H = 3/4\, H_S) \approx 1/5\, T_N(H = 0)$. In contrast, for the sister compound $LiNiPO_4$, an incommensurate phase exists at higher temperatures for fields up to 17.3 T [12]. In $LiCoPO_4$, however, no phase transition is observed above 10 K at 16 T, neither in the magnetization nor in the heat capacity (not shown here). This explains why the authors of Ref. [29] observed no magnetoelectric effect at 14 K for fields above ∼13 T. Although peculiar compared to the sister compounds, the shape of the phase boundary is similar to that found in other Co^{2+} Ising systems such as $BaCo_2V_2O_8$ [40]. This is true even if crystal structure and single-ion anisotropies differ greatly from those of $LiCoPO_4$.

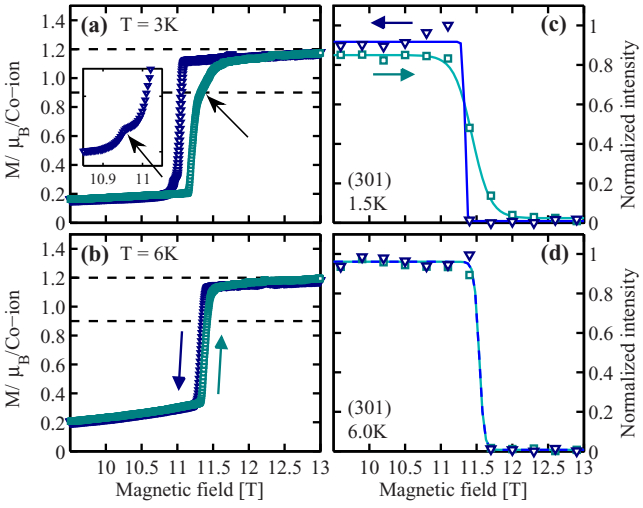

FIG. 2. Magnetization and neutron diffraction data from RITA-II as a function of field for both increasing (green squares) and decreasing (blue triangles) field. (a), (b) Show the magnetization at 3 and 6 K, respectively. The material exhibits hysteresis and the inset and arrows emphasize the special features at 3 K discussed in Sec. III C. These features are absent at 6 K. The dashed lines indicate $\frac{1}{3}$ and $\frac{1}{4}$ of the saturation magnetization. (c), (d) Show the integrated intensity of the magnetic Bragg peak (3,0,1) at 1.5 and 6 K, respectively. The solid lines are guides to the eye. Blue and green arrows indicate the field ramp directions.

B. Magnetic structure at intermediate fields

Neutron diffraction was employed to determine the magnetic structure in the field interval 11.9–20.5 T with $\frac{1}{3}$ magnetization. Having observed the disappearance of the Bragg peaks characteristic of the commensurate low-field phase [see Figs. 2(c) and 2(d)], we searched extensively for Bragg peaks in the $(H,0,L)$ scattering plane but with no success. Hence, the ordering vector is neither along a nor c nor a number of superpositions of those two directions. In the sister compound $LiNiPO_4$ the ordering vector is $(0,K,0)$ with K attaining both rational and irrational values depending on field and temperature [30]. It is therefore tempting to infer that the propagation vector is along b for $LiCoPO_4$ too. However, with the field applied vertically along this direction one needs a magnet with a sufficiently large opening angle and a detector with the ability to measure momentum transfers with finite out-of-plane components. Fortunately, D23 at the Institute Laue-Langevin offers such a setup. High-resolution scans along $(3,K,1)$ were performed at various field strengths and for increasing and decreasing field. Figure 3 shows intensity profiles as a function of K along the $(3,K,1)$ direction at selected field values. Figure 4 shows color plots produced from a series of such scans performed at 2 and 6 K. The ordering vector of the structure was determined to be $\mathbf{Q} = [0,0.33(1),0] \approx (0,\frac{1}{3},0)$ based on Gaussian fits to the observed

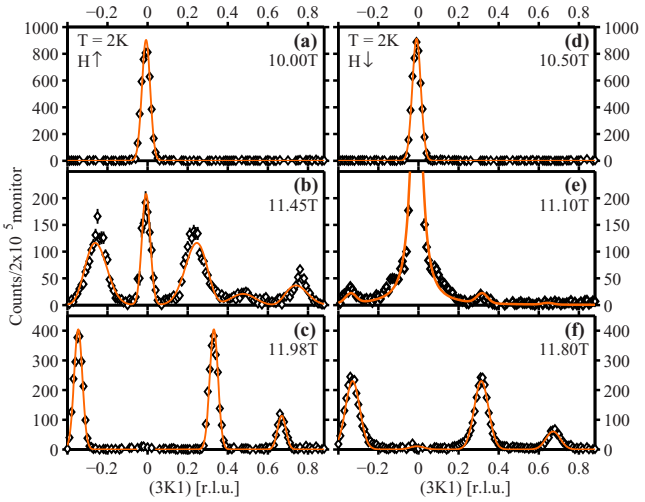

FIG. 3. Neutron scattering intensity as a function of $(3,K,1)$ for selected fields at 2 K for (a)–(c) increasing and (d)–(f) decreasing field. The selected fields are in the low-field commensurate phase (top panels), in the transition region (middle panels), and in the $\mathbf{Q} = (0,\frac{1}{3},0)$ phase (bottom panels). The actual field values are given in the plots. The solid lines are fits to the respective data sets as described in the text.

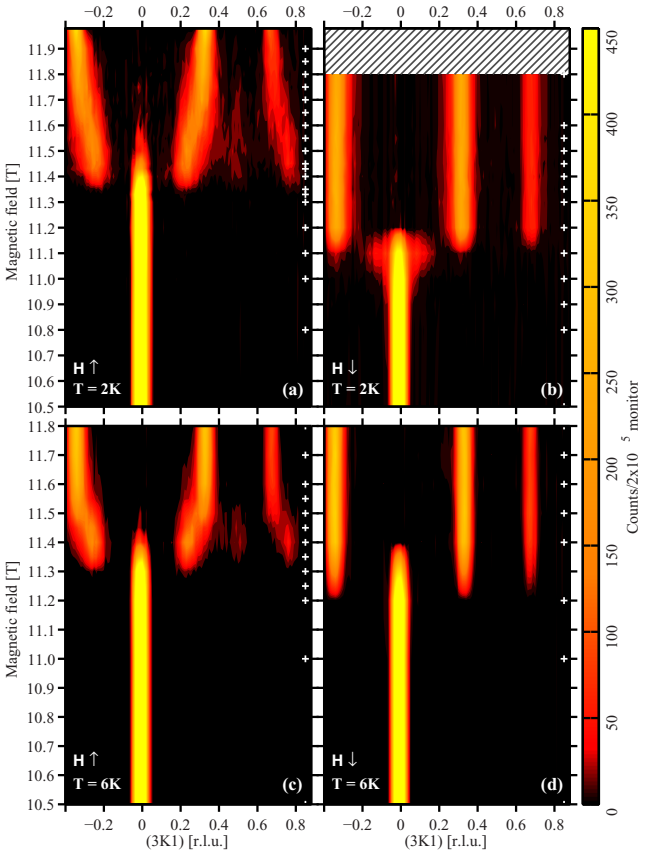

FIG. 4. Color plots of the intensity of $(3,K,1)$ as a function of magnetic field applied along b at (a), (b) 2 K and (c), (d) 6 K for both increasing and decreasing field as measured at D23. The white crosses to the right in each color plot denote the field values for which scans have been performed. Note the relatively few points in (d) and the difference in maximum field between the top and bottom panels. No data were collected in the hatched area.

resolution-limited incommensurate peaks at 2 K and 11.98 T [cf. Fig. 3(c)]. Consequently, the magnetic unit cell in the $\frac{1}{3}$ magnetization phase is tripled along the crystallographic b direction.

From the 91 incommensurate peaks collected at (2 K, 12 T), an elliptic cycloid structure was refined using FULLPROF [41]. Here, all spins on Co sites having identical spatial coordinate y, along the b axis, are aligned and form a ferromagnetic layer in the (a,c) plane. Spins in subsequent layers rotate $\sim$120° in the (b,c) plane upon advancing along the b axis. The ratio between the major and minor axes of the enveloping ellipse is 3.2(5) with the major axis along b. The calculated versus observed intensities are shown in Fig. 5(a). Refinement results for the crystal structure and Fourier components of the magnetic structure are given in Table I.

The $\frac{1}{3}$ magnetization implies an additional ferromagnetic component to be combined with the incommensurate structure. For the cycloid part of the structure there is as always an indeterminable phase shift which in this case has been set to $\pi/3$. This choice maximizes all spin lengths and allows $\frac{1}{3}$ of the spins to be along the easy b axis. The energy cost associated with the single-ion anisotropy is independent of the phase shift angle. Assuming $M_S = 3.6\,\mu_B$ [28] and choosing the phase shift to $\pi/3$ the cycloid and ferromagnetic components result in the structure illustrated in Figs. 5(b) and 5(c).

C. Hysteresis and phase coexistence

Hysteresis is observed both in the magnetization measurements and in the neutron diffraction data at the transition from the low-field collinear phase to the magnetized cycloid phase. At a first-order transition, one expects hysteresis to be present, but in the case of $LiCoPO_4$ the transition is accompanied by additional field ramp direction-dependent characteristics. How this is manifested is described in the following paragraphs.

TABLE I. Atomic positions for $LiCoPO_4$ obtained from FULLPROF refinement ($R_F = 5.23\%$) of 86 commensurate peaks collected at D23 at (30 K, 0 T) and using the *Pnma* space group. The Debye-Waller factor was refined globally to $B_{iso} = 0.08$ and a Becker-Coppens–type extinction correction has been applied. Fourier components for the cycloid formed by the magnetic Co^{2+} ions are given in the two rightmost columns. These were refined ($R_F = 11.1\%$) from 91 incommensurate peaks collected at (2 K, 12 T). R_m and I_m denote the real and imaginary Fourier coefficients, respectively. These correspond to the moment sizes in μ_B along the major and minor axes of the enveloping ellipsoid.

Atom	Site	x	y	z	R_m	I_m
Li	4*a*	0	0	0		
Co	4*c*	0.2771(9)	0.25	0.980(3)	4.13(5)	1.3(2)
P	4*c*	0.0951(6)	0.25	0.414(1)		
O1	4*c*	0.0975(4)	0.25	0.744(1)		
O2	4*c*	0.4542(4)	0.25	0.208(1)		
O3	8*d*	0.1663(2)		0.2814(5)		

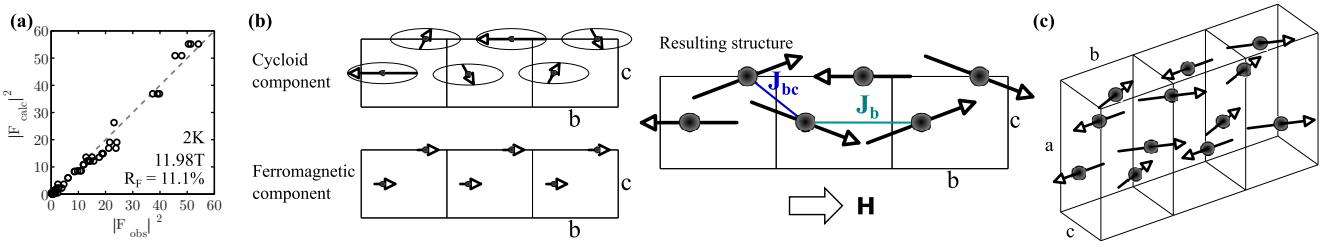

FIG. 5. Refined magnetic structure. (a) Calculated vs observed scattering intensities for the collected incommensurate peaks as obtained in FULLPROF for the refined magnetic structure. The dashed line shows $|F_{\mathrm{calc}}|^2 = |F_{\mathrm{obs}}|^2$. (b), (c) Magnetic structure for 11.9–20.5 T applied along b shown in the (b,c) plane and in 3D, respectively. The spins order in a superposition of an elliptic cycloid and a ferromagnetic component along b. This results in $\frac{2}{3}$ of the spins being almost parallel and $\frac{1}{3}$ being antiparallel to the field direction. In (b) the nearest- and next-nearest-neighbor interactions J_{bc} and J_b are shown.

In the field scans of the magnetization shown in Figs. 2(a) and 2(b), hysteresis is present at 3 K but significantly reduced at 6 K. Furthermore, at 3 K the shape of the magnetization curve depends on the field ramp direction as follows: for increasing field, the transition is first abrupt with the magnetization jumping to $\sim 1/4\, M_S$. Hereafter, it increases approximately linearly until the $\frac{1}{3}$ magnetization plateau is reached. Conversely, for decreasing field the transition is abrupt but the magnetization exhibits a minor bump before the system finally enters the low-field phase. At 6 K only minimal hysteresis is observed and the magnetization curves for increasing and decreasing field are similar to each other with just a single step from the low-field phase to $1/3\, M_S$.

Correspondingly, field scans of the strong (3,0,1) magnetic peak measured by neutron diffraction are shown in Figs. 2(c) and 2(d). At 1.5 K, a transition initiates at $\sim$11.4 T as a function of increasing field strength, in good agreement with earlier findings [28]. For decreasing field, the transition appears at a somewhat lower field $\sim$11.3 T. Again, the curve follows different trends depending on the field ramp direction: for increasing field the transition appears smooth, whereas for decreasing field it is abrupt. At 6 K both hysteresis and any other ramp direction-dependent behavior are absent. The slight differences in the observed transition fields when comparing neutron diffraction data and magnetization measurements may be explained by differences in temperature.

Likewise, hysteresis of about 0.3 T is evident when comparing Figs. 4(a) and 4(b). For increasing field, the transition commences around 11.4 T where the intensity of the commensurate (3,0,1) Bragg peak begins to decrease and peaks appear at $\sim(3, \pm 0.2, 1)$. Upon further increasing the field, they appear to move gradually to $(3, \pm 0.33, 1)$ where they lock in at $\sim$11.9 T. In addition, a less intense peak is observed at $\sim$(3,0.5,1) in the transition region 11.4–11.9 T, where some intensity is also still present at the commensurate position. In this region the incommensurate peaks are broadened and their shapes are asymmetric as can be seen by comparing Figs. 3(b) and 3(c). Above 11.9 T, the peaks become resolution limited and symmetric. We therefore identify 11.9 T as the transition field for increasing fields.

One possible explanation for the observed behavior is incommensurate order with a field-dependent unit-cell size. However, such long-range order would result in resolution-limited symmetric peaks and can therefore be ruled out. The peak broadening indicates finite domain sizes and the line-shape asymmetry may find its origin in overlapping peaks, possibly signifying several structures with different propagation vectors. The seemingly changing peak positions seen in Fig. 4(a) may then be attributed to the change in volume ratio between the different structures involved.

The fit to the 11.45-T scan shown in Fig. 3(b) is based on a model with ordering vectors $\mathbf{Q} = (0, \frac{1}{3}, 0)$, $(0, \frac{1}{4}, 0)$, and $(0, \frac{1}{2}, 0)$. While the $(0, \frac{1}{3}, 0)$ propagation vector is kept fixed at the value found at 11.98 T, the other two are fitted globally to all data sets in the transition region. The peak intensities are allowed to vary between data sets, but the intensities of the two peaks in a pair, $(3, \pm K, 1)$, are kept equal. The globally fitted propagation vectors are $[0, 0.26(1), 0] \approx (0, \frac{1}{4}, 0)$ and $[0, 0.48(3), 0] \approx (0, \frac{1}{2}, 0)$. Several other models were considered, including one involving an additional ordering vector $\mathbf{Q} = (0, \frac{1}{5}, 0)$ and another where the incommensurate peaks were fitted to a single but field-dependent position. Neither of these were successful.

The observation of several propagation vectors in the transition region suggests a substantial degree of frustration and the existence of a number of spin configurations with only small energy differences. Steps in the magnetization accompanied by magnetic structures of rational periods, the so-called devil's staircase, are characteristics of the axial Ising antiferromagnet [42,43]. Even though $LiCoPO_4$ may not be an entirely adequate model material for an Ising system, its spin configurations still seem to occur with rational periods. Hence, such behavior may not be limited to the strict Ising case.

For decreasing field, the transition proceeds entirely differently. For this ramp direction, the incommensurate $(3, \frac{1}{3}, 1)$ peak abruptly gives way to the commensurate (3,0,1) peak at 11.1 T, consistent with the RITA-II and magnetization data [compare Figs. 4(b) and 2(c)]. Note that the incommensurate peaks are wider for decreasing field than the resolution-limited peak measured at 11.98 T for increasing field [compare Figs. 3(c) and 3(f)]. This is likely due to the fact that the field was only ramped to 11.8 T before starting the measurements that produced the data in Fig. 4(b). The peak widths at 11.8 T in Figs. 4(a) and 4(b) are equal within the errors of the fits. In the picture with separate domains with ordering vectors $\mathbf{Q} = (0, \frac{1}{3}, 0)$ and $(0, \frac{1}{4}, 0)$, the system is trapped in the 11.8-T state. This is below 11.9 T where the peaks become resolution limited and the structure is described purely by $\mathbf{Q} = (0, \frac{1}{3}, 0)$.

At 11.1 T, the commensurate (3,0,1) peak is broadened and has a Lorentzian line shape, indicating disorder [see Fig. 3(e)].

Fitting a Lorentzian convoluted with a Gaussian describing the resolution, one can obtain the correlation length as $\xi = \frac{b}{2\pi\kappa}$, where b is the lattice parameter and κ is the Lorentzian width. The resolution is found by fitting the commensurate peak at 10.5 T (well below the transition) to a Gaussian [see Fig. 3(d)]. The correlation length is then found to be ∼120 times smaller just at the transition (11.1 T) compared to below (10.5 T). The observed peak broadening correlates with the bump seen in the magnetization [see Fig. 2(a)].

D. Magnetic structures at high fields

To access fields approaching the saturation field $\mu_0 H_S = 28.3$ T, a neutron diffraction experiment was performed at the HFM/EXED instrument. The maximum field was 25.9 T and thus enabled direct probing of the remaining magnetic phases at high fields indicated by the magnetization data of Ref. [28]. The required crystal orientation and the opening angle of the magnet limited the number of accessible Bragg peaks to $(\bar{3},0,\bar{1})$, $(\bar{2},0,\bar{1})$, $(\bar{1},0,\bar{1})$, $(1,0,\bar{1})$, $(\bar{1},0,0)$, $(0,0,\bar{1})$, and $(0,K,0)$ for $K \lesssim 10$. All peaks except $(0,K,0)$ were observed in the forward scattering detectors and, unfortunately, due to low flux at the required wavelengths, the neutron statistics of these peaks were only sufficient for alignment and confirmation of the zero-field structure. However, magnetic intensity above 20.5 T was observed in the backscattering detectors at the $(0,K,0)$ position. Intensity was found at $K = \frac{4}{3}$ for 20.5–21.0 T and at $K = 1$ above 21.0 T with the two peaks coexisting at 21.0 T. Neutron counts as a function of K along $(0,K,0)$ were obtained by integrating over a slice in reciprocal space of dimensions (given in r.l.u.) $\Delta H = 0.3$ and $\Delta L = 0.2$ and with bin sizes $\Delta K = 1 \times 10^{-3}$ and 3×10^{-3} for $K = 1$ and $\frac{4}{3}$, respectively. Background-subtracted line profiles at selected field strengths are shown in Fig. 6(a) and integrated intensities of $(0,1,0)$ and $(0,\frac{4}{3},0)$ found from Gaussian fits are shown in Figs. 6(b) and 6(c), respectively.

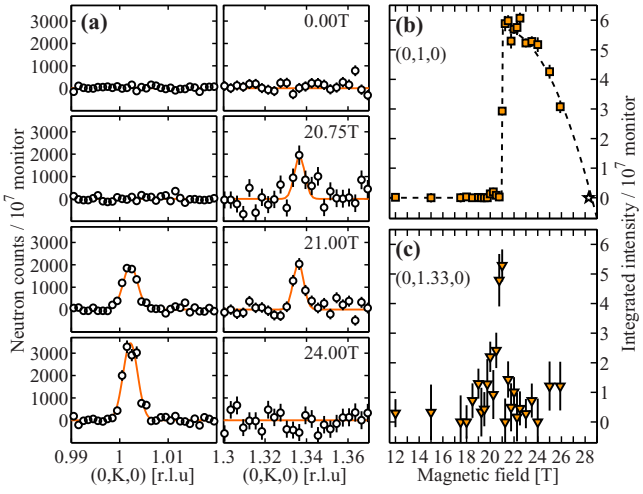

FIG. 6. Neutron diffraction results from HFM/EXED. (a) Neutron counts as a function of $(0,K,0)$ around $K = 1$ (left panels) and $K = \frac{4}{3}$ (right panels) at selected field values. Linear backgrounds have been fitted and subtracted for each data set. The orange lines are subsequential Gaussian fits. (b), (c) Integrated intensity as a function of magnetic field up to 25.9 T of $(0,1,0)$ and $(0,\frac{4}{3},0)$, respectively. The star symbol in (b) shows the expected zero intensity of $(0,1,0)$ at saturation [28]. The dashed line is a guide to the eye.

The ordering vector in the interval 20.5–21.0 T is thus $\mathbf{Q} = (0,\frac{1}{3},0)$. This is the same as for 11.9–20.5 T but the $(0,\frac{4}{3},0)$ Bragg peak was not observed at 12 and 15 T, i.e., it is not present in the cycloid phase. Although the period of the magnetic structure stays the same, the spin orientation must then change around 20.5 T. In Fig. 6(c) the transition appears abrupt, while it seems continuous in the magnetization data of Ref. [28]. One possibility consistent with these observations is a gradual transition from the cycloid to a conical structure with the cone base perpendicular to the propagation vector. In such a structure, the spins rotate in the (a,c) plane and have a ferromagnetic component along the b axis. However, since only a single magnetic Bragg peak was observed, a rigorous structure determination was impossible.

Above 21.0 T the neutron intensity at $(0,\frac{4}{3},0)$ vanishes and a new peak appears at $(0,1,0)$. This peak reflects a commensurate spin structure with symmetry $(\uparrow\uparrow\downarrow\downarrow)$, the same as in the zero-field phase where the spins are predominantly along b. Since neutron scattering is only sensitive to spin components perpendicular to the scattering vector, this Bragg peak is not observed in the zero-field phase. Conversely, the finite peak intensity above 21.0 T implies antiferromagnetic spin components along either a or c instead of b. Both susceptibility measurements and the magnetic structure refinement in the cycloid phase suggest that the c axis is easier than a. Therefore, we infer that above 21.0 T the major antiferromagnetic spin component is along c. In addition, there is a ferromagnetic component with $2/3\,M_S$ at 21.0 T which increases approximately linearly until saturation is achieved at 28.3 T [28]. The magnetic structure above 21.0 T may therefore be described as a magnetized spin-flop structure. The spins rotate towards the b axis with increasing field and the intensity of $(0,1,0)$ decreases with field accordingly. In fact, the field dependence of $(0,1,0)$ is consistent with its complete disappearance at saturation [see Fig. 6(b)].

The Bragg peaks at $(0,\frac{4}{3},0)$ and $(0,1,0)$ coexist in a short field interval [see Fig. 6(a)], suggesting that the phase transition from the $\mathbf{Q} = (0,\frac{1}{3},0)$ to the commensurate phase is of first order. This is also substantiated by hysteresis observed in previous pulsed-field magnetization measurements [28].

IV. DISCUSSION

A. Cycloid structure and a possible magnetoelectric effect

At first glance, the cycloid structure [Figs. 5(b) and 5(c)] seems counterintuitive when regarding the axial single-ion anisotropy and antiferromagnetic nearest-neighbor interactions. Neither exchange nor the single-ion anistropy energies are minimized. However, the deviations of the moments from the b axis remain relatively small such that interacting spin pairs are either nearly antiparallel or parallel. It is also noteworthy that the spins are in the (b,c) plane as opposed to the (a,b) plane, signifying that the energy cost for spins along c is smaller than along a as expected from both susceptibility measurements [23] and density functional theory [24].

$LiCoPO_4$ has a strong magnetoelectric effect in the commensurate low-field phase [9]. Here, an electric polarization

P_a is induced along a for magnetic fields applied along b and vice versa. The magnetoelectric properties of the phase with the $\frac{1}{3}$ magnetization plateau have also been studied with the conclusion that this phase does not display the same magnetoelectric effect [8,29]. However, from symmetry analysis the cycloid structure does actually support a magnetoelectric effect [5] but via a different mechanism: the inverse Dzyaloshinskii-Moriya effect. The direction of the allowed electric polarization is along $\mathbf{Q} \times (\mathbf{S}_i \times \mathbf{S}_j)$, and in the case of the cycloid in $LiCoPO_4$, $\mathbf{Q} \parallel \mathbf{b}$ and $(\mathbf{S}_i \times \mathbf{S}_j) \parallel \mathbf{a}$. Hence, the polarization would be along the c axis for magnetic fields applied along b. To our best knowledge, only P_a was measured in the previous studies and the allowed component P_c has not yet been probed. Therefore, the possibility of a magnetoelectric effect in the $\mathbf{Q} = (0, \frac{1}{3}, 0)$ cycloid structure is not definitely rejected and should be further investigated.

B. Hysteresis and stacking faults

The features observed in the magnetization and the occurrence of the $(3, \frac{1}{3}, 1)$, $(3, \frac{1}{4}, 1)$, and $(3, \frac{1}{2}, 1)$ incommensurate peaks in the interval 11.4–11.9 T are consistent with the behavior of the (3,0,1) intensity as a function of applied field seen in the RITA-II experiment. Similarly, field ramp direction-dependent differences in the curve shapes of the electric polarization were presented in Ref. [29]. Hence, extra features in the transition regime are established in several measurable quantities. Upon increasing the temperature, the effects weaken: at $T \gtrsim 6$ K the difference in curve shape in the magnetization is absent and the transition regime with multiple ordering vectors is largely reduced for increasing field as well as the Lorentzian broadening for decreasing field (compare top and bottom panels in both Figs. 2 and 4). In the following, a relatively simple model based on a mean-field approach is proposed in an attempt to understand these observations.

The magnetic structure above 11.9 T [Figs. 5(b) and 5(c)] provides a starting point for our model. The period of this structure is $n = 3$ (i.e., the size of the magnetic unit cell triples) and spins with the same spatial y coordinate form a layer in the (a,c) plane. The spins of each layer are then rotated with respect to those in the next layer upon advancing along b. In the present model, we crudely assume that all moments have maximum length, $M_S = 3.6\,\mu_B$, and that they are purely oriented along the easy axis. Hence, the canting of $\sim 20^\circ$ away from the b axis for $\frac{2}{3}$ of the spins is completely ignored here. This structure consists of two kinds of layers or building blocks: (i) layers with spins parallel to b and (ii) layers with spins antiparallel to b. Each crystallographic unit cell consists of two such layers. These blocks are denoted "+" and "−," respectively, and the $n = 3$ structure can then be described by the stacking sequence $[++-++-]$.

Additional magnetic structures are now constructed from the same building blocks such that they have period $n \in \mathbb{N}$ for $n > 1$ and magnetization $(1/n)\,M_S$. This is done by adding or removing layers of $+$ and $-$ in pairs along b. Thus, the $n = 4$ structure becomes $[++-++-+-]$ [see Fig. 7(a)]. It can be described by introducing *stacking faults* to the $n = 3$ structure in analogy with stacking faults in closed packed structures with layer stacking in, e.g., either $ABABAB$ or $ABCABC$ type sequences.

Note that the constructed structures are not associated with a single $(0,1/n,0)$ ordering vector but require higher harmonics for a full description. However, the associated Bragg peaks are too weak to be detected in our experiment. Furthermore, sufficiently large domains of a structure of period n must exist in the sample in order to observe an $(0,1/n,0)$ ordering vector. At this point, it should also be emphasized that the proposed model is not the outcome of a full statistical treatment but rather the proposed stacking fault structures are deliberately chosen to be consistent with experimental observations. It is therefore fully possible that other choices yield similar results. Nevertheless, as we shall see below, this rather crude model provides an explanation of the observed coexistence of several propagation vectors in the transition region.

To describe the energy of the system, the following Hamiltonian is employed:

$$\mathcal{H} = -\sum_{i,j} J_{ij}\,\mathbf{S}_i \cdot \mathbf{S}_j - \mu H \sum_i S_i.$$

Here, only J_{bc} and J_b are taken into account as the remaining exchange constants are generally small in the lithium orthophosphate family [33–35]. Since the easy axis is along b and the assumed spin structures have no components along a or c, no single-ion anisotropy terms are taken into account. H is the strength of the applied field along b and $\mu = g\mu_B S$ with the g-factor $g \approx 2$, the Bohr magneton μ_B, and $S = \frac{3}{2}$. The energy per Co^{2+} ion of the assumed stacking fault structures with period n is then

$$E_n = \frac{1}{n}([2(n-2)J_{bc} + (4-n)J_b]S^2 - \mu H), n > 2,\ n \in \mathbb{N}.$$

The zero-field structure, i.e., $n = 1$ (see Fig. 1), has the energy per ion $E_1 = (2J_{bc} - J_b)S^2$. By solving $E_1 = E_n$ one can determine the transition field from the zero-field structure to any stacking fault structure accordingly:

$$H_C = \frac{4S^2}{\mu}(-J_{bc} + J_b), \quad n > 2,\ n \in \mathbb{N}.$$

Peculiarly, the transition field is independent of the period n and, hence, all configurations of this particular kind are degenerate exactly at the phase transition. The energy difference between any two states m and n is readily calculated:

$$E_m - E_n = \left(\frac{m-n}{nm}\right)\mu\,(H - H_C),\ n,m > 2,\ n,m \in \mathbb{N}.$$

Hence, the energy difference does not depend directly on exchange interactions but merely on m and n as well as the field deviation from the transition value.

A short note on the $n = 2$ state is in place since the above calculations are only valid for $n > 2$. For $n = 2$ the stacking sequence results in a different expression for the energy, $E_2 = -\frac{1}{2}\mu H$, and a larger transition field follows. It is therefore unlikely that this structure is realized. Alternatively, the $n = 2$ Bragg peak seen in Fig. 4(a) could be due to nuclear distortion linked to the $n = 4$ magnetic structure or simply a completely different magnetic structure with period $n = 2$. An x-ray or polarized neutron experiment is needed in order to clarify this point.

Assuming $J_{bc} \approx 2J_b$ and using the measured transition field of 11.9 T, the nearest-neighbor coupling strength is estimated

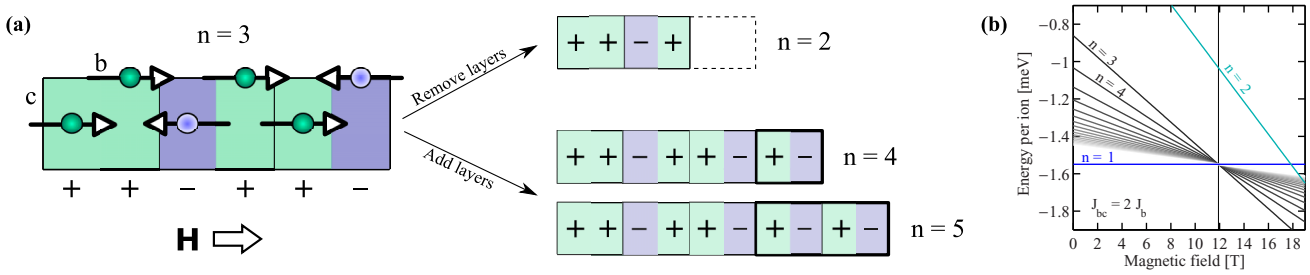

FIG. 7. Stacking faults. (a) Possible stacking fault structures with period $n \in \mathbb{N}$ for $n > 1$ and with magnetization $(1/n)\,M_S$. Spin direction is denoted by the ion color: green (along b) and blue (along $\bar{b}$). Only one layer of ions in the (b,c) plane is shown here. (b) Energy per magnetic ion as a function of applied field calculated from the stacking fault structures. $J_{bc} = 2J_b$ is assumed. The zero-field energy E_1 is shown with the solid blue line and $E_n \to E_1$ for $n \to \infty$. The energies for $n > 2$ cross at this level exactly at the transition field $H_C = 11.9$ T as shown with the vertical line.

to $J_{bc} \approx -0.46$ meV. With this assumption, energies for different n configurations are shown as a function of applied field in Fig. 7(b). The estimate of the relative strengths of J_{bc} and J_b is based on the other members of the lithium orthophosphate family [33,34,44,45]. The resulting value of the nearest-neighbor interaction is remarkably close to those found in $LiFePO_4$ [$J_{bc} = -0.46(2)$ meV [44]] and $LiMnPO_4$ [$J_{bc} = -0.48(5)$ meV [45]] and reasonably close to that measured for $LiCoPO_4$ [$J_{bc} = -0.7(2)$ meV [35,36], note the large uncertainty]. Additionally, in Ref. [28] the nearest-neighbor interaction of $LiCoPO_4$ was estimated to $J_{bc} = -0.23$ meV. However, this result is based on an incorrect magnetic propagation vector explaining the discrepancy from our result. It is worth emphasizing here that our result is obtained merely from a few simple but reasonable assumptions together with the measured transition field value.

It is clear from Fig. 7(b) that the energy difference between different m and n states is small close to the transition field. Hence, at low temperatures the thermal relaxation time may be sufficiently long such that regions of the sample are trapped in states with $n \neq 3$ in agreement with the observation of $n = 4$ order in the transition interval 11.4–11.9 T. At 11.9 T the $n = 3$ structure stabilizes and the other structures withdraw. At higher temperatures, the system is assisted by thermal fluctuations and rapidly finds its stable configuration. Thus, based on the disappearance of hysteresis at higher temperatures ($T \gtrsim 6$ K), it is suggested that more states, e.g., $n = 5,6$, may be populated at very low temperatures (mK regime) and that the hysteresis region is significantly expanded. Further experiments are needed in order to falsify or substantiate this hypothesis.

For decreasing field, the transition to the low-field antiferromagnetic ground state occurs abruptly even at low temperatures. A broadening of the commensurate Bragg peak is observed in a short-field interval at the transition around 11.1 T. Although very speculative, it may be suggested to originate from long-wavelength stacking fault structures like those introduced above, i.e., for $n \gg 1$. When a large number of [+−] layer pairs are added, the magnetization approaches zero and the structure resembles the zero-field structure.

The reason for the transition to occur more readily for decreasing field as compared to increasing field remains unexplained, but an analogy may be found in the water solid-liquid transition. Upon heating water ice it slowly melts when the temperature is above 0 °C. However, because of the need for nucleation sites, upon cooling, liquid water can reach temperatures below the freezing temperature (supercooling) before suddenly entering the ice phase. In this analogy, heating corresponds to increasing field.

C. Commensurability and magnetoelectric effect

Although only a single magnetic peak was observed above 21.0 T, it is possible to argue that the magnetic structure in this high-field phase is a commensurate, magnetized spin-flop structure with the same main antiferromagnetic symmetry component (↑↑↓↓) as the zero-field structure. Remarkably, this phase is magnetoelectric as was recently reported by Kharchenko *et al.* [29]. They found that an electric polarization P_a is induced along the a axis for a magnetic field applied along b. Thus, the active magnetoelectric tensor element α_{ab} is the same as in the low-field phase but ∼5 times weaker. Such reentrant magnetoelectric behavior has previously been observed in the sister compound $LiNiPO_4$ [29,32]. In Ref. [32], it was shown that an extension of the microscopic model explaining the low-field magnetoelectric effect succeeds in accounting for the high-field effect too. In $LiCoPO_4$ there is of yet no such microscopic model, but the two compounds have one characteristic in common: the magnetoelectric effect is linked to commensurate magnetic structures. This is interesting since other magnetoelectric materials such as Cr_2BeO_4 [46] and RMn_2O_5 [47] (R = rare earth) generally display incommensurate magnetic structures [5]. However, when recalling the above discussion on the possibility of a magnetoelectric effect in the cycloid structure, it appears that $LiCoPO_4$ may support a magnetoelectric effect for both commensurate and incommensurate structures. If this is the case, the effects are most likely caused by two different mechanisms.

V. CONCLUSIONS

We studied the phase diagram of $LiCoPO_4$ for fields up to 25.9 T applied along b using magnetization measurements and neutron diffraction. The magnetic structure for 11.9–20.5 T was determined. The ordering vector is $\mathbf{Q} = (0, \frac{1}{3}, 0)$, demonstrating a tripling of the magnetic unit cell in the b direction. The spin configuration is an elliptic cycloid with spins in the

(b,c) plane in superposition with a ferromagnetic component. The ratio of the major and minor axes is 3.2(5) with the major axis along b. The resulting structure has the spin direction alternating with $\frac{2}{3}$ of the spins almost parallel to and $\frac{1}{3}$ antiparallel to the field, consistent with the observed $\frac{1}{3}$ magnetization plateau [28]. This structure maintains the axial single-ion anisotropy character of $LiCoPO_4$. Furthermore, the refined structure allows for a magnetoelectric effect with an electric polarization induced along c for magnetic fields applied along b. The existence of this effect is still to be rejected or confirmed by further measurements.

The transition from the low-field to the cycloid phase exhibits hysteresis and the way the transition proceeds depends heavily on the field ramp direction. For increasing field, we have evidence for three coexisting propagation vectors: $\mathbf{Q} = (0, \frac{1}{4}, 0)$, $\mathbf{Q} = (0, \frac{1}{3}, 0)$, and $\mathbf{Q} = (0, \frac{1}{2}, 0)$, in the field interval 11.4–11.9 T. The occurrence of the additional ordering vectors may be rationalized by introducing stacking faults in the cycloid structure leading to states sufficiently close in energy to be populated until a single phase stabilizes at 11.9 T. For decreasing field, the transition is more abrupt and the commensurate peak has a Lorentzian line shape at the transition.

We identified further phase transitions at 20.5 and 21.0 T and determined the corresponding propagation vectors. In the field range 20.5–21.0 T the propagation vector is $\mathbf{Q} = (0, \frac{1}{3}, 0)$ but the spin orientation is different compared to the cycloid phase. Above 21.0 T, the structure is commensurate with an antiferromagnetic component along c as well as a ferromagnetic component along b.

ACKNOWLEDGMENTS

We greatly acknowledge N. H. Andersen for many fruitful discussions and O. Rivin, X. Liu, R. Wahle, and S. Gerischer for their support at the HFM/EXED facility at the Helmholtz-Zentrum Berlin. This work was supported by the Danish Agency for Science and Higher Education under DANSCATT. Neutron experiments were performed at the Swiss spallation neutron source SINQ at the Paul Scherrer Institute, Villigen, Switzerland, at the research reactor at the Institut Laue-Langevin, Grenoble, France and at the BER II research reactor at the Helmholtz-Zentrum Berlin, Germany. Research at Ames Laboratory is supported by the U.S. Department of Energy, Office of Basic Energy Sciences, Division of Materials Sciences and Engineering under Contract No. DE-AC02-07CH11358.

[1] A. P. Ramirez, Strongly geometrically frustrated magnets, Annu. Rev. Mater. Sci. **24**, 453 (1994).

[2] L. Balents, Spin liquids in frustrated magnets, Nature (London) **464**, 199 (2010).

[3] M. J. Harris, S. T. Bramwell, D. F. McMorrow, T. Zeiske, and K. W. Godfrey, Geometrical Frustration in the Ferromagnetic Pyrochlore $Ho_2Ti_2O_7$, Phys. Rev. Lett. **79**, 2554 (1997).

[4] P. W. Anderson, Resonating valence bonds: A new kind of insulators? Mater. Res. Bull. **8**, 153 (1973).

[5] T. Kimura, Spiral magnets as magnetoelectrics, Annu. Rev. Mater. Res. **37**, 387 (2007).

[6] K. Moorjani and S. K. Ghatak, Random exchange interactions and the "frustration effect," Solid State Commun. **26**, 357 (1978).

[7] R. P. Santoro, D. J. Segal, and R. E. Newnham, Magnetic properties of $LiCoPO_4$ and $LiNiPO_4$, J. Phys. Chem. Solids **27**, 1192 (1966).

[8] H. Wiegelmann, Magnetoelectric effects in strong magnetic fields, Ph.D. thesis, Universität Konstanz, 1994.

[9] M. Mercier, Étude de l'effet magnetoelectrique sur de composés de type olivine, perovskite et grenat, Ph.D. thesis, Université de Grenoble, 1969.

[10] D. Vaknin, J. L. Zarestky, L. L. Miller, J.-P. Rivera, and H. Schmid, Weakly coupled antiferromagnetic planes in single-crystal $LiCoPO_4$, Phys. Rev. B **65**, 224414 (2002).

[11] I. Kornev, M. Bichurin, J.-P. Rivera, S. Gentil, H. Schmid, A. G. M. Jansen, and P. Wyder, Magnetoelectric properties of $LiCoPO_4$ and $LiNiPO_4$, Phys. Rev. B **62**, 12247 (2000).

[12] T. B. S. Jensen, N. B. Christensen, M. Kenzelmann, H. M. Rønnow, C. Niedermayer, N. H. Andersen, K. Lefmann, J. Schefer, M. Zimmermann *et al.*, Field-induced magnetic phases and electric polarization in $LiNiPO_4$, Phys. Rev. B **79**, 092412 (2009).

[13] W. S. Wieglhofer and A. Lakhtakia, *Introduction to Complex Mediums for Optics and Electromagnetics* (SPIE, Bellingham, WA, 2003).

[14] A. K. Padhi, K. S. Nanjundaswamy, and J. B. Goodenough, Phospho-olivines as positive-electrode materials for rechargeable lithium batteries, J. Electrochem. Soc. **144**, 1188 (1997).

[15] K. Amine, H. Yasuda, and M. Yamachi, Olivine $LiCoPO_4$ as 4.8 V electrode material for lithium batteries, Electrochem. Solid-State Lett. **3**, 178 (2000).

[16] S.-Y. Chung, J. T. Bloking, and Y.-M. Chiang, Electronically conductive phospho-plivines as lithium storage electrodes, Nat. Mater. **1**, 123 (2002).

[17] R. E. Newnham and M. J. Redman, Crystallographic data for $LiMgPO_4$, $LiCoPO_4$ and $LiNiPO_4$, J. Am. Ceram. Soc. **48**, 547 (1965).

[18] F. Kubel, Crystal structure of lithium cobalt double orthophosphate, $LiCoPO_4$, Z. Kristallogr.-Cryst. Mater. **209**, 755 (1994).

[19] C. Ederer and N. A. Spaldin, Towards a microscopic theory of toroidal moments in bulk periodic crystals, Phys. Rev. B **76**, 214404 (2007).

[20] N. A. Spaldin, M. Fiebig, and M. Mostovoy, The toroidal moment in condensed-matter physics and its relation to the magnetoelectric effect, J. Phys.: Condens. Matter **20**, 434203 (2008).

[21] B. B. Van Aken, J.-P. Rivera, H. Schmid, and M. Fiebig, Observation of ferrotoroidic domains, Nature **449**, 702 (2007).

[22] A. S. Zimmermann, D. Meier, and M. Fiebig, Ferroic nature of magnetic toroidal order, Nat. Commun. **5**, 4796 (2014).

[23] J. G. Creer and G. J. Troup, The magnetic susceptibility of $LiFePO_4$ and $LiCoPO_4$, Phys. Lett. A **32**, 439 (1970).

[24] K. Yamauchi and S. Picozzi, Magnetic anisotropy in li-phosphates and origin of magnetoelectricity in $LiNiPO_4$, Phys. Rev. B **81**, 024110 (2010).

[25] A. Szewczyk, M. U. Gutowska, J. Wieckowski, A. Wisniewski, R. Puzniak, R. Diduszko, Y. Kharchenko, M. F. Kharchenko, and H. Schmid, Phase transitions in single-crystalline magnetoelectric $LiCoPO_4$, Phys. Rev. B **84**, 104419 (2011).

[26] J.-P. Rivera, The linear magnetoelectric effect in $LiCoPO_4$ revisited, Ferroelectrics **161**, 147 (1994).

[27] Y. Kharchenko, N. Kharchenko, M. Baran, and R. Szymczak, *Magnetoelectric Interaction Phenomena in Crystals (MEIPIC-5)*, edited by M. Fiebig, V. V. Eremenko, and I. E. Chupis (Kluwer-Academic, Dordrecht, 2004), p. 227.

[28] N. F. Kharchenko, V. M. Khrustalev, and V. N. Savitskii, Magnetic field induced spin reorientation in the strongly anisotropic antiferromagnetic crystal $LiCoPO_4$, Low Temp. Phys. **36**, 558 (2010).

[29] V. M. Khrustalyov, V. M. Savytsky, and M. F. Kharchenko, Magnetoelectric effect in antiferromagnetic $LiCoPO_4$ in pulsed magnetic fields, Low Temp. Phys. **42**, 280 (2016).

[30] R. Toft-Petersen, J. Jensen, T. B. S. Jensen, N. H. Andersen, N. B. Christensen, C. Niedermayer, M. Kenzelmann, M. Skoulatos, M. D. Le, K. Lefmann *et al.*, High-field magnetic phase transitions and spin excitations in magnetoelectric $LiNiPO_4$, Phys. Rev. B **84**, 054408 (2011).

[31] R. Toft-Petersen, N. H. Andersen, H. Li, J. Li, W. Tian, S. L. Bud'ko, T. B. S. Jensen, C. Niedermayer, M. Laver, O. Zaharko, J. W. Lynn, and D. Vaknin, Magnetic phase diagram of magnetoelectric $LiMnPO_4$, Phys. Rev. B **85**, 224415 (2012).

[32] R. Toft-Petersen, E. Fogh, T. Kihara, J. Jensen, K. Fritsch, J. Lee, G. E. Granroth, M. B. Stone, D. Vaknin, H. Nojiri, and N. B. Christensen, Field-induced reentrant magnetoelectric phase in $LiNiPO_4$, Phys. Rev. B **95**, 064421 (2017).

[33] T. B. S. Jensen, N. B. Christensen, M. Kenzelmann, H. M. Rϕnnow, C. Niedermayer, N. H. Andersen, K. Lefmann, M. Jiménez-Ruiz, F. Demmel, J. Li *et al.*, Anomalous spin waves and the commensurate-incommensurate magnetic phase transition in $LiNiPO_4$, Phys. Rev. B **79**, 092413 (2009).

[34] R. Toft-Petersen, M. Reehuis, T. B. S. Jensen, N. H. Andersen, J. Li, M. D. Le, M. Laver, C. Niedermayer, B. Klemke, K. Lefmann, and D. Vaknin, Anomalous magnetic structure and spin dynamics in magnetoelectric $LiFePO_4$, Phys. Rev. B **92**, 024404 (2015).

[35] W. Tian, J. Li, J. W. Lynn, J. L. Zarestky, and D. Vaknin, Spin dynamics in the magnetoelectric effect compound $LiCoPO_4$, Phys. Rev. B **78**, 184429 (2008).

[36] We have examined crystals from the same batch as that used in Ref. [35] and find a significantly lower transition temperature $T_N = 17.3(1)$K. Furthermore, a Rietveld refinement of our neutron diffraction data yields satisfactory results exclusively when introducing Ni as well as Co on the magnetic site. Hence, our results suggest that the crystals may not be pure $LiCoPO_4$, but possibly Ni doped from a crucible growth.

[37] P. Smeibidl, M. Bird, H. Ehmler, I. Dixon, J. Heinrich, M. Hoffmann, S. Kempfer, S. Bole, J. Toth, O. Prokhnenko, and B. Lake, First hybrid magnet for neutron scattering at helmholtz-zentrum berlin, IEEE Trans. Appl. Supercond. **26**, 4301606 (2016).

[38] O. Prokhnenko, W.-D. Stein, H.-J. Bleif, M. Fromme, M. Bartkowiak, and T. Wilpert, Time-of-flight extreme environment diffractometer at the Helmholtz-Zentrum Berlin, Rev. Sci. Instrum. **86**, 033102 (2015).

[39] O. Prokhnenko, M. Bartkowiak, W.-D. Stein, N. Stuesser, H.-J. Bleif, M. Fromme, K. Prokes, P. Smeibidl, M. Bird, and B. Lake, in *Proceedings of the 21st Meeting of the International Collaboration on Advanced Neutron Sources (ICANS XXI)* (JAEA, 2016), pp. 278–285.

[40] S. Kimura, M. Matsuda, T. Masuda, S. Hondo, K. Kaneko, N. Metoki, M. Hagiwara, T. Takeuchi, K. Okunishi, Z. He *et al.*, Longitudinal Spin Density Wave Order in a Quasi-1d Ising-Like Quantum Antiferromagnet, Phys. Rev. Lett. **101**, 207201 (2008).

[41] J. Rodriguez-Carvajal, Recent advances in magnetic structure determination by neutron powder diffraction, Phys. B (Amsterdam) **192**, 55 (1993).

[42] P. Bak, One-Dimensional Ising Model and the Complete Devil's Staircase, Phys. Rev. Lett. **49**, 249 (1982).

[43] P. Bak, The Devil's staircase, Phys. Today **39**(12), 38 (1986).

[44] Y. Yiu, M. D. Le, R. Toft-Peterson, G. Ehlers, R. McQueeney, and D. Vaknin, Hybrid excitations due to crystal-field, spin-orbit coupling and spin-waves in $LiFePO_4$, Phys. Rev. B **95**, 104409 (2017).

[45] J. Li, W. Tian, Y. Chen, J. L. Zarestky, J. W. Lynn, and D. Vaknin, Antiferromagnetism in the magnetoelectric effect single crystal $LiMnPO_4$, Phys. Rev. B **79**, 144410 (2009).

[46] R. E. Newnham, J. J. Kramer, W. A. Schulze, and L. E. Cross, Magnetoferroelectricity in Cr_20_4, J. Appl. Phys. **49**, 6088 (1978).

[47] H. Nakamura and K. Kohn, Magnetoelectric effect of rare earth manganese oxide RMn_2O_5, Ferroelectrics **204**, 107 (1997).

Paper III

Dzyaloshinskii-Moriya interaction in magnetoelectric $LiCoPO_4$
E. Fogh, O. Zaharko, J. Schefer, C. Niedermayer, S. Holm-Dahlin, M. K. Sørensen, A. B. Kristensen, N. H. Andersen, D. Vaknin, N. B. Christensen, and R. Toft-Petersen
(To be submitted to Physical Review B)

In this paper, the details of the zero-field magnetic structure in $LiCoPO_4$ are investigated and the magnitude of the Dzyaloshinskii-Moriya interaction is estimated. The analysis on the zero-field structure was largely assisted by Oksana Zaharko (TriCS, PSI).

Dzyaloshinskii-Moriya interaction in magnetoelectric $LiCoPO_4$

Ellen Fogh,[1] Oksana Zaharko,[2] Jürg Schefer,[2] Christof Niedermayer,[2] Sonja Holm-Dahlin,[3] Michael Korning Sørensen,[1] Andreas Bott Kristensen,[1] Niels Hessel Andersen,[1] David Vaknin,[4] Niels Bech Christensen,[1] and Rasmus Toft-Petersen[1]

[1] *Department of Physics, Technical University of Denmark, DK-2800 Kongens Lyngby, Denmark*
[2] *Laboratory for Neutron Scattering and Imaging, Paul Scherrer Institute, Villigen CH-5232, Switzerland*
[3] *Nano-Science Center, Niels Bohr Institute, University of Copenhagen, DK-2100 Copenhagen Ø, Denmark*
[4] *Ames Laboratory and Department of Physics and Astronomy, Iowa State University, Ames, Iowa 50011*

(Dated: November 12, 2018)

Magnetic structures are investigated by means of neutron diffraction in search of the microscopic origin of the magnetoelectric effect in $LiCoPO_4$. At zero field, a spontaneous spin canting of $\varphi = 7(1)^\circ$ is found. The spins tilt away from the easy b-axis towards c. Symmetry considerations lead to the magnetic point group m'_z which is consistent with the observed magnetoelectric effect and weak ferromagnetic moment. For magnetic fields applied along a, the ferromagnetic moment couples via the Dzyaloshinskii-Moriya interaction to yield an additional, field-induced spin canting. An upper limit to the size of the interaction is estimated from the induced canting angle.

I. INTRODUCTION

In a number of insulators, an external electric or magnetic field can induce a finite magnetization or electric polarization respectively. This so-called magnetoelectric (ME) effect was first theoretically predicted[1,2] and shortly thereafter experimentally observed in Cr_2O_3[3,4]. Since then, a selection of materials displaying the ME effect have been identified but the underlying microscopic mechanisms are not yet well understood.

The Dzyaloshinskii-Moriya (DM) interaction has proved to be a key ingredient in explaning the induced or spontaneous electric polarization in a number of compounds such as $R\mathrm{MnO_3}$ (R = Gd, Tb, Dy)[5], $Ni_3V_2O_8$[6] and $CuFeO_2$[7]. In these systems, the non-collinear incommensurate order of the magnetic moments results in a displacement of the oxygen ions situated in between neighboring moments and a net displacement of charge is generated[8]. Non-collinear order may also appear as a consequence of competing interactions, so-called spin frustration. Such systems are associated with large ME effects[8,9].

The DM interaction may also cause a ME coupling in collinear (anti)ferromagnets for magnetic fields applied *perpendicular* to the spin direction. First-principle calculations have shown that the spin-based contributions to the ME tensor, α ($P_i = \alpha_{ij}H_j$ with P_i the electric polarization, H_j the external magnetic field and $i,j = \{a,b,c\}$), are dominant and capture much of the experimental recordings. The computed ME coefficients, $\alpha_\perp$, are consistent with experimental values and the temperature dependence follows that of the (anti)ferromagnetic order parameter[10]. The situation is quite different for magnetic fields applied *along* the the spin direction. Here, *ab initio* calculations based on a Heisenberg exchange model predict $\alpha_{||} \to 0$ for $T \to 0\,\mathrm{K}$[11]. This is indeed the case for e.g. $LiMnPO_4$[12]. However, many collinear magnetoelectrics have a non-zero coupling coefficient, $\alpha_{||}$, at low temperatures (among these are Cr_2O_3, $LiFePO_4$ and $LiCoPO_4$). It was pointed out that the orbital contribution may explain the discrepancy since the moment in $LiMnPO_4$ is completely quenched whereas the orbital moments in $LiFePO_4$ and $LiCoPO_4$ are sizeable. In a recent *ab initio* study of $LiFePO_4$ both lattice and electronic orbital contributions were included. The results are in better agreement with observations at low temperatures than any previous studies but it is clear that there are still some issues[13].

The lithium orthophosphate family (space group $Pnma$), $LiMPO_4$ (M = Co, Ni, Mn, Fe), is in many ways an excellent model system for studying the ME effect. All family members exhibit commensurate antiferromagnetism as well as the ME effect in their low-temperature and low-field ground state and the ME tensor forms are dictated by the magnetic symmetry. Although *ab initio* calculations fail to predict the size and behavior of the tensor components, the temperature dependencies of α_{ij} still suggest two possible driving mechanisms: a spin-based one and an orbital-based one[13]. Furthermore, in recent studies, additional ME phases were found at high magnetic fields applied along the respective easy axes in $LiNiPO_4$[14] and $LiCoPO_4$[15]. In both materials, these high-field ME phases are accompanied by commensurate antiferromagnetic order[14,16].

In this paper, we focus on $LiCoPO_4$ which has, by far, the strongest ME effect in the lithium orthophosphate family[12,17]. Although intensively studied, there is as of yet no satisfactory theory for the underlying microscopic mechanism. $LiCoPO_4$ has lattice parameters $a = 10.20\,\text{Å}$, $b = 5.92\,\text{Å}$ and $c = 4.70\,\text{Å}$[18] and the four magnetic Co^{2+} ions ($S = 3/2$) of the crystallographic unit cell form an almost face-centered structure with the positions $\mathbf{r}_1 = (1/4+\varepsilon, 1/4, 1-\delta)$, $\mathbf{r}_2 = (3/4+\varepsilon, 1/4, 1/2+\delta)$, $\mathbf{r}_3 = (3/4-\varepsilon, 3/4, \delta)$ and $\mathbf{r}_4 = (1/4-\varepsilon, 3/4, 1/2-\delta)$ with the displacements $\varepsilon = 0.0286$ and $\delta = 0.0207$[19]. The zero-field commensurate antiferromagnetic structure of

$LiCoPO_4$ has spins along b (easy axis) and the four magnetic ions in a $C = (\uparrow\uparrow\downarrow\downarrow)$ arrangement[20]. Here $\uparrow/\downarrow$ denotes spin up/down for ions on site number 1-4, see also Table II. The transition temperature is $T_N = 21.6\,\mathrm{K}$[21,22] and the saturation field is $\sim 28\,\mathrm{T}$ with saturated moment $3.6\,\mu_\mathrm{B}/\mathrm{ion}$[23]. A number of studies[22,24–26] establish that the magnetic point group of the zero-field magnetic structure is $2'_x$ rather than mmm' as previously believed[20]. This is based on the observation of a weak ferromagnetic moment[24,25], non-zero elements of the susceptibility of optical second harmonic generation[26] and the discovery of a toroidal moment[9,27–29]. The magnetic phase diagram of $LiCoPO_4$ was previously characterized up to 25.9 T applied along b by magnetization measurements, neutron diffraction and electric polarization measurements[16,23,30]. At 11.9 T, the commensurate low-field structure gives way to an elliptic spin cycloid propagating along b with a period of thrice the crystallographic unit cell. The magnetic moments are in the (b, c)-plane with the major axis along b. In the field interval $20.5 - 21.0\,\mathrm{T}$, the magnetic unit cell remains the same but the spins re-orient. Above 21.0 T, there is a reentrance of commensurate magnetic order accompanied by the ME effect.

Here, we further investigate the zero-field magnetic structure of $LiCoPO_4$ by means of neutron diffraction. A spontaneous canting of spins away from the b-axis towards c is revealed. The resulting structure has magnetic point group m'_z and we discuss the implications related to the ME tensor form and with regards to previous studies. In order to investigate the DM interaction in $LiCoPO4_4$ we performed a neutron diffraction experiments with magnetic fields applied along a, i.e. perpendicular to the spin. The ferromagnetic moment couples via the DM interaction to yield a field-induced spin canting. We estimate the size of the DM interaction and discuss how this interaction may play an important role in explaining the ME effect in $LiCoPO_4$.

II. EXPERIMENTAL DETAILS

Vibrating sample magnetization measurements were performed with a standard CRYOGENIC cryogen free measurement system. Magnetic fields of $0 - 16\,\mathrm{T}$ were applied along a for temperatures in the interval $2 - 300\,\mathrm{K}$.

The zero-field magnetic structure was determined at the TriCS diffractometer at the Paul Scherrer Institute (PSI) employing an Euler cradle, a closed-cycle He refrigerator, open collimation and a Ge(311) monochromator with wavelength $\lambda = 1.18\,\text{Å}$. No $\lambda/2$ contamination of the beam is possible due to the diamond structure of Ge. 193 inequivalent peaks were collected at 30 and 5 K.

Canting components of the zero-field structure could not be unambigiously determined at TriCS due to extinction effects and the large absorption absorption cross section of Co. Instead, these components were investigated at the triple-axis spectrometer RITA-II at the PSI where a low background is obtained by energy discrimination. The instrument was operated in elastic mode with incoming and outgoing wavelength $\lambda = 4\,\text{Å}$. A PG(002) monochromator and 80' collimation between monochromator and sample were used and a liquid nitrogen cooled Be filter after the sample ensured removal of $\lambda/2$ neutrons. A cryomagnet supplied vertical magnetic fields up to 12.2 T along a and b for samples oriented with scattering planes $(0, K, L)$ and $(H, 0, L)$ respectively.

A high quality $LiCoPO_4$ single crystal measuring $2 \times 2 \times 5\,\mathrm{mm}^3$ ($\sim 20\,\mathrm{mg}$) was used for magnetization measurements for magnetic fields applied along a and for neutron diffraction experiments in zero field and with magnetic fields applied along b. A second sample with dimensions $3 \times 4 \times 4\,\mathrm{mm}^3$ ($\sim 40\,\mathrm{mg}$) was used for the neutron diffraction experiment performed with fields applied along a.

III. RESULTS AND DISCUSSION

The atomic and magnetic structures of $LiCoPO_4$ were determined by combining data from the TriCS and RITA-II experiments. Based on the *Pnma* space group and 241 Bragg peaks, atomic displacements of $\varepsilon = 0.0282$ and $\delta = 0.0201$ were refined in Fullprof[31] ($R_F = 11.9\%$) in fair agreement with literature[19]. The zero-field magnetic structure was determined from 130 Bragg peaks and is mainly of C_y symmetry ($R_F = 17.2\%$), a result conforming with earlier findings[20,22]. The refined magnetic moment is $3.54(5)\,\mu_\mathrm{B}$, consistent with previous magnetization measurements[23]. Refinement results are listed in Table I.

Other magnetic structures including a minor spin rotation towards c (C_z) or a spin canting towards c (A_z) were proposed but these refinements were not sufficiently different to distinguish them from the one regarding only a C_y component. Extinction effects and the large neutron absorption cross section of Co result in significantly different intensities for equivalent Bragg peaks and hence,

TABLE I. Atomic positions for $LiCoPO_4$ obtained from Fullprof refinement ($R_F = 11.9\%$) using 241 Bragg peaks collected at TriCS at $(30\,\mathrm{K}, 0\,\mathrm{T})$ and using the *Pnma* space group. The Debye-Waller factor was fixed to $B_\mathrm{iso} = 0.20$. The magnetic moment in μ_B as refined using a C_y symmetry component is given in the rightmost column. This results from refinement ($R_F = 17.2\%$) using 130 commensurate magnetic peaks collected at $(2\,\mathrm{K}, 0\,\mathrm{T})$.

Atom	Site	x	y	z	R_y
Li	4a	0	0	0	–
Co	4c	0.2782(2)	0.25	0.9799(2)	3.54(5)
P	4c	0.0945(8)	0.25	0.4186(2)	–
O1	4c	0.0986(7)	0.25	0.7428(2)	–
O2	4c	0.4545(7)	0.25	0.2034(1)	–
O3	8d	0.1669(5)	0.0463(7)	0.2826(9)	–

TABLE II. Absolute squares of structure and polarization factors for the magnetic basis vectors reflected by the key Bragg peaks used to establish the magnetic structure of $LiCoPO_4$. The factors are normalized to unit spin lengths. Note that the crystallographic directions a, b and c may be used interchangeably with x, y and z.

	$\lvert S_R(\mathbf{Q})\rvert^2$				$\lvert P_i(\mathbf{Q})\rvert^2$		
(H,K,L)	A	G	C	F	x	y	z
	$(\uparrow\downarrow\downarrow\uparrow)$	$(\uparrow\downarrow\uparrow\downarrow)$	$(\uparrow\uparrow\downarrow\downarrow)$	$(\uparrow\uparrow\uparrow\uparrow)$	a	b	c
$(3,0,1)$	0.07	0.22	11.73	3.98	0.34	1	0.66
$(0,1,0)$	0	0	16	0	1	0	1
$(1,0,0)$	15.51	0.49	0	0	0	1	1
$(0,2,1)$	0	15.71	0.29	0	1	0.28	0.72
$(0,1,2)$	0	1.14	14.86	0	1	0.86	0.14
$(0,0,1)$	0	15.71	0.29	0	1	1	0

the TriCS data only enabled identification of the major symmetry component, C_y.

Minor spin components in zero field and for magnetic fields applied along b and a were investigated at RITA-II by measuring a few key Bragg peaks: $(3,0,1)$, $(0,1,0)$, $(1,0,0)$, $(0,2,1)$, $(0,1,2)$ and $(0,0,1)$. Of these only $(0,1,0)$ has zero magnetic intensity. The calculated magnetic structure factors for the four basis vectors, $|S_R(\mathbf{Q})|^2$, $R=\{A,G,C,F\}$, and spin polarization factors, $|P_i(\mathbf{Q})|^2$, $i=\{x,y,z\}$, for these peaks are listed in Table II. The magnetic neutron intensity may be expressed as:

$$I(\mathbf{Q}) \propto S^2\, f(\mathbf{Q})^2 \sum_R |S_R(\mathbf{Q})|^2 \sum_i |P_i(\mathbf{Q})|^2, \qquad (1)$$

where $f(\mathbf{Q})^2$ is the magnetic form factor and S is the thermal average of the magnetic moment. The following analysis is based on a process of elimating possible structures.

A. Spontaneous spin canting at zero field

In addition to the major C_y spin component, a smaller symmetry component was identified by observation of magnetic intensity at the $(1,0,0)$ position. This peak mainly represents magnetic structures of A symmetry with spins polarized along either b or c. It is approximately one order of magnitude weaker than $(3,0,1)$ [compare Figs. 1(a) and 1(b)] which may be assumed to represent the major spin component when regarding the following argument: both $(3,0,1)$ and $(0,1,0)$ appear if a C component is present but the two peaks represent different spin polarizations. $(3,0,1)$ is present for any spin orientation whereas $(0,1,0)$ is only present for components along a or c. Since $(0,1,0)$ has no magnetic intensity [see Fig. 1(c)] we can exclude those two spin directions entirely. Hence, the $(3,0,1)$ magnetic Bragg peak may be assumed to solely represent a C_y spin arrangement.

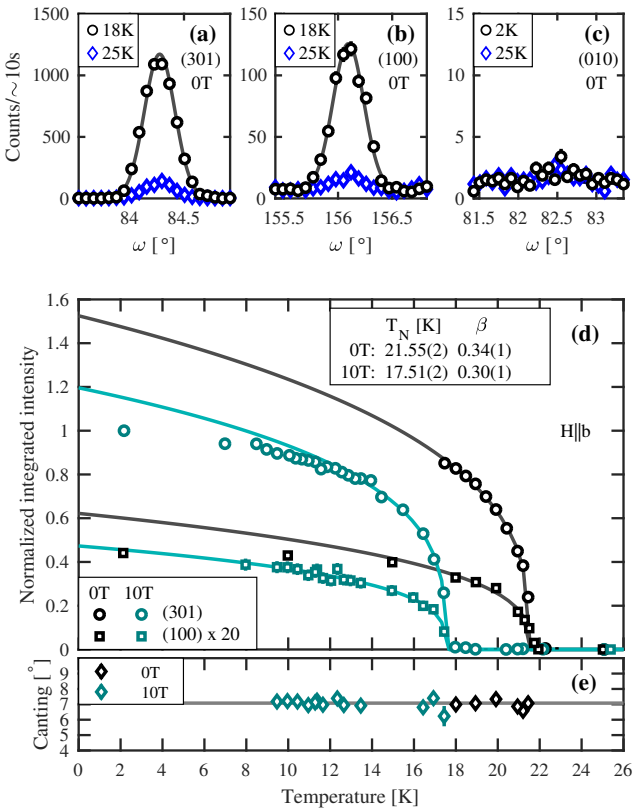

FIG. 1. Neutron diffraction data from RITA-II. (a)-(c) rocking curves of $(3,0,1)$, $(1,0,0)$ and $(0,1,0)$ at 18 or 2 K (black circles) and 25 K(blue diamonds), all at 0 T. The solid lines are Gaussian fits from which the integrated intensities are calculated. The canting angle of the zero-field structure is estimated from the intensity ratio between the magnetic contributions of $(3,0,1)$ and $(1,0,0)$. (d) Integrated magnetic intensity of $(3,0,1)$ (circles) and $(1,0,0)$ (squares) as a function of temperature at 0 T (black symbols) and 10 T along b (green symbols). The intensities have been normalized to the value of $(3,0,1)$ at the lowest temperature and the intensity of $(1,0,0)$ has been multiplied by 20 for a better comparison of the temperature profiles. Backgrounds at 25 K have been subtracted. The solid lines show fits to a power law, $I \propto (T-T_N)^\beta$, for $T > 17$ K at 0 T and $T > 13$ K at 10 T. The transition temperature, T_N, and critical exponent, β, were fitted collectively for the two peaks. (e) Spontaneous canting angle calculated from the intensity ratio of $(1,0,0)$ and $(3,0,1)$ for measurements done at 0 T (black symbols) and 10 T (green symbols). The horizontal line shows the value of the weighted mean of all data points, $\varphi = 7(1)^\circ$.

The thermal average of the spin is most often maximized at low temperatures. Since an A type component with spins along b would produce spins of varying lengths, it is therefore reasonable to assume that the observed magnetic intensity at $(1,0,0)$ is instead due to a spin component along c. The result is a canting of the spins in the (b,c)-plane and the canting angle, φ, can be estimated by comparing the intensities of $(1,0,0)$ with that of $(3,0,1)$. Following the above arguments, it is assumed

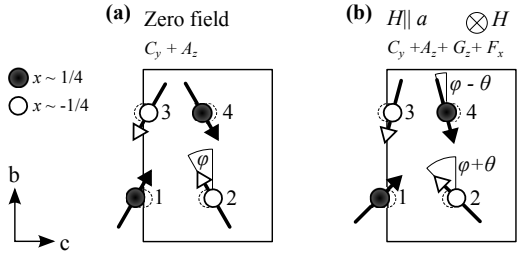

FIG. 2. Projections in the (b, c)-plane of the magnetic structures of $LiCoPO_4$ for (a) zero field and for (b) $H||a$. For clarity, only the four magnetic ions of the unit cell are shown and all angles are largely exaggerated. The ion positions deviate slightly from the high-symmetry positions (dashed circles). The applied field yields asymmetric total canting angles.

TABLE III. Irreducible representations for *Pnma*.

Γ_1	Γ_2	Γ_3	Γ_4	Γ_5	Γ_6	Γ_7	Γ_8
	F_x		G_x	C_x		A_x	
G_y		F_y			A_y		C_y
	G_z		F_z	A_z		C_z	

that $(3, 0, 1)$ represents only a C_y symmetry component and $(1, 0, 0)$ represents only an A_z component such that the measured intensities may be written as in Eq. (1)

$$I_{(1,0,0)} \propto \left|S_A^{(1,0,0)}\right|^2 \left|P_z^{(1,0,0)}\right|^2 f^2_{(1,0,0)},$$
$$I_{(3,0,1)} \propto \left|S_C^{(3,0,1)}\right|^2 \left|P_b^{(3,0,1)}\right|^2 f^2_{(3,0,1)},$$

The spontaneous canting angle is then calculated from the corrected intensities, $I^{\rm corr}_{(1,0,0)}$ and $I^{\rm corr}_{(3,0,1)}$, as $\tan\varphi = \sqrt{I^{\rm corr}_{(1,0,0)}/I^{\rm corr}_{(3,0,1)}}$. The usual Lorentz factor for two-axis diffractometers, $\sin(2\theta)$, is also employed and although not entirely correct for the triple-axis setup[32], the correction is estimated to introduce an error of maximum 10% for the two implicated Bragg peaks. The calculated angle is shown in Fig. 1(e) where both data at 0 T and 10 T along b are shown. The canting angle is temperature independent below the transition temperature and it is also independent of the applied magnetic field. The magnetic structure is thus locked in with a spontaneous canting angle of $\varphi = 7(1)^\circ$ as estimated from a weighed mean of all data points in Fig. 1(e). The resulting zero-field structure is illustrated in Fig. 2(a). Note that the $(3, 0, 1)$ Bragg peak is relatively strong compared to $(1, 0, 0)$ and is therefore, to a larger extent, subject to extinction and absorption effects. Consequently, the calculated angle may be overestimated.

Both $(3, 0, 1)$ and $(1, 0, 0)$ appear at the same transition temperature – see Fig. 1(d) – and therefore reflect the same order parameter. Indeed, a power law with collectively fitted transition temperature, $T_N = 21.55(2)$ K, and critical exponent, $\beta = 0.34(1)$, describe the recorded data well. However, the C type structure polarized along b and the A type structure polarized along b or c are not contained within the same irreducible representation of the lithium orthophosphates, see Table III.

The Bragg peaks $(0, 2, 1)$, $(0, 1, 2)$ and $(0, 0, 1)$ also have magnetic intensity at 0 T. These peaks are all present for a C_y structure but may also represent a G type component polarized along either a or b, see Table II. A G_y component is unlikely due to maximized moments at low temperatures and is not compatible with the observed ME effect, toroidal moment and weak ferromagnetism. Furthermore, G_x is paired with F_z in the irreducible representations, see Table III, and F_z is not present[25]. Therefore, the magnetic intensity at the $(0, 2, 1)$, $(0, 1, 2)$ and $(0, 0, 1)$ positions at 0 T may be subscribed to the major C_y spin component.

It is commented that the determined zero-field structure does not fully agree with earlier findings. A C_z type rotation of the spins away from the b-axis was reported in Ref. 22 based on the observation of the $(0, 1, 0)$ magnetic peak. However, as seen in Fig. 1(c), we observe zero magnetic intensity at the $(0, 1, 0)$ position. A maximum of the rotation angle of $0.7(3)^\circ$ is estimated from the error on the measured zero intensity. This is contrasted by the 4.6° reported in Ref. 22. At present, we have no explanation for the discrepancy.

It has been repeatedly suggested[22,26,33] that the zero-field structure of $LiCoPO_4$ has lower symmetry than the originally proposed magnetic point group mmm'[20]. The observed 4.6° rotation of spins restricts symmetry to $2'_x/m_x$ which is further reduced to $2'_x$ when requiring a weak ferromagnetic component along b. Indeed, optical second harmonic generation measurements advocate that the point group symmetry is $2'_x$[33]. This point group allows for a toroidal moment[34] and the linear ME effect with tensor elements $\alpha_{ab}, \alpha_{ba} \neq 0$[35], consistent with measurements[24]. In addition, $2'_x$ allows the tensor elements $\alpha_{ac}, \alpha_{ca} \neq 0$ which are not measurably different from zero[24] but the spin rotation angle introduces only a small deviation from mmm'. Furthermore, as the point group merely yields the *allowed* ME tensor elements they are not *necessarily* active.

Thus neutron diffraction[22], SQUID[36] and optical second harmonic generation measurements[28,29] all paint a picture of $LiCoPO_4$ having magnetic point group $2'_x$ in its zero-field state. In contrast, our observation of a spontaneous spin canting rather than a rotation leads to the magnetic point group $2_z/m'_z$. This point group also allows for a toroidal moment and the ME tensor elements $\alpha_{aa}, \alpha_{ab}, \alpha_{ba}, \alpha_{bb}, \alpha_{cc} \neq 0$ where only the off-diagonal elements are measurably different from zero. Again, we note that the canting angle only presents a small deviation from mmm'. $2_z/m'_z$ does not support a ferromagnetic moment along b rendering it inconsistent with observations. However, removing the twofold axis enables a ferromagnetic moment in the (a, b)-plane. Thus, the magnetic point group m'_z is consistent with our neutron diffraction data and a weak ferromagnetic moment along

b. Note, however, that it is not consistent with the observed optical second harmonic generation signal[26].

Interestingly, m'_z is also consistent with the previous neutron diffraction study when using a different – but still correct – interpretation of the presented data. The rotation of the spins towards c was established based on observation of the $(0,1,0)$ magnetic Bragg peak. However, this rotation might equally well be towards a. Assuming such a rotation results in magnetic point group $2_z/m'_z$ which again needs relaxing to m'_z to allow for a ferromagnetic moment along b. In addition, the C_x component belongs to the same irreducible representation as the A_z component, see Table III, and as is deducted in the next section, the two components combined yield a favorable energy term via the Dzyaloshinskii-Moriya interaction. Therefore, our observations may in fact be consistent with the previous studies and the magnetic point group of the zero-field structure of $LiCoPO_4$ is m'_z.

B. Field-induced spin canting for H||a

For magnetic fields applied along a, $LiCoPO_4$ is linearly magnetized with the field as seen in the magnetization data in Fig. 3(a). A ferromagnetic contribution to the spin structure is induced with $S^a = \alpha H$ and the fitted slope $\alpha = 0.0395(1)\,\mu_B/\mathrm{T}$. Furthermore, yet another antiferromagnetic component exists in addition to the established main structure of C_y symmetry and the minor A_z component. This extra component is manifested by an increase in the intensity of the $(0,2,1)$ magnetic Bragg peak as a function of applied field, see Fig. 3(b). The magnetic origin of the $(0,2,1)$ intensity is confirmed by its temperature dependency which follows a Curie-Weiss law squared, see Fig. 3(c).

The $(0,2,1)$ peak represents mainly spin arrangements of symmetry G and to a smaller extent structures of symmetry C. All spin orientations are possible, *cf.* Table II, and more information is therefore needed in order to pin down which magnetic structure the additional intensity of $(0,2,1)$ signifies. Again, the argument follows a process of elimination using two other magnetic Bragg peaks: $(0,1,2)$ and $(0,0,1)$.

The $(0,1,2)$ peak is present for any C spin structures. This peak has no additional field-induced intensity [see Fig. 3(b)] and consequently any additional C spin elements are ruled out. Finally, $(0,0,1)$ represents G symmetry with spins polarized along a or b. Again, this peak shows no change upon applying a magnetic field along a [see Fig. 3(b)] and these magnetic structure types may too be rejected. The only remaining possible magnetic structure as a contributor to the $(0,2,1)$ field-induced intensity is then G_z. This component comes as an addition to the already established major C_y component and the smaller A_z component. An asymmetry is introduced in the canting angles such that spins $(1,2)$ and $(3,4)$ form pairs with total canting angles $\phi+\theta$ and $\phi-\theta$ respectively. Here $\theta \equiv \theta(H)$ is the field-induced canting angle. The resulting magnetic structure for magnetic fields applied along a is shown in Fig. 2(b).

The size of θ is now estimated. As previously argued, it may be assumed that at 0 T, $(0,2,1)$ only reflects the C_y structure. Any additional intensity upon applying a field then originates from the G_z component:

$$I_{(0,2,1)}(H) - I_{(0,2,1)}(0\,\mathrm{T}) \propto \left|S_G^{(0,2,1)}\right|^2 \left|P_z^{(0,2,1)}\right|^2.$$

This is to be compared to the intensity of $(0,2,1)$ at 0 T:

$$I_{(0,2,1)}(0\,\mathrm{T}) \propto \left|S_C^{(0,2,1)}\right|^2 \left|P_y^{(0,2,1)}\right|^2.$$

Since only one peak is involved in the determination of the field-induced canting angle there is no need to correct for the magnetic form factor or Lorentz factor and any extinction or absorption effects may be neglected. The field-induced canting angle is then calculated as $\tan\theta = \sqrt{\frac{I^{\mathrm{corr}}_{(0,2,1)}(H) - I^{\mathrm{corr}}_{(0,2,1)}(0\,\mathrm{T})}{I^{\mathrm{corr}}_{(0,2,1)}(0\,\mathrm{T})}}$ and is to a good approximation linear as a function of applied field along a: $\theta = \beta H$ with fitted slope $\beta = 0.012(1)\,\mathrm{rad/T}$, see Fig. 3(a). The field-induced canting angle as deduced from the magnetization, $\sin\theta = M/M_S$, is also shown in Fig. 3(a) and substantiates the link between F_x and G_z. Furthermore, since the neutron intensity is proportional to the square of the ordered magnetic moment, a linear coupling between the ferromagnetic moment and canted moment would result in a quadratic increase in the neutron intensity of $(0,2,1)$ as a function of applied field. This is indeed the case as shown in Fig. 3(b). Here the solid line is a fit to a quadratic dependence, $I \propto H^2$. The measured intensity is clearly well described by the fit. Additionally, the symmetry elements G_z and F_x belong to the same irreducible representation, see Table III.

C. Dzyaloshinskii-Moriya interaction

An estimate of the size of the Dzyaloshinskii-Moriya (DM) interaction in $LiCoPO_4$ may be obtained from the field-induced spin canting. A similar calculation was performed for the sister compound $LiNiPO_4$ and the analysis in Ref. 37 is directly applicable here. Symmetry arguments lead to the only allowed DM coefficients $\mathbf{D}_{14} = (0, D^b_{14}, 0) = -\mathbf{D}_{23}$ and $\mathbf{D}_{12} = (0, D^b_{12}, 0) = \mathbf{D}_{34}$. These yield terms in the Hamiltonian of the form:

$$\begin{aligned}
\mathcal{H}^1_{\mathrm{DM}} &= \mathbf{D}_{14}\cdot(\mathbf{S}_1\times\mathbf{S}_4) - \mathbf{D}_{14}\cdot(\mathbf{S}_2\times\mathbf{S}_3)\\
&= D^b_{14}\left(S^c_1S^a_4 - S^a_1S^c_4 - S^c_2S^a_3 + S^a_2S^c_3\right) \quad \text{and}\\
\mathcal{H}^2_{\mathrm{DM}} &= \mathbf{D}_{12}\cdot(\mathbf{S}_1\times\mathbf{S}_2) + \mathbf{D}_{12}\cdot(\mathbf{S}_3\times\mathbf{S}_4)\\
&= D^b_{12}\left(S^c_1S^a_2 - S^a_1S^c_2 + S^c_3S^a_4 - S^a_3S^c_4\right).
\end{aligned}$$

The spin component along a is finite for $H||a$ and assumed equal at all sites, i.e. $S^a_1 = S^a_2 = S^a_3 = S^a_4 = S^a > 0$. In this case, both terms favor a G_z type order and this is exactly what we observe. The ferromagnetic moment

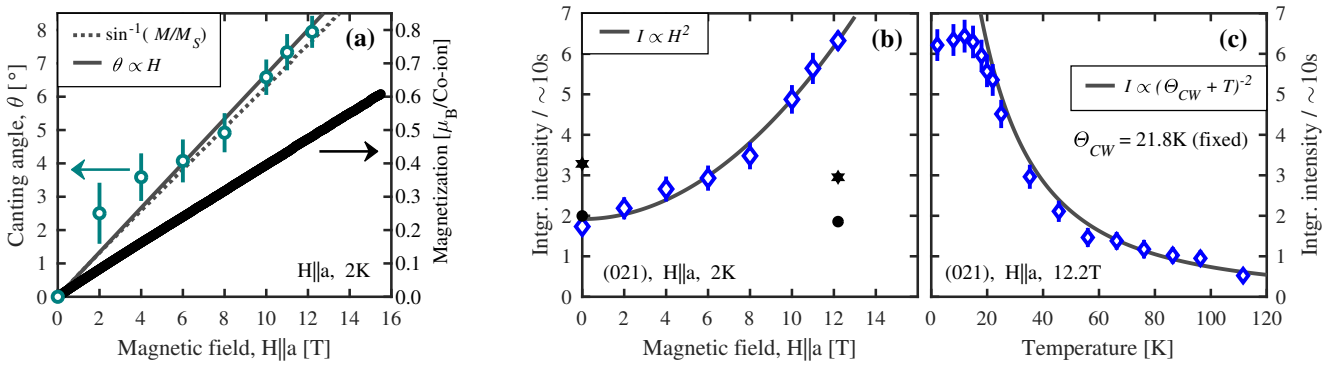

FIG. 3. Magnetization, field-induced canting angle and integrated neutron intensity of $(0, 2, 1)$ for magnetic fields applied along a. (a) magnetization (thick black line) and field-induced canting angle (green circles) calculated from the neutron intensity of $(0, 2, 1)$ as a function of applied field. Both are to a good approximation linearly proportional to the field strength. The solid line shows a linear fit to the canting angle whereas the dashed line shows the angle as calculated from the magnetization with $M_s = 3.6\,\mu_B$/ion. (b) and (c) integrated intensity (blue diamonds) of $(0, 2, 1)$ as a function of applied field at 2 K and as a function of temperature at 12.2 T respectively. The field dependence in (b) and the temperature dependence in (c) have been fitted to a quadratic and a Curie-Weiss law squared respectively (solid lines). The black symbols in (b) show intensities for $(0, 1, 2)$ (circles) and $(0, 0, 1)$ (stars) at 0 T and 12.2 T. Note that the intensities for these peaks are scaled to appear together with the intensity of $(0, 1, 2)$ in order to demonstrate that they show no or only little field dependency.

along a therefore induces – via the DM interaction – an antiferromagnetic spin component of symmetry G_z.

Note that the field-induced G_z component leaves the nearest neighbor spin pairs $(1, 4)$ and $(2, 3)$ antiparallel and hence no energy change is to be expected from the term $\mathcal{H}^1_{\rm DM}$ or from the nearest neighbor exchange term. On the other hand, the term $\mathcal{H}^2_{\rm DM}$ does indeed yield a finite energy contribution for a G_z. The strength of the DM interaction may be estimated by balancing the different energy contributions for spins deviating from the easy axis, b:

$$\left.\begin{aligned}\mathcal{H}_{\rm DM} &= 4D^b_{12}S^a S\sin\theta\\ \mathcal{H}_{\rm ani} &= 4\mathfrak{D}^c S^2\sin^2\theta\end{aligned}\right\} \Rightarrow \frac{D^b_{12}}{\mathfrak{D}^c} = \frac{-S\sin\theta}{S^a} \approx -S\frac{\theta}{S^a},$$

where $\mathfrak{D}^c$ is the single-ion anisotropy constant for spin components along c, $S = 3.6\,\mu_{\rm B}$ the saturated moment, $\sin\theta \approx \theta$ holds for small canting angles, $\theta = \beta H$ and $S^a = \alpha H$. With the fitted coefficients $\beta = 0.012(1)\,{\rm rad/T}$ and $\alpha = 0.0395(1)\,\mu_{\rm B}/{\rm T}$ the ratio becomes $D^b_{12}/\mathfrak{D}^c \approx -1.1$. Note that this is an upper bound for the size of the DM interaction as the above simple calculation neglects any competing exchange interactions which may also influence the spin canting.

Thus, the DM interaction in $LiCoPO_4$ may be as large as the single-ion anisotropy along c. The full spin Hamiltonian of $LiCoPO_4$ has not been determined as of yet, but limited inelastic neutron scattering data shows an almost dispersionless spin excitation along the $(0, K, 0)$ direction and a single-ion anisotropy constant of $\mathfrak{D}^c \approx 2.5\,{\rm meV}$ is suggested[22].

The DM interaction is related to the spin-orbit coupling and as mentioned in the introduction, the spin-orbit coupling is believed to play a role in explaining the large low-temperature ME tensor coefficients in $LiCoPO_4$. Previously, microscopic models based on the DM and exchange interactions were employed to explain the ME effects in $LiFePO_4$[14] and $LiNiPO_4$[14,37] respectively. In fact, there are many similarities between $LiFePO_4$ and $LiCoPO_4$: both have a zero-field magnetic structure with major spin component C_y and smaller component A_z. They both have finite ME tensor elements $\alpha_{ab}, \alpha_{ba} \neq 0$ and it appears that the DM interaction is at the core of explaining the ME effect in both cases[14,37]. However, the temperature dependence of the ME coefficient, α_{ab}, in $LiCoPO_4$ is very different from that of $LiFePO_4$. This emphasizes the need for more theoretical work and improved *ab initio* calculations in order to elucidate the missing mechanism(s) controlling the linear ME effect in $LiCoPO_4$.

IV. CONCLUSIONS

Intricate details of the zero-field magnetic structure of $LiCoPO_4$ were investigated in hope of elucidating the microscopic mechanism behind the large ME effect in $LiCoPO_4$. The Co^{2+} ions mainly order in a commensurate antiferromagnetic structure of C_y symmetry. Additionally, we discovered a spontaneous spin canting of $\varphi = 7(1)^\circ$ originating in a A_z spin component. The resulting zero-field magnetic structure belongs to the magnetic point group m'_z, consistent with previously reported experimental results.

For magnetic fields applied along a, a second minor spin component of symmetry G_z polarized along c is induced. The canting angle increases to a good approximation linearly with the applied field and is shown to be induced via the DM interaction from the ferromagnetic moment along a. The upper limit for the size of the DM

interaction was estimated to be approximately equal to that of the single-ion anisotropy constant for the Co^{2+} ion along c.

ACKNOWLEDGEMENTS

Work was supported by the Danish Agency for Science, Technology and Innovation under DANSCATT. Neutron diffraction experiments were performed at the Swiss spallation neutron source SINQ, Paul Scherrer Institute, Villigen, Switzerland.

[1] L. D. Landau and E. M. Lifshitz. *Electrodynamics of Continuous Media*. Pergamon Press 1960.

[2] I. E. Dzyaloshinskii. On the magneto-electrical effect in antiferromagnets. *J. Exp. Theor. Phys.* **37**, 881-882 (1959).

[3] D. N. Astrov. The magnetoelectric effect in antiferromagnetics. *J. Exp. Theor. Phys.* **38**, 984-985 (1960).

[4] D. N. Astrov. Magnetoelectric effect in chromium oxide. *J. Exp. Theor. Phys.* **40**, 1035-1041 (1961).

[5] I. A. Sergienko and E. Dagotto. Role of the dzyaloshinskii-moriya interaction in multiferroic perovskites. *Phys. Rev. B* **73**, 094434 (2006).

[6] M. Kenzelmann, A. B. Harris, A. Aharony, O. Entin-Wohlman abd T. Yildirim, Q. Huang, S. Park, G. Lawes, C. Broholm, N. Rogado, R. J. Cava, K. H. Kim, G. Jorge, and A. P. Ramirez. Field dependence of magnetic ordering in kagomé-staircase compound $Ni_3V_2O_8$. *Phys. Rev. B* **74**, 014429 (2006).

[7] T. Kimura, J. C. Lashley, and A. P. Ramirez. Inversion-symmetry breaking in the noncollinear magnetic phase of the triangular-lattice antiferromagnet $CuFeO_2$. *Phys. Rev. B* **73**, 220401 (2006).

[8] T. Kimura. Spiral magnets as magnetoelectrics. *Annu. Rev. Mater. Res.* **37**, 387-413 (2007).

[9] N. A. Spaldin, M. Fiebig, and M. Mostovoy. The toroidal moment in condensed-matter physics and its relation to the magnetoelectric effect. *J. Phys. Cond. Matt.* **20**, 434203 (2008).

[10] R. Hornreich and S. Shtrikman. Statistical mechanics and origin of the magnetoelectric effect in Cr_2O_3. *Phys. Rev. B* **161**, 506 (1967).

[11] M. Mostovoy, A. Scaramucci, N. A. Spaldin, and K. T. Delaney. Temperature-dependent magnetoelectric effect from first principles. *Phys. Rev. Lett.* **105**, 087202 (2010).

[12] M. Mercier. *Étude de l'effet magnetoelectrique sur de composés de type olivine, perovskite et grenat.* PhD thesis Université de Grenoble 1969.

[13] A. Scaramucci, E. Bousquet, M. Fechner, M. Mostovoy, and N. A. Spaldin. Linear magnetoelectric effect by orbital magnetism. *Phys. Rev. Lett.* **109**, 197203 (2012).

[14] R. Toft-Petersen, E. Fogh, T. Kihara, J. Jensen, K. Fritsch, J. Lee, G. E. Granroth, M. B. Stone, D. Vaknin, H. Nojiri, and N. B. Christensen. Field-induced reentrant magnetoelectric phase in $LiNiPO_4$. *Phys. Rev. B* **95**, 064421 (2017).

[15] V. M. Khrustalyov, V. M. Savytsky, and M. F. Kharchenko. Magnetoelectric effect in antiferromagnetic $LiCoPO_4$ in pulsed magnetic fields. *Low Temp. Phys.* **42**, 280-285 (2016).

[16] E. Fogh, R. Toft-Petersen, E. Ressouche, C. Niedermayer, S. L. Holm, M. Bartkowiak, O. Prokhnenko, S. Sloth, F. W. Isaksen, D. Vaknin, and N. B. Christensen. Magnetic order, hysteresis, and phase coexistence in magnetoelectric licopo$_4$. *Phys. Rev. B* **96**, 104420 (2017).

[17] W. S. Wieglhofer and A. Lakhtakia. *Introduction to Complex Mediums for Optics and Electromagnetics.* SPIE Press 2003.

[18] R. E. Newnham and M. J. Redman. Crystallographic data for $LiMgPO_4$, $LiCoPO_4$ and $LiNiPO_4$. *J. Am. Ceram. Soc.* **48**, 547 (1965).

[19] F. Kubel. Crystal structure of lithium cobalt double orthophosphate, $LiCoPO_4$. *Zeitschrift für Kristallographie* **209**, 755 (1994).

[20] R. P. Santoro, D. J. Segal, and R. E. Newnham. Magnetic properties of $LiCoPO_4$ and $LiNiPO_4$. *J. Phys. Chem. Solids* **27**, 1192-1193 (1966).

[21] A. Szewczyk, M. U. Gutowska, J. Wieckowski, A. Wisniewski, R. Puzniak, R. Diduszko, Yu. Kharchenko, M. F. Kharchenko, and H. Schmid. Phase transitions in single-crystalline magnetoelectric $LiCoPO_4$. *Phys. Rev. B* **84**, 104419 (2011).

[22] D. Vaknin, J. L. Zarestky, L. L. Miller, J.-P. Rivera, and H. Schmid. Weakly coupled antiferromagnetic planes in single-crystal $LiCoPO_4$. *Phys. Rev. B* **65**, 224414 (2002).

[23] N. F. Kharchenko, V. M. Khrustalev, and V. N. Savitskii. Magnetic field induced spin reorientation in the strongly anisotropic antiferromagnetic crystal $LiCoPO_4$. *Low Temp. Phys.* **36**, 558-564 (2010).

[24] J.-P. Rivera. The linear magnetoelectric effect in $LiCoPO_4$ revisited. *Ferroelectrics* **161**, 147-164 (1994).

[25] Yu. Kharchenko, N. Kharchenko, M. Baran, and R. Szymczak. Weak ferromagnetism in magnetoelectrics $LiCoPO_4$ and $LiNiPO_4$. *Magnetoelectric Interaction Phenomena in Crystals* (227-234) 2003.

[26] B. B. Van Aken, J.-P. Rivera, H. Schmid, and M. Fiebig. Anisotropy of antiferromagnetic 180° domains in $LiCoPO_4$ and $LiNiPO_4$. *Phys. Rev. Lett.* **101**, 157202 (2008).

[27] C. Ederer and N. A. Spaldin. Towards a microscopic theory of toroidal moments in bulk periodic crystals. *Phys. Rev. B* **76**, 214404 (2007).

[28] B. B. Van Aken, J.-P. Rivera, H. Schmid, and M. Fiebig. Observation of ferrotoroidic domains. *Nature Letters* **449**, 702-705 (2007).

[29] A. S. Zimmermann, D. Meier, and M. Fiebig. Ferroic nature of magnetic toroidal order. *Nature Communications* **5**, 4796 (2014).

[30] V. M. Khrustalyov, V. M. Savytsky, and M. F. Kharchenko. (H, T_i)-diagram of magnetic transformations induced by a pulsed magnetic field in antiferromagnetic $LiCoPO_4$. *Low Temp. Phys.* **43**, 1332-1337 (2017).

[31] J. Rodriguez-Carvajal. Recent advances in magnetic structure determination by neutron powder diffraction. *Physica B* **192**, 55-69 (1993).

[32] R. Pynn. Lorentz factors for triple-axis spectrometers. *Acta Cryst.* **B31**, 2555-2556 (1975).

[33] A. S. Zimmermann, B. B. Van Aken, H. Schmid, J.-P. Rivera, J. Li, D. Vaknin, and M. Fiebig. Anisotropy of antiferromagnetic 180° domains in magnetoelectric LiMPO$_4$ (M = fe, co, ni). *Eur. Phys. J. B* **71**, 355-360 (2009).

[34] H. Schmid. Some symmetry aspects of ferroics and single phase multiferroics. *J. Phys. Condens. Matter* **20**, 433201 (2008).

[35] J.-P. Rivera. A short review of the magnetoelectric effect and related experimental techniques on single phase (multi-) ferroics. *eur. Phys. J. B* **71**, 299-313 (2009).

[36] N. F. Kharchenko, Yu. N. Kharchenko, R. Szymczak, M. Baran, and H. Schmid. Weak ferromagnetism in the antiferromagnetic magnetoelectric crystal LiCoPO$_4$. *Low Temp. Phys.* **27**, 895 (2001).

[37] T. B. S. Jensen, N. B. Christensen, M. Kenzelmann, H. M. Rønnow, C. Niedermayer, N. H. Andersen, K. Lefmann, J. Schefer, M. Zimmermann, J. Li, J. L. Zarestky, and D. Vaknin. Field-induced magnetic phases and electric polarization in LiNiPO$_4$. *Phys. Rev. B* **79**, 092412 (2009).

Department of Physics
Fysikvej, Buildings 307-309-311-312
2800 Kongens Lyngby
Tlf. 45 25 33 44
Fax 45 93 23 99

www.fysik.dtu.dk